UNIVERSITÀ DEGLI STUDI DI NAPOLI "FEDERICO II"

Scuola di Dottorato in Scienze della Terra
XXV Ciclo
Tesi di Dottorato in Giacimenti Minerari

Ph.D. School in EARTH SCIENCES - *XXV Cycle*
DOCTORAL THESIS in ECONOMIC GEOLOGY

Supergene Nonsulfide Zinc-Lead Deposits: The Examples of Jabali (Yemen) and Yanque (Peru)

Ph.D. Student
Nicola Mondillo

Supervisors
Prof. Maria Boni
Dr. Giuseppina Balassone

TABLE OF CONTENTS

ABSTRACT

"Nonsulfide zinc" is a very general term, referred to a group of ore deposits consisting of Zn-oxidized minerals, mainly represented by smithsonite, hydrozincite, hemimorphite, sauconite and willemite, which are markedly different from sphalerite ores, typically exploited for zinc. Locally, Ag minerals can occur too. The supergene nonsulfide deposits form from low-temperature oxidation of sulfide-bearing concentrations. Objective of this study is to increase the knowledge on the geology, mineralogy and genetic processes of this kind of supergene zinc-lead ores. Two nonsulfide deposits were taken as example: Jabali in Yemen, and Yanque in Peru, whose characteristics were compared with the peculiarities of other known nonsulfide concentrations. The Jabali and Yanque deposits are totally different from each other, both in geological setting and in mineralogical association. Therefore, the identification of their features and possible genetic mechanisms should cover several characteristics possibly occurring in other deposits of the same kind. A particular attention has been given to the mineralogy of the ores, and to the relationship between the newly formed zinc minerals and the host rock, because the mineralogical characteristics are crucial in order to develop the metallurgical processes.

The Jabali deposit lies in a mountainous desert terrain about 110 km east of Sana'a, the capital of Yemen, along the western border of the Marib-Al-Jawf/Sab'atayn basin. In the Middle Age (7^{th} - 9^{th} century AD) Jabali was considered one of the most important mining areas for silver in the Muslim world. The Jabali nonsulfide concentration has a resource of 8.7 million tonnes at an average grade of 9.2% zinc.
The ore is hosted in the Jurassic carbonate rocks of the Shuqra Fm. (Amran Gp.) and the nonsulfide mineralization derives from the low temperature alteration of the primary sulfide deposit. The primary deposit shows the general features of Mississippi Valley-type ores, and consists of sphalerite, galena, and minor pyrite/marcasite (mainly as remnants) and other minor sulfide phases. Silver, cadmium, copper, arsenic, germanium and mercury are generally contained in sphalerite. Primary ore deposition has been accompanied by several hydrothermal dolomitization phases.
Smithsonite is the most abundant economic ore mineral in the secondary deposit. It occurs in two main phases: Smithsonite 1, which replaces the host dolomite and sphalerite, and Smithsonite 2, which occurs as cements and concretions precipitated in cavities and porosity of the host rock. In the gradational "bands" which mark the boundary between host dolomite and replacive smithsonite, dolomite is widely replaced by Zn-rich dolomite phases, where Zn has substituted for Mg. The ZnO content in this dolomite can reach 17-22 wt.% (~70 mol.% substitution). These phases indicate that the replacement of the host rock proceeded in stages: it started with a partial replacement of Mg by Zn in the dolomite lattice, and went on with a gradually higher amount of substitution of Mg by Zn, until a maximum measured

value of 70 mol.% Zn in the dolomite. Eventually, the dolomite lattice became totally unstable and smithsonite precipitated. Zn-dolomite appears to be an intermediate replacement phase between dolomite and smithsonite.
The Jabali smithsonites have variable $\delta^{18}O$ compositions in different parts the orebody. The measured values are generally lower than those of other supergene smithsonites, whereas the C-isotope composition is in the same range of values of smithsonites from other supergene nonsulfide ores. The $\delta^{18}O$ spread of values for the Jabali smithsonites could indicate: a precipitation from a low-temperature hydrothermal system, similarly to the Angouran (Iran) nonsulfide deposit, or a supergene precipitation from waters with variable O-isotope composition, as hypothesized also for the Coahuila-Sierra Mojada district (Mexico). The C-isotope composition is typical of supergene nonsulfide Zn deposits, and is generally interpreted as a result of mixing between host rock carbonates and soil/atmospheric CO_2. In the case of a low-temperature hydrothermal genesis, these compositions could also indicate the involvement of meteoric-surficial water in a deep, thermal circulation, or organic carbon values not related to soils, e.g. organic matter from black shales.
Another interesting characteristic of the Jabali deposit is the strict association of Ag-sulfides with smithsonite. Ag-sulfides are quite common at Jabali and are locally associated also to secondary greenockite; they mostly occur together with concretionary smithsonite and between lamellae of gypsum derived from weathering processes. They have never been detected in association with primary sulfides, but occur always together with the secondary phases. After literature data, the co-precipitation of Ag-sulfides and smithsonite under atmospheric conditions can happen only at neutral pH, and in an Eh range between 0 and -2 Volts, because the stability fields of the two phases are very near, though not superposed.
Comparing Jabali to other nonsulfide deposits in the world, it is possible to find some similarities with the SW Sardinia “Calamines” (Italy), and with the Upper Silesian ”Galmans” (Poland), because in both districts Zn-dolomite is also fairly abundant. In particular, Jabali shows the same Zn-dolomite replacement fronts of the host dolomite like in SW Sardinia.

The Yanque nonsulfide Zn-Pb deposit (inferred resources 12.5 Mt @ 3.5% Zn and @ 3.7% Pb) is located in the “Accha-Yanque Belt” (southern Peru), about 90 km southwest of the city of Cuzco, within the Andahuaylas-Yauri province.
The Andahuaylas-Yauri province covers an area of approximately 25,000 km^2 in southern Peru and extends for 300 km between the localities of Andahuaylas in the northwest and Yauri in the southeast. The belt hosts numerous Cu-porphyry and porphyry-related skarn deposits, spatially and temporally associated with the middle Eocene to early Oligocene (*ca.* 48-32 Ma) intrusion of the homonymous batholith into the sedimentary successions of Mesozoic age.
The Yanque deposit occurs within a base metal mineralized district, extended for about 20 km^2, which is centered on the Dolores Cu-porphyry. The zinc-lead deposit of Yanque is located 1.5 km west of Dolores Cu-porphyry. Other two small Zn-Pb mineralizations occur less than a kilometer on the east and northeast of the same porphyry. Both sedimentary and

igneous rocks constitute the backbone of the Yanque-Dolores area. The sedimentary lithologies belong to the Soraya, Mara and Ferrobamba Fms. (upper Jurassic-middle Cretaceous). They are bordered by a large apophysis of the Yauri batholith, and by the intrusive porphyries hosting the Dolores mineralization. The Yanque deposit itself is hosted by a complex breccia facies, constituted by a siliciclastic conglomerate in the northern part of the deposit, interfingered with a dolomite breccia more in the south. The breccia is stratigraphically located at the transition between Mara and Ferrobamba Fms. The Yanque economic deposit consists of Zn-Pb nonsulfide concentrations, derived from the secondary alteration of primary sulfides.

The Yanque protore could be considered as a distal polymetallic mineralization, genetically related to the emplacement of the Andahuaylas-Yauri batholith, like other mineral deposits in the region (porphyry copper and skarn). A possible genetical relationship with the nearest Cu-porphyry has been investigated through Pb-isotope geochemistry of ore minerals, as well as of sedimentary and magmatic rocks occurring in the district. The Pb-isotopic compositions of Yanque and Dolores sulfides (pyrite and galena) are similar, and correspond to the isotopic composition of the Tertiary magmatically derived ore bodies in this part of Peru. Looking more in detail, the three Pb-isotope ratios of the sulfides are affected by ubiquitous small but resolvable differences and disequilibria, probably because many components contributed to their final lead isotope signature. Igneous rocks show a large spread in the isotopic composition, possibly indicating variable degrees of country rock assimilation, or different isotopic compositions of the magma pulses. It is possible to resolve significant differences also for the sedimentary rocks sampled at Yanque. It is important to note that the hydrothermal cement, which impregnates these lithotypes, has the same composition of sulfides. Similar values have been detected in the hydrothermally affected igneous rock. This could indicate that the same hydrothermal fluids, which determined the phyllic/sericitic halo around the Cu-porphyry, deposited also the Yanque sulfides. However, the observed significant spread of the Pb isotopic compositions is not compatible with a simple genetic model involving just one fluid circulation episode.

The primary ores have been totally oxidized, and the economic concentrations at Yanque are dominated by supergene Zn-Pb nonsulfides. The remnants of the sulfide minerals are represented by moderate amounts of galena and pyrite, and only by traces of sphalerite. The nonsulfide ore association consists of sauconite, hemimorphite, smithsonite and cerussite. Zinc is allocated mainly in sauconite (Zn-smectite), rather than in carbonates: a factor strictly related to the prevailing siliciclastic character of the Yanque host rock. Sauconite is derived from a typical process of supergene wall-rock replacement and alteration, represented by the reaction:

K-feldspar (detrital) → sericite/illite and kaolinite (hydrothermal) → sauconite (supergene);

sericite/illite and kaolinite are enriched in zinc at the reaction boundaries with the replacing sauconite, this pointing to an almost progressive modification process of clays. Secondary Pb-minerals are mostly linked to direct replacement of galena.

The Zn-Pb Yanque deposit can be compared only with the Skorpion mineralization in Namibia, similarly hosted in silicate rocks. Both have sauconite as main economic mineral,

but it is characterized by different textures. Important differences exist also on the whole mineralogical association (e.g. the occurrence of Cu-secondary minerals at Skorpion, and of secondary Ag-sulfides and enrichments in Fe-hydroxides at Yanque).
Another important issue regards the different mobilization of the metals within the host rock. At Yanque Zn is mostly enriched in the topmost volumes of the orebody, whereas Pb is concentrated in the lowermost levels. Surprisingly, this corresponds to an inverse zonation, compared to usual geometry observed in many other Zn nonsulfide deposits, including Skorpion. In fact, Zn is generally concentrated in the more distal areas of the deposit, whereas Pb, that is less mobile, is accumulated *in situ*, near the sulfide protore. A possible explanation of the inverse zonation at Yanque can arise from the current almost total absence of sphalerite in the mineralized area. Zinc in nonsulfides could have originated from the dissolution of a primary sphalerite-rich ore, located somewhere in the eroded volumes of rock surrounding the actual site, and, after being transported by supergene solutions, migrated and precipitated in the porosity of the host conglomerates. This kind of genesis could bear the genetic concept of a Zn "exotic" mineralization, like those exploited around the Cu-deposit of Chuquicamata (Chile).
The occurrence of sauconite as main ore mineral at Skorpion has been added as an evidence that the deposit formed under semi-arid to arid conditions during several paleo-weathering episodes. Semi-arid climates are generally favorable to the deposition of smectite-type clay minerals: a similar consideration could be valid also for the Yanque sauconite ores.

The geological, mineralogical and geochemical investigation on the Jabali and Yanque deposits has shown that these Zn-Pb nonsulfide concentrations, though being considered to share the mainstream genetic concepts for supergene deposits, have some distinctive characteristics that could be of importance for their scientific as well as economic evaluation. The common occurrence of Zn-dolomite at Jabali is deleterious when considering the economic evaluation of the ore, because it can result in an unaccounted Zn loss. At Yanque, the issue related to the sauconite (which is mixed with other clays too) abundance is not simple to face from the processing point of view.
In conclusion, the nonsulfide Zn-Pb orebodies are a type of deposits far more complex than previously considered. The research carried out on the Jabali (Yemen) and Yanque (Peru) deposits has increased the knowledge on the nature and genetic mechanisms responsible for at least part of this mineralization type. The discovery of Zn-dolomite at Jabali, and of mixed Zn-clays at Yanque, represents an interesting step for a better understanding of the wall-rock replacement process. The observation of unusual C-O-isotope compositions in the Jabali smithsonite enriches the available geochemical "database" of the stable isotopes literature on Zn- and Pb carbonates. All the results of this research work can be a great help in avoiding too many straight simplifications on the nonsulfide characteristics and genesis.

RIASSUNTO

Le mineralizzazioni a nonsolfuri di Zn-Pb-(Ag) sono considerate a tutt'oggi di notevole interesse economico per i loro tenori e per la facilità di estrazione in *open pit*, ma sono spesso caratterizzate da una complessa associazione mineralogica, che può rendere notevolmente oneroso il processo metallurgico dei singoli giacimenti. La presente tesi di dottorato riguarda lo studio geologico, mineralogico e geochimico di due depositi mineralizzati a nonsolfuri di Zn-Pb-(Ag): Yanque (Perù) e Jabali (Yemen). La ricerca ha come principale obiettivo la piena comprensione dei processi genetici che portano alla formazione dei due giacimenti considerati, al fine di definire le relazioni che regolano la loro particolare associazione mineralogica, che ne determina quindi il valore economico.

Il giacimento di Jabali è una mineralizzazione a nonsolfuri di Zn-Pb in rocce carbonatiche di età Giurassica, localizzata in un'area desertica sul bordo occidentale del bacino del Sabat'ayn, circa 90 km a nordest di Sana'a. Il deposito è costituito da vari corpi mineralizzati sub-orizzontali, che seguono la giacitura delle rocce carbonatiche incassanti, tagliati da corpi sub-verticali che seguono invece gli andamenti delle strutture tettoniche presenti nell'area. Le rocce carbonatiche sono costituite principalmente da dolomie, nelle quali si possono riconoscere varie generazioni, caratterizzate da differenti strutture e tessiture. Le dolomie di tipo "geodico" (o "saddle" idrotermali) sono quelle associate alle mineralizzazioni primarie a solfuri. La mineralizzazione d'interesse economico è costituita da carbonati di zinco-piombo (smithsonite, cerussite e idrozincite), e solo limitatamente da silicati di zinco (emimorfite>>sauconite). Essa si è chiaramente formata in seguito all'ossidazione di una precedente mineralizzazione costituita da solfuri di Zn-Pb. Lo studio mineralogico del giacimento ha mostrato come il processo di alterazione della mineralizzazione primaria si sia sviluppato attraverso una serie di passaggi progressivi, iniziati con l'ossidazione dei solfuri (blenda e galena), e proseguiti con la sostituzione diretta della galena da parte della cerussite e la sostituzione della roccia incassante da parte della smithsonite. Il processo di sostituzione della roccia incassante, avvenuto attraverso la reazione chimica tra i fluidi contenenti zinco e la dolomite, è testimoniato dalla presenza nel deposito di fasi dolomitiche ricche in zinco (Zn-dolomite), che dal punto di vista tessiturale e mineralogico, si colloca al passaggio tra la dolomite inalterata e la smithsonite. Il rinvenimento di queste fasi dolomitiche miste rappresenta un notevole risultato della presente ricerca, perché chiarisce come si sviluppi il processo di formazione della smithsonite per sostituzione della roccia incassante nei giacimenti a ospite dolomitico, e permette di prevedere la parziale inefficacia, in fase di estrazione dello zinco, di processi metallurgici predisposti alla semplice "digestione" della smithsonite.

Le composizioni isotopiche C-O della smithsonite di Jabali hanno mostrato risultati diversi rispetto a quelle riscontrate in giacimenti dello stesso tipo investigati in precedenza, e sembrerebbero indicare una formazione parziale del carbonato di zinco per opera di fluidi

idrotermali a bassa temperatura, e non esclusivamente meteorici. Questa caratteristica rappresenta un altro risultato della mia ricerca, che amplia notevolmente il campo delle conoscenze su questa classe di depositi.

Il giacimento a nonsolfuri di Zn-Pb di Yanque si trova nelle Ande peruviane, circa 90 km a sud della città di Cuzco, in un'area montuosa in cui si alternano picchi che superano i 4500 m.s.l.m., e valli dissecate con quote fino a 2000 m.s.l.m. Il deposito si colloca all'interno di una regione caratterizzata dalla presenza di un gran numero di depositi del tipo Cu-porphyry e skarn, associati alla messa in posto di diverse intrusioni circa contemporanee e con dimensioni variabili, collettivamente denominate "batolite dell'Apurimac-Yauri". La mineralizzazione di Yanque si colloca inoltre all'interno di un distretto mineralizzato a metalli di base, con al centro un deposito a Cu-porphyry di medie dimensioni, contornato da una fascia di depositi a Zn-Pb, dei quali Yanque è il più importante.

Il rilevamento geologico ha mostrato che le caratteristiche delle rocce affioranti nel distretto sono abbastanza varie, pur nell'ambito delle serie Mesozoiche: nella parte bassa è presente una successione costituita da quarzareniti e arenarie, cui seguono calcari di piattaforma localmente dolomitizzati. Le mineralizzazioni di Yanque sono ospitate in un conglomerato silicoclastico che passa in eteropia di facies a una breccia sedimentaria con clasti di calcare e dolomia. Entrambe le litologie si collocano al passaggio tra la parte detritica e quella carbonatica della successione. Il conglomerato è costituito da clasti di varia natura, in una matrice di quarzo, feldspato e altri minerali detritici. La successione sedimentaria è intrusa da una serie di corpi ignei, comprendenti dioriti, monzoniti e tonaliti, ai quali è associato il Cu-porphyry. Lo studio petrografico dei sedimenti Mesozoici a Yanque ha mostrato che essi sono stati affetti da una forte alterazione idrotermale, che può mettersi in relazione alla messa in posto delle intrusioni magmatiche. L'associazione risultante da tale alterazione è costituita da sericite/illite, kaolinite, dolomite e quarzo.

La mineralogia del deposito a Zn-Pb di Yanque è costituita soprattutto da argille zincifere e cerussite, e in minore quantità da emimorfite e smithsonite. Lo studio petrografico ha mostrato che, per quanto riguarda i minerali di Pb, la cerussite altera e sostituisce direttamente la galena mentre, per quanto riguarda i minerali di Zn, si osservano dei processi sostanzialmente diversi. Infatti, si è potuto notare che vari tipi di argille alterano e sostituiscono i minerali della roccia incassante, mentre emimorfite e smithsonite tendono a precipitare come cementi tardivi in fratture e porosità della stessa roccia. Nel deposito non è stato possibile osservare alcuna traccia di blenda alterata e sostituita da minerali secondari di zinco. Questo farebbe ipotizzare che la maggior parte della mineralizzazione primaria abbia occupato volumi di roccia ora erosi, e che il deposito di Yanque attuale sia una mineralizzazione di tipo "esotico", simile a quelle presenti nelle zone laterali dei giacimenti di rame tipo Chuquicamata (Cile).

Per quanto riguarda la sauconite, una smectite contenente zinco che rappresenta il minerale economicamente più abbondante a Yanque, essa si è formata soprattutto per l'alterazione e la sostituzione delle fasi idrotermali sericite/illite e kaolinite. Queste ultime sono localmente arricchite in zinco. Il piombo è presente soprattutto come cerussite, formatasi direttamente a spese della galena. Un punto importante della ricerca è stato notare come la mineralogia del

giacimento a nonsolfuri sia notevolmente dipendente dalla natura della roccia incassante la mineralizzazione: a Yanque, infatti, la presenza di una roccia essenzialmente silicoclastica ha impedito quasi totalmente la formazione di carbonati di zinco.
Infine, lo studio degli isotopi del Pb dei solfuri dei giacimenti dell'intero distretto e delle rocce incassanti sembra confermare una genesi comune tra la mineralizzazione primaria a Zn-Pb di Yanque, e il vicino deposito a Cu-porphyry, analogamente ad altri tipi di mineralizzazioni polimetalliche in precedenza descritte in letteratura. Il risultato è di notevole interesse, poiché in questo caso il distretto di Yanque rappresenta la prima area caratterizzata da una mineralizzazione polimetallica descritta nella regione. Questo concetto genetico potrebbe avere notevole importanza per una nuova strategia di esplorazione nell'intero distretto dell'Apurimac-Yauri.

INTRODUCTION

The subject of this Ph.D. thesis is the study of two supergene nonsulfide Zinc-Lead deposits. The first is the Jabali deposit in Yemen, and the second is the Yanque deposit in Peru. The objective of the study is to increase the knowledge of the geology, mineralogy and genetic processes of the zinc-lead supergene deposits, comparing the known models with the particular features observed at Jabali and Yanque.

"Nonsulfide zinc" is a very general term, referred to a group of ore deposits consisting of Zn-oxidized minerals, mainly represented by smithsonite, hydrozincite, hemimorphite, sauconite and willemite, which are markedly different from sphalerite zinc ores, typically exploited for zinc (Large, 2001; Hitzman et al., 2003; Boni, 2005).

The principal use for the extracted zinc is for galvanizing, that is a process in which a zinc coating is applied to steel to prevent corrosion (Tolcin, 2010). Galvanized steel is used extensively in the automotive industry (for example, the vehicle autobody) and in the construction industry (in transmission towers, and transportation infrastructure). The next leading end use for zinc is brass. Other end uses for zinc include zinc-base alloys for die-casting, chemicals, and zinc semi-manufactures.

Prior to the development of extraction processes of zinc from sulfide ores, nonsulfide Zn deposits (often known collectively as "zinc oxides") were the principal source of zinc in the world. From the ancient Greeks and Romans, up to the beginning of the 20th century, the nonsulfide Zn ores, mainly known as "lapis calaminarius", "calamine", "galmei", or "galman", in the Latin, French, German and Polish speaking words, respectively, were used as source minerals for the production of brass.

A decade ago, zinc nonsulfide deposits were regarded as the salvation of the zinc business, offering mine-to-metal production costs of $0.17-$0.27/lb at a time when prevailing metal price were $0.35-$0.40/lb. The availability of new extractive technologies using acid-leaching (LTC), solvent-extraction (SX), and electrowinning (EW) stimulated a reassessment of all oxide-dominated deposits that had not, in the past, responded to conventional flotation (Allen, 2010). These technologies would permit zinc metal production on-site at lower costs than zinc production from sulfides, an advantage often paired with higher environmental sustainability of both exploitation and processing (Boni, 2005).

Furthermore, the nonsulfide concentrations are of higher grade than sulfide ores, with quite sharp natural *cut-off* and can be extracted more easily in an *open-pit* mode.
However, Skorpion (Namibia) and Angouran (Iran), which were the only big, new hydro-metallurgical plants to be built, have both produced less than expected. Capital costs, operating costs, acid consumption and metal recoveries have not met the feasibility study expectation, and other oxide resources (Mehdiabad - Iran, Sierra Mojada - Mexico) are mired in technology issues.
Notwithstanding the incomplete successes, zinc nonsulfide exploration has gone from an exotic concept in 2000 to a standard tool in the toolbox today (Allen, 2010). The major Zn mine closures (e.g. Skorpion, Lisheen, Brunswick and others) provided for the next years, and a probable increase of the zinc price and demand has renewed the interest for this deposit type (Fig. I.1).

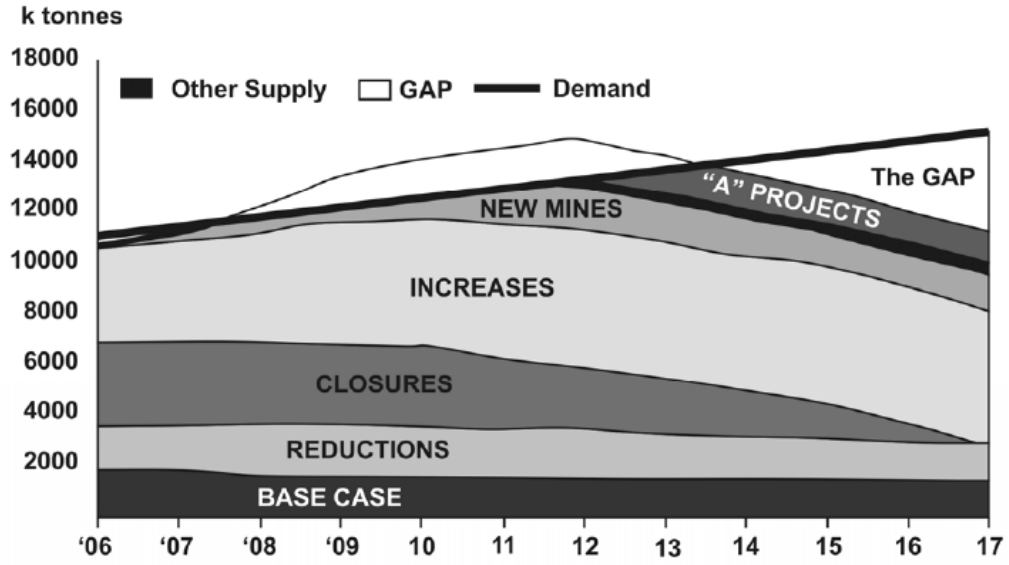

Fig. I.1. Zinc "gap" chart showing the zinc supply gap developing in 2011-2013; "A" projects = Announced projects (Allen, 2010).

Nonsulfide zinc deposits are classified in two major types (Hitzman et al., 2003): supergene and hypogene. Supergene deposits derive from weathering and oxidation of sulfide-bearing ores and consist principally of zinc carbonates and hydrous silicates. Supergene deposits are subdivided in three subtypes: direct-replacement, wallrock replacement and residual and karst-fill deposits (Hitzman et al., 2003). Hypogene deposits consist dominantly of zinc anhydrous silicates and oxides, and they commonly contain minor sphalerite as well.
A number of studies on supergene nonsulfide zinc deposits has been carried out and published: Sardinia, Italy (Boni et al., 2003; 2013), Skorpion, Namibia (Borg et al., 2003), Mae Sod, Thailand (Reynold et al., 2003), Shaimerden, Kazakhstan (Boland et al., 2003), Reocin, Spain (Velasco et al., 2003), Angouran, Iran (Boni et al., 2007), Belgium (Coppola et al., 2008), Galmoy and Silvermines, Ireland (Balassone et al., 2008), Polish district (Coppola et al., 2009), and Accha, Peru (Boni et al., 2009). Other papers, more focused on

the geochemistry of supergene nonsulfide zinc deposits, are Takahashi (1960), Sangameshwar and Barnes (1983), Williams (1990), McPhail et al. (2003), Reichert and Borg (2008), Gilg et al. (2008), Reichert (2009), and Boni et al. (2011).

In this Ph.D. thesis, I have done an attempt of verifying and applying the most recent genetic concepts to the study of two different supergene nonsulfide deposits. A particular attention has been given to the mineralogy of the deposits, and to the relationship between the newly formed zinc minerals and the host rock, because these characteristics are crucial for the metallurgical and extraction processes.

Jabali (Yemen) and Yanque (Peru) deposits have been chosen because they are totally different from each other. Therefore, the identification of their characteristics and possible genetic mechanisms should cover most possible peculiarities of this kind of deposits.

CHAPTER 1:
SUPERGENE NONSULFIDE ZINC-LEAD DEPOSITS

Based on the renewed interest on zinc nonsulfides, Hitzman et al. (2003) published an articulate description and classification of the most important among these deposits (Fig. 1.1), that is summarized in this chapter. The authors modify the previous classifications of Heyl and Bozion (1962) and Large (2001) and introduce a well documented distinction between deposits of supergene and hypogene origin. The supergene deposits form primarily from the oxidation of sulfide-bearing deposits in a weathering regime, and are constituted principally of smithsonite and/or hemimorphite. Three subtypes are recognized: direct-replacement, wallrock replacement, and residual and karst-fill deposits.

The hypogene deposits consist dominantly of zinc silicates and oxides, and may contain also sphalerite. They are subdivided into two subtypes: structurally controlled deposits, consisting of veins and irregular pipes of willemite-(sphalerite-hematite-manganese rich minerals) and stratiform deposits, consisting of commonly manganesiferous lenses of franklinite-willemite-zincite±gahnite.

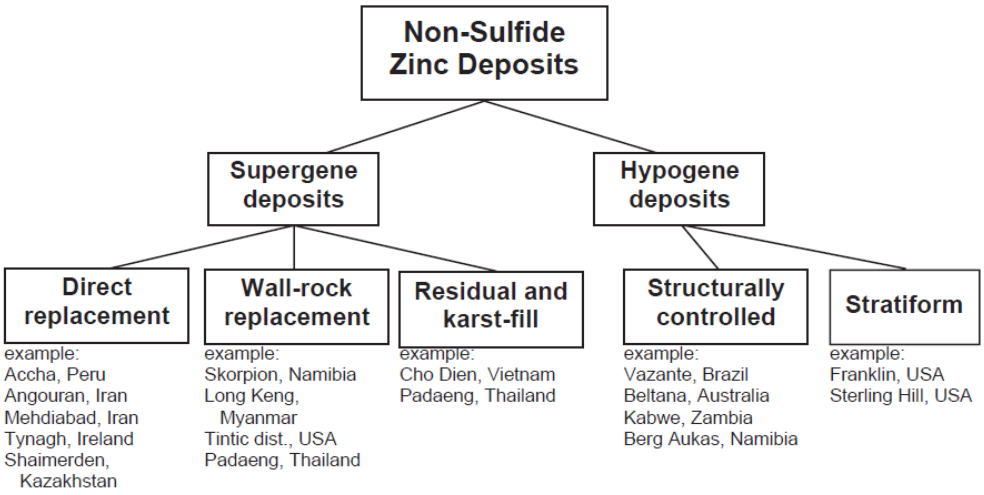

Fig. 1.1. Classification of nonsulfide Zn-deposits (Hitzman et al., 2003).

Supergene nonsulfide Zn-Pb deposit classification

The supergene deposits form primarily from low-temperature oxidation of sulfide-bearing deposits (Fig. 1.2). They are the most common type of nonsulfide zinc deposits and have a worldwide distribution (Fig. 1.3). Most supergene deposits occur in carbonate host rocks, owing to the high reactivity of carbonate minerals with acidic, oxidized, zinc-rich fluids derived from the breakdown of sphalerite-rich bodies. The majority of supergene deposits have either a Mississippi Valley-type (MVT) sulfide progenitor, or they may also form from SEDEX, VMS, CRD or skarn sphalerite deposits. These deposits contain mostly smithsonite, hydrozincite, hemimorphite and sauconite as economic minerals; however, their mineralogical association can comprise also uncommon Zn or Pb minerals.

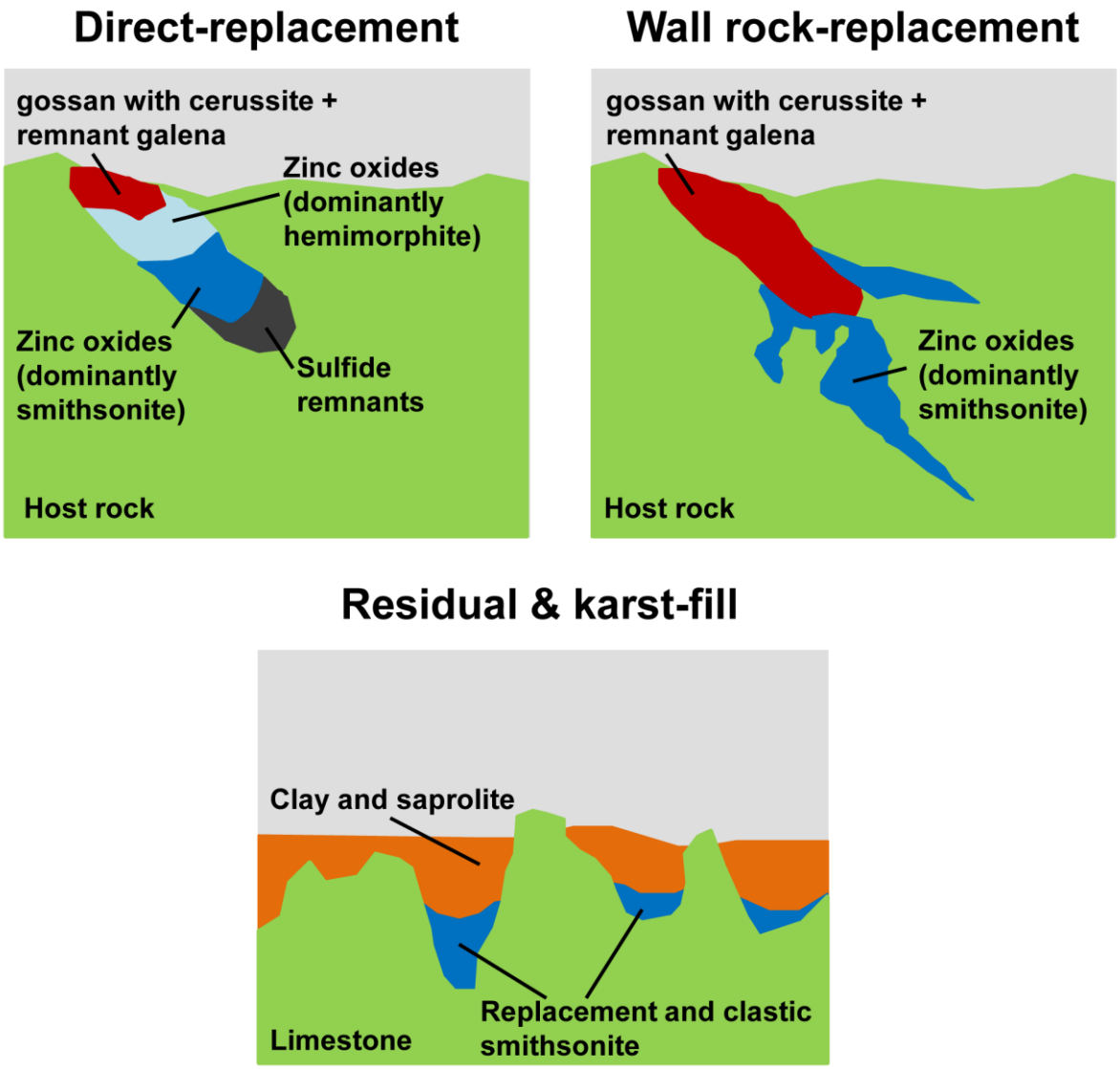

Fig. 1.2. Classification of supergene nonsulfide Zn-Pb- deposits (Hitzman et al., 2003).

Direct-replacement deposits are equivalent to Zn-rich *gossans*, where smithsonite and hydrozincite replace sphalerite and cerussite replaces galena. Many zinc sulfide deposits originally contained galena and copper-iron sulfides. These minerals are oxidized to carbonates, oxides, etc., but the whole mineralogy of direct-replacement deposits (and consequent metallurgy) can be quite complex, embracing a wide variety of minerals like those generally occurring in *gossans* (i.e. Cu-secondary sulfides, silicates or carbonates). The secondary deposits derived from MVT ores tend to be mineralogically simple and are dominated by smithsonite, hemimorphite and hydrozincite. Deposits formed from high-temperature, carbonate replacement-type (CRD) concentrations are commonly more mineralogically complex, owing to the abundance of metals present in these deposits (Megaw et al., 1988). Iron sulfide-rich zinc deposits tend to produce sufficient acid during weathering to completely leach zinc from the near-surface environment. Such complete leaching results in the formation of a vuggy jasperoid gossan with iron oxides, litharge, and cerussite with lesser plumbojarosite, hemimorphite, and copper carbonates.

Fig. 1.3. Location of the major supergene nonsulfide Zn-Pb deposits in the world.

Supergene *wall-rock replacement* zinc deposits form adjacent to, and down the groundwater flow gradient from, the original sulfide body and related direct-replacement deposits. As sulfide bodies are progressively oxidized, acidic ground waters migrate out into the carbonate host rock where they eventually react and precipitate Zn-carbonates. The latter derive by buffering reactions between acidic groundwater containing zinc and the carbonate host rocks. Many wall-rock replacement deposits are associated with direct-replacement ones, though in many cases the original sulfide body has been completely depleted of zinc and, occasionally, completely removed by erosion. A wall-rock deposit is favored by tectonic uplift of the lithologies hosting the primary ores and/or by the lowering of the

phreatic zone. A permeable host rock can also enhance the transport of zinc-bearing fluids out of the original sulfide deposit.
Because of the different metal solubilities, the process of dissolution, transport, and reprecipitation separates zinc from lead, copper, silver, and iron (Sangameshwar and Barnes, 1983). For this reason, wall-rock replacement deposits typically have a much simpler mineralogy than direct-replacement deposits. The simpler mineralogy makes this type of deposits a very attractive economic target.
Residual and karst-fill deposits result from either mechanical and/or chemical accumulation of secondary zinc minerals in a network of karst cavities. Such deposits occur in uplifted areas in tropical climates, where the oxidation of sulfide bodies results in the formation of acidic, oxidized solutions that promote karst development. Deposits where residual karst accumulation is the dominant process tend to be small in size and highly irregular. Metal grades can be very high, though.
Many supergene deposits include components of more than one of these "standard" categories, leading to mixed subtypes of deposits.
Hitzman et al. (2003) concluded that the formation of economically significant supergene nonsulfide zinc deposits depends on:

- the occurrence of a pre-existing zinc deposit (main requirement),
- efficient oxidation promoted by tectonic uplift and/or prolonged, seasonal deep weathering,
- a permeable host rock to allow for ground-water movement,
- an effective trap site for the newly formed minerals (generally the carbonate host rock),
- a hydrologic environment that does not allow the dispersion of Zn-bearing fluids,
- a considerable iron sulfide content in the precursor deposit.

Genesis of supergene nonsulfide Zn-Pb deposits

Nonsulfide supergene deposits, formed by oxidation of a sulfide bearing protolith, are based on a predictable series of reactions between meteoric waters, metal sulfides, and reactive host rocks (Sangameshwar and Barnes, 1983). Oxidation of sulfides provides low pH sulfate-bearing solutions, capable of transporting metals. Although sphalerite and galena (the latter to a much lesser extent) are very susceptible to oxidation (Bladh, 1982; Boyle, 1994), they produce relatively small quantities of acid sulfate-bearing solutions (Williams, 1990). Sangameshwar and Barnes (1983) show that, at temperatures between 25°C and 60°C and in an oxidizing environment, zinc remains in solution as Zn^{2+} under acid pH conditions (Fig. 1.4A, B); lead instead, tends to form minerals (sulfates or carbonates) at any pH-Eh range. For this reason, pyrite oxidation and the relative acid production play an important role in the genesis of supergene nonsulfide ores (Hitzman et al., 2003; Reichert and Borg, 2008). In fact, acids produced by oxidation of iron sulfides can maintain for long zinc in solution and drive to a complete leaching of this metal from the system (Sangameshwar and Barnes,

1983). In general, the buffering action of the host rocks neutralizes the acidity of the solutions and allows zinc to precipitate. Under these conditions, smithsonite, hemimorphite, and hydrozincite are the common products of oxidation of the sphalerite-rich deposits, operated through the contact with meteoric waters (Sangameshwar and Barnes, 1983; Hitzman et al., 2003).

In a comprehensive review of the relative stabilities of the three main Zn-minerals in the supergene environment, where temperature is ~25°C and pressure approximately 1 atmosphere, Takahashi (1960) determined that pH, activity of CO_2, and activity of SiO_2 of ambient ground waters were the main factors controlling the paragenesis and distribution of zinc minerals. In particular, the conversion of smithsonite to hydrozincite is controlled by both pH and partial pressure of carbon dioxide.

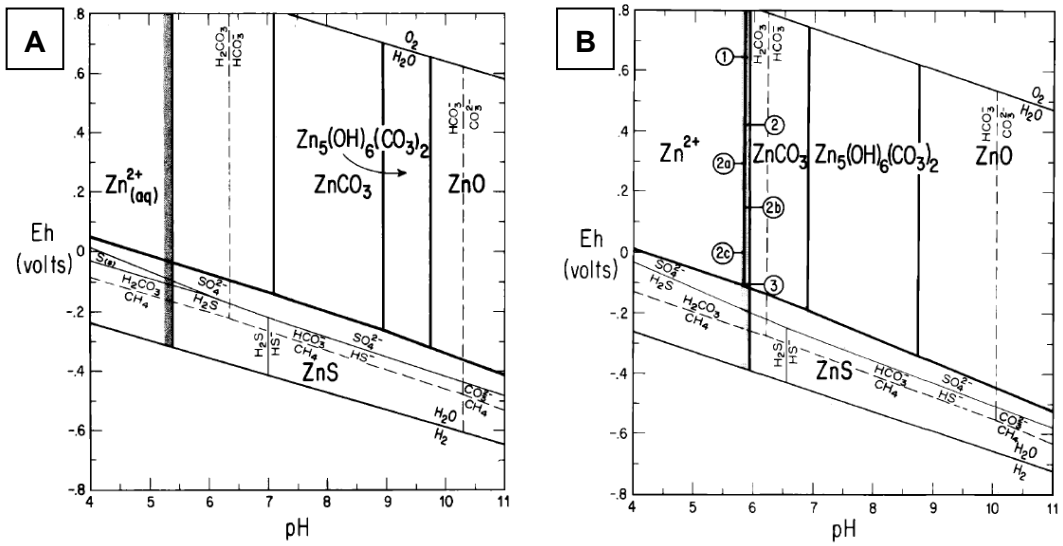

Fig. 1.4. A) Eh-pH stability relations at 25° and 1 atm of zinc compounds. The activity of Zn^{2+} is $10^{-5.17}$. B) Eh-pH stability relations at 60° and 1 atm of Zinc compounds. The activity of Zn^{2+} is $10^{-3.70}$ (Sangameshwar and Barnes, 1983).

In the arid environments, hydrozincite is much more common than smithsonite at the surface; deeper in the weathering profiles the relative proportions of both minerals are reversed. Takahashi (1960) explains the situation in terms of CO_2 content, such that dissolution of carbonate host rocks by acids released by the weathering of sulfide minerals produces carbon dioxide. Above the water table, carbon dioxide escapes to the atmosphere, thereby lowering the activity of CO_2 and stabilizing hydrozincite. Below the water table, carbon dioxide is soluble and, owing to its slow rate of diffusion, results in an elevated activity of CO_2 and in the consequent stability of smithsonite. In a more humid environment, Takahashi (1960) found that hydrozincite was generally not abundant because the ambient conditions (partial pressure of $CO_2 = 3\times10^{-4}$) favor the stability of smithsonite. This process is substantially confirmed by McPhail et al. (2003) and Reichert and Borg (2008) (Fig. 1.5). The authors agree that it is not possible to precipitate smithsonite from an aqueous solution which is in

equilibrium with the atmosphere, because the present day atmospheric $P_{CO2(g)}$ is much lower than the minimum conditions required for smithsonite precipitation (log $P_{CO2(g)}$=0.4 kPa at 298.2 K). Aqueous solutions at deeper levels, or water-saturated zones are in disequilibrium with the atmospheric CO_2(g) and reach values favorable for the precipitation of smithsonite (Reichert and Borg, 2008).

Hemimorphite precipitation depends on the availability of silica in the system. It is stable at lower pH values than either smithsonite or hydrozincite and with the buffering action of carbonate host rocks it might not be expected to form under normal, nearly neutral weathering conditions. Characteristically, hemimorphite forms where sufficient acid is generated by sulfide weathering to achieve and maintain low pH conditions and low total carbonate activity (Takahashi, 1960). Willemite can also form during low temperature oxidation of zinc sulfide, but it is relatively rare (Takahashi, 1960; Jeong and Lee, 2003).

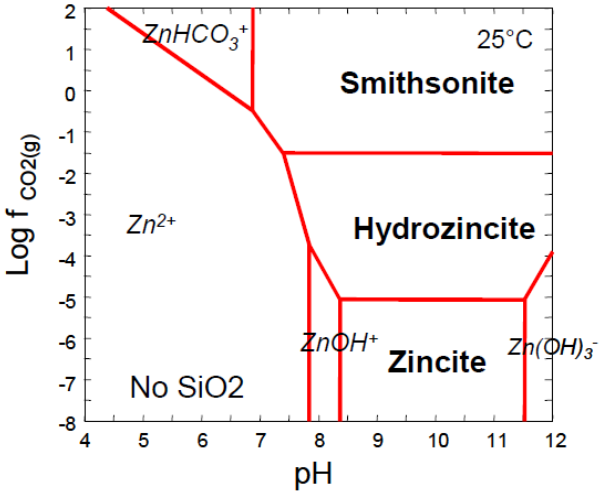

Fig. 1.5. Zinc mineral stabilities in the chemical system Zn-O-H-C (25°C). The activity of Zn^{2+} is 10^{-5}. Atmospheric CO_2(g) is log $f_{CO2(g)}$ = -3.5 (McPhail et al., 2003).

Another very important Zn-silicate in nonsulfide deposits is the Zn-smectite sauconite, which is the main component of the Skorpion deposit (Borg et al., 2003). This clay forms as normal weathering product of a silicate rock in presence of zinc; it may derive from the alteration of feldspar, plagioclase and micas in relative alkaline environments (Borchardt, 1989; Boni et al., 2009).

Galena reacts during weathering to form both cerussite and anglesite. The stability boundary between anglesite and cerussite lies at a pH that is function only of activities of H_2CO_3 and SO_4^{2-}, with anglesite more stable at acid pH, and cerussite prevailing in neutral conditions (Sangameshar and Barnes, 1983).

Carbon dioxide occurring in the aqueous solutions, and regulating the stabilities of the carbonate phases, can have different sources. Well-known sources are biological processes and the oxidation of organic matter, which are reflected in the isotopically light carbon component of smithsonites from many supergene ores in several mining districts (Fig. 1.6)

(Boni et al., 2003; Gilg et al., 2008). Another source derives by the release of CO_2 after the reaction of the acidic aqueous solutions with carbonate host rocks (Gilg et al., 2008).
An important issue is the metal mobility in the fluids. Many experiments carried out on tailings (e.g. Jurjovec et al., 2002) confirm that metal mobility greatly depends on pH. For an orebody containing mixed sulfides, and continuously leached in a column experiment, metals can be divided in three groups based of their mobility: Zn, Ni, and Co are mobile at pH of 5.7, Cd, Cr, V, and Pb become mobile under pH=4.0, whereas Cu remain unaffected by changes in pH (Jurjovec et al., 2002). In the Zn-Pb deposits, as said before, zinc results more mobile than lead, and tends to migrate toward the lower portions of the original sulfide body; lead instead is relatively immobile and remains in the original sulfide body as galena, replaced by anglesite and cerussite (Sangameshar and Barnes, 1983). Carbonate gangue and low total sulfide content favor the formation of a direct replacement nonsulfide zinc deposit *in situ*. High permeability and low buffering capacity in the protolith sulfide body favor transport of zinc out of the body as it is the case of the vuggy dolostone host rocks of many Mississippi Valley-type deposits.

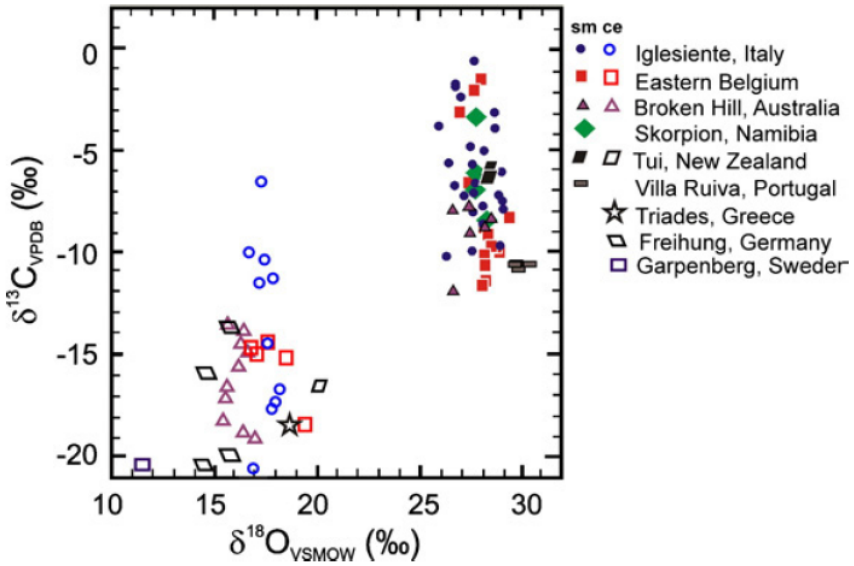

Fig. 1.6. Carbon and oxygen isotope composition of smithsonite (sm) and cerussite (ce) from supergene oxidation zones of several Zn-Pb deposits (Gilg et al., 2008).

Absence of carbonate gangue and high sulfide content favor the removal of zinc from the sulfide body and formation of a wall rock-replacement zinc deposit, providing a geochemical trap occurs down the pathway of the fluid flow (Hitzman et al., 2003).
The different metal mobility can produce the mixed subtypes of deposits quoted before in text, generally characterized by two different zones called “red zinc ore” and “white zinc ore” by Reichert and Borg (2008), and very well illustrated by white smithsonite manto and the red iron oxide manto at Sierra Mojada, Mexico (Hye In Ahn, 2010). The first one corresponds to a “gossanous” zone proximal to sulfides, in which heavy immobile metals

can concentrate, with a substantial *direct replacement* character; the second is more distal, and here zinc is accumulated essentially through *wall-rock replacement* processes.

A critical component in the formation of a economically significant nonsulfide zinc deposit is the existence of an effective trap site (Hitzman et al., 2003). For many highly pyritic, shale-hosted Zn-Pb ores and zinc-rich volcanogenic massive sulfide deposits there is no effective trap in the system, and the zinc derived during weathering is generally lost to dispersion.

Wall-rock composition significantly influences the mineralogy of nonsulfide zinc deposits. Deposits set in low-impurity carbonate rocks tend to be dominated by smithsonite and hydrozincite. Rapid pH change caused by interaction of low-pH zinc-rich fluids with carbonate rocks generally forms smithsonite under oxidizing conditions (Sangameshwar and Barnes, 1983). Deposits in siliciclastic or impure calcareous rocks, or in areas where siliceous soils are present, tend to form hemimorphite- and sauconite-bearing assemblages owing to the availability of Al and Si. In more reduced conditions also secondary sulfides can precipitate (Hitzman et al., 2003).

The fluid pathways are critical in determining the location of a nonsulfide deposit relative to the precursor sulfide body. Fluid pathways are partly controlled by host-rock lithology and structure, and by weathering conditions. Sulfide deposits in carbonate rocks characterized by low permeability, and also lacking significant fracturing, will be difficult to oxidize. In this situation, supergene zinc deposits form relatively close to the original sulfide bodies through gravity-driven solution movement. In mixed carbonate-clastic sequences, fluid flow may be dominated by the greater permeability of clastic units, and a significant component of horizontal stratal-fluid movement is possible (Hitzman et al., 2003).

Climatic history and morphological evolution are of considerable significance with respect to metals transport. Unlike copper “oxide” deposits, which are preserved in climates characterized almost exclusively by arid to semiarid conditions, supergene zinc deposits are currently found in both arid and temperate-to-tropical environments. However, many of the best supergene nonsulfide zinc deposits recognized to date apparently occur (formed?) in semiarid environments (Reichert and Borg, 2008). Tectonic uplift and resulting water table descent in semiarid to monsoonal climatic conditions enhance the transport of zinc out of the original sulfide body. This situation favors the formation of high-grade wall-rock replacement deposits and the geochemical separation of zinc from metals other than iron. High rainfall climates and resulting enhanced rates of ground-water flow tend to disperse zinc-bearing fluids if no effective trap site is encountered close to the primary sulfide body. Uplift combined with high rainfall and consequent high erosion rates generally mitigate against the formation of geochemically significant zinc-bearing supergene fluids where host sequences are impure carbonate (Hitzman et al., 2003; Reichert and Borg, 2008).

CHAPTER 2:
SAMPLING STRATEGY AND ANALYTICAL METHODS

More than 400 samples were collected in the Yanque (Peru) and Jabali (Yemen) deposits. The samples were selected following two main criteria:
1) geological and ore grade representativity of the mineral deposits;
2) different mineralogical assemblages.
Regarding the evaluation of ore grade representativity, the sampling strategy consisted in choosing a number of drillcore sections, of the same length as those used for the chemical assays, with an average grade similar to the indicated grade of the ore deposit, and an ore minerals association typical of the economic mineralization.
Regarding the identification of mineralogical assemblages, in order to highlight the mineral varieties occurring in each deposits, the study was further extended to a great number of representative outcrop samples corresponding to different facies at macroscopic scale.
It is worth to note that the drillcore samples are of basic relevance for metallurgical and economic geology studies, allowing a quantitative evaluation in three-dimensions of the ore grade variability. The outcrop samples are instead important to trace the genetic processes for ore formation, and the related *P-T-X* environmental conditions, which are fundamental for basic research.
Several analytical methods were used for the present work: they are described in the following paragraphs.

X-ray powder diffraction (XRPD)

General outlines

XRPD is a standard method for detecting and identifying crystalline (and poorly crystalline) phases, forming natural and synthetic materials and mixtures. Then, it is a feasible method for a great variety of topics.

When used for rock analysis, it allows to fully identify both the qualitative mineralogical composition and quantitative mineral percentages in different matrices, with the help of devoted computational data processing methods (Quantitative Phase Analysis = QPA).

This instrumental technique is based on the property of crystallographic planes occurring in the mineral structures to diffract the X-rays according to the Bragg's Law, an equation which relates the X-ray diffraction to lattice parameters of the crystalline phases:

$$n\lambda = 2d_{hkl} \sin\theta$$

where n is an integer, λ is the X-ray wavelength, d is the lattice spacing and θ is the diffraction angle (Fig. 2.1).

The X-ray diffraction phenomenon can be successfully described through the reciprocal lattice and the Ewald's sphere concepts; in few words, considering that the reciprocal lattice is constructed on the basis of a vector $d^*_{hkl} = 1/d_{hkl}$, whenever one point of the reciprocal lattice intersects the Ewald's sphere the diffraction condition represented by the Bragg's law is satisfied and an X-ray is diffracted by the crystal at the same intersection point.

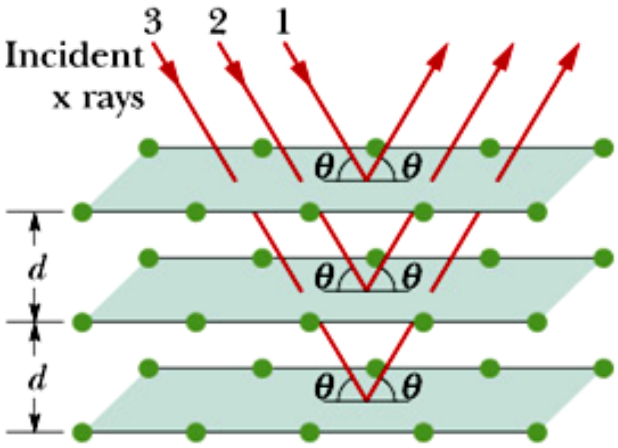

Fig. 2.1. Diffraction geometry, after Bragg's law.

The most widespread diffractometers are based on the Bragg-Brentano (semi-)focalizing geometry. There are two possible settings, i.e. the θ/θ and θ/2θ types (with horizontal or vertical geometry). In θ/2θ diffractometer, both sample and detector move with angular velocities equal to 1:2. In θ/θ diffractometer, the sample does not move, whereas the X-ray tube and the detector rotate with the same angular velocity.

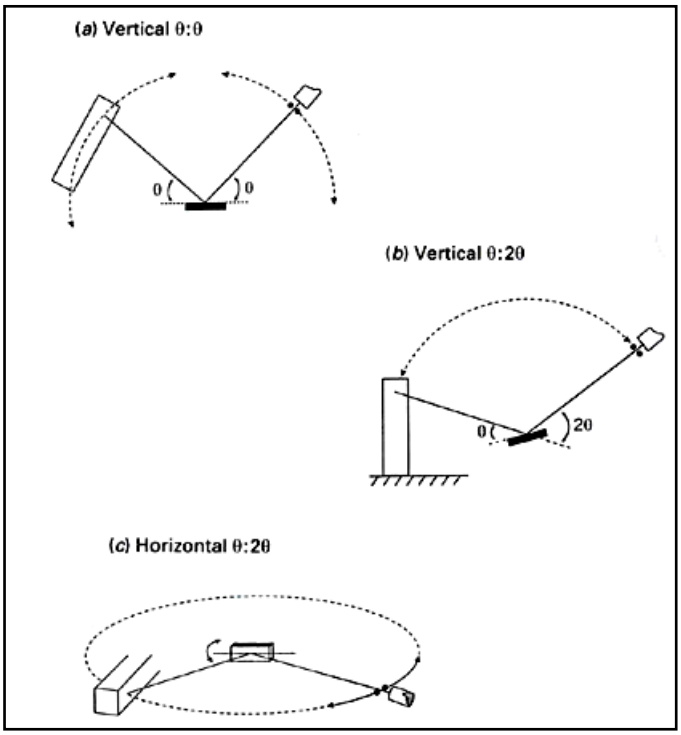

Fig. 2.2. Diffractometer geometries.

Even if the geometries can be different, all the instruments are composed of the same basic components: X-ray source (X-ray tube), collimation system, goniometer, sample lodge, X-ray detector (±radiation monocromator).

The X-ray tube with a metallic anode produces a focalized X-ray beam. The most common anode materials are Cu, Mo (heavily absorbing sample), Co (for ferrouginous samples), Fe, W, Cr.

The distances between X-ray tube and sample, and sample and detector must be the same. At the beginning of the analysis (sample 0° θ, and detector 0° 2θ), the source, the sample surface, detector point, and rotation instrumental axes, must lay in the same plane.

The output intensity data of a powder are reported in a XY pattern, where the horizontal scale is calibrated in °2θ and the vertical scale shows the intensity of the diffraction X-rays. XRD patterns of a mono- or polycrystalline matrix are constituted by a sequence of characteristic peaks, with various intensities at specific 2θ positions, which are diagnostic for each mineral structure, in agreement with the Bragg's law.

Many mineral databases exist, aimed to identify all the crystalline phase, like the ICDD-PDF (international centre for diffraction data, powder diffraction files) and the ICSD (inorganic crystal structure database)

Comparing the XRPD pattern of any crystalline mixture, as a rock sample, with the standard minerals of a database, it is possible to identify the mineral compounds by an automated search-match procedure between the measured peaks and the standard ones. Many types of software are available for this Boolean searching procedure.

Computational methods, like those based on the intensity peak ratio or on the internal standard reference intensity ratio, but also more complicated crystal structure refinement procedures (e.g. Rietveld method), allow evaluating the relative amounts of the minerals occurring on the mixture, e.g. the quantitative mineralogical composition.

Analytical details

For the present work, XRD analysis was carried out with the aim to get information on the bulk mineral assemblages, by means of the following instruments:

1) a Seifert–GE ID3003 diffractometer (Dipartimento di Scienze della Terra, dell'Ambiente e delle Risorse, Università di Napoli Federico II), with CuKα radiation, Ni-filtered at 40 Kv and 30 Ma, 3-80 °2θ range, step scan 0.02°, time 10 sec/step, and the RayfleX (GE) software package; a silicon wafer was used to check the instrumental setting. Sample holder was a zero-background plate of quartz crystal cut and polished 6° of the *c*-axis.

2) a Philips PW3020 automated diffractometer (XRD) (University of Heidelberg, Germany), with CuKα radiation, 40 Kv and 30 Ma, 10 seconds per step and a step scan of 0.02° 2θ, and data collection in the range 3-110° 2θ.

Quantitative phase analysis was carried out on the drillcore samples of the Jabali deposit, in order to evaluate the average mineralogical composition of the orebody. It has been elaborated using the Rietveld method (Rietveld, 1969; Bish and Howard, 1988; Bish and Post, 1993; Hill, 1991), and tested with chemical analyses. X-ray powder diffraction data were analyzed using the GSAS package (General Structure Analysis System, Larson and Von Dreele, 2000) and its graphical interface EXPGUI (Toby, 2001).

The specimens used for XRPD measures, were previously ground in a pestle in order to obtain granulometrically homogeneous powders (fraction <200μm).

Specific XRD analyses were performed for the characterization of Yanque clay minerals. The particle size fraction lower than 2 μm was separated from the bulk samples by dispersion in water of the fraction lower than 50 μm and centrifugation according to Stoke's law (Moore and Reynolds, 1997). Oriented aggregates were prepared by sedimentation on glass slides and analyzed in air-dried, glycolated and heated at (550°C) forms, from 3 to 40° 2θ, at a step scan of 0.02° 2θ and 1 second counting time (Dipartimento di Scienze del Suolo, della Pianta, dell'Ambiente e delle Produzioni Animali, Facoltà di Agraria, Università di Napoli Federico II).

Transmitted light and cathodoluminescence (CL) microscopy

General outlines

Cathodoluminescence (CL) is an optical and electrical phenomenon where a beam of electrons-generated by an electron gun (e.g. cathode ray tube) – that impacts on a material, causes the excitement of atoms hosted in the material, and the emission of visible light (luminescence). Cathodoluminescence in rock minerals depends on crystallographic defects and trace elements contained in the crystal lattice. In particular, some elements activate the luminescence whereas others quench it. Depending on the type of mineral and the

activator/quencher quantitative ratio, different colors and/or intensity of brightness may result (Fig. 2.3).

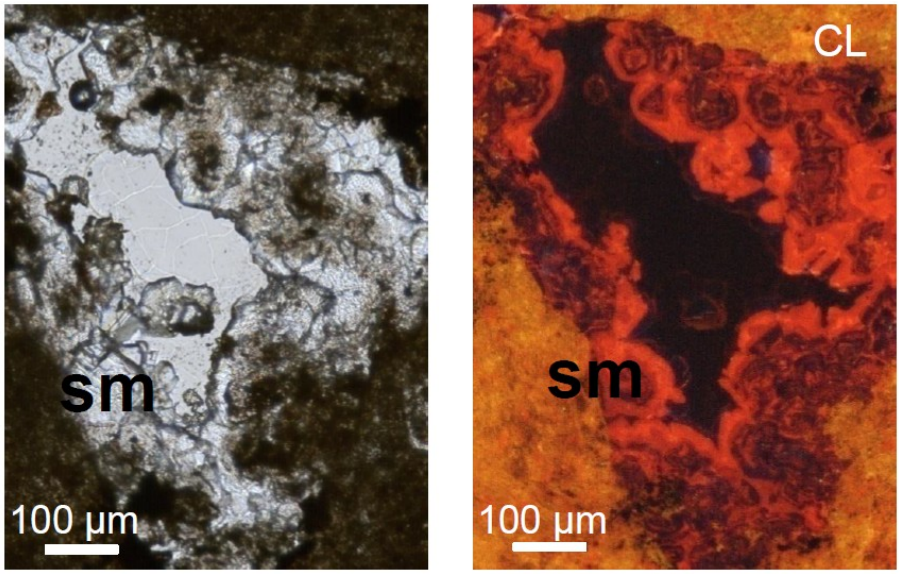

Fig. 2.3. Cathodoluminescence of a smithsonite geode (CL).

The most commonly used optical-CL system is termed a cold-cathode CL. It is an attachment to a microscope that allows the sample to be examined optically with the microscope and with CL in the same area. In this system the electron beam is generated by the discharge that takes place between the cathode at negative high voltage and anode at ground potential in ionized gas at a moderate vacuum of ~10^{-2} Torr. The result is relatively low-intensity CL in most CL-active silicate minerals. Because some of the electrical charges at the discharge may reach the sample and neutralize the static charge built up, it is not necessary to coat the sample with a conductive coating.
The CL response in the sample can be viewed through the objective lens of the microscope or the image can be recorded with high-speed film or with a digital camera (http://serc.carleton.edu/research_education/geochemsheets/opticalcl.html).

Analytical details
More than 200 polished thin sections were prepared from the most representative samples of the Yanque and Jabali deposits. For polished thin section preparation, the samples were impregnated with Araldite D and Raku Hardener EH 2950 in a commercial laboratory specialized in soft sediments (OMT, Aosta, Italy). Polished thin sections (~30 µm thick) were then observed under a petrographic microscope, in both transmitted and reflected light mode, to identify the main petrographic characteristics of the rocks.
CL microscopy was carried out with a Hot Cathode Instrument at the Heidelberg University for the thin sections of the Jabali deposit, in order to characterize the behavior of the carbonate minerals. In fact, carbonates are a group of minerals generally affected by wide ranges of element substitutions within the lattice, and can be well distinguished with this technique.

Scanning electron microscopy (SEM) and energy-wavelength dispersive X-ray detection (EDS – WDS)

General outlines

The scanning electron microscope (SEM) is an electronic instrument allowing a high-resolved and high-zoomed observation of a sample material, up to enlargements of 1-10 μm. This technique is based on an incident electron beam focused with magnetic lenses and accelerated by a high potential on the sample specimen. The interaction between electron beam and sample surface produces the emission of backscattered electrons, secondary electrons, Auger electrons, characteristic X-rays, and visible light. Secondary electrons provide high-resolution imaging of fine surface morphology. When the sample surface has been polished, like when analyzing thin section specimens, and the electron beam is orthogonal to the section, backscattered electron imaging provides elemental composition variation, as well as surface topography.

The efficiency of production of backscattered electrons is proportional to the sample material's mean atomic number, which results in image contrast as a function of composition, for instance material with higher atomic number appears brighter than material with lower atomic number (BSE image).

The X-rays, produced by the interaction of the incident electron beam with the specimen, have energy and wavelength, which depend on the atomic species constituting the specimen, following the Planck's Law:

$$E = h\, c/\lambda,$$

with E (Joule), λ (m), c ($3\cdot10^{8}$ m/s), h ($6.63\cdot10^{-34}$ Js).

Two different types of detector, installed on an electron microprobe, can measure energy and wavelength of X-rays from the specimen; these equipments are called energy-dispersive X-ray spectroscopy (EDS) and wavelength-dispersive spectroscopy (WDS) detectors, and allow a point-to-point qualitative and quantitative chemical analysis of the sample specimen. WDS technique is based on a detection system implying multiple spectrometers, commonly represented by the following four synthetic crystals:

Crystal	Formula	2d(Å)	Analytical range		
			K	L	M
TAF	$C_8H_50_4T1$	25.75	F-P	Mn-Mo	La-Hg
PET	$C_5H_{12}0_4$	8.74	Si-Fe	Sr-Ho	W-U
LIF	LiF	4.026	Sc-Sr	Te-U	—
ODPb	$(C_{l8}H_{35}0_2)_2Pb$	100	B-O	C-V	—

A comparison between the performances given by the two techniques is reported below (Aurisicchio and Gianfagna, 2005):

Technical features	EDS	WDS
Sensitivity	10000 c/s/Na	1000 c/s/Na
Beam current	~0.5 Na	1 – 100 Na
Measure time	50-l00 s	20 s
(15 keV)	(all elements)	(per element)
Analyzed elements (Z)	Na (11) – U (92)	Be (4) –U(92)
Resolution	(MnKα ~5.9 keV) 150 Ev	(quartz 1011) 6 Ev
Peak/background ratio	10-100	100-1000
Detection limit	1000 ppm	100 ppm

Analytical details

Secondary electron imagining by scanning electron microscopy (SEM) on the thin sections was carried out with a Jeol JSM 5310 (CISAG, Università di Napoli, Italy) and with a Jeol JSM 5900LV (Natural History Museum, London, UK). No analytical bias was observed between the two instrumental measurements. All the analyzed samples were coated with a 15μm carbon film.

Element mapping, qualitative energy-dispersive (EDS) spectra and quantitative analyses were obtained with the INCA X-stream pulse processor and the 4.08 version Inca software (Oxford Instruments detector), interfaced with the Jeol JSM 5310. The following reference standards were used: albite (Si, Al, Na), orthoclase (K), wollastonite (Ca), diopside (Mg), almandine (Fe), rutile (Ti), barite (Ba), strontianite (Sr), Cr_2O_3 (Cr), rhodonite (Mn), sulphur (pyrite), sphalerite (Zn), galena (Pb), fluorite (F), apatite (P), chlorine (sylvite), smithsonian phosphates (La, Ce, Nd, Sm, Y), pure vanadium (V) and Cornig glass (Th and U). Analytical errors are 1% rel. for major elements and 3% rel. for minor elements.

Quantitative data sets of selected samples were obtained by wavelength dispersion spectrometry (full WDS), using a Cameca SX50 electron microprobe operating at 15 Kv, 15 Na, and 10 μm spot size (Natural History Museum, London, UK). The following reference standards were used: jadeite (Na), diopside (Mg, Si), potassium bromide (K), wollastonite (Ca), aragonite (Ca), pyrophanite (Ti, Mn), eskolaite (Cr), hematite (Fe), bunsenite (Ni), corundum (Al), smithsonite (Zn), celestine (Sr, S), vanadinite (Pb), barite (Ba), greenockite (Cd). Detection limits for WDS are in the order of 0.01 wt%.

The CO_2 contents in carbonates and water content in hydrated carbonates and silicates were calculated by stoichiometry.

QEMSCAN® analysis

General outlines

QEMSCAN® is an automated technique for the rapid characterization of mineral/inorganic species and relationships in polished samples by scanning electron microscopy with energy dispersive X-ray spectrometry (SEM-EDS). The main benefit is the rapid, spatially resolved mineralogical data set inferred from chemical spectra, which provides increased information on mineral species, fully quantitative and statistically valid values on ore mineral abundances, particle size and shape distributions, as well as quantitative data on mineral associations. QEMSCAN® analysis allows a high resolution chemical-mineralogical map of a whole section to be produced (small rock fragments or concentrate), with different degrees of detail and different "chemical" resolution, as well as the modal quantitative evaluation of the identified phases (Fig. 2.4).

The basic QEMSCAN® methodology and analytical modes were published by Gottlieb et al. (2000), Pirrie et al. (2004) and Goodall and Scales (2007).

Among the supergene ore types for which QEMSCAN® analysis can be extremely useful, are the Ni-laterites (Andersen et al., 2009), the nonsulfide Zn ores (Rollinson et al., 2011) and the bauxites (Boni et al. in press).

Analytical details

QEMSCAN® test analyses were performed on two thin sections from Jabali deposit. QEMSCAN® analysis was carried out at the Camborne School of Mines, University of Exeter, UK, using a QEMSCAN® 4300, which is built on a Zeiss Evo 50 SEM platform with four light element Bruker Xflash Silicon Drift energy dispersive X-ray detectors.

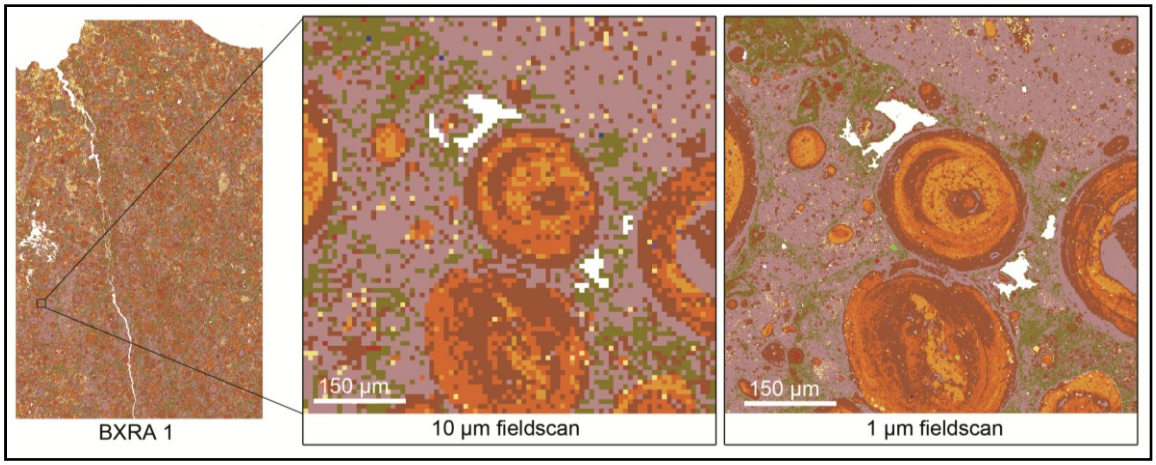

Fig. 2.4. QEMSCAN® analysis of a bauxite specimen (Boni et al., in press).

The software used were iMeasure v. 4.2 for the data acquisition and iDiscover v. 4.2 for the spectral interpretation and data processing. The fieldscan measurement mode was used to collect X-ray data every 10 µm across the polished sample surfaces of thin sections (4 cm by 2.5 cm), with X-rays acquired at 1000 total X-ray counts per spectrum. The LCU5 SIP provided with the QEMSCAN® (containing common minerals) was modified to include the

nonsulfide mineral components. The chemistry and density data input into the primary list of the SIP database for QEMSCAN® used the average composition for bauxite minerals (www.webmineral.com). Issues relating to similar X-ray spectra include minerals that differ primarily by the concentration of light elements that are not directly detected (H), or have limited detection in the X-ray signals (C, O).

Major, minor and trace element analysis (ICP-MS)

General outlines

Many techniques are used to measure the minor and trace to ultratrace elements in minerals and/or whole rocks. The most common are the ICP-AES and ICP-MS, i.e. Inductively Coupled Plasma – Atomic Emission Spectrometry and Mass Spectrometry, respectively. The ICP-AES is based on the measurement of wavelengths of radiations emitted by plasma, containing the vaporized sample. The ICP-MS put together an inductively coupled plasma with a mass spectrometer.

A typical plasma-mass spectrometer is composed by the following parts:

- sample introduction system
- ICP source
- radiofrequence generator
- mass spectrometer
- detector
- PC-controlled system

Analytical details

Whole rock chemical analyses of major, minor and trace elements were carried out from the ore deposit samples.

For the present work, major, minor and trace elements of ore deposit samples were mostly measured by ACME (Vancouver) laboratory. Samples were dissolved by *aqua regia* and 4-acid digestion. Loss on ignition (LOI) was not evaluated. The minimum detection limits were 0.5 ppm to 0.05 %.

C, O, and S stable isotopes geochemistry

General outlines

Stable isotope geochemistry is concerned with variations of the isotopic compositions of elements, arising from physicochemical processes rather than nuclear processes (Faure, 1986). The elements of greatest interest for stable isotope geochemistry are O, H, C and S. These element have some common characteristics: low atomic number, large mass difference between their isotopes, they form bonds with a high degree of covalent character, they exist in many oxidation states, the abundance of the rare isotope is sufficiently high to facilitate the analysis.

Variations in stable isotope ratios are commonly reported as *permil* deviations, δ, from some standard, following the example equation of the O-isotopic composition relative to SMOW composition (standard mean ocean water):

$$\delta^{18}O = \left[\frac{\left(^{18}O/^{16}O\right)_{sam} - \left(^{18}O/^{16}O\right)_{SMOW}}{\left(^{18}O/^{16}O\right)_{SMOW}}\right] \times 10^3$$

O-isotopic composition can be also reported relative to the Pee Dee Belemite (PDB) carbonate standard, which is related to SMOW by:

$$\delta^{18}O_{PDB} = 1.03086\,\delta^{18}O_{SMOW} + 30.86$$

C-isotopic composition is expressed relative to PDB standard, instead S-isotopic composition is related to Canyon Diablo Troilite (CDT) standard.

Isotopic composition of these light elements in a material depends on fractionation processes. Isotopes of the same element, having different masses, will have different physical and chemical behaviors. The isotope with lighter mass is generally more reactive than the heavier isotope. A different behavior of two isotopes during a reaction from phase A to phase B, such as the mineral precipitation, produces changes of the isotopic ratio of the element from the first phase to the second, by following the process called "fractionation". Each isotope reaction is defined by the temperature dependent fractionation coefficient α:

$$\alpha = Ra/Rb$$

where *Ra* and *Rb* are the isotope ratios in phase A and phase B respectively.

The fractionation factor (α) is correlated to absolute temperature by the following equation:

$$ln\ \alpha = A + B/T^2$$

where A and B are coefficients determined experimentally, and T is the absolute temperature in Kelvin.

Only a few of the lighter elements, such as Oxygen and Carbon, have isotopes with sufficient relative mass difference to cause detectable fractionation in nature. The two most abundant stable isotopes of oxygen are ^{16}O (99.757%) and ^{18}O (0.205%). The two stable isotopes of carbon are ^{12}C (98.93%) and ^{13}C (1.07%). The absolute concentration of single isotopes is difficult to measure, but on the other hand, isotopic ratio can be determined easily and accurately.

This method has applications in many sectors of Earth Science. Its applications are exhaustively discussed in Faure (1986), Tucker and Wright (1990), Clauer and Chaudhuri (1992) and Hoefs (1997).

Stable O- and C-isotope geochemistry of carbonate minerals associated to hydrothermal, diagenetic and magmatic sulfide deposits is applied to evaluate the temperature of formation, origin and evolution of metal-bearing fluids and mechanism of emplacement (Ohmoto and Rye, 1979; Field and Fifarek, 1985; Zheng and Hoefs, 1993; Schwinn et al., 2006). Such isotope studies can be applied also to carbonate minerals occurring in nonsulfide deposits,

and allow to distinguish between supergene and hypogene deposits, as well as evaluating the temperature of mineral precipitating fluids (Gilg et al., 2008).
S-isotope composition of sulfides and sulfates in mineral deposits is also related to genetic processes forming the deposit, and can be useful, for example, to distinguish between sedimentary and magmatic sulfide deposits (Faure, 1986).

Analytical details
C- and O- stable isotope geochemistry has been applied to Zn-carbonates of the Jabali deposit. Analyses have been carried out at the University of Erlangen-Nuremberg (Germany). Carbonate powders and pure minerals were collected by mechanical hand picking separation of pure minerals, and reacted with 103% phosphoric acid at 70°C using a Gasbench II connected to a Thermo Finnigan Five Plus mass spectrometer. All values are reported in per mil relative to V-PDB by assigning a $\delta^{13}C$ value of +1.95‰ and a $\delta^{18}O$ value of -2.20‰ to NBS19. Reproducibility was checked by replicate analysis of laboratory standards and was better than ± 0.07 ‰ (1σ) for both carbon and oxygen isotope analyses. Oxygen isotope values of dolomite and smithsonite were corrected using the phosphoric acid fractionation factors given by Kim et al. (2007), Rosenbaum and Sheppard (1986) and Gilg et al. (2008).
S-isotope analyses of sulfides and sulfates of both Jabali and Yanque deposits were carried out at Actlabs (Ancaster, Ontario, Canada). Single crystals and mineral fragments were collected with a dental drill from the cores and outcrop samples. Pure $BaSO_4$ and sulfide samples were combusted to SO_2 gas under ~10^{-3} tor of vacuum. The SO_2 was inlet directly from the vacuum line to the ion source of a VG 602 Isotope Ratio Mass Spectrometer (Ueda, 1986). Quantitative combustion to SO_2 was achieved by mixing 5 mg of sample with 100 mgs of a V_2O_5 and SiO_2 mixture (1:1). The reaction was carried out at 950˚C for 7 minutes in a quartz glass reaction tube. Pure copper turnings were used as a catalyst to ensure conversion of SO_3 to SO_2. Internal Lab Standards ($SeaWater_{BaSO4}$ and $Fisher_{BaSO4}$) were run at the beginning and at end of each set of samples and were used to normalize the data as well as correct for any instrument drift. All results are reported in the permil (‰) notation relative to the international CDT standard. Precision and Reproducibility using this technique is typically better than 0.2‰ (n = 10 Internal Lab Standards).

Pb-isotopes geochemistry

General outlines
Lead occurs in nature as four stable isotopes, of which three are radiogenic daughter products of radioactive decay: ^{208}Pb is produced by the decay of ^{232}Th, ^{207}Pb by that of ^{235}U, and ^{206}Pb by that of ^{238}U. ^{204}Pb is not the product of any radioactive decay and its amount has not changed. Because radioactive decay is irreversible; as a rule, terrestrial rocks have Pb isotope ratios ($^{208}Pb/^{204}Pb$, $^{207}Pb/^{204}Pb$, and $^{206}Pb/^{204}Pb$) that increase monotonically with time. The one exception are sulfide ores. Uranium is not incorporated in sulfides (e.g. galena), so that, in these particular ores, the Pb isotopic composition is frozen at the time of

the ore forming event, when U and Th removal stopped adding radiogenic Pb daughter isotopes. This ensures that, once a sulfide ore is formed, it will retain a constant Pb isotopic composition, i.e., gains an individual Pb fingerprint (Villa, 2009). Pb sulfide ore fingerprint depends by various factors, e.g. mixing between different Pb sources; by comparing Pb isotopic sulfide compositions with those of sedimentary, igneous and/or metamorphic host rocks, it is possible to understand the amount of mixing and the characteristics of forming fluids.

Analytical details

Lead isotope analyses of sulfides, pure minerals, and igneous and sedimentary rocks of Yanque deposit were performed using a Nu Instruments^{TM} multicollector inductively coupled plasma mass spectrometer (MC-ICP-MS) at the Laboratory of Isotope Geology at the University of Bern. The samples were dissolved in Aqua Regia and purified using the Sr•Spec™ cation exchange resin according to the procedure by Villa (2009). All samples were spiked with thallium for correction of the mass bias. The measured values of NIST SRM 981 compare favorably with those reported in the literature, thus, further bias corrections ware not necessary. The errors indicated for individual analyses are calculated as the square root of the square in-run error plus the square of the dispersion of the standard measurements for the corresponding day of analysis.

Differential thermal analysis (DTA)

General outlines

When a material is heated, generally is affected by physical and chemical transformations, e.g. loosing of water, formation of more stable phases, recrystallization, and finally also melting. Thermal analysis is a general term, which includes a group of techniques, characterized by the measurement of variations of physical properties of a material, while it is heated with a stable increase of temperature. These techniques are the thermogravimetry (TG), the derivative thermogravimetry (DTG), and the differential thermal analysis (DTA). TG, DTG and DTA are generally done together, and, while the sample is heated by a constant increase of temperature, they provide the measurement of weight variation (weight loss) (TG), derivative weight loss (DTG), and temperature difference between the sample specimen and a reference standard (generally alumina), which is thermally inert (DTA). TG, DTG and DTA analyses are plotted on binary diagrams, with the temperature on the horizontal axes, and on vertical axes respectively: weight loss % (TG), derivative weight loss (DTG), and difference of temperature "ΔT" (DTA) (Fig. 2.5).

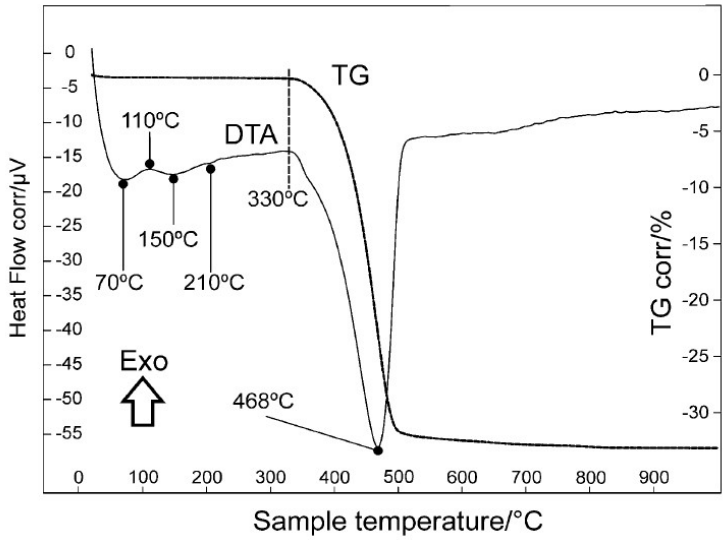

Fig. 2.5. Thermal analysis of smithsonite: exothermic reaction at 110°C corresponds to recombination of (water) proton and hydroxyl with smithsonite fibres; endothermic reaction at 468°C corresponds to smithsonite decomposition, associated to CO_2 volatilization (Garcia-Guinea et al., 2009).

In rock analysis, the TG pattern is characterized by a monotonous decrease of vertical values at corresponding temperature increases, that can be due e.g. at volatile phase losing, and results constituted by horizontal segments, indicating no reaction, linked by vertical paths, located at those temperatures where sample undergoes physical-chemical variations. DTG pattern allows a better identification of reaction temperatures, because, in place of vertical paths, positive peaks occur. DTA pattern is generally similar to DTG pattern, in fact it is constituted of peaks located in correspondence of reaction temperatures, but DTA allows to distinguish between the occurrence in the sample of endothermic reactions (negative "ΔT", negative peaks), and exothermic reactions (positive "ΔT", positive peaks).
Thermal analysis allows to identify unknown compounds in a rock specimen, which are reactive to heat, and to determine the composition of a mineral species, by analysing its reaction temperatures and weight loss amounts.

Analytical details
Thermal analysis (DTA, TG) has been performed only on Jabali dolomite samples. The samples were analyzed at the CISAG Laboratory of the University of Napoli, on a Netsch Instrument model STA 409, under air atmosphere. A sample mass of 100 mg was heated from room temperature to 1100°C, at the rate of 10°C min^{-1}. Two pure dolomite samples from the Norian of Southern Apennines (Italy) have been analyzed for comparison.

CHAPTER 3:
THE JABALI Zn-Pb NONSULFIDE DEPOSIT (YEMEN)

Introduction

The Jabali zinc deposit lies in mountainous desert terrain about 110 km east of Sana'a, the capital of Yemen, along the western border of the Marib-Al-Jawf/Sab'atayn basin, at an altitude of 1,800 m above sea level (Fig. 3.1). In the Middle Age (7^{th} - 9^{th} century AD) this was considered one of the most important mining areas for silver of the Muslim world. The Jabali nonsulfide concentrations, hosted by carbonate rocks, with their 8.7 million tonnes of ore at an average grade of 9.2% zinc, are currently considered the major zinc resource of Yemen (Watts, Griffis, and McOuat Ltd., 1993; Grist, 2006; Yemen Geological Survey and Mineral Resources Board, 2009).

The exploitation and development rights to the Jabali zinc deposit are owned by Jabal Salab Company (Yemen) Limited ("Jabal Salab"), in which ZincOx Resources plc. held a 52% interest, and Ansan Wikfs Investments Limited, a company owned by a prominent Yemeni business family, held the balance. In March 2013, ZincOx announced to be entered into an agreement for the sale of its entire issued share capital to Ansan Wikfs.

The Jabali deposit has been already subjected to scientific research in the past. The resulting data have been reported in: Christmann et al. (1989), Al Ganad (1991), Al Ganad et al. (1994), and in several unpublished reports for mining companies (e.g. Allen, 2000; SRK Consulting, 2005). Different hypotheses about the nature of the primary sulfide concentrations have been proposed, ranging from a paleokarst-hosted Mississippi Valley deposit (Al Ganad et al., 1994) to a Carbonate Replacement Deposit (Allen, 2000). On the origin of the secondary supergene mineralization there are again different opinions. Al Ganad et al. (1994) propose a long period of oxidation, extended from Cretaceous to Present, whereas Allen (2000) is more inclined to sustain a single oxidation stage started in Miocene until Present. The secondary deposit at Jabali has been considered by most authors a typical supergene Zn-(Pb) nonsulfide mineralization, consisting of smithsonite and hydrozincite with associated silver minerals. Further characterization of ore and host rock minerals has been only partly carried out (Mondillo et al., 2011).

Fig. 3.1. View of Jabali site and mine camp, looking NE.

The deposit has been maintained operative up to 2011, when politic instability in the country started. In that period, Jabal Salab (ZincOx) was considering a number of mineral processing routes, for developing the Jabali processing plant. A good recovery (80%) from the bulk ore was reached in metallurgical tests carried out on a number of composite nonsulfide samples with the LTC (leach-to-chemical) method, using ammonia-based solutions (Grist, 2006). This method selectively recovers the zinc contained in smithsonite and hydrozincite and, when compared with the classical acid-leach, there is no interaction between the chemical solutions and the gangue minerals (Woollett et al., 2002), which would cause high acid consumption during metal extraction. But it has proven impossible to raise the recovery above this level, especially in those samples bearing a low metal grade (Fig. 3.2). In order to investigate the possible cause of the remaining non-recoverable phase, it was necessary to carry out a wide mineralogical and geochemical study in the nonsulfide ore zone, to identify how the metal is trapped in non-extractable phase (Mondillo et al., 2011).

A key part of the original deposit evaluation by Jabal Salab was to apply the calculated recoveries when considering the recovered material that will be extracted from the reserve. This is normal in the mining industry, as recoveries are almost never 100%, but can often be improved by later work on recovery technique.

The various genetical controversies and the cited metallurgical problems are essentially caused by an incomplete knowledge of the mineralogy and geochemistry of the Jabali nonsulfide orebody. In the present study I try to fill this gap, identifying the mechanisms of the supergene oxidation process, whose mineralogical products can explain the incomplete recovery of Zn during ore processing.

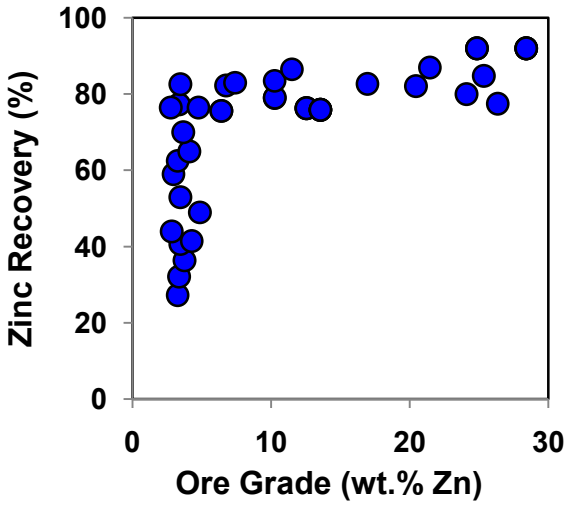

Fig. 3.2. Diagram showing the results of the metallurgical tests (Zn recovery vs. Zn grade) on the Jabali samples (ZincOx Resources plc.). Samples with a Zn ore grade higher than 5% show a very high (around 80%) recovery, samples with an ore grade below 5% have a variable recovery, also on very low values.

Geological setting

Yemen is located in the southwest corner of the Arabian Peninsula. The country is bordered by Saudi Arabia (north) and Oman (east), and by Red Sea (west) and Gulf of Aden (south) (Fig. 3.3).

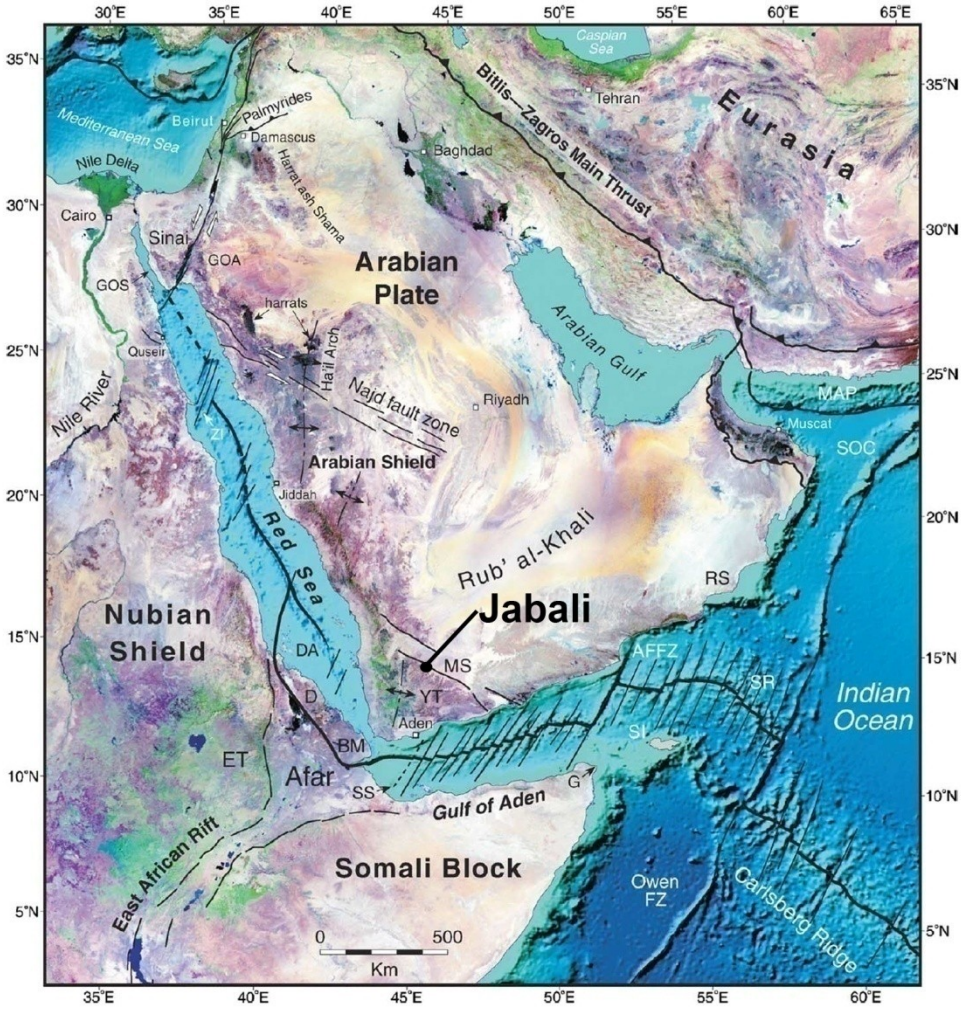

Fig. 3.3. Landsat imagine of Red Sea/Gulf of Aden region, showing the Jabali location (Bosworth et al., 2005). AFFZ = Alula-Fartaq fracture zone; D = Danakil horst; DA = Dahlak archipelago; ET = Ethiopian trap series; G = Cape Gwardafuy; GOA = Gulf of Aqaba; GOS = Gulf of Suez; MAP = Makran accretionary prism; MER = main Ethiopian rift; MS = Mesozoic Marib-Sab'atayn Basin; SI = Socotra Island; SOC = Semail oceanic crust; SR = Sheba Ridge; SS = Shukra al Sheik discontinuity; RS = Ras Sharbithat; YT = Yemen trap series; ZI = Zabargad Island.

The geology of Yemen comprises: 1) Precambrian basements, transected by a failed Jurassic rift system, formed during the break-up of the Gondwana supercontinent; 2) Jurassic pre-, syn-, and post-rift carbonate and clastic sediments; 3) Tertiary to Recent sediments and magmatites associated to the opening of the Gulf of Aden-Red Sea rift (Fig. 3.4) (Menzies et al., 1994).

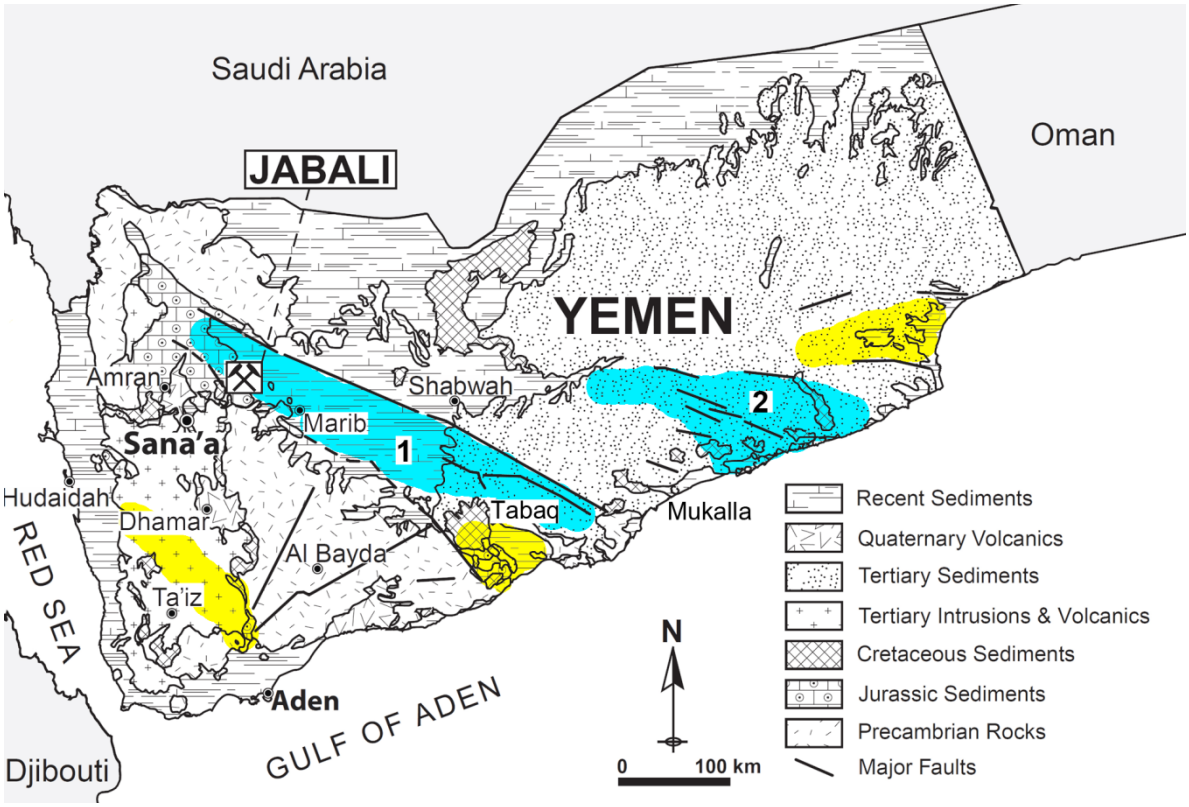

Fig. 3.4. Geological map of Yemen, showing the Jabali position (Yemen Geological Survey and Mineral Resources Board, 2009, modified). 1 = Sab'atayn basin; 2 = Say'un-Masilah basin. Light blue = hydrocarbon producing Mesozoic basins; yellow = other Mesozoic basins.

The basement rocks of Yemen are considered as part of the Proterozoic Arabian-Nubian shield, which covers northeast Africa and the Arabian Peninsula. They consist of metavolcanic and metasedimentary suites, deposited in arc environments, intruded by post-tectonic granites and granodiorites (Whitehouse et al., 1998). At the end of Proterozoic, the southern Arabian Peninsula underwent an extensional intraplate regime, characterized again by volcanism and magmatism. In late Precambrian this extension caused uplift and erosion processes of the basement rocks, followed by the formation of several basins, related to major wrench-fault-systems (e.g. Najd fault-system; Ellis et al., 1996). The basins are filled by Paleozoic-early Mesozoic clastic sequences, deposited in marine epicontinental to deltaic environments, locally containing evaporites (Beydoun, 1997).

During Triassic to middle Jurassic, Yemen was part of the Afro-Arabian plate of western Gondwanaland. The Jurassic break-up of Gondwana caused the separation of the Arabian plate from the original supercontinent. Rifting was oriented along tectonic trends inherited from the Precambrian wrench-fault systems (Bosence, 1997; Ahlbrandt, 2002, and references therein). In Yemen, the Mesozoic extensional tectonics resulted in the formation of five basins (Fig. 3.4): 1) Siham-Ad-Dali', 2) Sab'atayn, 3) Say'un-Masilah, 4) Balhaf, and 5) Jiza'-Qamar (As-Saruri et al., 2010).

The Sab'atayn and the Say'un-Masilah basins are the only hydrocarbon producing basins in Yemen (Ahlbrandt, 2002; As-Saruri et al., 2010). The Jabali mineral deposit is located on the western border of the Sab'atayn basin.

Pre-rift sedimentation within the basins (Toarcian-Bathonian) is initially represented by the continental clastic sediments of the Kuhlan Fm., which include fluviatile and arkosic red-beds, passing upward to shallow-marine facies, representing the early transgressive phases of the late Jurassic seas (Bathonian-Callovian) (Fig. 3.5) (Beydoun et al., 1998). Late Jurassic marine deposits are comprised in a unique Group, which takes its name from the city of Amran, and consists of pre-rift sediments, as well as of syn- and post-rift sequences (Csato et al., 2001). This Group shows throughout Yemen several lateral changes of facies in the stratigraphy and thickness variations. These differences had the effect of inducing several distinct descriptions (with different formational names) of the same stratigraphic sections in the geological literature (Menzies et al., 1994). Beydoun et al. (1998), in a review on the stratigraphy of Yemen, established the "official" subdivision of the Amran Gp. The authors distinguish four main Formations in the Group (Fig. 3.5): 1) Shuqra Fm. (Callovian-Oxfordian), consisting of marine fossiliferous limestones; 2) Madbi Fm. (Kimmeridgian-Tithonian), consisting of marly-shaly rocks; 3) Sabatayn Fm., mainly made up of evaporites; and 4) Naifa Fm. (upper Tithonian-Berriasian), consisting of carbonates. These Formations have been further subdivided in several Members, which correspond with their diversity to the various facies heteropies of the sequence (Beydoun et al., 1998). The Shuqra Fm. has been deposited after the Kuhlan Fm., in a pre-rift regime. The Madbi and Sabatayn Fms., instead, have the characteristics of syn-rift sediments. The Naifa Fm. should be considered a post-rift deposit (Csato et al., 2001). Both the Shuqra and the Madbi Fms. outcrop in large part of Yemen, from the western high plateaus to the eastern basins, wherever the general characteristics of the Amran Gp. have been recognized. The Sabatayn Fm., instead, occurs within the Sab'atayn basin, and along its western flank. The Nayfa Fm. can be especially observed in the eastern basins (Beydoun et al., 1998).

The Shuqra Fm. is characterized by the following lithological units: 1) basal interval of detrital intertidal limestone, 2) marls and thinly bedded carbonaceous biomicrite, 3) foraminiferal biomicrite interbedded with chert nodules, 4) dolomitic marl interbedded with dolostone, sandy oolitic-oncolitic limestone interbedded with fossiliferous argillaceous limestone and bioclastic sandstone, 5) coral-algal stromatolitic limestone, containing organic fragments, oncolite grains and black foraminiferal biomicrite (Youssef, 1998). The Shuqra Fm. is the most widespread Jurassic Formation in the country (Beydoun et al., 1998).

The Madbi Fm. is made up by organic-rich-bituminous marine shales, deltaic sandstones, debris flow breccias, well bedded limestones, and turbidites (As-Saruri et al., 2010). Thin interbeds of marly and fossiliferous limestones also occur (Youssef, 1998). The organic-rich shales of this Formation are the main source rocks for hydrocarbons in Yemen (Ahlbrandt, 2002; As-Saruri et al., 2010).

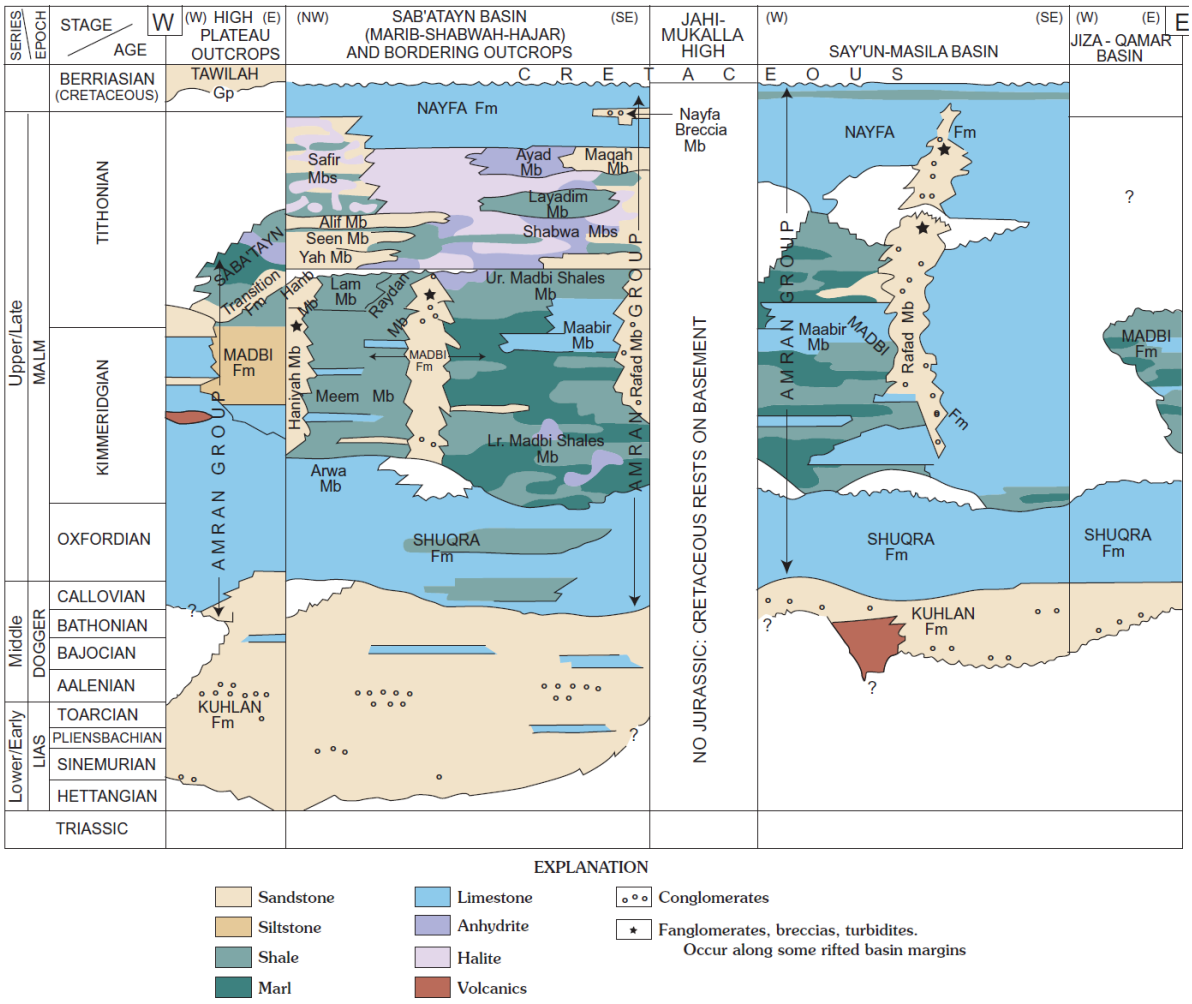

Fig. 3.5. Jurassic lithostratigraphy, correlations, and spatial stratigraphic distribution for Yemen (Beydoun et al., 1998, modified; Ahlbrandt, 2002).

The Sabatayn Fm. is constituted mainly by evaporites, salts, and shales (Beydoun et al., 1998). The Nayfa Fm. consists of marine platform carbonates and marine clastics, dolostones and dolomitic shales, marls and silts, and fine-grained shelly limestones, locally yielding a rich ammonite fauna (Menzies et al., 1994; Beydoun et al., 1998).

Cretaceous sediments, ranging in age from Berriasian to Maastrictian (Tawilah Gp.), completed the filling of the Jurassic grabens (Beydoun et al., 1998). In western Yemen, the main Cretaceous lithofacies are medium to very coarse-grained, cross-bedded sandstones, where numerous paleosols have been developed. In eastern Yemen, instead, the Cretaceous succession is prevailingly siliciclastic, but it contains also shales and limestones. The total thickness of the Tawilah Group is very variable, being around a few hundred meters in the Sana'a area, and reaching a few thousand meters within the Sab'atayn basin (Beydoun et al., 1998). From the western to eastern Yemen, a transition from continental (braided, fluvial-channel deposits) to marine facies could be observed within the Group (Beydoun et al., 1998).

A second rifting phase, after the already mentioned Jurassic break-up, is associated with the opening of the Red Sea and the Gulf of Aden during Oligocene and Miocene. At that time, a widespread volcanism followed by a denudation phase affected the whole western Yemen, whereas the eastern part of the country was characterized by continuous sedimentation, and complete absence of magmatic activity (Menzies et al., 1994). Volcanism in western Yemen was associated with the Afar plume upwelling beneath the Africa-Arabian plate (Bosworth et al., 2005). The Oligocene igneous rock association is known as the "Yemen volcanic group" or "Yemen trap series" (Moseley, 1969), and consists of more than 3 km thick magmatic deposits, spanning from flood basalts and bimodal products, erupted between ~31 Ma and ~29 Ma, to acid massive ignimbrites, dated between ~29 Ma up and 26 Ma (Baker et al., 1996; Coulié et al., 2003). The base of the volcanic series is diachronous but conformable with the underlying Tawilah Group., and this points to a limited pre-volcanic tectonics (Menzies et al., 1994). A stratigraphic gap, extended from ~26 to ~19 Ma, accompanied by a marked unconformity at the top of the deformed “Yemen volcanic group”, indicates instead that the main rifting phase started in late Oligocene or early Miocene (Ukstins et al., 2002). Early Miocene magmatic products consist of small plutonic bodies (near Dhala, age ~22-21 Ma), and abundant mafic and felsic dikes (Radfan area, age ~25-16 Ma), both emplaced along the Red Sea margin (Zumbo et al., 1995). Massive alkali granite bodies, instead, outcrop more inland (near Taiz, ~21 Ma; Huchon et al., 1991). The Miocene volcanism is related to the extension responsible for the Red Sea faulting, and testifies a movement of Yemen away from the focus of Afar plume (Menzies et al., 1997; Huchon et al., 2003).

In the Jabali area Tertiary volcanism produced numerous trachytic dykes and sills (dated at 22 Ma - early Miocene). Large alkaline granites occur in the area located about 15 km to the west of Jabali minesite (Jabal as Saad) (Al Ganad et al., 1994; Allen, 2000). Late Miocene volcanism (12-10 Ma) formed small basaltic plateaus and volcanic centers, showing marked angular unconformities on the underlying Oligo-Miocene flood deposits (Capaldi et al., 1983; Huchon et al., 1991). Plio-Quaternary volcanism is fairly widespread within the country, in the areas NW of Sana'a-Amran, Dhamar-Rada, Marib-Sirwah, Balhalf-Bir Ali, and Shuqra (Menzies et al., 1994).

In eastern Yemen, marine sedimentation continued during Eocene, resulting in sedimentary successions displaying continental, evaporite, and shallow to deep marine carbonate and siliciclastic facies. Miocene to Recent sedimentation occurred in coastal embayments, along a coastline very similar in shape to the actual coast (Menzies et al., 1994).

Apatite fission tracks data of the Yemen Red Sea rift flank indicate a considerable exhumation at ~17-16 Ma, associated with the main phase of Red Sea continental extension (Menzies et al., 1992). Fossil beaches along the Gulf of Aden record continuous tectonic uplift during Plio-Quaternary (Brannan et al., 1997).

Cenozoic climate is believed to have been analogous to actual; in fact, global climatic fluctuations were buffered by the low latitude location of the region. Today, the climate of the region is hot and arid, and affected by variations essentially due to topographic effects, with rain produced by air masses forced up over the western plateau of Yemen (Menzies et al., 1994). The result is a volume of precipitation highly variable from a side to another of

the country. Along the coastal plains the average annual rainfall is about 130 mm/y, whereas over the high mountains the registered volumes are between 500 to 800 mm/y. Rainfall is sporadic, and generally occurs during the summer months (NWRA, 2007). Air temperatures in the region are generally very high (25°-40°C, in the coastal plains; 10°-30°C, in the high plateaus). Meteoric water infiltrates the more elevated areas of the Yemen plateau, feeding local aquifers, hosted in intra-mountain basins (Farquharson et al., 1996). From these aquifers, more than 100 thermal springs are known to be currently active (Mattash et al., 2005). They are scattered throughout the country, although often grouped around the Tertiary and Quaternary volcanic centers. Travertine formation is also associated with igneous rocks: some of them are possibly of Tertiary age (Minissale et al., 2007).

Minissale et al. (2007) in a study on the current geothermal activity in Yemen, report the occurrence of three important springs in the Sab'atayn basin, one located about 30 km north of Jabali, and other two about 25 km south of Jabali, near the city of Sirwah (Marib). These springs have water temperatures comprised between 30° and 35°C, and pH comprised between 5.8 and 7.5. The $\delta^{18}O$ of water ranges between -3.64‰ and -4.18‰ SMOW (Minissale et al., 2007). Considering the air temperature of the sites, the springs can be defined as "cold". In the Sirwah area Pliocene to Holocene travertines indicate the existence of hot springs at the time, genetically related to the igneous activity of the Marib volcanic field (Weiss et al., 2009). A thick travertine deposit occurs also 15 km to the west of Jabali, south of Jabal as Saad (Allen, 2000), this clearly indicating that thermal springs were active (Tertiary-Quaternary?) also in this area.

The major onshore petroleum systems of Yemen are hosted by the Mesozoic sediments of the Sab'atayn and the Say'un-Masilah basins (Ahlbrandt, 2002; As-Saruri et al., 2010). Main petroleum reservoirs are represented by the clastic and carbonatic members of the Madbi Fm., which have been sealed by the salt deposits of the Sabatayn Fm. in the Sab'atayn basin, and by the carbonate and shale members of the Tawilah Gp. in the Say'un-Masilah basin (Ahlbrandt, 2002). Source rocks of hydrocarbons are the shales of the Madbi Fm. (Csato et al., 2001). Oil generation is believed to have started in late Cretaceous, after the deposition of the early sediments of the Tawilah Gp. (Fig. 3.6). In fact, thermal maturation modeling shows that the rocks have expelled oil in two main phases: from 135 to 90 Ma and from 85 to 50 Ma, with high and low heat flows, respectively (Csato et al., 2001). Salt sealing the Sab'atayn petroleum system was mobilized during early Cretaceous, shortly after the deposition of the Nayfa Fm. The activities that occurred within the basin: e.g. Cretaceous differential sedimentation, Tertiary faults reactivation, and volcanism caused further movements of the salt bodies during the entire period (Csato et al., 2001).

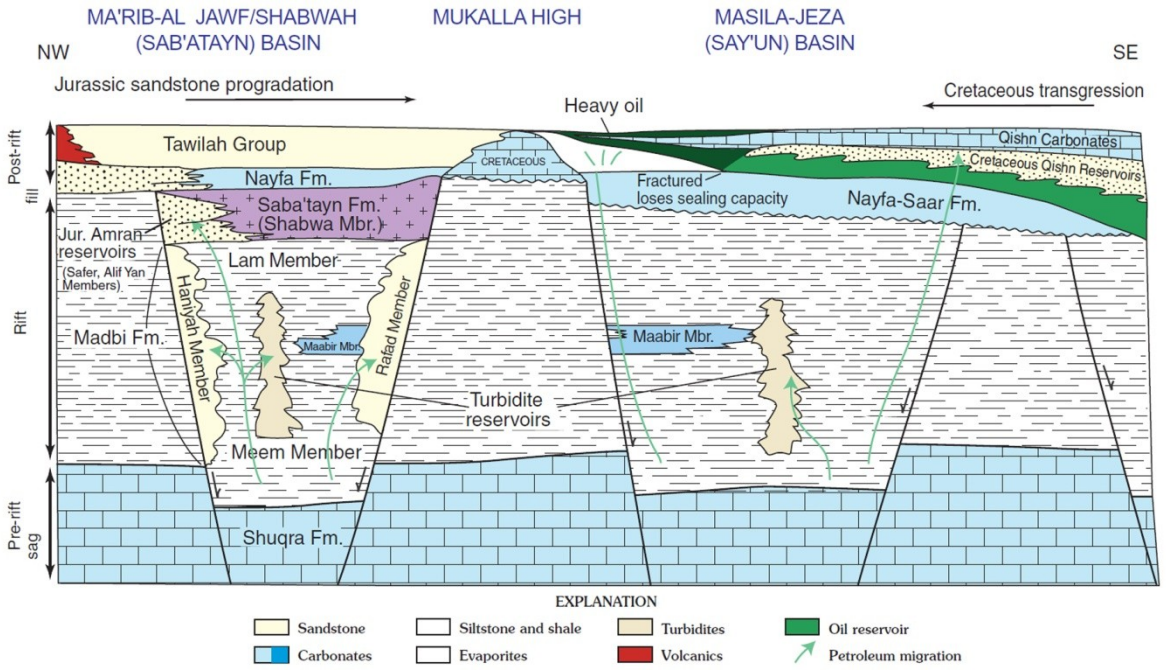

Fig. 3.6. Schematic diagram of petroleum systems in Sab'atayn and the Say'un-Masilah basins (Ahlbrandt, 2002).

Zinc-lead deposits in Yemen

Ore minerals occurrences in Yemen comprise gold, lead, zinc, copper, silver, nickel, iron, titanium, REE, tungsten, tin, and radioactive elements (Yemen Geological Survey website, 2009).

Less than twenty zinc-lead mineralizations have been discovered in Yemen; most of them are located along the margin of the rifts (e.g. the Sab'atayn basin), or in rift-affected blocks. Lead and zinc ore deposits are hosted by Jurassic to Paleocene carbonate rocks within the Sab'atayn basin, and form two main clusters, occurring in the Jabali and Tabaq areas (Fig. 3.4) (Yemen Geological Survey and Mineral Resources Board, 1994, 2009).

The Jabali area comprises several ore concentrations hosted by carbonate rocks of the Jurassic Amran Gp., located on the western flank of the Sab'atayn basin, about 60 km northwest of the town of Marib. Here, the Amran Gp. overlies the Precambrian basement rocks, and is intruded by Tertiary magmatites. Eight minor Zn-Pb occurrences can be also observed in the Jabali area. These small ore bodies consist of variously extended gossans containing limited zinc and lead concentrations, hosted in dolomite breccias. The principal sites are Barran, Al-Kwal, and Haylan, which are characterized by maximum grades of 16.5% Zn and 6% Pb, and by a very limited areal extension (Yemen Geological Survey and Mineral Resources Board, 1994, 2009).

The Tabaq area is located approximately 360 km east-northeast of Aden, in southern Yemen, in the same rift system hosting the Jabali deposit, but 500 km east of the Jabali minesite (Fig. 3.4). Here, nine small Pb-Zn occurrences have been identified. The mineralized occurrences are hosted in the Jurassic to Paleocene carbonate sequence, and are associated to zones of

dolomitization and strong faulting. Maximum values of 12% Zn and 3.8% Pb have been measured at Tabaq along a 30 m-strike section; at Wadi Rama and Jabal Al-Jubal, the other two major sites of the area, the mineralized rock (which contains also some barite) generally shows a lower grade. No mineralogical information is available for all these minor occurrences (Yemen Geological Survey and Mineral Resources Board, 1994, 2009).
Another base metal mineralized district is located in the southwest part of the Say'un-Masilah basin, in the Mukalla area (Fig. 3.4). Mineralization is fault-controlled, and consists of veins of barite and galena. A secondary mineralization containing willemite, smithsonite, cerussite, descloizite, calcite, pyrolusite and celestine, with anomalous grades of Ag, Cd, Ga, Ge, and Mo also occurs in this area (Mattash, 2008).

Jabali deposit - Exploration history

Jabali is the most significant base metal deposit in Yemen (Yemen Geological Survey and Mineral Resources Board, 1994, 2009). The artisanal workings in the area are thought to be over 2,500 years old (Fig. 3.7). Around 1,000 A.D. the geographer Al Hamdani considered Jabali the greatest silver mine in the Muslim world, with over 400 furnaces producing "one camel load of metal" per week (Christmann et al., 1983). Old mine workings extended over an area of about 10 hectares, tracing cavities filled by relatively soft oxidized ore, locally rich in silver. The ore was processed on site. Waste dumps contain about 120,000 t, at average grades of 24% Zn, 3.5% Pb, and 160 ppm Ag. The artisanal metallurgical process was not effective, since slags still contain 23% Zn, 6.5% Pb, and 40 ppm Ag (SRK Consulting, 2005).
The site was re-discovered by the Bureau de Recherché Geologique et Miniere (BRGM) and the Yemen Geological Survey and Mineral Resources Board (YGSMRB) in 1980. Between 1981 and 1986, an exploration and evaluation programme, based on 57 drill holes reported an accessible-by-open-pit resource of 3.0 Mt, at 15.2% Zn, and an amenable-by-underground mining volume of 1.24 Mt at 13% Zn. BRGM and YGSMRB during and after the period of exploration at Jabali, produced several scientific papers on the characterization and genesis of the deposit (Christmann et al., 1989; Al Ganad et al., 1994) and a Ph.D. thesis (Al Ganad, 1991). Allen (2000) in an unpublished report expressed a concept on the genesis of the mineralization much different from those previously formulated by the BRGM team. No further scientific paper on Jabali has been produced in recent years, with the exception of Mondillo et al. (2011),
In June 1993, after 3 years of studies, "Watts, Griffis and McOuat Ltd.", concluded a pre-feasibility report, indicating reserves of 3.6 Mt at 16.37% Zn. In 1996, Minorco and Ansan Wikfs granted a licence over the deposit. In 1998, ZincOx Resources entered into joint ventures with Minorco and Ansan Wikfs, thus becoming the manager and operator for the development of the deposit. In 2004-2005 ZincOx, together with SRK Consulting, concluded the feasibility study on the deposit, and reported total resources of 12.6 Mt at 8.9% Zn, 1.2% Pb, and 68 ppm Ag.

Actually the exploitation and development rights to the Jabali zinc deposit are owned by Jabal Salab Company (Yemen) Limited, in which ZincOx previously held a 52% interest, and Ansan Wikfs held the balance (48%). In January 2008, the company upgraded for a more quick development of a mine at Jabali. In October 2009, due to slower than expected progress on the project, the project went into default, and due to the difficult international economic conditions at that time, the bond holders decided to retire the bond and reclaimed the cash held in the project development company's account. The situation has worsened due to the turmoil related to the so-called “Arab spring” uprising. As a consequence work at the site has stopped (www.zincox.com).

Fig. 3.7. View of the Wadi Jabali, looking NE: old mine workings.

The Jabali deposit - Geology and mineralization

The Jabali deposit (15°37'N latitude, 44°46'W longitude) covers an area of about 2 km^2, striking in a NW direction, at an altitude comprised between 1,850 and 1,950 m.s.l. (Fig. 3.8). The deposit is located in correspondence of a small plateau, on the eastern flank of a NW-SE-elongated mountainous area that is a segment of the western boundary of the Sab'atayn basin, which extends for several km^2 in the adjacent lowland. The mountainous area is called "Jabal Salab", and has a maximum elevation of 2,250 m.s.l. A small crest, occurring on the NW part of the Jabali plateau, is called "Jabal Barrik" (~2,000 m.s.l.); a small valley named "Wadi Jabali" delimits this area from the SE part of the plateau, where the ore bodies outcrop. The plateau is dissected by another valley ("Wadi Khaynar") further SE. These valleys cut vertically the mineralized formations, which are exposed along the valley flanks.

Even though the Jabali orebodies are hosted by sedimentary rocks, also small igneous sills and dikes occur at the minesite.

Sedimentary rocks

The sedimentary rocks hosting the Jabali orebody belong to the Amran Gp. (Al Ganad et al., 1994). In the Jabali area these lithologies overlie directly the Proterozoic basement and, contrary to the standard basin stratigraphy (Beydoun et al., 1998), are reduced to a maximum of 300 m in thickness (Al Ganad et al., 1994). Al Ganad (1991) and Al Ganad et al. (1994) have subdivided the Amran Gp. sequence at the minesite into the nine following lithostratigraphic units (starting from the base) (Fig. 3.8, 3.9):

Unit 1 (10 m): sandstone and conglomerate, transgressive over the late Proterozoic basement;

Unit 2 (25 m): gypsiferous mudstone overlain by dolomitized calcarenite, interbedded with marl and nodular limestone (unknown age);

Unit 3 (50 m): micritic and biomicritic limestone (Callovian), containing nodular concretions and chert layers;

Unit 4 (15 m): micritic limestone and finely bedded lagoonal/lacustrine dolomite (unknown age);

Unit 5 (40 m): Partly dolomitized bryozoan calcarenite (Late Oxfordian-Early Kimmeridgian), overlain by coral-bearing oolitic and oncolitic limestone. A local disconformity occurs at the top;

Unit 6 (80 m): greenish gypsiferous mudstone passing to micritic ammonite-bearing limestone interbedded with marls and calcareous sandstone (Kimmeridgian);

Unit 7 (80 m): massive bioclastic and biomicritic limestone, locally oolitic with coral bioherms (Kimmeridgian) (Fig. 3.10), partly dolomitized. This unit outcrops at the top of the plateau where the Jabali deposit is located, and is affected by strong karstic erosion;

Unit 8 (0-30 m): black mudstone and argillite with gypsum crystals and dolomite intercalations, grading laterally to micritic ammonite-bearing limestone (Late Kimmeridgian-Tithonian); a slight disconformity occurs at the top;

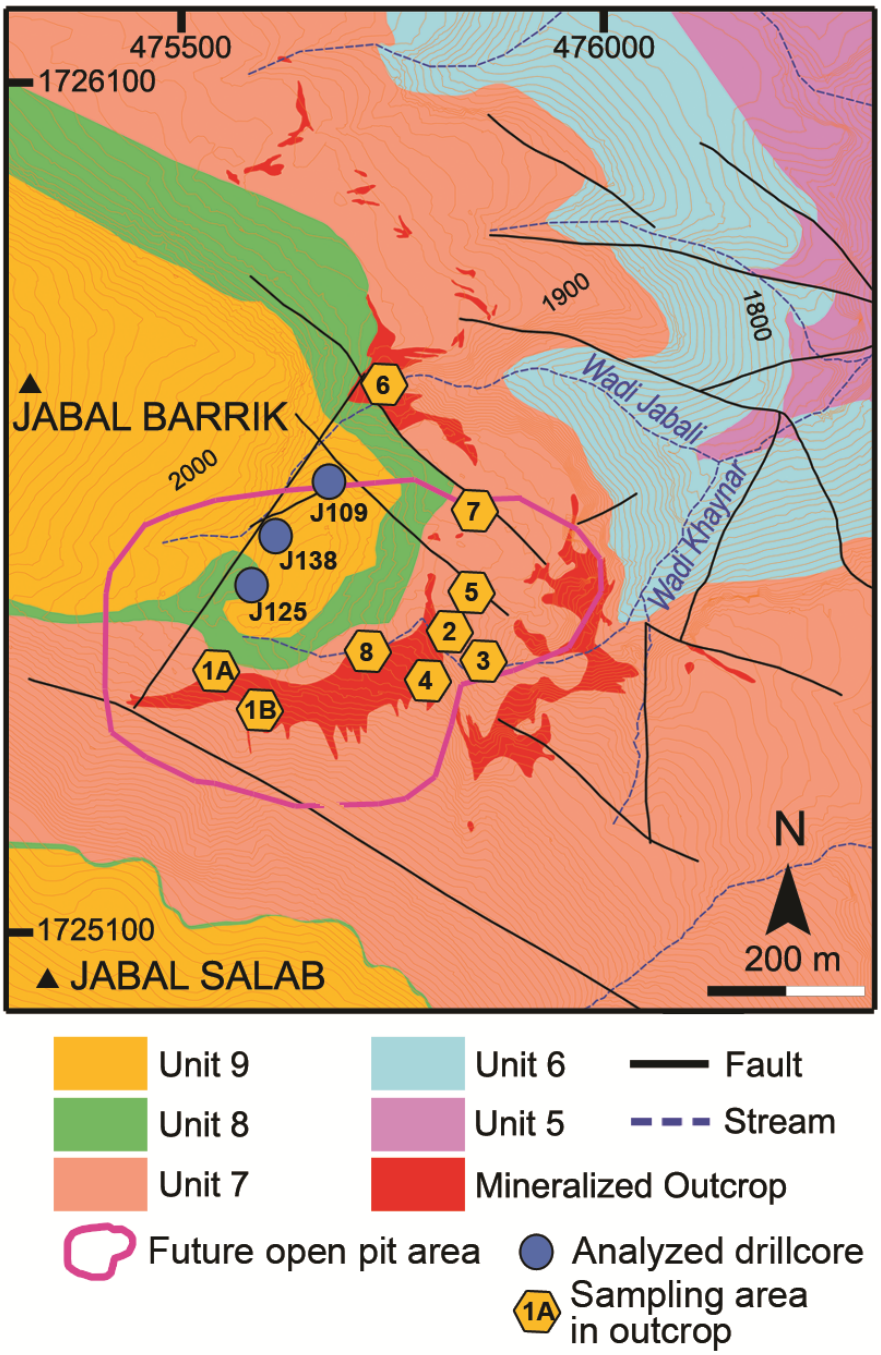

Fig. 3.8. Geological map of the Jabali mining site with the location of analyzed drillcores, and the future open pit area (modified from SRK Consulting, 2005). Description of the Units is in the text and in Fig. 3.9.

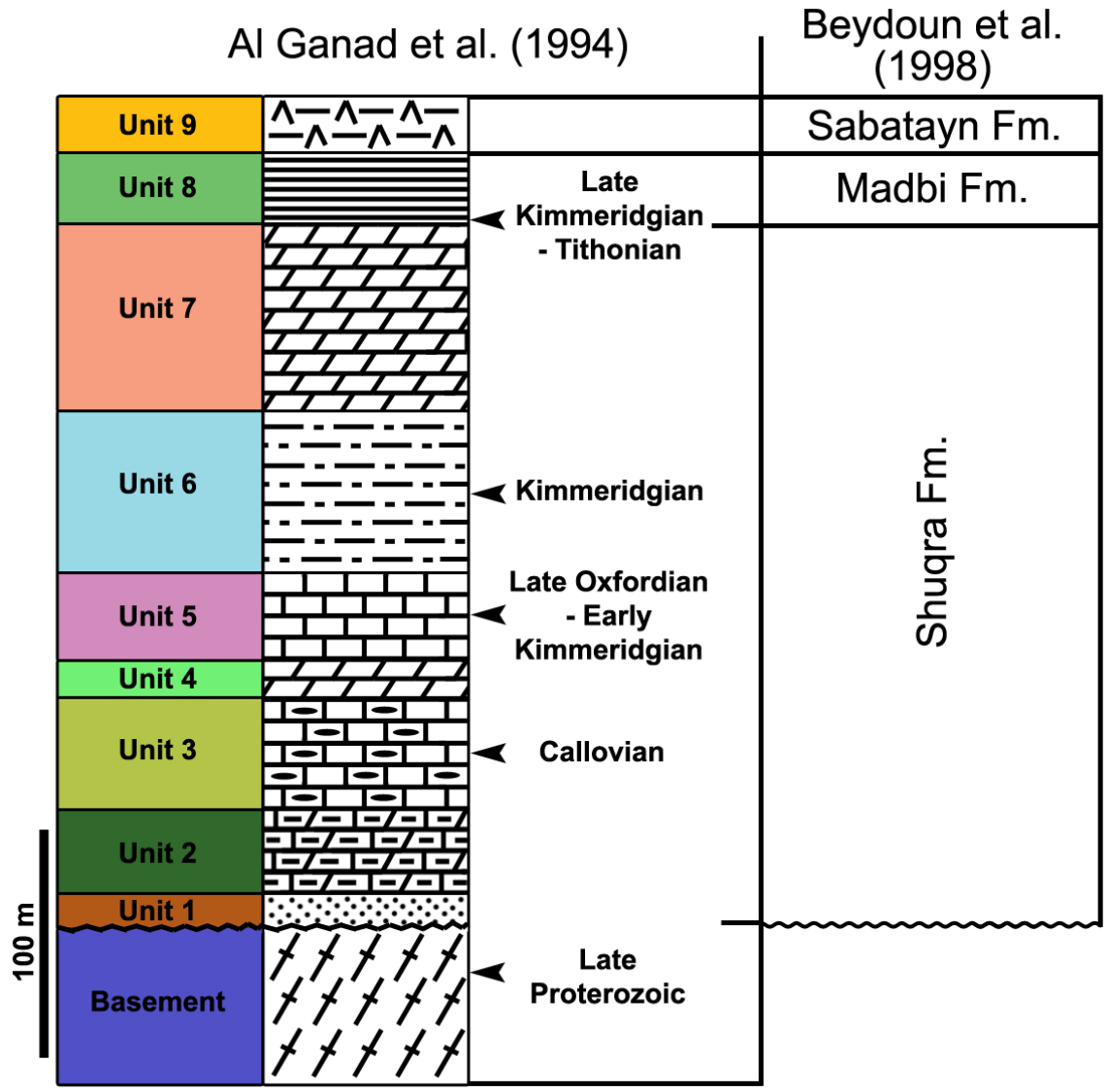

Fig. 3.9. Stratigraphy of the Jabali area with the Units established by Al Ganad et al. (1994) (modified), correlated with the correspondent Formations of the "standard" Amran Gp. of Beydoun et al. (1998). Unit 1: sandstone and conglomerate, transgressive over the Late Proterozoic basement; Unit 2: gypsiferous mudstone overlain by dolomitized calcarenite, marl and nodular limestone; Unit 3: micritic and biomicritic limestone (Callovian) with nodular concretions and chert layers; Unit 4: micritic limestone and finely bedded lagoonal/lacustrine dolomite; Unit 5: partly dolomitized bryozoan calcarenite (Late Oxfordian-Early Kimmeridgian), overlain by coral-bearing oolitic limestone. A local disconformity at the top of Unit 5; Unit 6: greenish gypsiferous mudstone grading to micritic limestone (Kimmeridgian) and marls; Unit 7: massive bioclastic and biomicritic limestone, locally oolitic with coral bioherms (Kimmeridgian). The Unit is dolomitized and affected by karstic erosion at the top; Unit 8: black mudstone and argillite with gypsum crystals and dolomite intercalations, grading laterally to micritic ammonite-bearing limestone (Late Kimmeridgian-Tithonian); Unit 9: biomicrite with oncolites and bio-oocalcarenite (Late Jurassic).

Unit 9 (>20 m): biomicrite with oncolites and bio-oocalcarenite with intercalations of gypsum and lenses of arcosic sandstone ("Transition Beds"; Late Jurassic-Early Cretaceous). The last two units outcrop along the Jabal Barrik crest, which constitutes a relief over the Jabali plateau.

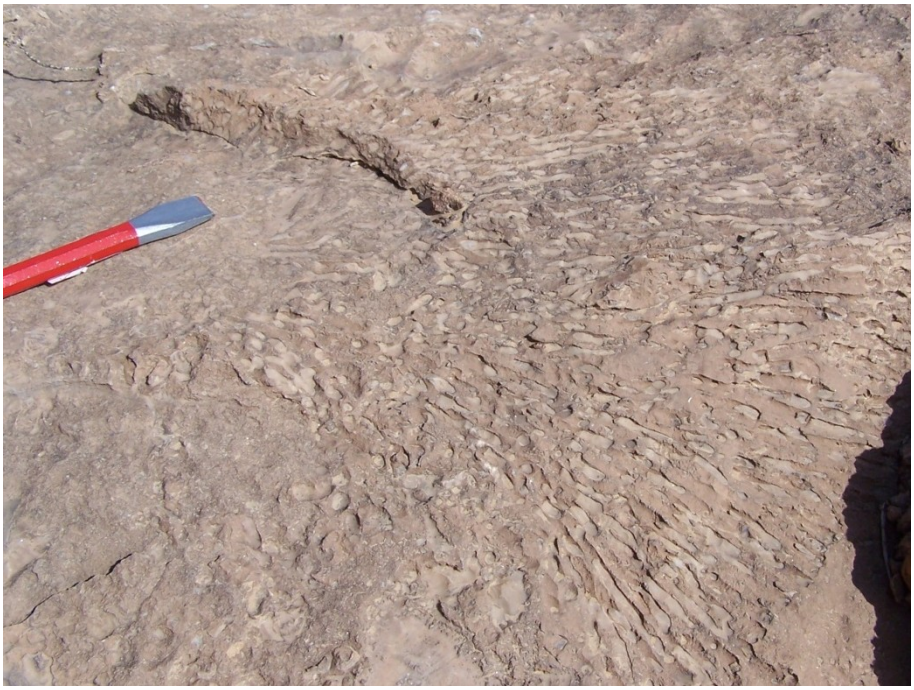

Fig. 3.10. Outcrop at Jabali. Non-dolomitized Unit 7: bioherms.

Fig. 3.11. Outcrop at Jabali. Unit 8: argillite.

The sedimentation in the Jabali area was relatively homogeneous with that in the basinal zones up to the end of the Oxfordian, with no significant changes in facies thickness. The sedimentation became, instead, strongly inhomogeneous starting from the Kimmeridgian-Tithonian, contemporarily to the main tectonic evolution and deepening of the Sab'atayn basin (Al Ganad et al., 1994).
Comparing the lithostratigraphy of Al Ganad et al. (1994), with the "standard" stratigraphic subdivision of the Amran Gp. (Beydoun et al., 1998), it is possible to correlate the first seven units (from the unconformity above the Proterozoic basement to the base of the black mudstone and argillite) with the Shuqra Fm. (Callovian-late Kimmeridgian). Unit 8, for its characteristics and age, is clearly correlable with the Madbi Fm., whereas Unit 9 has been associated with the lower section of the Sabatayn Fm. The differences existing between the thicknesses of the "standard" Formations with those of the corresponding "Units" at Jabali, are related to the different tectonic regime at the time of sedimentation, as mentioned also by Al Ganad et al. (1994). The Shuqra Fm. was deposited in a pre-rift regime (Beydoun et al., 1998), with a relatively high tectonic stability. The Madbi and Sabatayn Fms., instead, are characterized by syn-rift sedimentation (Beydoun et al., 1998), and then by strong variation in thickness over small areas. The Madbi and Sabatayn Fms. are very thin at Jabali, because this site, located on the border of the basin, should have been affected during upper Jurassic rifting by partial uplifts and limited sediment deposition.
The Jurassic series is intruded by numerous trachytic dykes and sills, related to Tertiary alkaline volcanism of the area (early Miocene). The travertine deposit occurring near the Jabal as Saad Tertiary intrusive is located at an elevation of 1,500 m (Allen, 2000).

Structural setting
The structural setting at the Jabali site is essentially controlled by the extensional tectonics produced during rifting, and the rocks are affected mostly by brittle deformation. The sedimentary succession follows its natural orientation, and lies almost horizontally on the flank of the basin (Fig. 3.11). Small slightly tilted sectors are characterized by westward dipping strata.
The prominent fault trend is 120° to 140° (Fig. 3.8). This fault set includes the main Jabal Salab fault, that acts as a synthetic fault, and borders the shoulder of the plateau below the Jabal Salab peak, and the associated sub parallel structures (antithetic faults). A conjugate set is trending from 065° to 080°, and includes the Wadi Jabali valley. A further major system is developed at 000° to 005°. A more subtle fracture direction measured in the field trends 025° to 040° (SRK Consulting, 2005, and references therein). The planes have dip angles ranging between 60° and 80°.

Fig. 3.11. View of the Wadi Khaynar valley, looking ESE. Beds of Unit 7 are gently inclined. A magmatic dyke (red arrow) cuts the sedimentary succession.

Mineralization and previous work

The Jabali ore bodies are mainly hosted by the dolomitized section of Unit 7 (Al Ganad et al., 1994; SRK Consulting, 2005), and are only partly outcropping. In fact, at least half of the mineralized lithologies occur in the subsurface, below Jabal Barrik (SRK Consulting, 2005). The ore is almost completely oxidized, but in the volumes underlying Unit 8, primary sulfides have been partly preserved from oxidation by the impervious cover of black mudstone and argillite (Al Ganad et al., 1994).

The mineralization is structurally and lithologically controlled, and this control is reflected in the morphology of the various orebodies, that are both tabular and parallel to stratigraphy, and vertical along fractures, faults and at the intersection of these structures. In particular, the structurally controlled mineralization is developed along the three main tectonic trends measured on site, striking from 120° to 140°, 065° to 080° and 000° to 005°, and may also occur as "keel" like features. The same directions seem to have controlled the distribution of the epigenetic dolomitization phases. At the intersection of faults, the mineralization forms big vertical bodies, which are like "chimneys". The stratiform bodies, parallel to stratigraphy, occur in three different zones: a laterally extensive "Upper" zone, and more sporadic "Lower" and "Middle" zones. These bodies are generally flat but, at the base of the Jabal Salab massif, along the NW-SE fault they dip towards NE with angles greater than 30° (Fig. 3.8) (SRK Consulting, 2005).

The nonsulfide ore is massive, semi-massive and disseminated, and is characterized by vuggy to highly porous, brown-orange to white zinc nonsulfide minerals (Fig. 3.12A). A porous cellular boxwork structure accompanied by numerous cavities coated with zinc minerals, dolomite and calcite is quite common.

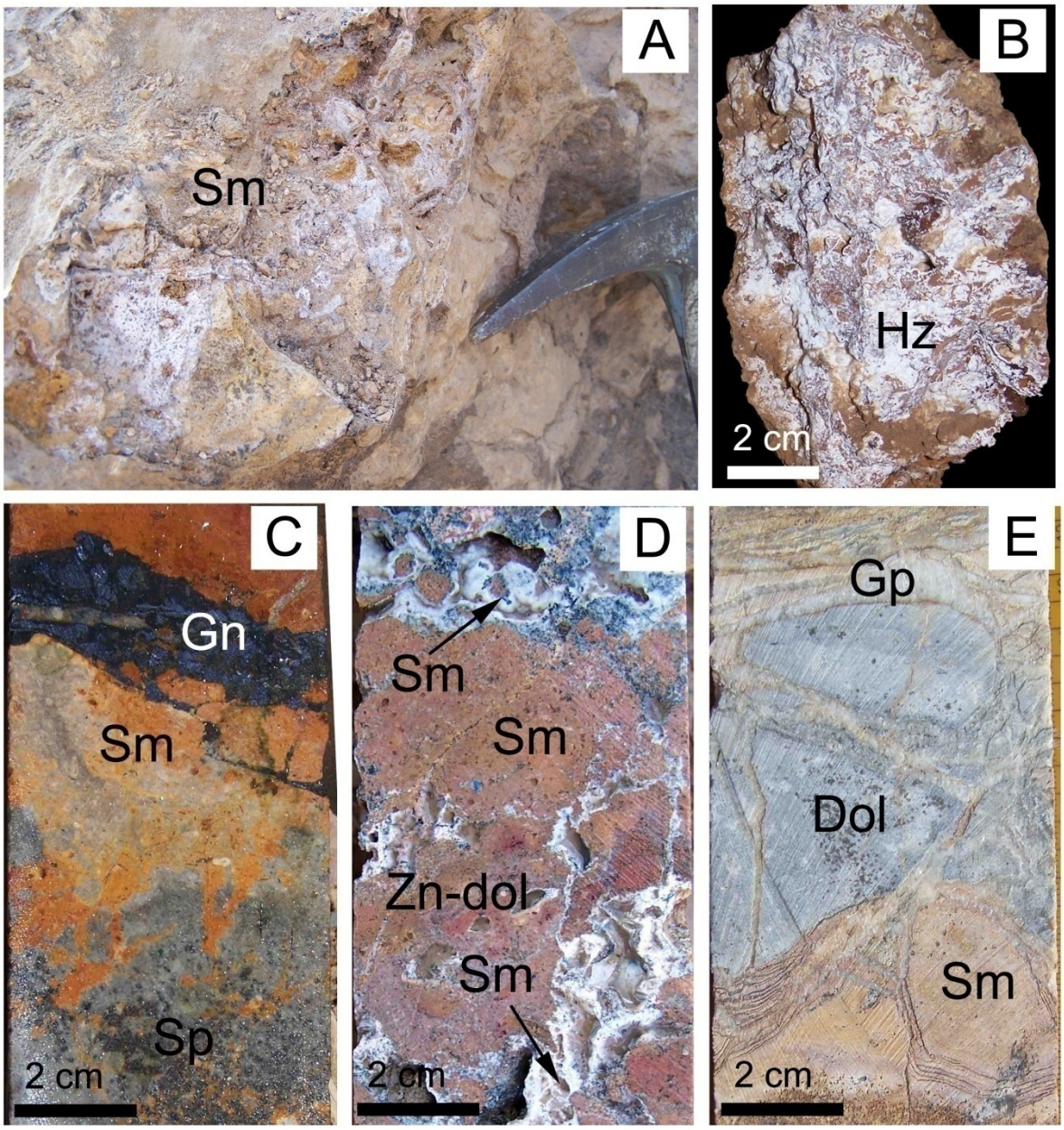

Fig. 3.12. Mineralized rocks. A) JS MON 3. Smithsonite in outcrop, with a vuggy-highly porous texture. B) JS MON 28. Hydrozincite coating smithsonite and host rock. C) J125-2. Partly oxidized ore, with remnants of sphalerite and galena. D) J125-15. Massive smithsonite, replacing Zn-dolomite, and smithsonite crusts in cavities. E) J125-3. Gypsum veins, cutting both dolomite and smithsonite. Dol = dolomite; Hz = hydrozincite; Gn = galena; Gp = gypsum; Sm = smithsonite; Sp = sphalerite.

The most common secondary zinc mineral is smithsonite, intimately intergrown with dolomite (Fig. 3.12A). Fine to granular amorphous aggregates of hydrozincite have been observed in outcrop (Fig. 3.12B), but are very uncommon at depth and in drill cores. Hemimorphite occurs in minor amounts. Lead is present both as cerussite and anglesite. The nonsulfide ore replaces primary sulfides (Fig. 3.12C) and the dolomite host rock (Fig.

3.12D), that is also dedolomitized and patchily replaced by calcite. Iron staining is common throughout the mining area, resulting in variable concentrations of goethite, hematite, and Mn(hydr)oxides. Silver is contained in Ag-sulfide and as native metal. Gypsum can be very abundant through the entire mineralized area (Fig. 3.12E).

Remnants of the primary sulfide association can be observed in outcrop and drillcores, and consist of sphalerite (predominant), galena, and pyrite/marcasite. Sphalerite occurs as two distinct generations, a first dark colored, and a second more abundant and represented by zoned euhedral to subhedral honey-colored or brownish-red crystals. Sphalerite contains iron and silver, cadmium, copper, germanium and mercury (Al Ganad et al., 1994).

Fluid inclusions of sphalerite have bimodal homogenization temperatures to the liquid, between 60-85°C and 85-110°C, and salinity of 10-14 eq. wt% NaCl and 19-23 eq. wt% NaCl respectively (Al Ganad et al., 1994).

Lead isotope composition of galena and cerussite range between: 18.85 and 18.95 $^{206}Pb/^{204}Pb$, 15.66 and 15.72 $^{207}Pb/^{204}Pb$, and 39.71 and 39.92 $^{208}Pb/^{204}Pb$. These compositions are similar to the lead isotopic composition of other Zn-Pb deposits of the Sab'atayn basin, and are interpreted as "indicative of the contribution of an early Proterozoic crustal component", e.g. basement of the basin (Stacey and Hedge, 1984; Al Ganad et al., 1994).

Al Ganad et al. (1994) distinguish two periods of dolomitization in Unit 7, each of them comprising two successive stages: a first stage, interpreted as early diagenetic (D1+D2), and a second stage, syn- post-contemporaneous with sulfide deposition (D3+D4). D1 dolomite corresponds to the first limestone replacement into a gray mosaic dolosparite, which preserves remnants of bioclastics and allochems. D2 dolomitization is associated with an increase of grain size, and a major replacement of original limestone, also producing assemblages of small euhedral, zoned dolomite crystals. D1 and D2 dolomites contain disseminated pyrite. D3 and D4 stages are characterized by “baroque” crystals (*saddle* dolomite, Radke and Mathis, 1980), with sizes comprised from a few hundred microns to few millimeters, and are characterized by small amounts of iron. D3+D4 dolomite phases occur within cavities, and fill fractures crosscutting the previous dolomite generations (Al Ganad et al., 1994). Al Ganad et al. (1994) recognized also a late dedolomitization phase associated to sulfide oxidation, which transformed dolomite into calcite.

The basic geological concepts of Al Ganad et al. (1994) have been confirmed in the reports of Allen (2000) and SRK Consulting (2005), but the genetic model for the primary and secondary mineralization has remained an open-matter, and is still strongly debated.

After Al Ganad et al. (1994), the lead isotope composition of galena indicates a source of the metals from the basement; the sphalerite fluid inclusions have a basinal character and show salinities/temperatures similar to many carbonate-hosted Pb-Zn deposits (Roedder, 1976). The authors consider the primary mineralization being deposited by fluids migrating from the Sab'atayn basin during Mesozoic rifting. The fluids circulated in karst cavities related to the emersion surface at the top of Unit 7, and were emplaced slightly later than sedimentation of Unit 8 (Late Jurassic-Cretaceous). The black shales of Unit 8 should have acted as an impermeable barrier to the migration of fluids. Ore deposition has been

accompanied by several phases of hydrothermal dolomitization, as generally occurs for Zn-Pb MVT ores (Diehl et al., 2010).
A different genetic concept has been presented in the unpublished report of Allen (2000). Allen hypothesizes a hybrid CRD-MVT character for the primary mineralization at Jabali; though acknowledging some of the MVT characteristics outlined by Al Ganad et al. (1994), e.g. the high Ge values, he points to some other features of the mineralization, that could be more related to a CRD, like: young Pb-isotopes as at Angouran, Fe-rich sphalerite, abundant ore associated to Fe-Mn carbonate alteration, low pyrite, high Zn/Pb ratio, polymetallic geochemistry (As, Mo, Bi, Sn, Ag, Mn), large Tertiary alkaline granites with Sn-W-F-Fe skarns in the nearby area, and abundant trachyte dykes (~22 Ma age) within the Jabali host rock. The mineralization at Jabali should then have been generated by the circulation of CRD-MVT hybrid fluids along extensional structures related to Red Sea rifting, contemporarily to the development of magmatic activity in the region (~22 Ma) (Allen, 2000).
The oxidation of sulfides is again a debated-matter. Al Ganad et al. (1994) believe that oxidation has begun during Cretaceous, developed mainly during Paleogene, and continued up to Present. Allen (2000), considering various textural characteristics of the rocks, suggests a very simple single-stage of oxidation, of late Miocene to Present age, favored by a severely depressed palaeo-water table, and very deep surfaces of oxidation, which are testified by the height (above sea level) of the Plio-Pleistocene travertine deposit to the south of Jabal as Saad granite.

Methods of study

During this Ph.D. thesis I have carried out a mineralogical study on 40 samples from the Jabali cores J109, J125 and J138 (each sample consisting of a quarter core 1 m long) (TABLE 3.1). The three selected cores (J109, J125, J138) were drilled by ZincOx Resources during 2004, in the Jabal Barrik area, in correspondence of the central position of the future planned pit (Fig. 3.8). The drillcores were selected considering their position respectively to the pit: J125 is located in correspondence of the center of the pit, J109 on the north-centre and J138 on the east side of the future pit. The batch is considered representative of the Jabali orebody. The cores cross the barren Units 8 and 9, and reach the mineralized Unit 7 at a depth of about 60 m, sampling the "subsurficial" orebody. Several samples (35) from outcropping mineralization have also been studied (TABLE 3.2; Fig. 3.8).
The core fragments (65), and the outcrop samples (20) have been observed under petrographic microscope and under cathodoluminescence. This study has been followed by scanning electron microscopy (SEM) observation, and qualitative energy dispersive X-ray spectroscopy (EDS) analyses. SEM examination was carried out using a Jeol JSM 5310 instrument at the University of Napoli (CISAG). Element mapping and EDS spectra were obtained by the INCA microanalysis system (Oxford Instruments).

TABLE 3.1. Jabali drillcore samples. Drillcore location from Fig. 3.8.

Drillcore n.	From (m)	To (m)	ZincOx Assay n.	Sample n.
J109	57.3	58.3	1	J109-1
	58.3	59.3	2	J109-2
	59.3	60.3	3	J109-3
	60.3	61.65	4	J109-4
	61.65	62.7	5	J109-5
J125	50.78	51.78	1	J125-1
	51.78	53.1	2	J125-2
	53.1	54.73	3	J125-3
	54.73	55.73	4	J125-4
	55.73	56.73	5	J125-5
	57.92	59.45	6	J125-6
	59.45	60.97	7	J125-7
	60.97	62	8	J125-8
	62	64	9	J125-9
	64	65	10	J125-10
	65	66	11	J125-11
	66	67	12	J125-12
	67	68	13	J125-13
	68	69	14	J125-14
	69	70	15	J125-15
	74.5	75.5	19	J125-19
	75.5	76.5	20	J125-20
	76.5	77.5	21	J125-21
	77.5	78.5	22	J125-22
	78.5	79.5	23	J125-23
	79.5	80.5	24	J125-24
	84.5	85.5	29	J125-29
	85.5	86.5	30	J125-30
	86.5	87.5	31	J125-31
	87.5	88.5	32	J125-32
	88.5	89.5	33	J125-33
	89.5	90.5	34	J125-34
	90.5	91.5	35	J125-35
J138	68	69	4	J138-4
	69	70	5	J138-5
	70	71	6	J138-6
	71	72	7	J138-7
	72	73	8	J138-8
	73	74	9	J138-9
	74	75	10	J138-10

TABLE 3.2. Jabali outcrop samples. Sampling area n. from Fig. 3.8.

Sampling area n.	Sample n.	Sample description
1A	JS MON 1	Yellowish-brown concretionary smithsonite
	JS MON 2	Weathered red-brown dolomite, with sulfide remnants
	JS MON 3	Smithsonite ore, encrusted by hydrozincite
	JS MON 4	Brownish dolomite, partly de-dolomitized by calcite
	JS MON 5	Porous smithsonite, encrusted by hydrozincite
	JS MAR 1	Massive smithsonite, with galena remnants
	JS MAR 2	Massive smithsonite, with macrocrystalline galena remnants
1B	JS MON 6	Reddish-brown massive ore
	JS MON 7	Brown massive ore
	JS MON 8	Gossan; (hydr)oxide black-red crusts
	JS MON 9	Reddish-brown massive ore; few smithsonite crusts in voids
	JS MON 10	Reddish-brown massive ore; few smithsonite crusts in voids
	JS MON 11	Clay sample from gossan
	JS MON 12	Gossan sample
	JS MON 13	Smithsonite - dolomite transition
	JS MON 36	Dedolomitized dolomite
	JS MAR 3	Massive smithsonite, with hydrozincite coatings
2	JS MON 14	Smithsonite breccia, encrusted by hydrozincite and hemimorphite
	JS MON 15	Smithsonite breccia, encrusted by hydrozincite and hemimorphite
	JS MON 16	Gossan and smithsonite ore
	JS MON 17	Gossan sample
	JS MAR 5	Rusty dolomite with galena spots
	JS MAR 6	Smithsonite breccia, with hydrozincite encrustations
3	JS MON 18	Gossan sample
	JS MON 19	Silicified gossan sample with calcite spots
	JS MON 20	Smithsonite-hydrozincite massive ore
4	JS MON 21	Smithsonite-hydrozincite massive ore
	JS MON 22A	Smithsonite-hydrozincite massive ore
	JS MON 22B	Smithsonite-hydrozincite massive ore
	JS MON 23	Massive dolomite
	JS MON 24	Smithsonite-hydrozincite ore
	JS MON 25	Gossan sample
	JS MON 26	Smithsonite-hydrozincite ore
	JS MON 27	Smithsonite-hydrozincite ore
	JS MON 28	Smithsonite-hydrozincite massive ore
5	JS MON 29	Smithsonite-hydrozincite massive ore; hemimorphite spots
	JS MON 30	Gossan sample, with hydrozincite
	JS MON 31	Gossan sample
6	JS MON 32_1	Smithsonite-hydrozincite massive ore; hemimorphite spots
	JS MON 32_2	Smithsonite-hydrozincite massive ore; hemimorphite spots
	JS MON 33	Massive dolomite, partly dedolomitized, with galena veins
	JS MON 34	Trachyte dyke
	JS MON 35	Trachyte dyke
7	JS MAR 7	Gossan sample
	JS MAR 8	Massive smithsonite, with hydrozincite spots
8	JS MAR 4	Massive smithsonite, with hydrozincite spots
Jabal Salab area	JS MON 37	Barite vein
	JS MON 38	Limestone with bioherms of Unit 7
	JS MON 39	Gossan sample

X-ray diffraction has been carried out on all samples, with the aim of identifying the occurring mineral phases. The core samples (40) have been crushed to 1 mm and fully homogenized, to have the representative mineralogy of each entire core sample. XRD analyses have been done on a Philips PW 3020 automated diffractometer (XRD) at the University of Heidelberg, with CuKα radiation, 40kV and 30mA, 10 seconds per step and a step scan of 0.02° 2θ. The data were collected from 3 to 110° 2θ. Quantitative phase analysis (QPA) of all the core samples was performed on the XRD traces using the Rietveld method (Rietveld, 1969; Bish and Howard, 1988; Bish and Post, 1993; Hill, 1991). X-ray powder diffraction data were analyzed using the GSAS package (General Structure Analysis System, Larson and Von Dreele, 2000) and its graphical interface EXPGUI (Toby, 2001).
Only semiquantitative XRD analyses, instead, have been performed on the outcrop samples.
QEMSCAN® test analyses were performed on two thin sections from the samples J109-5 and JS MON 2. QEMSCAN® analysis was carried out at the Camborne School of Mines, University of Exeter, UK, using a QEMSCAN® 4300, which is built on a Zeiss Evo 50 SEM platform with four light element Bruker Xflash Silicon Drift energy dispersive X-ray detectors. The software used were iMeasure v. 4.2 for the data acquisition and iDiscover v. 4.2 for the spectral interpretation and data processing. The fieldscan measurement mode was used to collect X-ray data every 10 μm across the polished sample surfaces of thin sections (4 cm by 2.5 cm), with X-rays acquired at 1000 total X-ray counts per spectrum. The LCU5 SIP provided with the QEMSCAN® (containing common minerals) was modified to include the nonsulfide mineral components. The chemistry and density data input into the primary list of the SIP database for QEMSCAN® used the average composition for bauxite minerals (www.webmineral.com). Issues relating to similar X-ray spectra include minerals that differ primarily by the concentration of light elements that are not directly detected (H), or have limited detection in the X-ray signals (C, O). A more complete study using QEMSCAN® analysis is currently ongoing at the Camborne School of Mines as a subject of another Ph.D. thesis (L. Santoro).
Whole rock chemical analyses (CA) of major and minor elements for the same core samples were committed by the Jabal Salab Company (JSC) to OMAC Laboratories Ltd. (Co. Galway, Ireland). Diamond drill cores have been split and the entire half-core samples have been homogenized and pulverized to obtain 30 g of pulps for chemical analysis. After *aqua regia* digestion, the samples have been analyzed by multi-element inductively-coupled plasma mass spectrometry (ICP-MS). Samples holding > 9% Zn have been also analyzed by atomic absorption spectrometry (AAS), with an excellent agreement between the two data sets (SRK Consulting, 2005). Whole rock chemical analyses (CA) of major and minor elements for the outcrop samples were committed at the ACME Laboratories (Vancouver). After *aqua regia* digestion, the samples have been analyzed by multi-element inductively-coupled plasma mass spectrometry (ICP-ES/ICP-MS).
Thermal Analysis (DTA, TG) has been performed only on two dolomite samples, which were chosen with the aim of testing this technique for a future exploration perspective of nonsulfide deposits (Mondillo et al., 2011). The samples were analyzed at the CISAG Laboratory of the University of Napoli, on a Netsch Instrument model STA 409, under air

atmosphere. A sample mass of 100 mg was heated from room temperature to 1100°C, at the rate of 10°C min^{-1}. Two pure dolomite samples from the Norian of Southern Apennines (Italy) have been analyzed for comparison.

Stable C-O-isotope analyses have been carried out at the University of Erlangen-Nuremberg (Germany). Carbonate powders and pure minerals were collected by mechanical hand picking separation of pure minerals, and reacted with 103% phosphoric acid at 70°C using a Gasbench II connected to a Thermo Finnigan Five Plus mass spectrometer. All values are reported in per mil relative to V-PDB by assigning a $\delta^{13}C$ value of +1.95‰ and a $\delta^{18}O$ value of -2.20‰ to NBS19. Reproducibility was checked by replicate analysis of laboratory standards and was better than ± 0.07 ‰ (1σ) for both carbon and oxygen isotope analyses. Oxygen isotope values of dolomite and smithsonite were corrected using the phosphoric acid fractionation factors given by Kim et al. (2007), Rosenbaum and Sheppard (1986) and Gilg et al. (2008).

Sulfur isotope analyses of a few sulfides and sulfates were carried out at Actlabs (Ancaster, Ontario, Canada). Single crystals and mineral fragments for analysis were collected with a dental drill from the core and outcrop samples. Pure $BaSO_4$ and sulfide samples were combusted to SO_2 gas under ~10^{-3} tor of vacuum. The SO_2 was inlet directly from the vacuum line to the ion source of a VG 602 Isotope Ratio Mass Spectrometer (Ueda, 1986). Quantitative combustion to SO_2 was achieved by mixing 5 mg of sample with 100 mgs of a V_2O_5 and SiO_2 mixture (1:1). The reaction was carried out at 950˚C for 7 minutes in a quartz glass reaction tube. Pure copper turnings were used as a catalyst to ensure conversion of SO_3 to SO_2. Internal Lab Standards ($SeaWater_{BaSO4}$ and $Fisher_{BaSO4}$) were run at the beginning and at end of each set of samples and were used to normalize the data as well as correct for any instrument drift. All results are reported in the permil (‰) notation relative to the international CDT standard. Precision and Reproducibility using this technique is typically better than 0.2‰ (n = 10 Internal Lab Standards).

XRD quantitative mineralogy (QPA) - Evaluation of the Jabali orebody from drillcores

In Fig. 3.13, the sampled core intervals are positioned along the borehole logs. The results from Quantitative Phase Analysis (QPA) of the Jabali core sample set are shown in TABLE 3.3, while in TABLE 3.4 are recorded the data from the ICP-MS chemical assays (CA). In TABLE 3.5 I have listed the Zn percentages calculated from the minerals indicated by the QPA Rietveld analyses of the core samples, the comparison with the amounts quoted in the chemical assays, and the difference between the two sets of data to indicate the excess or defect in metal contents. These data have been published by Mondillo et al. (2011).

J109 - 57.3-62.7 m:

The section refers to the "Upper zone" of the orebody (SRK Consulting, 2005); it consists of red-gray dolomite, highly fractured and brecciated. Dolomite is the most abundant mineral in the core (amounts comprised between 76.9 and 86.5 wt.%). Calcite reaches a maximum content of 15.3 wt.% in the J109-3 sample (depth of 59.3-60.3 m). Smithsonite represents the main Zn-mineral of the core: it increases toward the bottom of the selected interval, from an initial content of 1.5 wt.%, up to 17.7 wt.%. Sphalerite occurs in traces only in a sample (J109-4, between 60.3-61.65 m). Pb-minerals (cerussite and galena) occur only in low amounts in the J109-3 sample. Clays (kaolinite and sauconite) have been detected in the J109-1 sample (57.3-58.3 m). Goethite is ubiquitous, occurring around 1-3 wt.% in all the samples.

J125 - 50.78-70 m, 74.5-80.5 m, and 84.5-91.5 m:

In the core there are three distinct mineralized sections, representing the three "stratiform zones" in which the Jabali orebody has been subdivided (SRK Consulting, 2005), and for this reason it was considered one of the best cores of Jabali (B. Grist, pers. comm.). The dolomite host rock has a gray color, which becomes red, and orange to brown in the most mineralized intervals; the mineralized rock is vuggy and fractured. The first interval ("Upper zone") is comprised between 50.78 and 80 m, and directly underlies the shales of Unit 8. The second section ("Middle zone") comprises the lithological interval between 74.5 and 80.5 m. The third, and deeper interval ("Lower zone") extends between 84.5 and 91.5 m. Dolomite is the most abundant mineral of the core, reaching a maximum content of 97.5 wt.% in the deepest sample, but it is totally absent in the most mineralized samples (e.g. J125-8, between 60.97-62 m). In the Upper and Lower zones, the lack of dolomite is compensated by smithsonite, whose amounts can reach 82.8 wt.%. In the Middle zone, instead, up to 76.9 wt.% of calcite has been detected, while calcite is almost totally absent in the Upper zone. Dolomite and smithsonite abundances show an inverse relationship: the higher is smithsonite, the lower dolomite. The Upper zone, directly below the boundary with Unit 8, contains high amounts of gypsum (up to 52.5 wt.%), sphalerite (up to 7.6 wt.%), and anglesite (up to 3.7 wt.%). These minerals are completely lacking in all the other samples. Galena and cerussite have been randomly detected in low amounts. Low, but ubiquitous contents of chalcophanite (~0.5 wt.%), hematite (~1 wt.%), and goethite (~4 wt.%) could be identified in all samples. Sauconite is rare and kaolinite occurs only in few samples. However, the latter clay mineral represents the 30 wt.% of the whole sample J125-21.

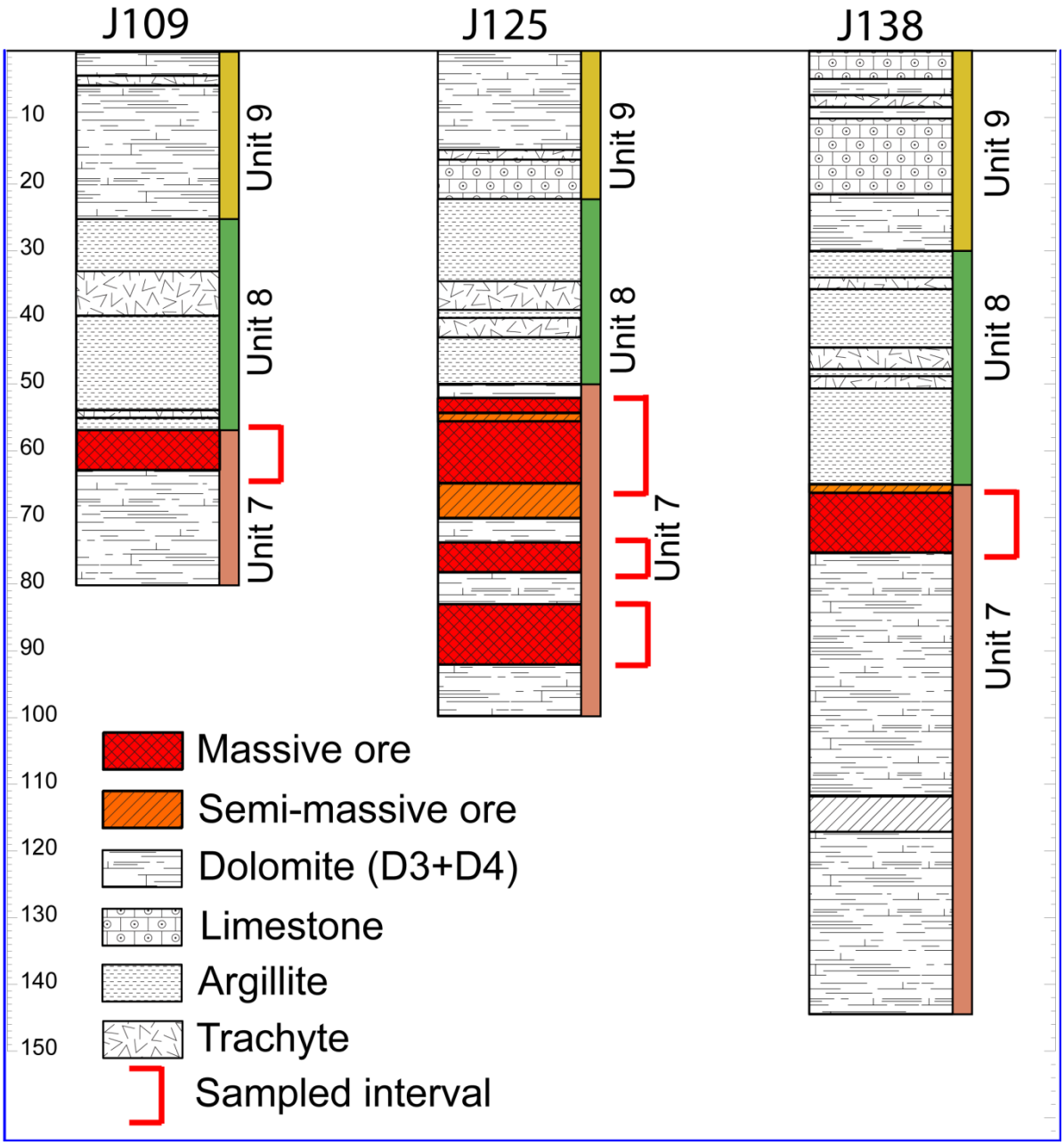

Fig. 3.13. Stratigraphic logs of sampled drillcores. The selected intervals are indicated in red. The color bars on the right of the logs indicate the relative stratigraphic Unit (see Figs. 3.8, 3.9).

J138 - 68-75 m:

All the samples of this core were collected from the Upper mineralized zone. The color of the core lithology is gray-brown. Dolomite represents the most abundant mineralogical phase (62.1-95.9 wt.%). Calcite occurs only in the deepest sample, and reaches a value of 29.7 wt.%. Smithsonite is the main mineral of economic interest and, in the central section of the core it has values comprised between 6.4 and 16 wt.%. Remnants of sulfides have been be detected, with galena (1-2 wt.%) more abundant than sphalerite (~0.5 wt.%). Goethite is again ubiquitous, being around 2-3 wt.% in all samples.

TABLE 3.3. Mineral abundances in the Jabali cores samples as deduced from X-ray quantitative phase analysis (QPA).

Sample n.	Dol	Cal	Sm	Cer	Gp	Ang	Sp	Gn	Cha	Hem	Gth	Kln	Sau	Ilt	Qz
							(wt.%)[a]								
J109-1	82.3	8.0	1.5								3.2	4.7	0.4		
J109-2	85.1	9.8	3.5						0.1		1.6				
J109-3	76.9	15.3	5.2	0.7				0.8			1.2				
J109-4	86.5	4.0	7.8				0.3		0.2		1.2				
J109-5	78.6	1.3	17.7						0.2		2.1				
J125-1	94.0		0.1		2.6		2.8			0.1	0.4				
J125-2	83.6		3.3		7.8		4.7	0.3			0.3				
J125-3	2.7		38.0		52.5	3.7	0.1				3.0				
J125-4	92.9	0.1	0.9		3.2		2.1	0.3				0.4			
J125-5	77.9	0.2	5.9		7.7		7.6	0.5		0.1					
J125-6	19.5		63.3		8.7	2.6	0.7	0.4			3.2	1.6			
J125-7	46.0		36.8		11.1	0.6	2.0	0.6			1.2	1.7			
J125-8			82.5		8.9	2.6					3.8	2.2			
J125-9	2.6		82.8	4.0	5.1	3.1					2.4				
J125-10	61.1		34.5	0.9	1.7				0.2		1.7				
J125-11	94.0		2.4		1.1				0.3	1.1	1.1				
J125-12	95.1		1.7		0.3				0.4	1.0	1.6				
J125-13	91.3	0.4	2.2						0.4	3.2	2.1	0.5			
J125-14	93.7		1.9						0.2	1.3	1.8	1.1			
J125-15	95.7	0.1	2.9		0.1				0.1		1.2				

Notes: Mineral abbreviations mostly after Whitney and Evans (2010). Dol; dolomite; Cal, calcite; Sm, smithsonite; Cer, cerussite; Gp, gypsum; Ang, anglesite; Sp, sphalerite; Gn, galena; Cha, chalcophanite; Hem, hematite; Gth, goethite; Kln, kaolinite; Sau, sauconite; Ilt, illite; Qz, quartz.

[a] Statistical indicators ranges: Rp 5.11-6.40%, wRp 6.65-8.85%, c2 1.199-1.825, Dwd 0.398-1.711.

Continue... TABLE 3.3.

Sample n.	Dol	Cal	Sm	Cer	Gp	Ang	Sp	Gn	Cha	Hem	Gth	Kln	Sau	Ilt	Qz
							(wt.%)[a]								
J125-19	53.2	41.4			1.6				0.2		3.6	0.1			
J125-20	56.4	32.9	5.8								4.4	0.5			
J125-21	15.6		45.4								7.7	30.8	0.4	0.5	
J125-22	30.6	38.1	10.4								5.5	15.0	0.3	0.3	
J125-23	20.8	76.9									2.0				0.4
J125-24	47.9	50.5								0.1	1.7				
J125-29	76.3	16.6	4.1							0.2	2.8				
J125-30	55.0		39.0	0.4				0.2			2.1	3.3			
J125-31	85.6		10.5								3.8				
J125-32	16.9	0.1	78.1	0.3						0.1	4.6				
J125-33	59.4	0.1	35.6	0.4						0.2	4.3				
J125-34	93.9		0.5							0.7	4.9				
J125-35	97.5										2.5				
J138-4	86.9	8.9	0.6				0.2		0.1		3.3				
J138-5	95.9										2.5	1.6			
J138-6	82.8		9.8	1.3				1.4			4.2	0.5			
J138-7	76.9	3.4	16.1	0.5				0.6			2.4				
J138-8	89.4		6.4	0.1				0.1		1.6	2.3				
J138-9	83.8		10.1	1.8				2.3			2.1				
J138-10	62.1	29.7	2.0	0.7			0.6	0.9			3.9				

Notes: Mineral abbreviations mostly after Whitney and Evans (2010). Dol; dolomite; Cal, calcite; Sm, smithsonite; Cer, cerussite; Gp, gypsum; Ang, anglesite; Sp, sphalerite; Gn, galena; Cha, chalcophanite; Hem, hematite; Gth, goethite; Kln, kaolinite; Sau, sauconite; Ilt, illite; Qz, quartz.

[a] Statistical indicators ranges: Rp 5.11-6.40%, wRp 6.65-8.85%, c2 1.199-1.825, Dwd 0.398-1.711.

TABLE 3.4. Major and minor element concentrations derived from whole rock ICP chemical assays (ZincOx).

Sample no.	Zn	Fe	Mg	Pb	Ca	Mn	S	Ag	Cd	Cu	Ni	P
				(wt.%)[a]						(ppm)[b]		
J109-1	4.55	3.86	8.94	1.05	19.89	0.48	0.03	3	670	25	30	300
J109-2	5.31	2.74	9.26	0.13	21.06	0.58	0.19	3	760	25	5	50
J109-3	5.98	1.99	8.73	5.55	20.13	0.55	0.58	11	750	25	5	50
J109-4	6.29	2.30	10.08	0.12	20.61	0.65	0.15	22	550	25	5	50
J109-5	14.16	2.32	8.36	0.06	15.57	0.60	0.03	31	1330	70	5	50
J125-1	1.30	5.05	8.84	0.02	19.68	0.66	2.71	5	90	25	10	500
J125-2	11.49	2.39	8.71	1.37	17.39	0.65	5.61	56	1120	90	5	100
J125-3	21.78	2.99	0.69	9.33	9.37	0.13	7.75	567	1380	240	5	100
J125-4	3.15	3.57	10.58	1.18	19.90	0.59	4.44	45	130	25	10	200
J125-5	12.16	1.92	8.88	2.75	16.68	0.50	5.00	50	760	25	5	200
J125-6	24.44	2.14	4.02	3.65	7.91	0.80	3.12	210	1330	50	20	300
J125-7	19.41	1.91	5.73	3.36	12.23	0.48	4.62	118	1250	25	5	100
J125-8	37.62	5.52	0.75	4.11	1.46	0.41	1.59	231	1830	190	20	300
J125-9	38.02	2.21	0.54	13.20	0.54	0.39	1.37	230	2550	210	10	300
J125-10	25.43	2.74	6.13	1.58	8.78	0.58	0.25	289	1470	70	20	200
J125-11	2.30	2.44	12.27	0.18	20.34	0.71	0.06	21	280	25	5	200
J125-12	2.76	1.87	12.17	0.16	20.62	0.55	0.03	24	270	25	5	200
J125-13	3.55	3.56	11.37	0.39	19.46	0.58	0.03	44	420	25	10	100
J125-14	3.09	3.40	11.32	0.07	19.75	0.60	0.03	24	280	25	10	100
J125-15	5.93	2.06	10.71	0.10	19.69	0.61	0.13	14	640	25	5	200
J125-19	1.06	2.15	6.85	0.06	28.97	0.53	0.26	5	70	25	5	300
J125-20	12.43	3.61	5.29	0.43	19.29	0.52	0.03	3	1290	25	20	400
J125-21	29.10	7.36	1.83	0.68	2.70	0.48	0.03	3	1430	25	60	600
J125-22	15.53	4.57	2.36	1.10	16.18	1.33	0.03	3	850	25	40	500
J125-23	1.13	1.99	2.10	0.25	35.32	0.53	0.03	5	80	25	5	300
J125-24	2.27	1.97	7.38	0.45	27.18	0.57	0.03	9	320	25	5	300
J125-29	8.05	3.32	8.56	0.91	17.16	0.42	0.03	102	780	25	20	400
J125-30	24.93	4.73	3.93	3.63	7.44	0.32	0.24	433	2060	100	20	500
J125-31	14.42	3.44	7.45	0.95	15.62	0.55	0.03	81	1320	25	20	500
J125-32	37.14	3.93	2.72	0.83	3.70	0.36	0.03	264	2120	90	20	300
J125-33	29.32	3.54	4.67	1.91	7.59	0.48	0.07	353	1160	25	20	200
J125-34	5.03	5.78	9.48	0.97	18.62	0.59	0.03	15	330	25	10	300
J125-35	4.32	2.60	10.26	0.64	20.25	0.65	0.03	18	380	25	5	200
J138-4	3.77	3.60	8.46	0.68	23.24	0.98	0.03	10	260	25	5	100
J138-5	4.66	3.42	10.14	0.75	19.73	0.65	0.03	11	330	25	10	100
J138-6	6.32	4.05	7.51	1.31	15.84	0.58	0.03	44	440	25	30	600
J138-7	9.45	3.18	8.66	2.38	18.03	0.78	0.12	116	560	50	20	200
J138-8	9.96	3.59	8.63	1.41	17.07	0.66	0.08	143	740	50	20	400
J138-9	11.53	2.99	7.22	10.12	14.61	0.68	0.90	93	990	70	20	200
J138-10	5.42	3.18	6.35	4.60	23.51	0.86	0.43	112	440	25	20	200

[a] Detection limits (wt.%): Zn 0.0001, Fe 0.01, Mg 0.01, Pb 0.01, Ca 0.01, Mn 0.0001, S 0.05.

[b] Detection limits (ppm): Ag 0.5, Cd 0.5, Cu 0.5, Ni 0.5, P 5.

TABLE 3.5. Zinc amounts calculated from whole rock chemical assays (CA), compared with the metal percentages derived from the Zn-bearing minerals measured by X-ray quantitative method (QPA). The columns CA-SQPA correpond to defect or excess of Zn percentages calculated with CA respect to QPA method.

Sample n.	Zn (wt.%)					
	CA	QPA			S_{QPA}[a]	CA-S_{QPA}
		Sm	Sp	Cha		
J109-1	4.55	0.78			0.78	3.77
J109-2	5.31	1.83		0.02	1.84	3.47
J109-3	5.98	2.71			2.71	3.27
J109-4	6.29	4.07	0.19	0.03	4.29	1.99
J109-5	14.16	9.23		0.03	9.26	4.90
J125-1	1.30	0.05	1.79		1.85	-0.55
J125-2	11.49	1.72	3.01		4.73	6.76
J125-3	21.78	19.82	0.06		19.88	1.90
J125-4	3.15	0.47	1.35		1.81	1.34
J125-5	12.16	3.08	4.87		7.95	4.21
J125-6	24.44	33.01	0.45		33.46	-9.02
J125-7	19.41	19.19	1.28		20.47	-1.06
J125-8	37.62	43.02			43.02	-5.40
J125-9	38.02	43.18			43.18	-5.16
J125-10	25.43	17.99		0.03	18.03	7.40
J125-11	2.30	1.25		0.05	1.30	1.00
J125-12	2.76	0.89		0.07	0.95	1.81
J125-13	3.55	1.15		0.07	1.22	2.33
J125-14	3.09	0.99		0.03	1.03	2.06
J125-15	5.93	1.51		0.02	1.53	4.40
J125-19	1.06			0.03	0.03	1.03
J125-20	12.43	3.02			3.02	9.41
J125-21	29.10	23.68			23.68	5.42
J125-22	15.53	5.42			5.42	10.11
J125-23	1.13					1.13
J125-24	2.27					2.27
J125-29	8.05	2.14			2.14	5.91
J125-30	24.93	20.34			20.34	4.59
J125-31	14.42	5.48			5.48	8.94
J125-32	37.14	40.73			40.73	-3.59
J125-33	29.32	18.57			18.57	10.75
J125-34	5.03	0.26			0.26	4.77
J125-35	4.32					4.32
J138-4	3.77	0.31	0.13	0.02	0.46	3.31
J138-5	4.66					4.66
J138-6	6.32	5.11			5.11	1.21
J138-7	9.45	8.40			8.40	1.05
J138-8	9.96	3.34			3.34	6.62
J138-9	11.53	5.27			5.27	6.26
J138-10	5.42	1.04	0.38		1.43	3.99

Notes: mineral abbreviations as in Table 3.3.

[a] S_{QPA} is the sum of Zn wt.% from smithsonite (Sm), sphalerite (Sp) and chalcophanite (Cha).

To summarize the results of quantitative mineralogy:
1) the most abundant zinc mineral in the Jabali cores is the Zn-carbonate smithsonite [$ZnCO_3$], which is generally ranging from a few % to 20 wt.%. The maximum abundance is of about 80 wt.% in core J-125. Sphalerite [ZnS] (up to 8 wt.%) occurs in several samples also in the J125 core, but only in the Upper zone. Sauconite (Zn-smectite) and other clay minerals have restricted distribution, and can locally reach values only of a few %. Other Zn-minerals, like hemimorphite [$Zn_4Si_2O_7(OH)_2H_2O$] and hydrozincite [$Zn_5(CO_3)_2(OH)_6$] were not detected in the analyzed drillcores, but can be fairly abundant in the outcrop samples.
2) Cerussite [$PbCO_3$] is not always present, but it may have values from 0.1 to 4 wt.%. Anglesite [$PbSO_4$] has been found only in five samples (up to 4 wt.%). Galena [PbS] is ubiquitous but usually below 3 wt. %.
3) All the analyzed core samples contain dolomite, generally over 50 wt.%, but seldom below 20 wt.%, together with variable amounts of calcite and Fe-Mn(hydr)oxides. A few samples from the J-125 core contain up to 52 wt.% gypsum. The amount of Fe(hydr)oxides (goethite>hematite) is always below 5 wt.%. Zn-Mn(hydr)oxides and Pb-Mn(hydr)oxides (chalcophanite [$(Zn,Fe^{2+},Mn^{2+})Mn^{4+}{}_3O_7\cdot 3(H_2O)$]) occur in many samples (below 1 wt.%).

XRD semiquantitative mineralogy of the outcrop samples

The semiquantitative analyses of the outcrop samples are shown in TABLE 3.6. The samples were collected from the areas of the Jabali minesite, where both high-grade ore and gossanous rocks occur. It is possible to observe that also in outcrop the most abundant ore mineral is smithsonite, with over or around 60 wt.%. Differently from the drillcores, also hydrozincite and hemimorphite can be detected in outcrop. Hydrozincite is generally quite rare, but it has been locally also in amounts around 40-60 wt.%. Hemimorphite is slightly less abundant. Cerussite and galena have been detected only in two samples, located near a fault zone. Dolomite amount is very high in the samples characterized by low Zn grades. Calcite occurs with discrete amounts, ranging between 20 and 40 wt.%. Quartz is abundant only in a silicified gossanous crust (JS MON 19). Goethite is ubiquitous: together with hematite it is the main "oxide mineral" in the gossanous samples (e.g. JS MON 8). Traces of pyrolusite [MnO_2] have been also detected in several samples.
In the gossan several metallic sulfate minerals have been identified: plumbojarosite [$Pb_{0.5}Fe^{3+}{}_3(SO_4)_2(OH)_6$], jarosite [$KFe^{3+}{}_3(SO_4)_2(OH)_6$], dietrichite [$(Zn,Fe^{2+},Mn^{2+})Al_2(SO_4)_4\cdot 22H_2O$], and rozenite [$Fe^{2+}SO_4\cdot 4H_2O$].

TABLE 3.6. Semiquantitative mineral abundances from XRD-analysis of outcrop samples.

Sample n.	Sm	Hz	Hm	Cer	Gn	Dol	Cal	Mg-cal	Qz	Gth	Hem	Prls	Kln-Mnt	Mnt	Dtrch	Pb-jrs	Jrs	Roz	Gp
JS MON 3	OOOOO	OO	-	-	-	OO	O	-	-	O	-	-	-	-	-	-	-	-	-
JS MON 6	OOOOO	-	-	-	-	O	O	-	-	OO	-	-	O	-	-	-	-	-	-
JS MON 8	-	-	-	-	-	-	OO	-	-	OOOOO	OOO	-	-	-	-	-	-	-	-
JS MON 9	OOOOO	-	-	-	-	-	O	-	-	O	O	O	-	-	-	-	-	-	-
JS MON 10	OOOOO	-	-	-	-	O	O	O	O	O	O	-	-	-	-	-	-	-	-
JS MON 13	OOOO	-	-	-	-	OOOO	-	-	-	O	-	-	O	-	-	-	-	-	-
JS MON 14	OOOO	OO	O	-	-	OOO	OO	-	-	O	-	-	O	-	-	-	-	O	-
JS MON 15	OOO	O	O	-	-	OOO	OOO	-	-	O	-	-	O	-	-	-	-	-	-
JS MON 18	O	-	-	-	-	O	OOO	OO	O	OO	O	-	O	-	-	OO	O	-	-
JS MON 19	-	-	-	-	-	-	OOO	-	OOOOO	OO	O	-	-	-	O	-	-	-	-
JS MON 21	OOOOO	OO	-	-	-	-	-	-	-	OO	O	O	O	O	-	-	-	-	-
JS MON 22A	OOOOO	OO	-	-	-	-	-	-	-	O	-	-	-	-	-	-	-	-	-
JS MON 22B	O	OOOO	OOO	-	-	-	O	O	-	OO	-	-	-	-	-	O	-	-	-
JS MON 28	OOOOO	OOO	O	-	-	-	-	-	-	O	-	-	-	-	-	O	-	-	-
JS MON 29	OOO	OOOO	OO	-	-	-	O	-	-	O	-	-	O	-	-	-	-	-	-
JS MON 32_2	OO	OO	O	O	-	OOOO	OO	-	-	O	-	-	O	-	-	-	-	-	O
JS MON 33	-	-	-	O	OO	OOOOO	OO	-	-	O	-	-	O	-	-	-	-	-	O

"-" not found, "O" <5 wt.%, "OO" 5< <20 wt.%, "OOO" 20< <40 wt. %, "OOOO" 40< <60 wt. %, "OOOOO" >60 wt.%

Sm, smithsonite; Hz, hydrozincite; Hm, hemimorphite; Cer, cerussite; Gn, galena; Dol, dolomite; Cal, calcite; Mg-cal, Mg-calcite; Qz, quartz; Gth, goethite; Hem, hematite; Prls, pyrolusite; Kln-Mnt, kaolinite-montmorillonite; Mnt, montmorillonite; Dtrch, dietrichite; Pb-jrs, plumbojarosite; jrs, jarosite; Roz, rozenite; Gp, gypsum

Petrography and chemistry of the Jabali ore and gangue minerals

Dolomite, which is the main constituent of the host rock, displays a variety of fabrics and crystal forms, as already reported by Al Ganad et al. (1994). All dolomite phases are strongly fabric destructive and have obliterated both depositional and diagenetic features of the precursor limestone (Fig. 3.14A). In the D1 phase remnants of the original fossils can be still recognized. D2 dolomite phases are characterized by a non-planar texture (Sibley and Gregg, 1987), and by anhedral and interlocked crystals with lobate or curved intercrystalline boundaries. Brown to yellowish material, probably representing the residue of the dissolution and replacement of the precursor limestone, irregularly coats the dolomite crystals or is concentrated in their centers. These features point to a late diagenetic, post-compaction, replacive origin for the dolomite. Small pyrite/marcasite crystals (generally oxidized) are scattered throughout the dolomite. Sparry dolomite crystals, belonging to the D3 and D4 phases, occur within veins and cavities, and crosscut the previous dolomite generations (Fig. 3.14B,C). D3 and D4 crystals are interlocked, coarse to very coarse crystalline (0.2-2 mm), clearer than the replacive dolomites, and display the undulose extinction typical of *saddle* dolomite (Radke and Mathis, 1980) (Fig. 3.14D,E). The final growth stage of the *saddle* dolomites consists of mm-sized dolomite crystals, whose shape ranges from rhombohedral with straight boundaries to symmetrical saddle forms (Fig. 3.14E). The outermost part of these crystals may exhibit zones with Fe-(hydr)oxides coatings. The late diagenetic phases are not-luminescent under cathodic light, and is generally pure. Saddle dolomite, instead, in its latest generations, has a red-bright color (Fig. 3.14E,F). By SEM-EDS it was verified that, as it is usual, this color is "activated" by variable contents of Mn (up to 2 wt.% MnO), hosted within the crystal in the Mg structural site; saddle dolomite also locally contains Fe amounts (up to 6 wt.% FeO) (Fig. 3.14G,H). A calcite phase is associated with saddle dolomite, and mainly occurs as a late cement, filling the dolomite geodes.

All the dolomite phases are affected by two different types of replacement. The first is a typical dedolomitization: dolomite is transformed in calcite; manganese and iron, previously contained in the dolomite lattice, are precipitated as (hydr)oxides in the interstices of the crystals and in small vugs and fissures (Fig. 3.15A,B).

A latest calcite, different from the previous, fills geodic cavities and veins (Fig. 3.15C,D), and locally contains lead (up to ~5 wt.% PbO) and cadmium (up to ~2 wt.%). The second type of replacement is associated to the ore oxidation process, in fact it is evident mostly in the wide gradational “bands” which mark the boundary between host dolomite and replacive smithsonite.

Fig. 3.14. *(next page)* Dolomite host rock. A) J125-2. Dolomite facies in drillcores. B) J109-4. Non-planar (hydrothermal) dolomite. NII. C) J125-2. Zoned idiomorphic dolomite. NII. D) J138-6. Zoned idiomorphic dolomite growing in cavity. N+. E) & F) J125-15. Saddle dolomite crystal. NII & CL. G) & H) J125-7. Hydrothermal dolomite with pyrite spots: dolomite containing Fe and Mn is light gray colored, pure dolomite is dark gray. SEM- BSE-EDS. Dol = dolomite; Fe-Mn-dol = Fe-Mn-dolomite; Py = pyrite.

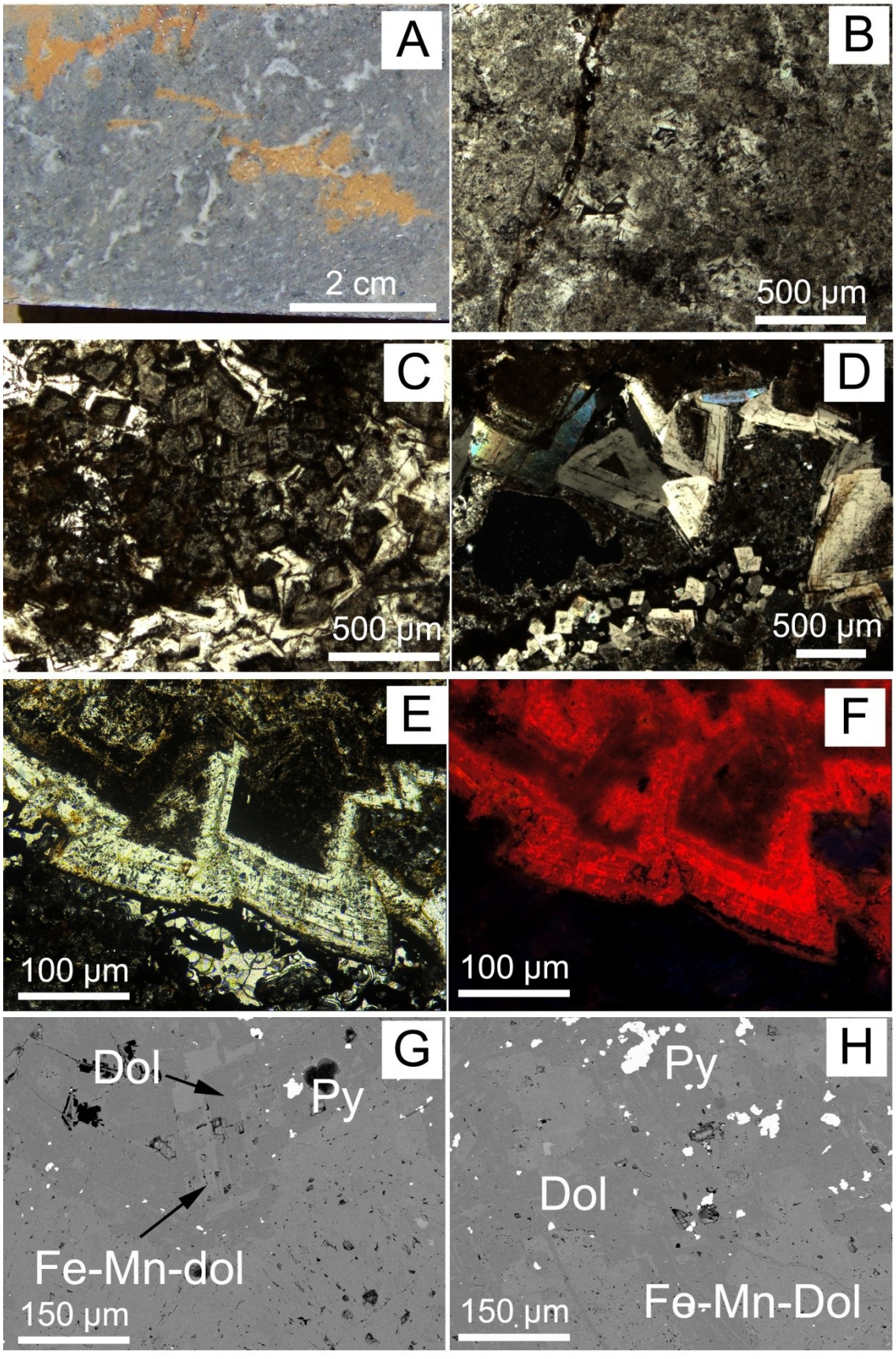
A
2 cm
B
500 µm
C
500 µm
D
500 µm
E
100 µm
F
100 µm
G
Dol
Py
Fe-Mn-dol
150 µm
H
Py
Dol
Fe-Mn-Dol
150 µm

In these volumes the rock assumes a reddish-brown color, and it is possible to recognize features of the host rock, like the texture dominated by rhombohedral shapes of dolomite crystals (Fig. 3.16A,B). At microscope, crystals appear clear and transparent along their margins, whereas are generally opaque and brown colored in their cores (Fig. 3.16B). In these colored phases, Mg of the original dolomite has been substituted by Zn. In fact, at SEM-EDS, it is possible to see that ZnO content in the altered dolomite can reach 17-22 wt.%, and it is inversely related to MgO content; locally also Cd can be present, with CdO amounts around 1.5 wt.% (Fig. 3.16C,D). Ca content remains stable, and analogous to that occurring in the "standard" dolomites. The original Fe and Mn remain in the altered dolomite lattice (Fig. 3.16E,F). Zn-dolomite has a yellowish-orange color under cathodic light (Fig.3.17). It is well known that the yellow color of the dolomite under cathodic light is related to Mn located within the Ca structural site (Richter et al., 2003). It is therefore possible that the Mn^{+2}, which occurred in the Mg site (activating the red color in the hydrothermal dolomite), had been oxidized together with Fe during weathering. When Mg was replaced by Zn, the Mn had been excluded from the dolomite lattice. This has caused a quenching of the red color in the Zn-dolomite, thus evidencing the effects of residual Mn within the lattice, i.e. Mn hosted in the "unaltered" Ca site.

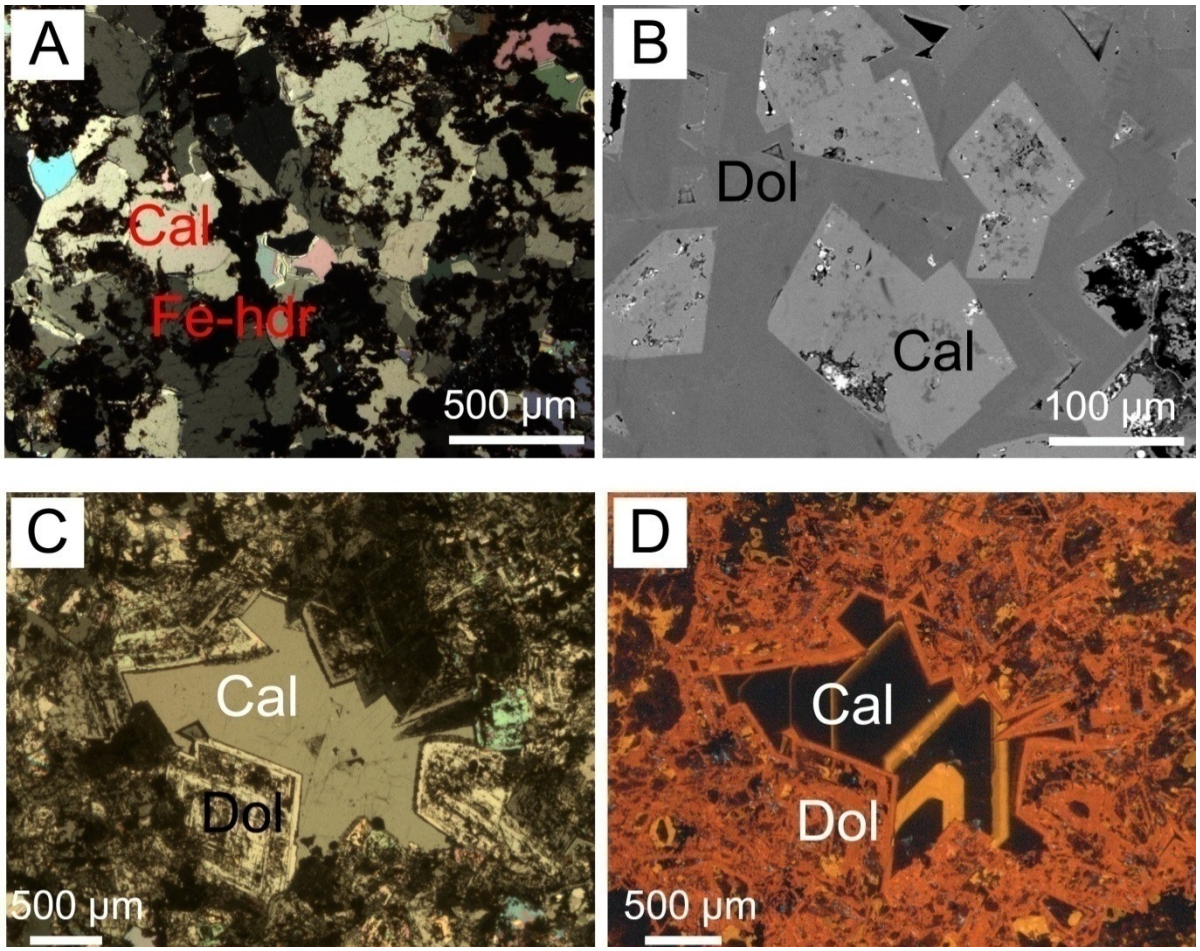

Fig. 3.15. Dedolomitized dolomite. A) J138-10. Calcite and Fe-Mn-(hydr)oxides replacing dolomite. N+. B) J125-20. Dolomite cores replaced by calcite. SEM-BSE-EDS. C) & D) J138-10. Latest calcite filling geodic cavities. N+ & CL. Cal = calcite; Dol = dolomite; Fe-hdr = Fe-Mn-(hydr)oxides.

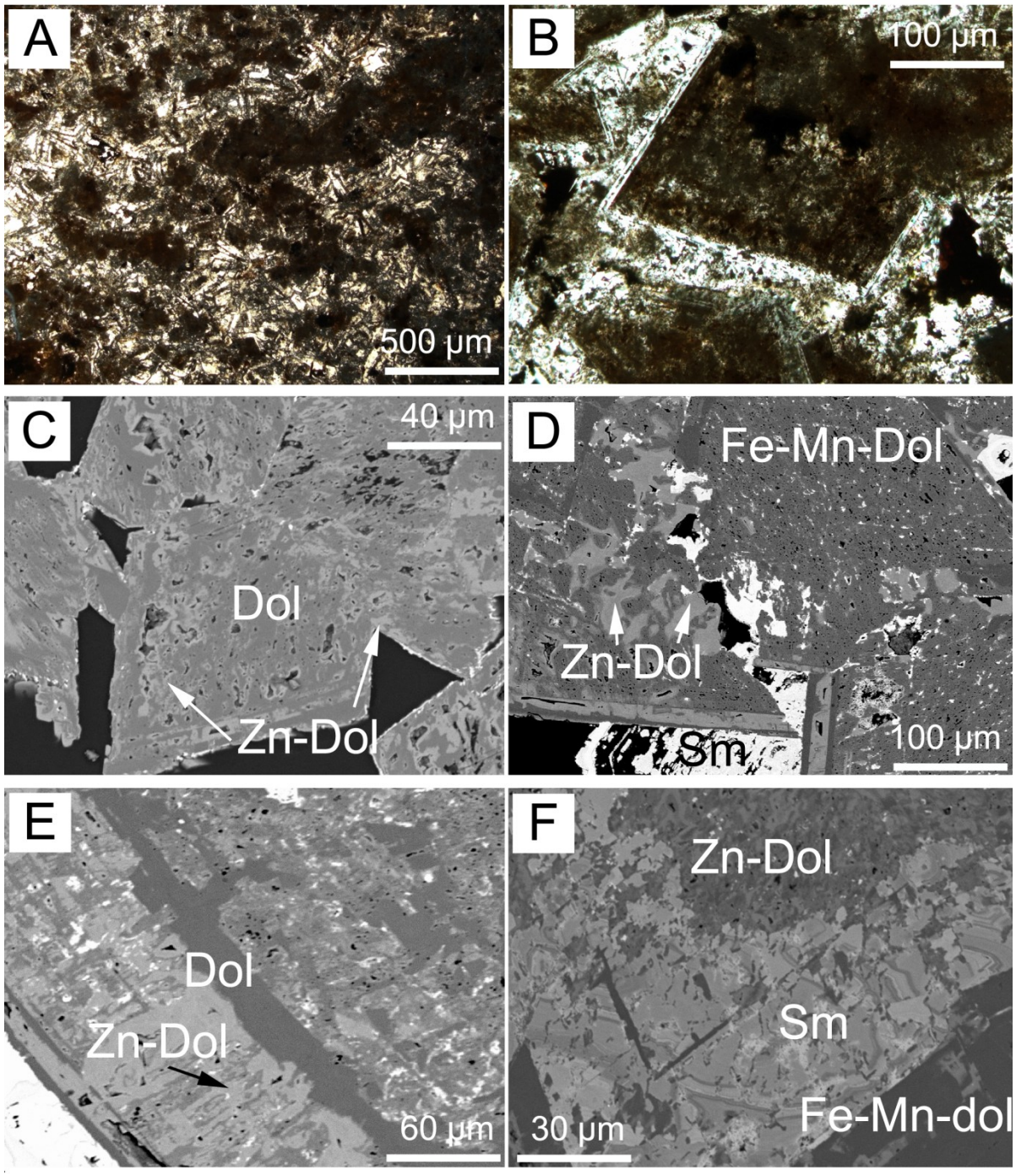

Fig. 3.16. Zn-dolomite. A) J125-6. Zn-dolomite replacing hydrothermal dolomite. NII. B) J125-4. Zn-dolomite replacing a dolomite crystal core. NII. C) J125-31. Zn-dolomite patchily replacing dolomite crystals. SEM-BSE-EDS. D) J109-5. Zn-dolomite patchily replacing dolomite crystals along fractures. SEM-BSE-EDS. E) J109-5. Zn-dolomite pervasively replacing the border of a dolomite crystal. SEM-BSE-EDS. F) JS MON 2. Smithsonite and Zn-dolomite replacing dolomite. SEM-BSE-EDS. Dol = dolomite; Fe-Mn-Dol = Fe-Mn-dolomite; Sm = smithsonite; Zn-Dol = Zn-dolomite.

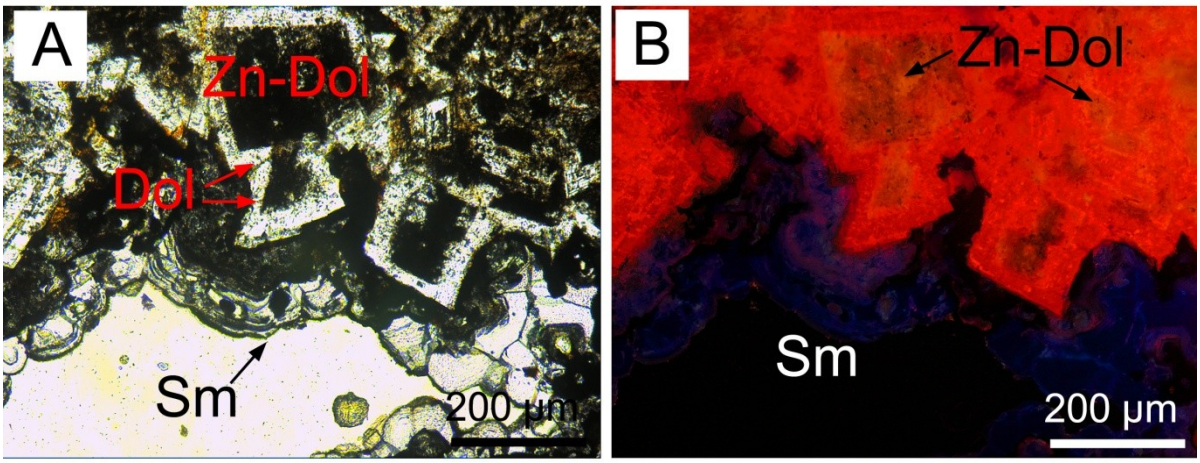

Fig. 3.17. J125-5. Zn-dolomite. A) Zn-dolomite replacing dolomite crystal cores. NII. B) Zn-dolomite shows yellowish-orange colors under CL, smithsonite crusts are dark blue. CL. Dol = dolomite; Sm = smithsonite; Zn-Dol = Zn-dolomite.

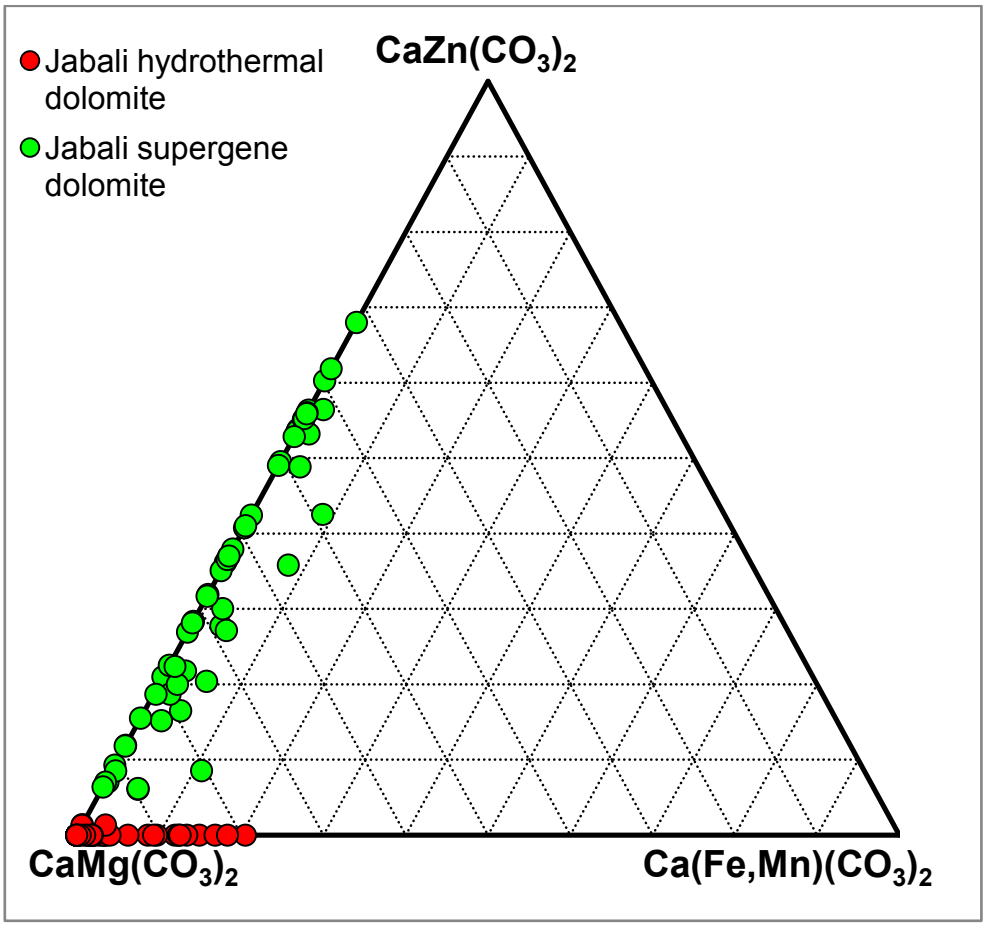

Fig. 3.18. Composition of Jabali dolomite in the system $CaMg(CO_3)_2$-$Ca(Fe,Mn)(CO_3)_2$-$CaZn(CO_3)_2$. Red circles = Hydrothermal dolomite; Green circles = Supergene Zn-dolomite.

In Fig. 3.18 the Jabali dolomite compositions are plotted in the system $CaMg(CO_3)_2$-$Ca(Fe,Mn)(CO_3)_2$-$CaZn(CO_3)_2$. It is possible to see that the composition of proper minrecordite (a dolomite where Mg is almost totally replaced by 29 wt.% Zn, Garavelli et al., 1982) has not been reached, but Zn substitutes Mg up to 70 % within dolomite lattice.
QEMSCAN® analyses, performed on two thin sections from the samples J109-5 and JS MON 2, allowed to gain a rough idea about the amount of Zn-dolomite occurring within the orebody (Fig. 3.19). In these sections, Zn-dolomite occurs with a modal abundance comprised between 40% and 50%, that is a very high value, considering that by a "metallurgical point of view" this dolomite should have been pure.

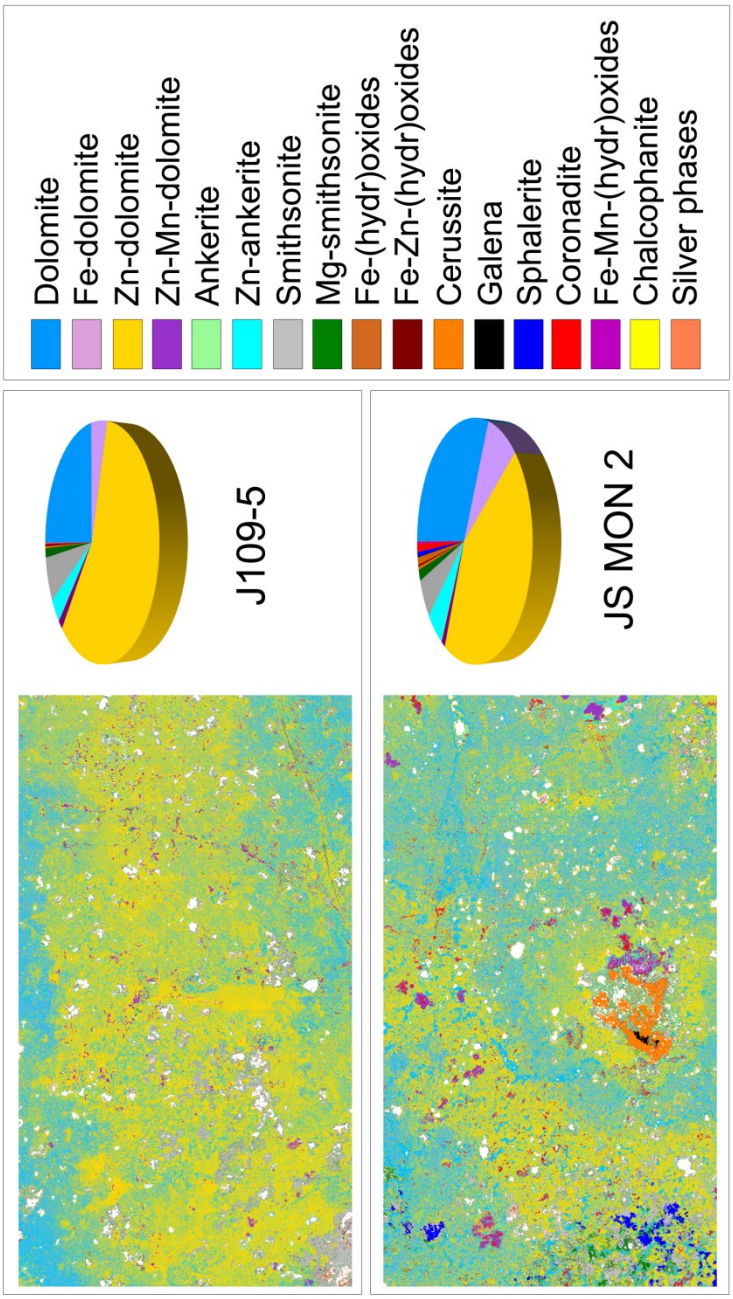

Fig. 3.19. Quantitative QEMSCAN® analysis on thin sections from the samples J109-5 and JS MON 2. Zn-dolomite is the most abundant phase within the sections.

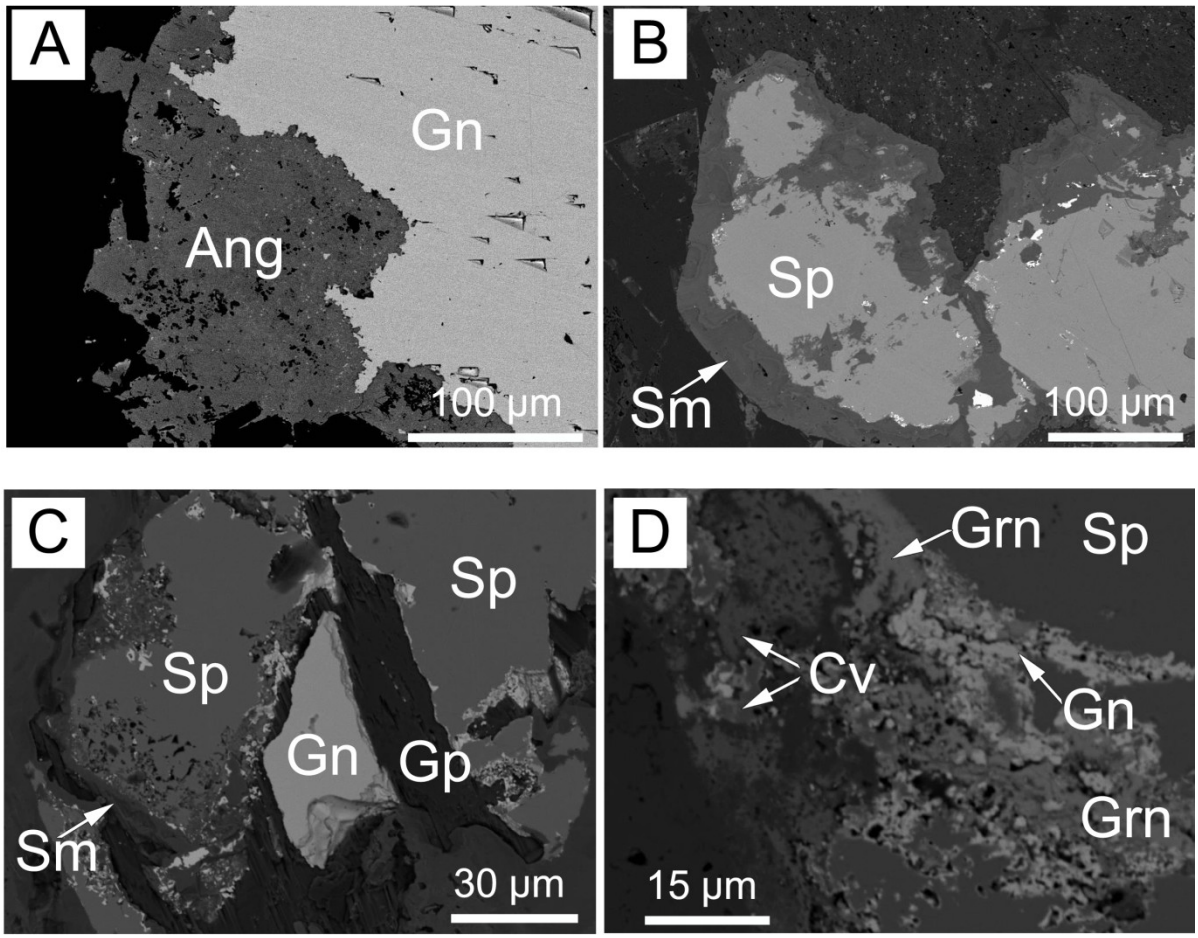

Fig. 3.20. Sulfides. A) J125-7. Anglesite replacing primary galena. B) JS MON 2. Smithsonite replacing primary sphalerite. C) J125-7. Gypsum and smithsonite replacing primary sphalerite; primary galena is unaltered; sphalerite is coated by small spots of secondary galena. D) J125-3. Secondary sulfides at border of altered sphalerite: galena, greenockite, covellite (locally containing Ag). SEM-BSE-EDS. Ang = anglesite; Cv = covellite; Gn = galena; Gp = gypsum; Grn = greenockite; Sm = smithsonite; Sp= sphalerite.

Primary galena crystals and veins are widespread in many samples. Though galena is more resistant than sphalerite to supergene alteration, local cerussite and anglesite coatings and thin veins have been identified. Galena occurs either as remnant patches, or as newly deposited crusts between gypsum and smithsonite. Original galena is generally coated by replacing cerussite and anglesite (Fig. 3.20A). The last generation of galena, as well as greenockite belong to the supergene mineral assemblage. Locally, it is possible to detect also small crystals of pyromorphite [$Pb_5(PO_4)_3Cl$].

Sphalerite (mainly observed at the top of core J125) occurs as two phases, as recorded by Al Ganad et al. (1994). Zoned sphalerite crystals and agglomerates have been observed sporadically, with the characteristics also indicated by Al Ganad et al. (1994). The mineral chemical composition is frequently not pure, with Fe values around 5 wt.%, Pb amounts of 2-3 wt.%, and Cd contents of 1.5-2 wt.%. Sphalerite is often altered and replaced by smithsonite, but also by gypsum (Fig. 3.20B,C). At the boundary between sphalerite and smithsonite, we could detect secondary sulfides (Fig. 3.20D): greenockite [CdS], galena

[PbS], and covellite [CuS]. Abundant greenockite is diffused also in other samples. It occurs as microcrystalline intergrowths along the lamellae of gypsum. Sphalerite is progressively altered and replaced by smithsonite, Fe-(hydr)oxides, and locally by gypsum.
Silver sulfide is also a quite common mineral at Jabali, even though it occurs in very small inclusions in other minerals. The most common occurrence is together with concretionary smithsonite (Fig. 3.21A), between gypsum lamellae (Fig. 3.21B), locally associated to greenockite, and also as small spots within hemimorphite. The mineral has not been ever detected within the fresh rock, but it is always associated to the secondary facies.

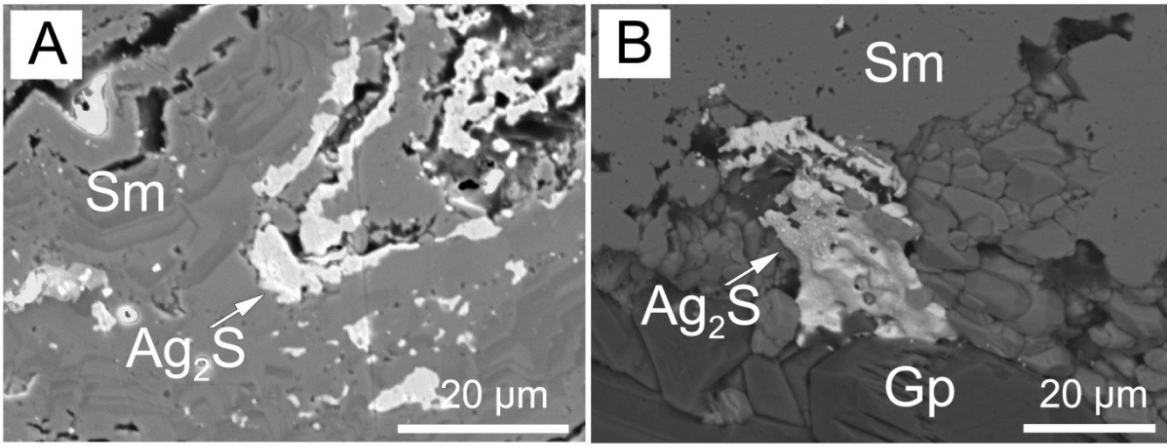

Fig. 3.21. J125-32. A) Ag-sulfide and smithsonite concretions. B) J125-3. Ag-sulfides between smithsonite and gypsum. SEM-BSE-EDS. Gp = gypsum; Sm = smithsonite.

Smithsonite is the main ore mineral detected at Jabali both in the cores and on outcrop. The boundary between the barren host dolomite and replacive smithsonite can be very gradational: in most cases it is very difficult to distinguish only by microscopic observation the difference between a "dirty", oxidized dolomite and a "real" smithsonite, also because replacive smithsonite generally mimics the dolomite host rock texture. As in many other nonsulfide deposits of the world (see Accha, Boni et al. 2009), smithsonite can be also roughly intergrown with Fe-(hydr)oxides in reddish concretional agglomerates, as well as with thin layers of clays.
Smithsonite occurs in two main phases: smithsonite 1, replacing directly dolomite (Fig. 3.22A), and smithsonite 2, occurring in vugs and cavities as neoformed crystals and concretions (Fig. 3.22B). Smithsonite 1 replaces the bulk of dolomite, surrounding and replacing sphalerite located in the dolomite porosity. It is possible to observe that smithsonite tends to replace more often dolomite D3 and D4, than D1 and D2. This replacive smithsonite has a very fine texture, constituted by ovoidal/rice-shaped microcrystals, which form agglomerates mimicking/following the original macrocrystalline rhombohedral habitus of the replaced dolomite. The result is that, under optical microscope observation, the presence of fine-grained microcrystalline agglomerates that have inherited the shape of the original dolomite, could induce to believe that smithsonite occurs in form of perfect rhombohedral crystals of discrete grain size (Fig. 3.22C). Smithsonite 1 assumes a red color, if solicited by cathodic light (CL) (Fig. 3.22D).

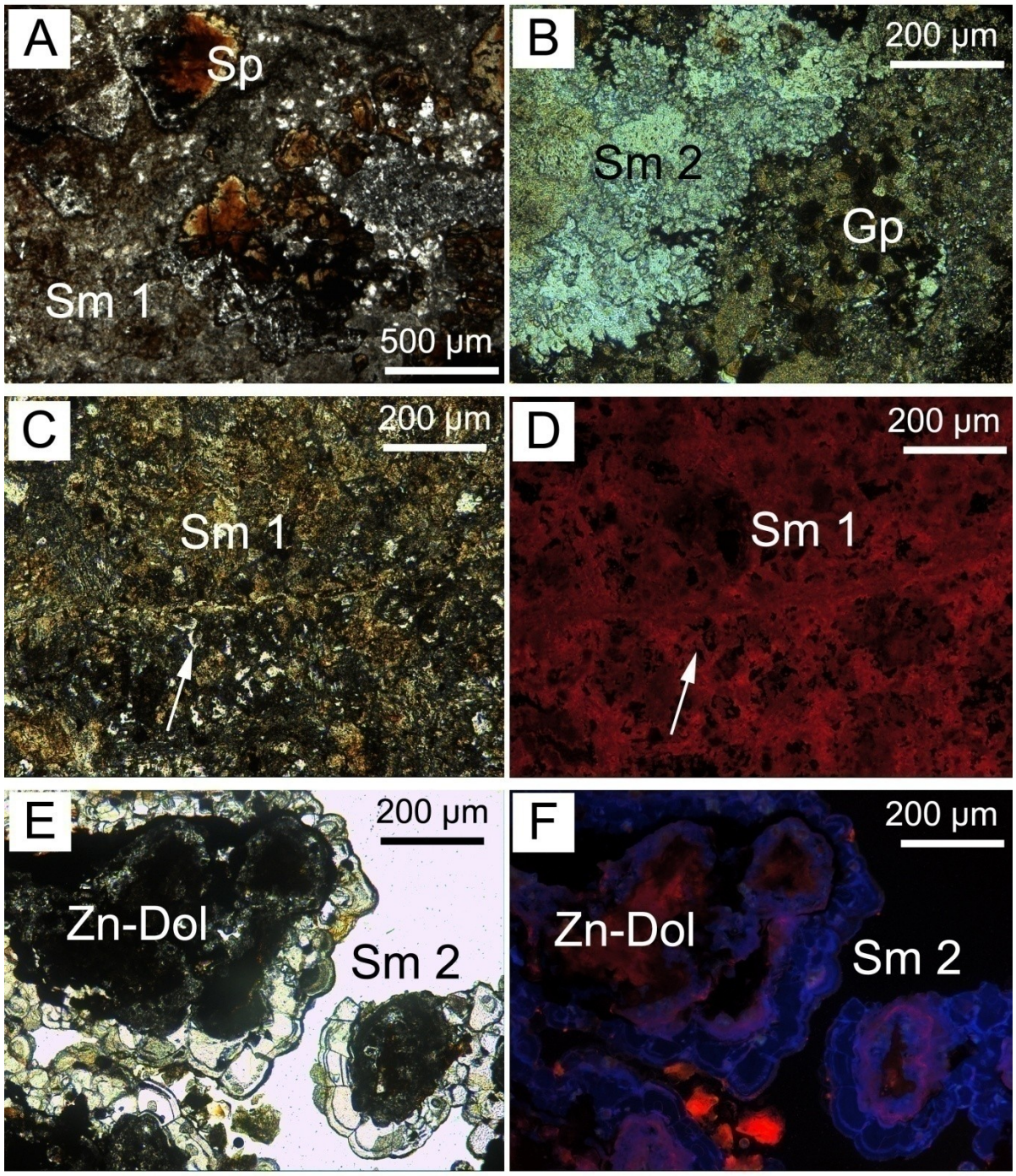

Fig. 3.22. Smithsonite. A) J125-5. Smithsonite 1 replacing dolomite and primary sphalerite. NII. B) J125-3. Concretionary smithsonite 2, precipitated together with gypsum. NII. C) & D) J125-7. Smithsonite 1, microcrystalline texture; the arrow indicates a "rhombohedral shape", based on the texture of replaced dolomite. NII & CL. E) & F) J125-15. Smithsonite 2 zoned concretions; they are mainly blue under CL. NII & CL. Gp = gypsum; Sm 1 = smithsonite 1; Sm 2 = smithsonite 2: Zn-Dol = Zn-dolomite.

Smithsonite 2 consists of different cement generations. The crystal size generally increases from the earliest generations to the latest. In a very general view, it is possible to recognize a first generation with colors variable from brown, to orange and yellow that is encrusted directly over smithsonite replacing dolomite. Other generations may follow, generally white colored under the eye, and clear and transparent at microscope, which grow over the first concretions, or directly coat the replacive smithsonite or the altered dolomite. All these concretionary phases are commonly zoned (Fig. 3.22E). The crystal habit of the elements within the concretions is more often "smoothed" (rice-shape), than "sharp" rhombohedral; “rounded” concretionary textures prevail also at the fine microscale.

At cathodoluminescence it is possible to see that concretionary phases have different colors: the first phases are red colored, whereas the latest are blue colored (Fig. 3.22F).

All the smithsonite phases contain amounts of Mg (Fig. 3.23A). Smithsonite replacing dolomite contains Mg amounts locally reaching 8-10 wt.% MgO (Fig. 3.23B); it can also contain amounts of Mn (up to ~3 wt.% MnO), Fe (up to 5-6 wt.% FeO), and Ca (up to 6 wt.% CaO). Concretionary smithsonite (Fig. 3.23C,D), can be characterized by up to 20 wt.% MgO amounts (a substitution of Mg for Zn in the smithsonite lattice around 70%), up to ~2 wt.% MnO, up to ~2 wt.% CdO, up to ~1.5 wt.% CaO, up to ~1.5 wt.% PbO.

The smithsonite concretionary phases (Smithsonite 2) are pre- to syn-precipitated with gypsum veins, which cut the replacive Smithsonite 1.

Hydrozincite and hemimorphite have been detected almost exclusively in outcrop samples. Hydrozincite generally shows a fine-grained texture, and acicular crystal habit, and occurs as smithsonite replacement, vein and porosity filling, and crusts (Fig. 3.24A). It has a pure composition. Petrographic observations on the samples collected from the mineralized outcrops have shown that hydrozincite occurs as surface coatings, in vugs, as well as with a local replacive character. Hydrozincite filaments replacing former smithsonite have been commonly observed. Hemimorphite has been observed in cm-size fan agglomerates of tabular crystals, dispersed into the most mineralized outcropping rock, and as small crystals in voids and cavities. Generally it occurs over hydrozincite. Several spots with crystalline hemimorphite in veins, which is locally replaced by Fe-(hydr)oxides are quite widespread. Hemimorphite has been detected in the J125-3 core sample as a microcrystalline radial agglomerate, into a gypsum vein (Fig. 3.24B). Small particles of Ag-sulfide surprisingly occur also between these hemimorphite crystals. Zn-smectite, like sauconite, is not very common at Jabali, but can be locally associated with kaolinite and illite, filling the porosity of the host rock.

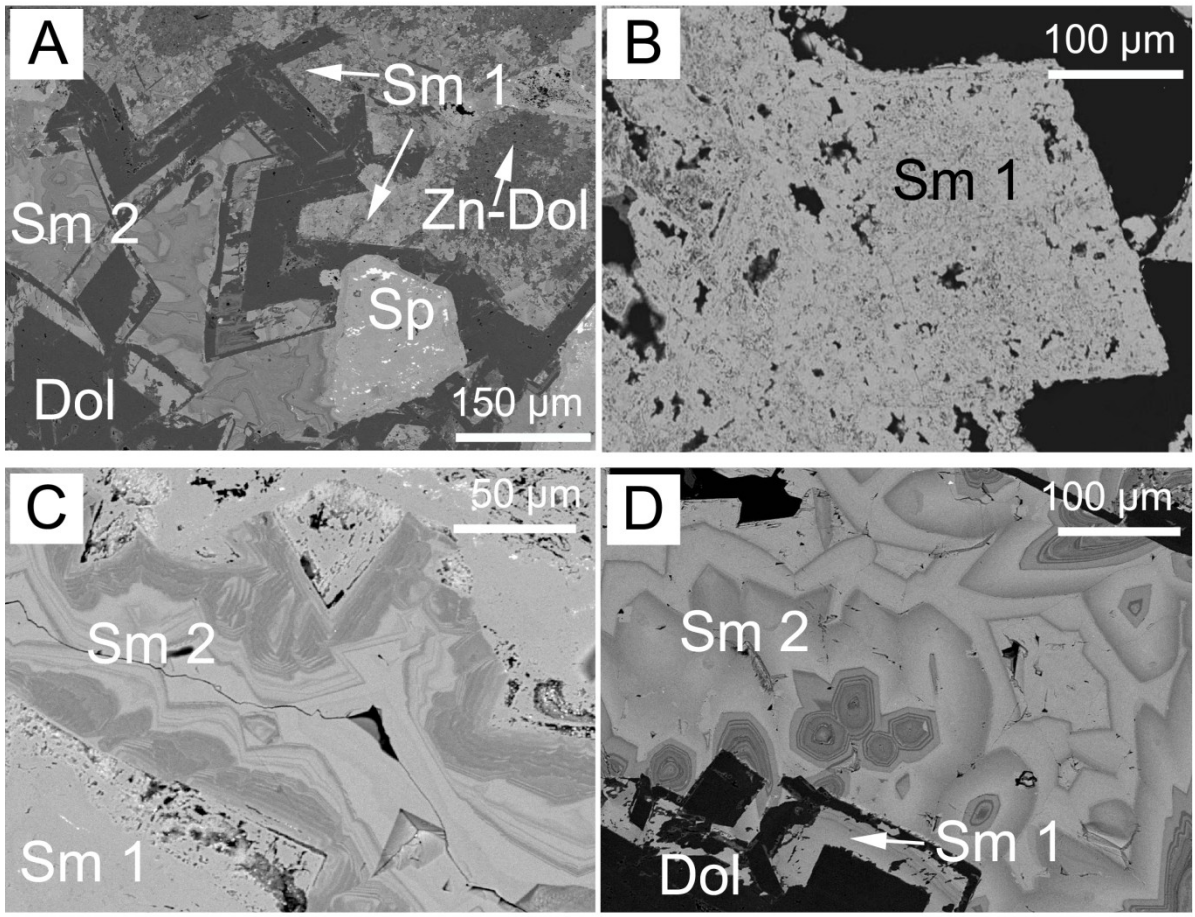

Fig. 3.23. Smithsonite containing Mg (dark gray), and pure smithsonite (bright gray). A) JS MON 2. Smithsonite 1 (and Zn-dolomite) replacing dolomite; Smithsonite 2 precipitated in the cavity. B) JS MON 10. Smithsonite 1 mimicking the rhombohedral habitus of a dolomite crystal. C) JS MAR 1. Smithsonite 1 replacing dolomite; smithsonite 2 concretions very enriched in Mg. D) JS MON 2. Smithsonite 1 replacing dolomite; smithsonite 2 concretions very enriched in Mg. SEM-BSE-EDS. Dol = dolomite; Sm 1 = smithsonite 1; Sm 2 = smithsonite 2: Zn-Dol = Zn-dolomite.

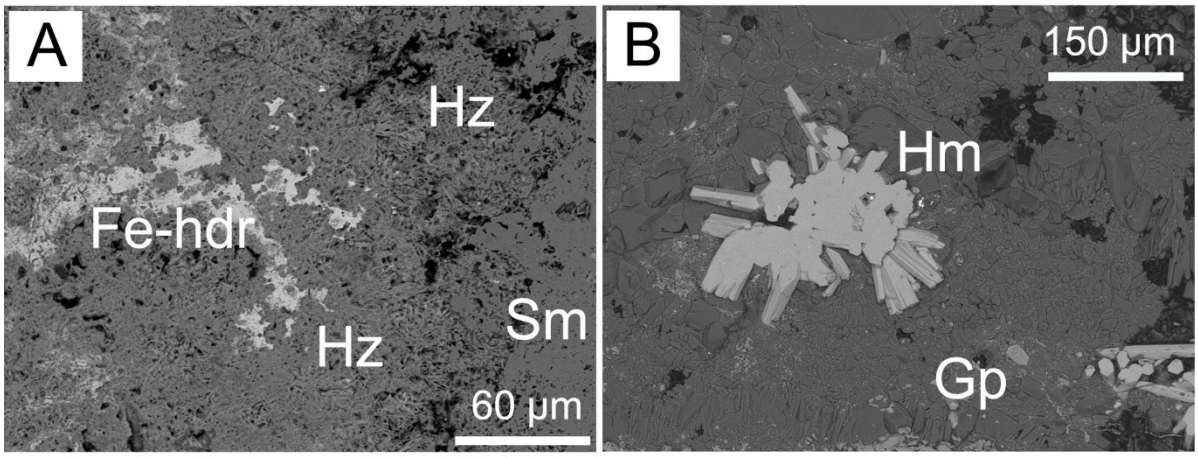

Fig. 3.24. A) JS MON 10. Hydrozincite replacing smithsonite. B) J125-3. Hemimorphite (containing Ag-sulfide spots) precipitated within gypsum. SEM-BSE-EDS. Fe-hdr = Fe-(hydr)oxides; Gp = gypsum; Hm = hemimorphite; Hz = hydrozincite; Sm = smithsonite.

Gypsum has been mostly detected in the top part of the J-125 drill core. It occurs as acicular crystals in veins cutting smithsonite, as crystalline microconcretions and cavity fillings within smithsonite, and as replacement of sphalerite. Gypsum textures vary between fibrous, partially deformed crystals, perpendicular to the vein boundaries, and agglomerates of crystals filling the porosity of the mineralized lithotypes (Fig. 3.25). The fibrous crystal form, perpendicular to the veins, points to a crystal growth contemporary to their opening.

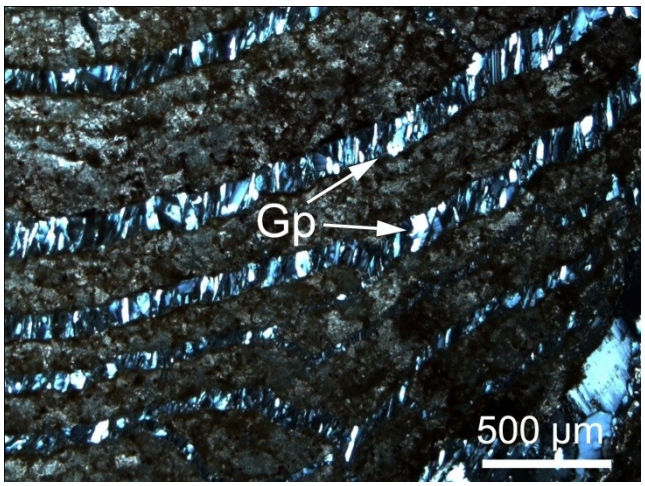

Fig. 3.25. J125.3. Gypsum veins: acicular crystals perpendicular to vein boundaries. N+.

The Fe(hydr)oxides at Jabali have not the typical goethite composition: they contain not only FeO, but also ZnO (up to 12 wt.%), PbO (up to 7 wt.%) and SiO_2 (up to 6 wt). Also most Mn(hydr)oxides consist not only of chalcophanite (which should contain only Mn and Zn), but of possibly amorphous phases containing Mn-Pb-Fe in variable proportions (PbO ~20-30 wt.%, FeO ~10 wt.%).

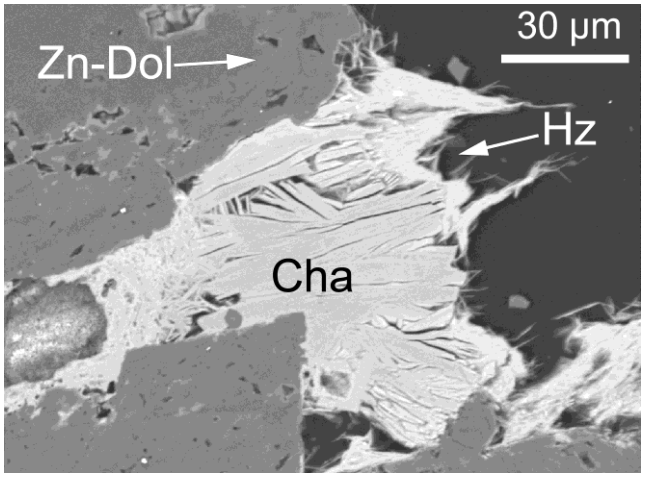

Fig. 3.26. JS MAR 4. Chalcophanite. SEM-BSE-EDS. Cha = chalcophanite; Hz = hydrozincite; Zn-Dol = Zn-dolomite.

Major and minor element geochemistry

Chemical analyses of the samples from Jabali drillcores (ZincOx plc.) are shown in TABLE 3.4. In TABLE 3.7, instead, I have recorded the chemical composition of several outcrop samples.

The outcrop samples can reach high Zn contents, reaching locally over 50 wt.% Zn. The highest Zn amounts (e.g. JS MON 22A, JS MON 29) are due to the amounts of smithsonite or to the association of smithsonite-hydrozincite-hemimorphite. Samples characterized by discrete Pb contents (~5-6 wt.% Pb) are low in Zn. In these samples silver is not correlated with Zn nor Pb.

The gossan samples are marked by very high iron values (over 30 wt.% Fe). High sulfur concentrations are associated with the rocks rich in supergene sulfates (e.g. JS MON 18).

Mn has a maximum value around 1 wt.%. Cadmium generally occurs with higher amounts than silver, and locally reaches more than 3000 ppm. Thallium is not abundant at Jabali, reaching maximum concentrations of 50 ppm. Only a slight positive correlation exists between Zn and Cd, and a slight negative correlation between Zn and Ca-Mg.

Drillcore samples give the better information on the Jabali geochemistry. The highest Zn grades are reached in the J125 drillcore (38.02 wt.% Zn in the Upper zone). Correlating the concentrations between the three drillcores, it is possible to notice that the Upper Zone is characterized in the J125 core by higher grades than in the J109 and J138 cores. In core J125 there are more than 6 m where zinc grades over or around 20 wt.% Zn, whereas in cores J109 and J138 the most mineralized sections are 1 and 3 m thick respectively, and have grades up to a maximum of 10 wt.% Zn. In the J125 drillcore, the Middle zone is characterized by 2 m at 12-15 wt.% Zn, and 1 m at 29.1 wt.% Zn, whereas the Lower zone consists of a 4 m-long interval with 1 m at 14.4 wt.% Zn, 2 m at 25-29 wt.% Zn, and 1 m at 37 wt.% Zn. Lead generally is not very high, and reaches a maximum amount of 13 wt.%. Ca and Mg are the main constituents of the host rock, and can be locally very abundant. They show an inverse relation with zinc. Sulfur occurs with concentrations of 5-7 wt.% in the Upper zone of J125 core, where unaltered sulfides and gypsum have been detected. The iron content generally remains on low values (~4-5 wt.% Fe), and manganese is generally under 1 wt.%.

In some intervals within the cores, silver can be over 400 ppm, but notable concentrations of around 200-300 ppm Ag have been currently detected. Silver is not strictly correlated with any other element, but occurs in notable amounts only in the most mineralized intervals. Cadmium can be over 2000 ppm and is strictly correlated with Zn.

Arsenic, molybdenum, bismuth, and antimony are very scarce.

TABLE 3.7. Major element concentrations (wt.%) of outcrop samples derived from ICP analysis.

Sample n.	Zn	Fe	Mg	Pb	Ca	Mn	Ti	Al	Na	K	P	S
JS MON 4	3.42	2.32	6.6	0.41	24.8	0.656	0.002	0.1	0.01	<0.01	0.03	<0.05
JS MON 6	38.29	13.7	0.4	0.71	0.1	0.515	0.008	0.3	<0.01	<0.01	0.02	0.05
JS MON 9	42.05	8.54	0.7	0.56	0.09	0.462	0.002	0.1	<0.01	<0.01	0.02	<0.05
JS MON 12	2.96	18.7	0.2	7.42	0.24	0.048	0.04	1.2	0.06	0.67	0.03	5.79
JS MON 13	29.26	12.6	2.5	1.06	3.81	0.783	0.006	0.1	0.02	0.02	0.02	<0.05
JS MON 14	36.37	2.73	2	0.61	6.41	0.699	0.004	0.4	<0.01	<0.01	0.02	0.06
JS MON 15	19.70	14.5	1.9	1.12	11.4	0.493	0.006	0.3	<0.01	<0.01	0.02	0.09
JS MON 17	1.15	34.6	0.1	1.17	11.6	0.01	0.049	0.3	0.03	0.16	0.06	0.47
JS MON 18	2.47	32.3	0.1	5.70	6.72	0.236	0.012	2	0.08	0.08	0.08	1.9
JS MON 19	1.30	24.6	0.2	0.11	8.55	0.275	0.025	0.7	0.18	0.02	0.11	0.12
JS MON 20	23.37	35.5	0.1	0.55	0.11	0.078	0.007	0.1	0.07	0.04	0.03	0.2
JS MON 21	34.57	19.8	0.1	1.14	0.15	0.014	0.012	0.3	0.01	<0.01	0.03	0.1
JS MON 22A	47.20	5.3	0.2	0.64	0.24	0.078	0.003	0.1	<0.01	<0.01	0.01	<0.05
JS MON 22B	41.96	12.8	0.1	1.24	1.16	0.184	0.009	0.2	0.01	<0.01	0.03	0.23
JS MON 28	48.30	5.83	0.2	0.61	0.16	0.386	0.004	0.1	<0.01	<0.01	0.01	<0.05
JS MON 29	51.04	2.38	0.2	0.02	0.27	0.855	0.009	0.4	0.04	0.04	0.02	<0.05
JS MON 32_1	41.58	2.46	0.6	1.23	4.71	1.068	0.006	0.6	<0.01	<0.01	0.02	0.08
JS MON 32_2	23.52	3.2	5.1	0.99	12.5	0.424	0.003	0.2	<0.01	<0.01	0.01	0.17
JS MON 33	1.39	2.43	8.7	7.95	19.9	0.611	<0.001	0.1	<0.01	<0.01	0.01	0.82
JS MON 36	0.13	1.79	2.5	0.00	33.8	0.635	0.002	0	<0.01	<0.01	0.01	<0.05

Detection limits (wt.%): Zn 0.01, Fe 0.01, Mg 0.01, Ca 0.01, Mn 0.0005, Ti 0.001, Al 0.01, Na 0.01, K 0.01, P 0.001, S 0.05.

Continue... TABLE 3.7. Minor element concentrations (ppm) of outcrop samples derived from ICP analysis.

Sample n.	Ag	Cd	Mo	Cu	Ni	Co	As	Th	Sr	Sb	V	La	Cr	Ba	Hg	Sc	Tl	Ga	Se
JS MON 4	9.4	319	1.4	13.8	9.5	1.8	6	<0.5	55	<0.5	16	5.7	9.6	41	0.35	1.2	1.1	<5	2
JS MON 6	3.4	1439.7	3.6	49.1	128.3	8.4	<5	<0.5	<5	<0.5	11	4.9	5	<5	0.19	1	0.5	<5	17
JS MON 9	5.1	2307.5	2.9	30.4	152.6	6.2	<5	<0.5	<5	<0.5	11	2.5	3.8	<5	0.25	1.2	0.7	<5	20
JS MON 12	37.9	22.1	3.3	76.8	23.4	3.9	7	2.7	117	<0.5	19	10.3	22	400	1.32	1.9	52.8	<5	9
JS MON 13	9.6	3722.7	4.4	25.9	240.6	17.8	<5	<0.5	5	<0.5	10	5	8.4	11	1.04	0.9	5.2	<5	9
JS MON 14	44.4	1358.2	5.3	14	38.7	9.1	<5	<0.5	26	<0.5	11	3.2	3.6	22	0.18	2	13.2	<5	17
JS MON 15	58.4	715.3	6.4	9.2	43.5	4.9	18	0.5	134	<0.5	16	3.7	4.7	21	0.28	2.9	4.1	6	9
JS MON 17	3.9	546.9	29.8	30.7	12.5	1.3	8	0.9	41	<0.5	180	1.9	48.7	56	0.2	2.5	<0.5	16	<2
JS MON 18	119.6	38.5	5.8	60	52	13.7	33	1.4	160	<0.5	21	14.6	20.9	80	0.2	7.1	2.1	27	<2
JS MON 19	3.4	69.3	8.3	378.9	74.4	166.4	<5	1.8	96	<0.5	54	15.7	47.2	75	<0.05	3.3	2.9	28	2
JS MON 20	3.6	185.9	7.5	7.3	34.8	2.2	23	<0.5	9	<0.5	15	2.4	6.3	<5	0.36	4	0.9	<5	8
JS MON 21	10.9	1499.8	2.2	79.2	19.5	1.7	34	<0.5	8	<0.5	15	1.1	6.4	<5	0.4	1.3	<0.5	10	14
JS MON 22A	108	2952.6	0.9	308.1	37	4.9	<5	<0.5	6	<0.5	<10	0.6	2.1	<5	0.44	1.1	<0.5	22	22
JS MON 22B	63.6	952.3	2.7	604.5	35.9	5.9	6	<0.5	29	0.9	11	1.6	5.7	14	1.06	2.8	<0.5	68	23
JS MON 28	13.8	2225	1.9	122.9	63.9	12	5	<0.5	7	<0.5	11	1.2	3	<5	1.41	1.6	1.1	<5	21
JS MON 29	21.9	603.2	3	4	53.2	12.1	<5	0.6	9	<0.5	11	9.8	3.6	158	0.22	2	3.5	<5	22
JS MON 32_1	15.3	1224	6.2	100.7	11.3	8.2	21	0.9	26	1.2	14	4.8	7.7	9	0.25	2.8	<0.5	13	16
JS MON 32_2	81.6	1639.5	2.6	86.3	6.4	2.9	6	<0.5	37	<0.5	<10	9.9	2.9	8	0.17	2.7	<0.5	26	10
JS MON 33	350.7	73.8	1.8	7.6	4.5	1.6	5	<0.5	126	<0.5	13	20	4.1	30	0.37	0.6	0.5	<5	<2
JS MON 36	0.9	<0.5	<0.5	1.3	<0.5	<0.5	<5	<0.5	72	<0.5	<10	3.3	1.1	9	<0.05	<0.5	<0.5	<5	<2

Detection limits (ppm): Ag 0.5, Cd 0.5, Mo 0.5, Cu 0.5, Ni 0.5, Co 0.5, As 5, Th 0.5, Sr 5, Sb 0.5, V 10, La 0.5, Cr 0.5, Ba 5, Hg 0.05, Sc 0.5, Tl 0.5, Ga 5, Se 2.

C-O stable isotope geochemistry

C-O stable isotope analyses were carried out on several carbonates of Jabali. The selected phases are: limestone (bioherms from Unit 7), saddle dolomite (associated with sulfide mineralization), Zn-dolomite from drillcores, smithsonite (drillcores and outcrop), and hydrozincite (TABLE 3.8, Fig. 3.27).

Two limestone samples from Unit 7 gave different results: in a coral sample values of -0.97 ‰ δ^{13}C-PDB and -6.83‰ δ^{18}O-PDB have been measured, while the carbonate matrix between the bioherms shows a composition of -2.30‰ δ^{13}C-PDB, and -7.75‰ δ^{18}O-PDB. The δ^{13}C values are roughly in the range of compositions for Jurassic (Kimmeridgian-Tithonian) marine carbonates; δ^{18}O compositions are, instead, lower than those reported in the literature (Jenkyns et al., 2002) and could be related to diagenetic modifications.

The saddle dolomite shows δ^{13}C and δ^{18}O ratios typical of other hydrothermal dolomites in the world (Diehl et al., 2010; Boni et al., 2013), with δ^{13}C-PDB comprised between -1.14‰ and 0.23‰ and δ^{18}O-PDB comprised between -10.70‰ and -9.12‰.

The Zn-dolomite phase is characterized by δ^{13}C-PDB values comprised between -1.85‰ and -0.97‰ and δ^{18}O-PDB between -11.95‰ and -10.42‰. The δ^{18}O compositions are broadly in a hydrothermal range, whereas the δ^{13}C compositions are slightly lower than those of saddle dolomites.

Smithsonite from boreholes was sampled only from the J125 core. It was possible to differentiate between clear concretionary and replacive smithsonite only in a limited number of cases. Smithsonite strictly intergrown with gypsum was discarded.

The main difference between the isotopic compositions of the various smithsonite samples seems to be related to their provenance from the Upper, Middle, or Lower zones. Smithsonite from the Upper zone is characterized by δ^{13}C-PDB comprised between -4.68‰ and -2.88‰ and δ^{18}O-PDB comprised between -11.41‰ and -10.50‰, and the only sample from the Middle zone has a composition of -4.56‰ δ^{13}C-PDB and of -9.57‰ δ^{18}O-PDB. Smithsonite from the Lower zone has δ^{13}C-PDB values between -5.71‰ and -4.69‰ and δ^{18}O-PDB between -9.99‰ and -9.20‰. A smithsonite from the JS MON 22A outcrop sample has a composition of -6.06‰ δ^{13}C-PDB and of -8.80‰ δ^{18}O-PDB, comparable with smithsonite from the deeper samples.

Summarizing the smithsonite data: samples from different mineralized zones have distinct C-O isotopic composition; in particular they differ for δ^{18}O composition which, after Gilg et al. (2008), indicates the effects of temperature-related fractionation. The δ^{13}C compositions, instead, are comparable with those of supergene smithsonites from other Zn-nonsulfide deposits in the world (Gilg et al., 2008) . Hydrozincite has stable isotope ratios between -7.37‰ and -6.62‰ δ^{13}C-PDB and -4.90‰ to -0.79‰ δ^{18}O-PDB: these values are in the range of most supergene hydrozincites elsewhere (Gilg et al., 2008).

TABLE 3.8. Carbon and Oxygen Isotope data of Jabali carbonates, from outcrop and drillcore samples.

Sample n.		Mineral	Description	δ^{13}C-PDB (‰)	δ^{18}O-PDB (‰)	δ^{18}O-SMOW (‰)
JS MON 38	Outcrop	Cal	coral fossils from limestone	-0.97	-6.83	23.82
JS MON 38		Cal	calcite matrix between bioherms from limestone	-2.30	-7.75	22.87
JS MON 3		Sm	concretionary smithsonite	-2.61	-9.03	21.55
JS MON 22A		Sm	concretionary smithsonite	-6.06	-8.80	21.79
JS MAR 4		Hz	hydrozincite crust	-6.75	-0.79	30.04
JS MON 22A		Hz	hydrozincite crust	-7.37	-4.90	25.81
JS MON 22A		Hz	hydrozincite crust	-6.62	-4.82	25.89
Core sample n.	depth (m)	Mineral	Description	δ^{13}C-PDB (‰)	δ^{18}O-PDB (‰)	δ^{18}O-SMOW (‰)
J125-6	59.2	Dol	hydrothermal dolomite crystal	-1.10	-9.36	21.21
J125-7	60.8	Dol	hydrothermal dolomite crystal	-1.14	-9.12	21.46
J125-15	69.2	Dol	hydrothermal dolomite crystal	0.23	-10.70	19.83
J109-5	62.6	Zn- Dol	dolomite crystal with Zn dolomite core	-1.85	-11.29	19.22
J125-11	65.2	Zn- Dol	dolomite crystal with Zn dolomite core	-0.97	-11.95	18.54
J125-11	65.8	Zn- Dol	dolomite crystal with Zn dolomite core	-1.17	-11.16	19.36
J125-15	69.8	Zn- Dol	dolomite crystal with Zn dolomite core	-1.19	-10.42	20.11
J125-9	63.7	Sm	vacuolar smithsonite	-3.75	-11.19	19.33
J125-10	64.1	Sm	massive smithsonite	-3.40	-10.83	19.70
125 -10	64.2	Sm	concretionary smithsonite	-4.16	-10.50	20.03
J125-14	68.7	Sm	smithsonite concretion	-2.88	-11.41	19.10
J125-15	69.1	Sm	smithsonite concretion	-4.68	-11.41	19.09
125-21	77.0	Sm	massive smithsonite	-4.56	-9.57	20.99
125-30	85.6	Sm	smithsonite concretion	-5.48	-9.85	20.70
125-30	85.65	Sm	smithsonite concretion	-4.85	-9.99	20.56
J125-30A	85.7	Sm	mixed massive-concretionary smithsonite	-5.22	-9.87	20.69
J125-30B,	85.7	Sm	smithsonite micro-concretions	-5.47	-9.93	20.62
J125-32	87.6	Sm	massive smithsonite	-4.83	-9.20	21.38
125-32	87.7	Sm	concretionary smithsonite	-4.92	-9.49	21.08
125-32A	87.75	Sm	smithsonite concretion	-5.71	-9.78	20.78
J125-32B	87.75	Sm	smithsonite concretion	-4.69	-9.85	20.71

Abbreviations: Cal = calcite; Dol = dolomite; Hz = hydrozincite; Sm = smithsonite; Zn-Dol = Zn-dolomite.

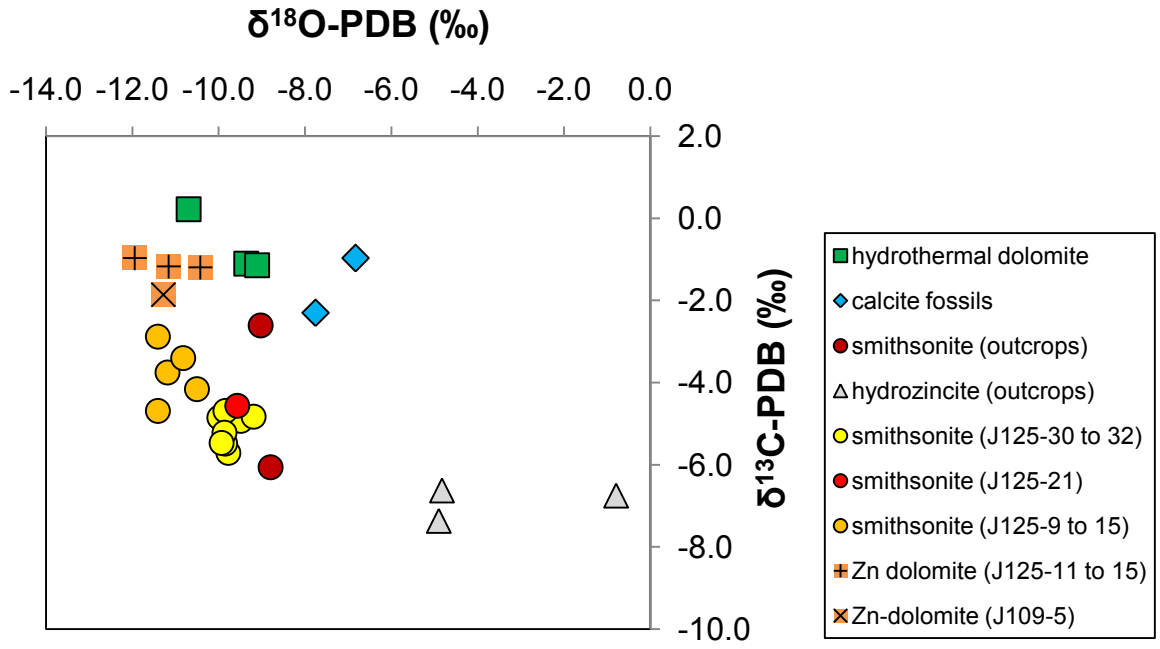

Fig. 3.27. δ^{18}O-PDB vs. δ^{13}C-PDB compositions of Jabali carbonates.

Sulfur isotope geochemistry

Sulfur isotope analyses have been carried out on few sulfides and sulfates from Jabali (TABLE 3.9). Two sphalerite, sampled from the J125-2 and J125-5 intervals, have composition of 7.13‰ δ^{34}S CDT and 6.47‰ δ^{34}S CDT respectively. Galena was sampled from an outcropping vein, and has a composition of -3.58‰ δ^{34}S CDT. These values are in the range of other sediment-hosted Zn-Pb deposits (Leach et al., 2005).
Gypsum from sample J125-3 has a composition of 7.34‰ δ^{34}S CDT, which is very similar to the δ^{34}S composition of sphalerite.

TABLE 3.9. Sulfur isotope data of Jabali sulfides and sulfates.

Sample n.	Mineral	Description	δ^{34}S CDT (‰)
JS MAR 2	Gn	Macrocrystalline galena agglomerate	-3.58
J125-2	Sp	Sphalerite vein	7.13
J125-5	Sp	Sphalerite vein	6.47
J125-3	Gp	Gypsum vein within smithsonite	7.34

Abbreviations: Gn = galena; Gp = gypsum; Sp = sphalerite.

Differential thermal analysis (DTA)

Thermal analysis is a quick method to provide additional information on specific minerals and/or mineral assemblages, and can be useful in the exploration of nonsulfide ores in carbonate rocks (Zabinski, 1959). Therefore, thermodifferential/thermogravimetric analysis was carried out on two Jabali samples showing different zinc grades, i.e. samples J125-31 (14.4 wt.% Zn), and J125-34 (5.1 wt.% Zn). The DTA trace of J125-31 sample records endothermic reaction peaks at 400°C, 500°C, 685°C, 750°C and 870°C (Fig. 3.28). The 400°C and 500°C peaks are in the range of the dehydratation values for smithsonite (Garcia-Guinea et al., 2009), while the 750°C and 870°C peaks are show the dolomite dehydratation signatures. In fact, the decomposition of dolomite takes place through two different steps: a first around 800°C, which can be associated with the decomposition of the $MgCO_3$ layers in the structure, and a second around 900°C, bound to the decomposition of the $CaCO_3$ layers. The 685°C peak, recorded at Jabali, does not belong to any of the above-mentioned minerals. A Norian (Triassic) dolomite from Southern Apennine (Italy), analyzed as a standard compound, shows two dehydratation peaks at 810°C and 890°C. Both temperatures are perfectly comparable with existing literature data for pure dolomite (Rowland and Beck, 1952; Gunasekaran and Anbalagan, 2007 and references therein).

The DTA trace of sample J125-34 exhibits some differences: it is possible to identify the goethite dehydratation peak (290°C), and three endothermic peaks at 685°C, at 745°C and 880°C respectively (Fig. 3.28). As in the previous sample, the peaks at 745°C and 880°C should correspond to the dolomite dehydration, whereas the 685°C peak could not be attributed to any of the minerals determined by XRD in the chosen samples.

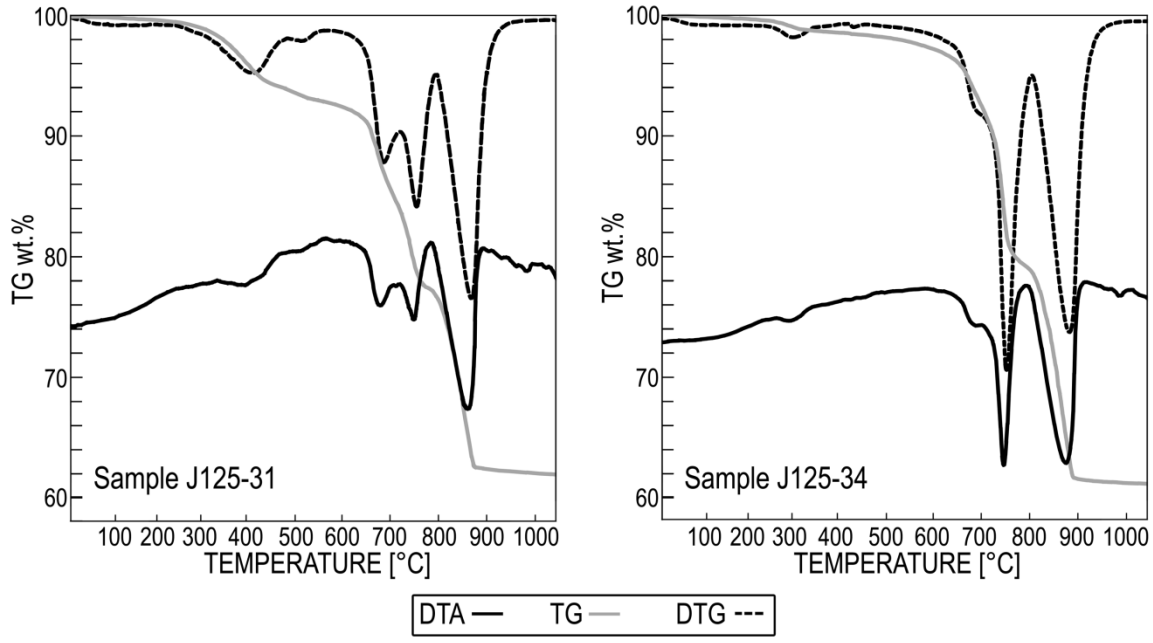

Fig. 3.28. DTA-TG-DTG curves of J125-31 and J125-34 samples.

Discussion

Genesis of the primary mineralization

Jabali deposit is located on the border on the Sab'atayn basin, which is one of the most important onshore petroleum areas of Yemen. The geology of the basin, synthesized by Beydoun et al. (1998), Ahlbrandt (2002), As-Saruri et al. (2010), etc., allows some considerations about the genesis of primary and secondary mineralization at Jabali. Al Ganad et al. (1994) considers the primary mineralization as deposited by fluids migrating from the Sab'atayn basin during Late Jurassic (Kimmeridgian) rifting, and the secondary mineralization related to an oxidation period during a period extended from Cretaceous to Present. Allen (2000), instead, hypothesizes a sulfide mineralization generated by the emplacement of CRD-MVT hybrid fluids along extensional structures related to Red Sea rifting, contemporarily to the development of magmatic activity in the region (~22 Ma), and a short oxidation stage, lasting from Miocene to Present.

If we evaluate the genetic hypothesis of Allen (2000), there are no proofs possibly testifying the emplacement of a CRD (Carbonate Replacement Deposit) mineralization. Young Pb-isotopes are not crucial to distinguish between a MVT- or CRD-character of a Zn-Pb sulfide mineralizations. In fact, as reported by Leach et al. (2005), many MVT deposits show a very young Pb-isotopic composition, despite to very old "true" ages, determined by sphalerite absolute geochronology. Moreover, low pyrite content does not result a diagnostic characteristic of CRD deposits either, as well as a high Zn-Pb ratio (Leach et al., 2005). Sphalerite fluid inclusions have temperatures ranging from 90 to 140°C, and maximum salinities of 23 % eqv. NaCl (Al Ganad et al., 1994), which are also typical of MVT ores. About the polymetallic character of the Jabali mineralization, chemical analyses of samples collected for this study generally show not-so-high amounts of As, Mo, Bi, and Sb (and those elements may have been added or concentrated during the oxidation stage). High Ag concentrations, that are generally typical of CRD-type ores, have been also measured in several deposits considered by Leach et al. (2005) as MVT.

These observations clearly weaken the CRD hypothesis, and confirm the prevailing MVT (*sensu lato*) character of the primary mineralization.

The hydrothermal circulation causing the MVT mineralization could have been related to extensional tectonics and fluid motion, associated with petroleum migration within the Sab'atayn basin. Oil migration from the shales of the Mabdi Fm. to the clastic and carbonate reservoirs, which were then sealed by the salt of Sabatayn Fm. (Ahlbrandt, 2002), took place during two main periods: from 135 to 90 Ma, and from 85 to 50 Ma (Csato et al., 2001). During these periods, the Jabali site, being on the border of the rifted basin, should have been uplifted above the petroleum source rocks located within the Sab'atayn basin (at a depth of about 2,700 m; Csato et al., 2001). Fluids could have interacted with the basement, have been enriched of metals, and migrated in the overlying sedimentary rocks, depositing the sulfide ores. Moreover, the oil geochemical data from the Sab'atayn basin fields show a notable sulfur content (Ahlbrandt, 2002). It could be then possible that petroleum migration

has also involved sedimentary sulfates (evaporites), and that the oil brines could possibly have had an adequate sulfur content to deposit sulfides.
However, the $\delta^{34}S$ compositions of sphalerite and galena are in the isotopic range of other Zn-Pb sediment-hosted deposits (Leach et al., 2005), and are different from the isotopic composition of Mesozoic evaporites, occurring in the sedimentary succession of the Jabali district (Strauss, 1999; Kampschulte and Strauss, 2004). Several fractionation stages should have taken place.

Genesis of the secondary nonsulfide mineralization
Smithsonite, which is the most abundant ore mineral of the deposit, occurs in two main phases: Smithsonite 1, which replaces host dolomite and sphalerite, and Smithsonite 2, which occurs as cement and concretions precipitated in cavities and in the porosity of the host rock. The replacement of the host rock proceeded in stages: the alteration process started with a partial replacement of Mg by Zn in the dolomite lattice, and went on with a gradually higher amount of substitution of Mg by Zn, until a maximum measured value of 70 mol.% Zn in the dolomite (Fig. 3.18). Finally, the dolomite lattice became totally unstable and smithsonite formed. Zn-dolomite appears as an intermediate replacement phase, between dolomite and smithsonite.
This type of wall-rock replacement process in supergene conditions has been also observed in the Iglesias mining district (Italy), where it has been analyzed by C-O-isotope geochemistry of smithsonite and Zn-dolomite (Boni et al., 2003, 2013). The C-O-isotopic data of smithsonite from the Iglesias mines (Sardinia) (Fig. 3.29) clearly indicate the precipitation of this mineral in a supergene environment (Boni et al., 2003), and the equilibrium temperature, as revised in Gilg et al. (2008), indicates a mineral formation between 11° and 23°C. Zn-dolomites from the same district have C-O-isotope compositions comprised between that of hydrothermal dolomite of the host rock and those of supergene smithsonite. Hence, the Zn-dolomites of the Iglesiente district have been interpreted as intermediate phases, formed during the supergene process (Boni et al., 2013).
Contrary to the "standard" values of the supergene smithsonites quoted in Gilg et al. (2008), the Jabali smithsonites have variable $\delta^{18}O$ compositions in different parts the orebody. Smithsonites from the "Upper" zone have $\delta^{18}O$ comprised between 19.09‰ and 20.03‰ SMOW, smithsonites in the "Middle" and "Lower" zones have $\delta^{18}O$ values between 20.56‰ and 21.38‰ SMOW, and a smithsonite from an outcrop sample shows a composition of 21.79‰ SMOW.
The $\delta^{13}C$ values are always negative, but variable at Jabali, being heavier in the smithsonites from the "Upper" zone than in smithsonites from the "Middle" and "Lower" zones; the outcrop sample characterized by the lowest C-isotopic composition. The measured C-isotope composition is in the "standard" range of values for supergene smithsonites in other nonsulfide ores (Gilg et al., 2008), whereas the O-isotope composition is lower and expresses a variability of values compared with other supergene smithsonites (Gilg et al., 2008). The C-O-isotopic composition of hydrozincite is instead clearly in the range of supergene Zn-carbonates.

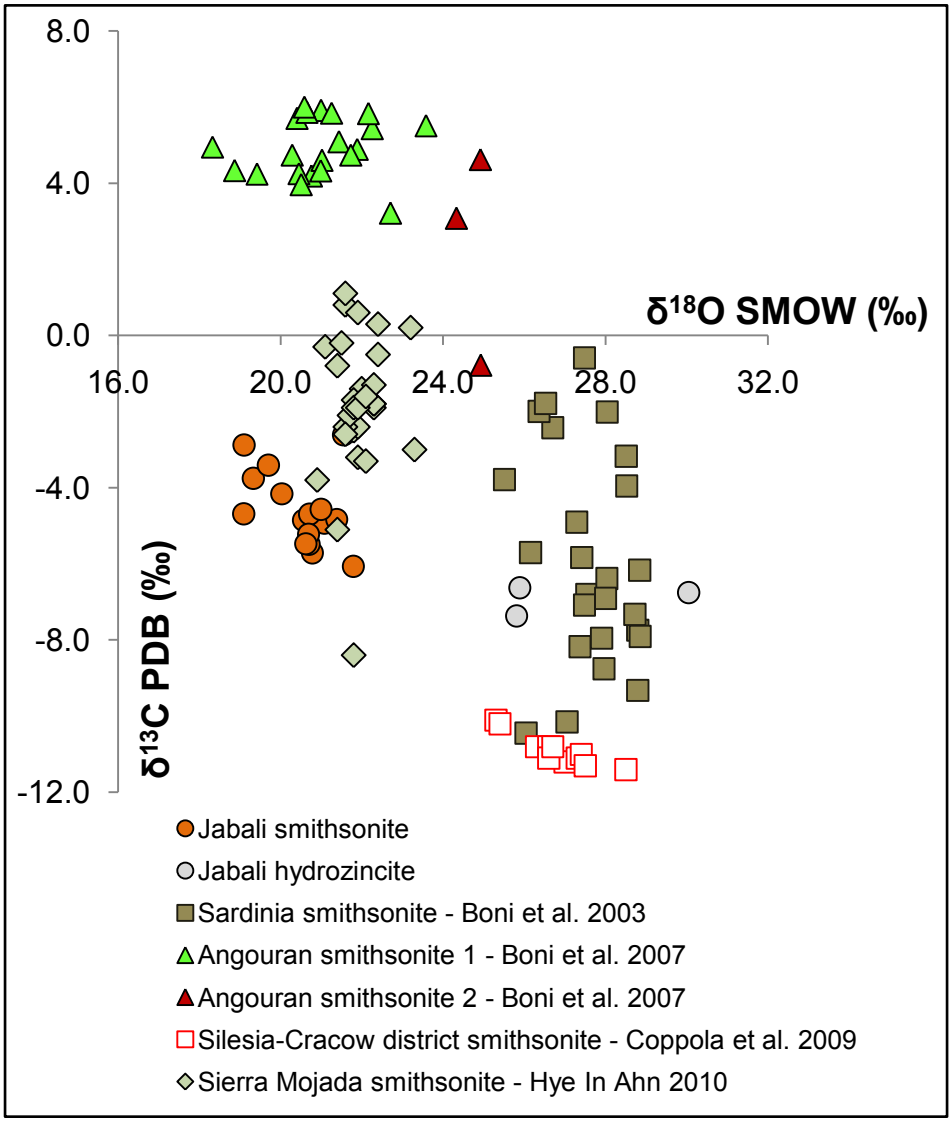

Fig. 3.29. δ^{18}O-PDB vs. δ^{13}C-PDB compositions of Jabali Zn-carbonates and of smithsonites from other nonsulfide deposits/districts: Iglesias, Sardinia, Italy (Boni et al., 2003); Angouran, Iran (Boni et al., 2007); Silesia-Cracow district, Poland (Coppola et al., 2009); Sierra Mojada, Mexico (Hye In Ahn, 2010).

The measurements of δ^{18}O generally allow to estimate the temperature of precipitation of smithsonite (Gilg et al., 2008). Provided the δ^{18}O composition of precipitating water is known, it is possible to calculate the temperature when the mineral was formed, using the following equation:

$$1000 \ln \alpha_{\text{smithsonite-water}} = 3.10 (10^6/T^2) - 3.50.$$

In the Jabali region, some springs relatively far from the mining site have an O-isotopic composition comprised between -4.18‰ and -3.64‰ SMOW (Minissale et al., 2007). If the smithsonites from the ore deposit had been deposited by fluids with the same δ^{18}O composition of the modern groundwaters, we should imagine that the precipitation temperature was comprised between ~55° and ~65°C, i.e. a low-temperature hydrothermal

environment. Interestingly, the modern rainwater in Yemen have a $\delta^{18}O$ composition varying from -8.03‰ to +10.54‰ SMOW (Al-Ameri, 2011), and the $\delta^{18}O$ data of Pleistocene-Holocene speleothems from various caves of Saudi Arabia and Yemen, point to a composition of precipitating waters ranging between ~ -12‰ and ~0‰ SMOW (Fleitmann et al., 2004, 2011). This means that both rainwater and groundwater in the region are characterized by a wide variation of $\delta^{18}O$: a situation that could be extended back to at least part of the Tertiary. It is not possible, therefore, to be sure if the O-isotope composition of the fluids that precipitated smithsonite at Jabali was the same of the modern springs sampled in the whole region. Anyway, using the lowest known $\delta^{18}O$ values of rainwater and cave water, it was possible to calculate for the Zn-carbonates a temperature of precipitation ranging between 20° and 45°C, i.e. not exactly a typical supergene environment. The negative C-isotope composition could indicate: 1) in the case of supergene origin of the alteration, the typical values related to soil carbon; 2) in the case of low-temperature hydrothermal alteration, the involvement of meteoric-surficial water in a deep, thermal circulation; 3) organic values of carbon not related to surficial environment, e.g. organic matter in black shales. However, the variable C-isotope composition in the negative realm is typical of most supergene nonsulfide Zn deposits (Gilg et al., 2008), and is interpreted as a result of mixing between carbonate carbon from the host rock, and the soil/atmospheric CO_2 (Gilg et al., 2008).

Another issue worth considering is that the different mineralized zones at Jabali are characterized by smithsonites with distinct isotopic values, forming restricted C-O-compositional clusters. This probably confirms variable precipitation temperature of the Zn-carbonate at different depths, as well as the occurrence of different periods/stages of alteration and smithsonite formation.

A similar situation, i.e. unusually low and variable $\delta^{18}O$ values in smithsonite was also observed in the Sierra Mojada mineralized district by Hye In Ahn (2010) (Fig. 3.29). The author, using a particularly low $\delta^{18}O$ composition of a modern groundwater in the area (-8‰ SMOW), estimated a deposition temperature of about 33°C for Zn-carbonate precipitation (Hye In Ahn, 2010).

A low-temperature hydrothermal origin could be also possible for the Jabali secondary ores, considering the occurrence in the Marib area of several travertine successions, as it is the case of the Angouran (Iran) nonsulfide deposit (Fig. 3.29) (Boni et al., 2007). However, as in Sierra Mojada, the possibility of a supergene smithsonite precipitation, from waters with unusual O-isotope composition, must not be excluded, considering the great variability observed both in modern rainwater and in the ancient groundwater that deposited speleothems.

A favorable geotectonic setting for the development of supergene alteration in the rocks of the Sab'atayn basin started from ~17 Ma (Miocene), i.e. at the beginning of major uplift and exhumation in Yemen, which happened during the main phase of Red Sea continental extension (Menzies et al., 1992). A possible low temperature hydrothermal alteration could be related in Jabali to the magmatic-induced geothermal activity of the area (Miocene-Holocene), as testified by travertine deposits of the Sab'atayn basin.

An evidence of secondary alteration is the occurrence in Jabali of gypsum, both in veins cutting smithsonite, and replacing sphalerite. Gypsum in these supergene ores is not related to Mesozoic evaporites (occurring in the stratigraphic succession). In fact $\delta^{34}S$ composition of the gypsum veins at Jabali is very different from the published Mesozoic values (Strauss, 1999; Kampschulte and Strauss, 2004), but very similar to $\delta^{34}S$ sphalerite from the primary ore. This similarity could mean that the gypsum sulfur is the same sulfur of sphalerite, which has not been fractionated after sulfides alteration. Obviously, the source of calcium is the host dolomite. The alteration process can be exemplified by the following chemical reactions:

Oxidation of sphalerite

$$1)\ ZnS + 2O_2 \rightarrow Zn^{2+} + SO_4^{2-}$$

$$2)\ ZnS + 4H_2O \rightarrow Zn^{2+} + SO_4^{2-} + 8H^+ + 8e^-$$
$$O_2 + 4H^+ + 4e^- \rightarrow 2H_2O$$

Formation of Zn-minerals, gypsum and calcite (?)

$$Zn^{2+} + SO_4^{2-} + CaMg(CO_3)_2 + 2H_2O \rightarrow$$
$$(Zn_{0.90},Mg_{0.10})CO_3 + Ca(Mg_{0.90},Zn_{0.10})(CO_3)_2 + CaSO_4 \cdot 2H_2O\ (?+\ CaCO_3)$$
(Mg)smithsonite Zn-dolomite gypsum calcite

The paragenesis comprehending Ag-sulfides and secondary Zn-oxidized phases (smithsonite and hemimorphite) plus gypsum, is not common in most nonsulfide deposits and can be considered a very distinctive feature of Jabali. Owing to their paragenetic position in association with the oxidized minerals, the Ag-sulfides should have precipitated during secondary processes at relatively low temperature. Following Sangameshwar and Barnes (1983), who traced the chemical reactions forming nonsulfide deposits at the Burgin mine (USA) and Tynagh (Ireland), the co-precipitation of smithsonite and Ag-sulfide can be allowed, at atmospheric temperature, only at neutral pH, if Eh varies between 0 and -2 Volts, because the stability fields of the two phases are very near, but not superposed.

The occurrence of greenockite and covellite together with gypsum and smithsonite indicates that Cd and Cu, previously contained in sphalerite (Al Ganad et al., 1994), have been mobilized and reprecipitated during weathering.

The last feature of the secondary alteration of host rock is a typical dedolomitization, consisting of a strong replacement of dolomite by calcite, derived from the reaction between Ca-rich meteoric waters and dolomite (Fairbridge, 1978). This is a common phenomenon at Jabali (Al Ganad et al., 1994), due to the abundance of gypsum in the sedimentary succession, which causes occasionally a Ca-saturated groundwater. In the process of dedolomitization of hydrothermal, metal-bearing dolomites, the dolomite crystals are replaced by newly formed calcite, while Mn and Fe, which are usually contained in the

hydrothermal dolomite lattice, precipitate in a network of (hydr)oxides, giving the carbonate rocks of many mining districts their typical brownish, "rusty" appearance.
A possible paragenesis of the mineralogical phases occurring at Jabali, is shown in Fig. 3.30.

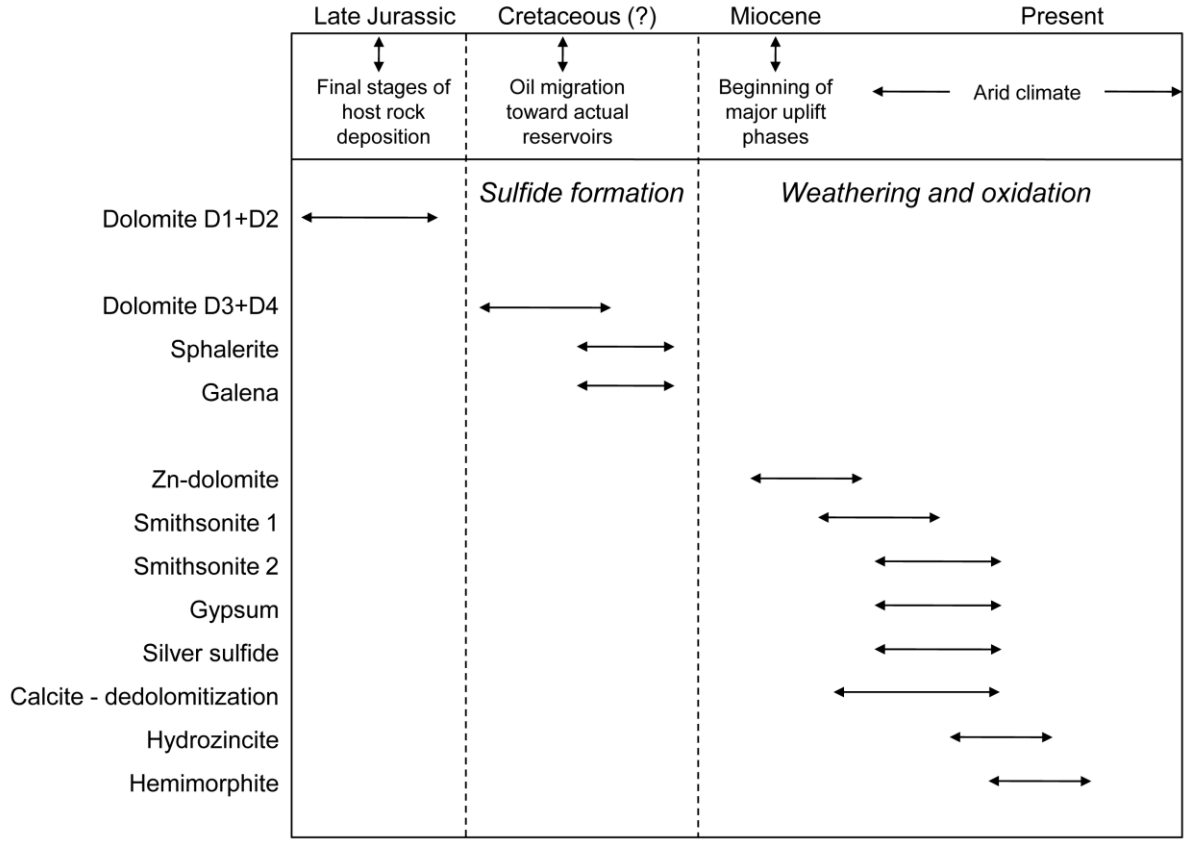

Fig. 3.30. Paragenesis of the main mineralogical phases observed at Jabali.

Zn-dolomite evaluation

Discrepancies have been commonly detected between the zinc contents recorded in the chemical assays and those stoichiometrically calculated by QPA of the Zn-minerals (smithsonite and locally sphalerite and chalcophanite) detected in the Jabali core samples (TABLE 3.5) (Mondillo et al., 2011). Therefore, the quantitative mineralogy of the analyzed samples is not always in accord with the metal grade derived from the assays. In fact, in some samples the zinc values in the assays are higher than the corresponding zinc content calculated from the mineralogy; moreover, there are samples, showing some Zn percentage in the assays (~5 wt.% Zn), where smithsonite, or other Zn-minerals were not detected. This may be due either to a high proportion of zinc concealed in an unknown phase, or to sampling issues, or to elaboration problems during QPA. Sampling issues can be due to a not-homogeneous distribution of minerals in the core, considering that the samples collected for the current work have been taken from the remaining quarter core available, when the complementary half core was used for assay, and another quarter was fragmented due to previous analyses. Elaboration issues during QPA are also possible, e.g. isorientation of minerals during XRD-powder sample preparation, high background noise, etc. However, the presence of several dolomite phases with variable Zn content, as well as the local occurrence of Mg-smithsonite in many samples, fully testified by SEM-EDS and QEMSCAN® analyses, seems to be an important reason for such discrepancies. In fact, also samples without Zn-minerals can contain significative amounts of Zn metal.

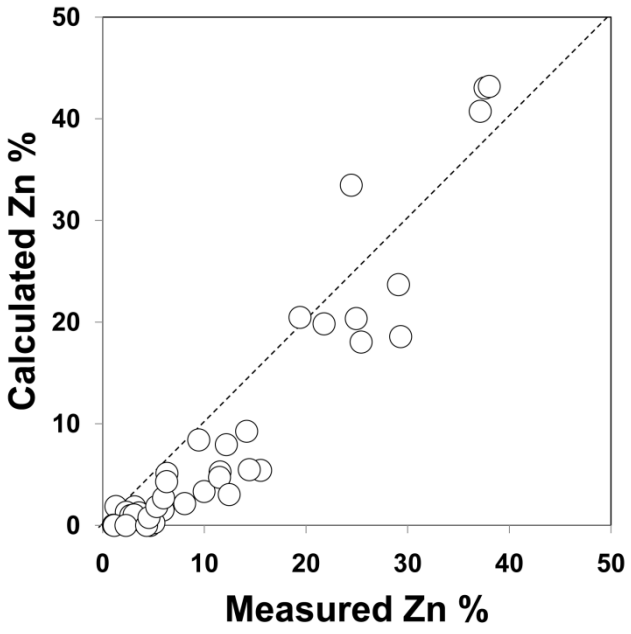

Fig. 3.31. Zinc contents, calculated from the amounts of smithsonite, sphalerite and chalcophanite determined by QPA, is plotted versus zinc contents measured in the assays (data in TABLE 3.5). The dotted line indicates the theoretical unitary correlation.

In the diagram of Fig. 3.31, the Zn values detected from the drillcore assays are plotted vs. those calculated from the amounts of Zn-minerals determined with XRD-QPA (data in

TABLE 3.5). In a hypothetical case of perfect stoichiometry for all the minerals occurring in the deposit, the Zn calculated by XRD-QPA minerals and that measured directly in the samples should be the same (excluding possible measurement errors). In consequence, all the points in this diagram should be in a straight line with an unitary coefficient. In contrast, many measured points lie away from this direct line. The samples located below the line contain more zinc than the corresponding calculated values, whereas the samples located above the line contain less zinc than calculated. Samples positioned below the line indicate to the presence of Zn-dolomite, fully testified by SEM-EDS and QEMSCAN® analyses. Samples positioned above the line, having less zinc than calculated, may contain Zn-minerals where Zn has been partially replaced by other elements, e.g. Mg-smithsonites.

A problem encountered in the X-ray QPA is that the Zn-dolomite spectrum could not be distinguished from those of the other dolomite phases in the analyzed samples.

A better way to detect the possible occurrence of Zn-dolomite may arise from the use of thermodifferential/thermogravimetric (DTA/TG) analysis, as firstly mentioned by Hurlbut (1957) and Zabinski (1959) and confirmed by Zabinski (1980). The DTA of a pure dolomite sample is mirrored by a spectrum with two distinct dehydratation peaks, which are related to the two cations Ca and Mg in the crystal structure. The position and dimension of the peaks depend on the dolomite composition. There have been many attempts to register how the variations in composition, induced by the substitution of metallic ions in the dolomite structure could modify the DTA trace, and if it was possible to clearly distinguish the related peaks. Several studies have been carried out to check the effects due to the substitution of certain metals (e.g. Pb) in the Ca positions (A sites, second endothermic reaction), and of others (e.g. Zn, Fe, Mn, Co) in the Mg positions (B sites, first endothermic reaction). The DTA analyses carried out by Hurlbut (1957) on Zn-Pb dolomites from Tsumeb (Namibia) showed a progressive decrease in temperature of the first endothermic reaction, with an increasing amount of zinc in the dolomite (Fig. 3.32). A Mg:Zn substitution of 10:1 should reduce the temperature of the related peak from 815°C to 740°C and Mg:Zn of 3.3:1 to 725°C. Fig. 3.32 also shows the DTA curve of a mixed nonsulfide zinc ore from the Warynski Mine in Upper Silesia (Poland) measured by Zabinski (1959), with the following endothermic peaks for the carbonate minerals: a peak at 400°C caused by the dissociation of smithsonite, followed by two endothermic peaks at 680°C and at 900°C related to dolomite dissociation. Considering the marked drop in temperature of the first dissociation effect of the dolomite, in respect to the standard values (Rowland and Beck, 1952), a partial substitution of Mg by Zn in the structure of the Warynski dolomite can be assumed. In Fig. 3.32, DTA traces of some Jabali samples are compared with those obtained by Hurlbut (1957) and Zabinski (1959) for the dolomites of Tsumeb and of the Warynski zinc mine, respectively. In the samples considered for this study, the above-mentioned unknown peak centered at 685°C could be attributed to the first endothermic peak of a Zn-rich dolomite phase.

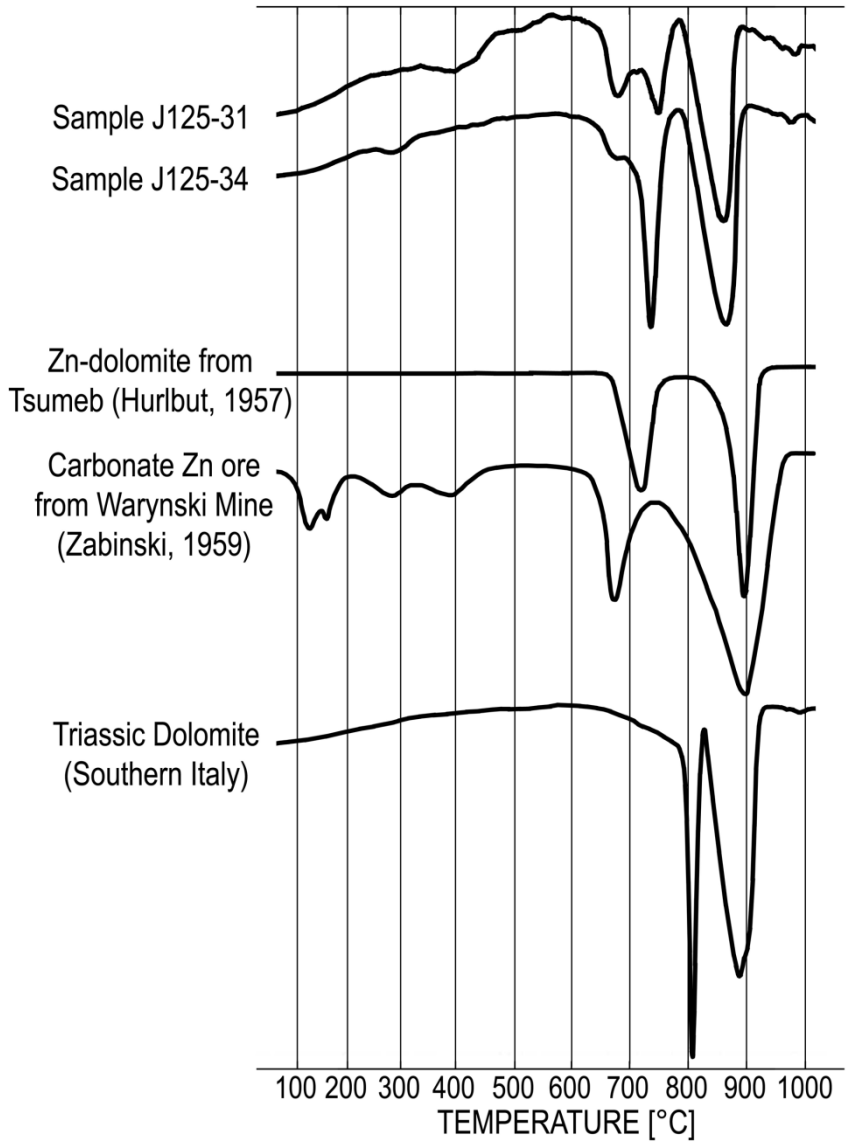

Fig. 3.32. Comparison between DTA traces from various sites: Jabali dolomites 1) J125-31, and 2) J125-34; 3) Tsumeb Zn-dolomite (Hurlbut, 1957); 4) Warynski Mine "Carbonate Zn-ore" (Zabinski, 1959); 5) Triassic dolomite from Southern Italy. The first endothermic peaks of the Zn-dolomite in the carbonate zinc ore from the Warynski mine (Poland) and the Tsumeb dolomite (Namibia) are located around 700 °C, about 100 °C below the first peak of the dolomite standard (Triassic of Southern Italy, 800 °C). The other endothermic peaks are compatible with the second peak of the dolomite standard (900 °C). The samples J125-31 and J125-34 have two "first" endothermic peaks: one is below 700 °C, and is related to the Zn-rich dolomite phases, the other is above 700 °C, and comprehends both Zn-poor and stoichiometric dolomites. The other peaks, which are around 900 °C, can be considered compatible with those of the standard dolomite.

Metallurgy

After Woollett et al. (2002), the Jabali process flowsheet consisted of five main unit operations: ore crushing and screening, grinding and classification, desliming, lead/silver concentrate production, and zinc concentrate production. The concentrate production stages are very important, because determine the final recovery of the metals. Lead sulfide and carbonate minerals would have been recovered together using a mixture of xanthate, carbonate and clay dispersant and sulfidization reagents. Silver associated with lead would also have been recovered in this step. Zinc oxide minerals (predominately smithsonite) should be selectively recovered from dolomite using a reagent mixture consisting of primary amine acetate, xanthate, carbonate and clay dispersant and sulfidization reagents. The final product is pure zinc oxide. Zinc recovery was estimated around 83%.

Grist (2006) refers to this hydrometallurgical process, with the name of "LTC technology" (leach-to-chemical). He confirms that the method using ammonia-based solutions has a substantial major convenience than the classical leaching in dilute sulfuric acid.

The particularity of the method is the selective recovery of the zinc contained in smithsonite and hydrozincite, and the absence of interaction between the chemical solutions and the dolomite gangue. As mentioned above, it has proven impossible to increase the recovery above ~80%, especially in those samples bearing a low metal grade (Fig. 3.2). From the mineralogical study, it was clear that this incomplete recovery is related to the occurrence of part of zinc in the dolomite, which is very abundant especially in the low-grade samples.

Conclusions

The study sheds new light on many characteristics of the Jabali primary and secondary mineralization and on the related genetical mechanisms.

Our limited researches on the genesis of primary sulfide ores support the hypothesis of Al Ganad et al (1994) of a MVT mineralization *sensu lato*. However, we discard the idea of the above authors of a Jurassic paleokarst-hosted ore deposit: the hydrothermal circulation causing the MVT mineralization could have been instead related to extensional tectonics and fluid motion, associated with petroleum migration within the Sab'atayn basin (Cretaceous).

Smithsonite is the most abundant and economic ore mineral in the secondary deposit, and occurs in two main phases: Smithsonite 1, which replaces host dolomite and sphalerite, and Smithsonite 2, which occurs as cements and concretions. It is clear that the replacement of the host rock at Jabali was developed throughout several stages: the alteration process starts with a partial replacement of Mg by Zn in the dolomite lattice, and continues with gradually higher substitution of Mg by Zn, up to smithsonite formation. Zn-dolomite appears to be an intermediate substitution phase between dolomite and smithsonite.

The Jabali smithsonites have variable $\delta^{18}O$ compositions in different parts of the orebody. The measured values are generally lower than those of other supergene smithsonites, whereas the C-isotope composition is in the same range of values of supergene smithsonites from other nonsulfide ores (Gilg et al., 2008). The $\delta^{18}O$ values of smithsonite could indicate: a precipitation from a low-temperature hydrothermal system, similarly to the Angouran

nonsulfide deposit (Boni et al., 2007), or a supergene precipitation from waters with variable O-isotope composition.
The C-isotope composition is typical of supergene nonsulfide Zn deposits (Gilg et al., 2008), and is interpreted as a result of mixing between host rock carbonates and soil/atmospheric CO_2 but, in the case of a hydrothermal genesis at low-temperature, it could also indicate the involvement of meteoric-surficial water in a deep, thermal circulation, or organic values of carbon not related to soils, e.g. organic matter in black shales.
The replacement of part of Mg with Zn in the dolomite host rock has many implications on the economic evaluation of the deposit. In fact, considering that the LTC-metallurgical process chosen for the Jabali deposit is mineralogically specific, and recovers selectively smithsonite and hydrozincite discarding the other phases, as dolomite, the Zn contained in the latter currently represents a non-recoverable phase. This "concealed" zinc at Jabali reaches discrete amounts, up to several percents. The mineralogical study shows how widespread this process may be, and the importance of understanding the extent of its occurrence in the exploration of dolomite-hosted nonsulfide ores.
As in many other nonsulfide Zn deposits (Boni et al., 2011), at Jabali it is extremely difficult to define with quantitative diffractometric methods alone the zinc contained in phases like Zn-dolomites, instead of that contained in the better-known nonsulfide Zn-minerals, like smithsonite, hemimorphite or hydrozincite. The DTA and QEMSCAN® analytical methods can show immediately if the chosen samples contain significant amounts of Zn-dolomite, mixed to stoichiometric dolomite. Further developments of both methods could bring to a quantitative evaluation of the Zn-dolomite (and hence of the so far non-extractable metal), as well as other unwelcome components contained in the ore.

CHAPTER 4:
THE YANQUE Zn-Pb NONSULFIDE DEPOSIT (PERU)

Introduction

The Yanque nonsulfide Zn-Pb deposit (inferred resources 12.5 Mt @ 3.5% Zn and @ 3.7% Pb, www.zincoremetals.com) (Fig. 4.1), is located in the "Accha-Yanque Belt" (Boni et al., 2009), about 90 km southwest of the city of Cuzco (southern Peru). This area, comprising many Zn- and Pb-mineralized sites, is located within the Andahuaylas-Yauri province (Perelló et al., 2003). The Yanque deposit is currently under exploration by Zincore Metals Inc. and First Quantum Minerals, as the Accha nonsulfide zinc (Boni et al., 2009) and the Dolores Cu-porphyry deposits nearby.

The Andahuaylas-Yauri province covers an area of approximately 25,000 km^2 in southern Peru and extends for 300 km between the localities of Andahuaylas in the northwest and Yauri in the southeast. The belt hosts numerous porphyry copper and porphyry-related skarn deposits, spatially and temporally associated with the middle Eocene to early Oligocene (~48-32 Ma) intrusion of the homonymous batholith into the sedimentary successions of Mesozoic age (Perelló et al., 2003). The largest deposits of the belt include the large clusters of Tintaya and Las Bambas (Zweng et al., 1997; Guillen et al., 2012), as well as the isolated deposits of Los Chancas, Haquira, Alicia, Cotabambas and Costancia (Perelló and Posso, 2011).

The "Accha-Yanque Belt" covers the area surrounding the northern part of one of the apophyses of the Andahuaylas-Yauri batholith, north of the Santo Tomás town, and extends between the Accha and Yanque sites (Boni et al., 2009). Since many years this district has been explored for Zn-Pb mineralizations: among others, the Accha and Yanque prospects have the biggest potential so far (www.zincoremetals.com). The Dolores Cu-Mo-(Au) porphyry body was discovered in 2008, 2 km east of Yanque. The Alicia Cu-porphyry deposit (Strait Minerals Inc., Moss et al., 2012) is located 15 km to the north of Yanque.

Fig. 4.1. View of the Yanque site and mine camp, looking north.

The Yanque deposit occurs within a sort of base metal mineralized district, extended for about 20 km^2, centered on the Dolores porphyry copper, and completed by other two small Zn-Pb mineralizations (Yanque East and Puyani), which occur less than a kilometer on the east and northeast of the same porphyry. Owing to the location of the Yanque deposit, at very close contact with the intrusive rocks of the Yauri batholith, the primary sulfide bodies have been considered a distal product of a magmatic-related mineralization event (Mondillo et al., 2010). However, their possible relationships with the near Cu-porphyry (Dolores), similarly to the well-known "porphyry-related polymetallic mineralizations" (Bendezù and Fontboté, 2009), have been never directly investigated. This class of deposits is generally characterized by a metal zonation at the district/deposit scale, with Cu-rich cores, and Zn-Pb- outer bands. Lead and zinc occur in epithermal veins, or as manto-chimney carbonate replacement bodies, and are described as Cordilleran, Butte-type, or high- and/or intermediate sulfidation epithermal deposits, related to the late stages of porphyry copper systems (Meyer et al., 1968; Guilbert and Park, 1986; Bartos, 1989; Bendezù and Fontboté, 2009; Sillitoe, 2010; Catchpole et al., 2011).

In this chapter, I will report about the setting of the Yanque deposit, in the general frame of the geological evolution of the whole district, followed by a detailed mineralogical and petrographic description of the nonsulfide ores on site, which currently represent the economic concentrations at Yanque. A thorough geochemical investigation, which includes lead- and sulfur isotope analyses, has been carried out in order to complete the genetic background of the primary and secondary mineralization. The spatial and geochemical relationships between the Yanque sulfide-nonsulfide deposit and the Dolores Cu-porphyry have been also investigated, to confirm the possibility that the Yanque primary deposit is a "porphyry-related mineralization", genetically related to the Dolores Cu-porphyry.

The Andahuaylas-Yauri district, with respect to the geological setting and mineralization of the Andes of Peru

The Andahuaylas-Yauri belt is located in southern Peru, at a distance of 250-300 km from the Peru-Chile trench, in the northern part of the so-called "Central Andean Orocline". The Central Andean Orocline is a segment of the Central Andes, set between ~13°S and 28°S, characterized by the thickest continental crust of any subduction zone worldwide (>70 km), and extending over southern Peru, Bolivia, northern Chile, and northwestern Argentina (width locally >850 km) (James, 1971; Beck et al., 1996; Yuan et al., 2002).

The Andes are considered as an exceptional example of an orogen produced by subduction of an oceanic plate beneath a continental margin (Jaillard et al., 2002). This orogenic belt is generally subdivided in three major geological provinces: Northern, Central, and Southern Andes (Gansser, 1973).

The Northern Andes consist of oceanic terranes accreted during Mesozoic and Tertiary (Mégard, 1987; Jaillard et al., 2002, and references therein). As result, the Western Cordillera of Colombia and Ecuador is mainly constituted of oceanic rocks, related to ophiolite obduction, with important penetrative deformation and metamorphism (locally up to the blueschist facies) (Kellogg and Vega, 1995; Spikings et al., 2001).

The Central Andes form the largest and most mountainous segment of the Cordillera. This segment is subdivided into the northern Central Andes (5°30'- ~13°S; entirely located in Peru), the Central Andean Orocline (~13-28°S; in southern Peru, Bolivia, northern Chile, northwestern Argentina), and the southern Central Andes (28-37°S; in central Chile and west-central Argentina) (James, 1971; Beck et al., 1996, Yuan et al., 2002).

The boundaries of the Central Andean Orocline coincide with those of the Central Active Volcanic Zone (Stern, 2004), which coincides with the segment of the belt represented by southern Peru and northern Chile, characterized by a normal subduction regime (Cahill and Isacks, 1992). The northern part of the Central Andean Orocline, to which the Andahuaylas-Yauri belt belongs, marks the boundary between the normal subduction zone and a flattening zone of the subduction, corresponding to the north-central Peru (Cahill and Isacks, 1992).

In the transversal structure of the Central Andean Orocline is possible to recognize (Fig. 4.2): 1) a forearc zone, corresponding to the Pacific slope and offshore areas; 2) an arc zone, represented by the present chain, constituted by the Coastal Cordillera (Coastal Peruvian belt), and the so-called "Western Cordillera" and "Altiplano"; 3) a back arc area, which includes the "Eastern Cordilleras" and the subandean zone underlain by foreland basins (Jaillard et al., 2002).

The Coastal Cordillera consists of Proterozoic and Paleozoic metamorphic rocks, intermediate-to-basic Jurassic-Cretaceous magmatites, and of the Cretaceous-Paleocene Coastal Batholith (Wörner et al., 2000; Roperch et al., 2006). The Western Cordillera corresponds to the Cenozoic magmatic arc. The Altiplano (14-21°S) corresponds to a series of internal basins, mostly filled with gently deformed Cenozoic synorogenic sediments and volcanics (Allmendinger et al., 1997). The Eastern Cordillera, a doubly vergent belt, mainly consisting of Precambrian crystalline rocks and Paleozoic sedimentary and igneous lithologies, whose deformation was active until late Miocene, represents the eastern

boundary of the Altiplano (Benavides-Cáceres, 1999). Mesozoic sediments, deposited in extensional basins coeval with active oceanic subduction, are widespread along the entire sector of the Central Andes (Jaillard et al., 1990; Flint et al., 1993; Parnaud et al., 1995; Ramos and Alemán, 2000; Jaillard et al., 2002). In the Peruvian Coastal Cordillera, western Altiplano and along the Chilean Precordillera north of 22°S, Proterozoic mafic basement rocks outcrop discontinuously: these are collectively known as the "Proterozoic Arequipa terrane" or the "Arequipa massif" (Tosdal, 1996; Wörner et al., 2000; Loewy et al., 2004).
The main tectonic shortening, initiated at ~30 Ma and observed in the Central Orocline, is considered the main cause of the imposing crustal thickening (Isacks, 1988; Gregory-Wodzicki, 2000; Garzione et al., 2008; Sempere et al., 2008). The main uplift of the chain is documented to have happened between ~10 and 6 Ma (Garzione et al., 2006, 2007; Hartley et al., 2007; Sempere et al., 2008), but the reason of this rapid event is still matter of controversy (Husson and Sempere, 2003; Garzione et al., 2006, 2007, 2008; Mamani et al., 2010).

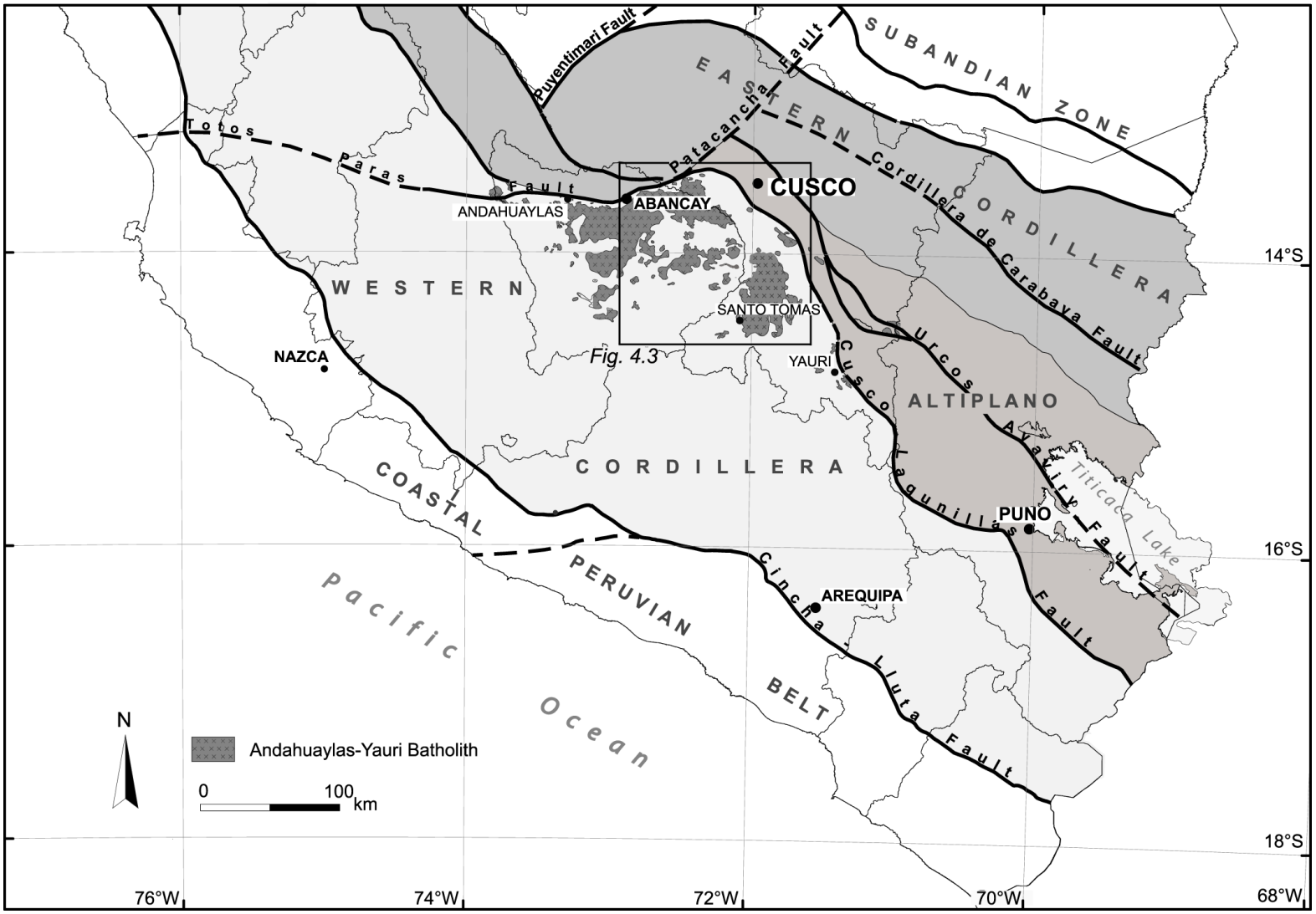

Fig. 4.2. Morphostructural map of southern Peru (Carlotto, 2013, modified).

The Andahuaylas-Yauri belt encompasses parts of the intermontane depressions between the Eastern and the Western Cordilleras and the northern extremity of the Altiplano (Carlier et al., 1996; Chávez et al., 1996). The region is characterized by a rugged, mountainous topography where ranges and snow-capped peaks above 4,500 m are incised by deep (>2,000 m) and steep-sided canyons. These canyons constitute the main drainage system of the region and include the Santo Tomás, Urubamba, Apurímac, Vilcabamba, Mollebamba, and Antabamba rivers, all of which drain toward the Amazon basin (Perelló et al., 2003) (Fig. 4.3).

The stratigraphy of the region is made up of Jurassic and Cretaceous sedimentary successions (Fig. 4.4A). From the older to the younger deposits, these successions consist of early Jurassic limestone, and of middle-to-late Jurassic quartzarenite and shale of the Lagunillas and Yura Gps. (Soraya Fm.), passing upward to the siliciclastic sediments of the Mara Fm. (upper Jurassic-early Cretaceous), and to the massive micritic limestone and black shale of the Ferrobamba Fm. (early-middle Cretaceous) (Marocco, 1978). This Mesozoic succession was deposited in a palaeogeographic setting characterized by two main basins (Fig. 4.4B): the Western (Arequipa) and Eastern (Putina) Peruvian basins, separated by the Cuzco-Puno basement high (Vicente et al., 1982; Carlotto et al., 1993; Jaillard and Soler, 1996). The Mesozoic rocks are unconformably overlain by the sedimentary deposits of the San Jerónimo Gp. (Eocene-early Oligocene), deposited in fluvial to pull-apart basin environments, and by the dominantly volcanic Anta Fm. (Eocene-early Oligocene) (Carlotto, 1998; Perelló et al., 2003, and references therein).

The late Oligocene to Miocene sedimentary deposits of the region include the Punacancha and Paruro Fms. In the latter formations, the sedimentation is interpreted to have taken place in a fluvial environment of braided rivers, flood plains and alluvial fans merging in structurally controlled basins (Carlotto et al., 1996a, 1997). The Oligocene and Miocene volcanic rocks are largely dominated by the calc-alkaline sequences of the Tacaza (Oligocene) and Sillipaca (Miocene) Gps. In addition, small shoshonitic volcanic centers of Pliocene to Quaternary age occur in the region (Wasteneys, 1990; Carlier et al., 1996; Carlotto, 1998).

The large igneous bodies -known as the Andahuaylas-Yauri batholith- intruded the above described succession in a period ranging between Eocene and early Oligocene (~48-32 Ma) (Carlier et al., 1989; Perelló et al., 2003). The batholith consists of a multitude of intrusions that crop out discontinuously for more than 300 km between the towns of Andahuaylas in the northwest and Yauri in the southeast (Perelló et al., 2003). The early-stage intrusions of cumulates (gabbro, troctolite, olivine gabbro, gabbro-diorite and diorite) are followed by magmatic rocks of intermediate composition (monzodiorite, quartz diorite, quartz monzodiorite, and granodiorite). Subvolcanic rocks of dominantly granodioritic/dacitic composition, locally associated with porphyry style mineralization, represent the terminal stage of the magmatic activity in the area (Perelló et al., 2003).

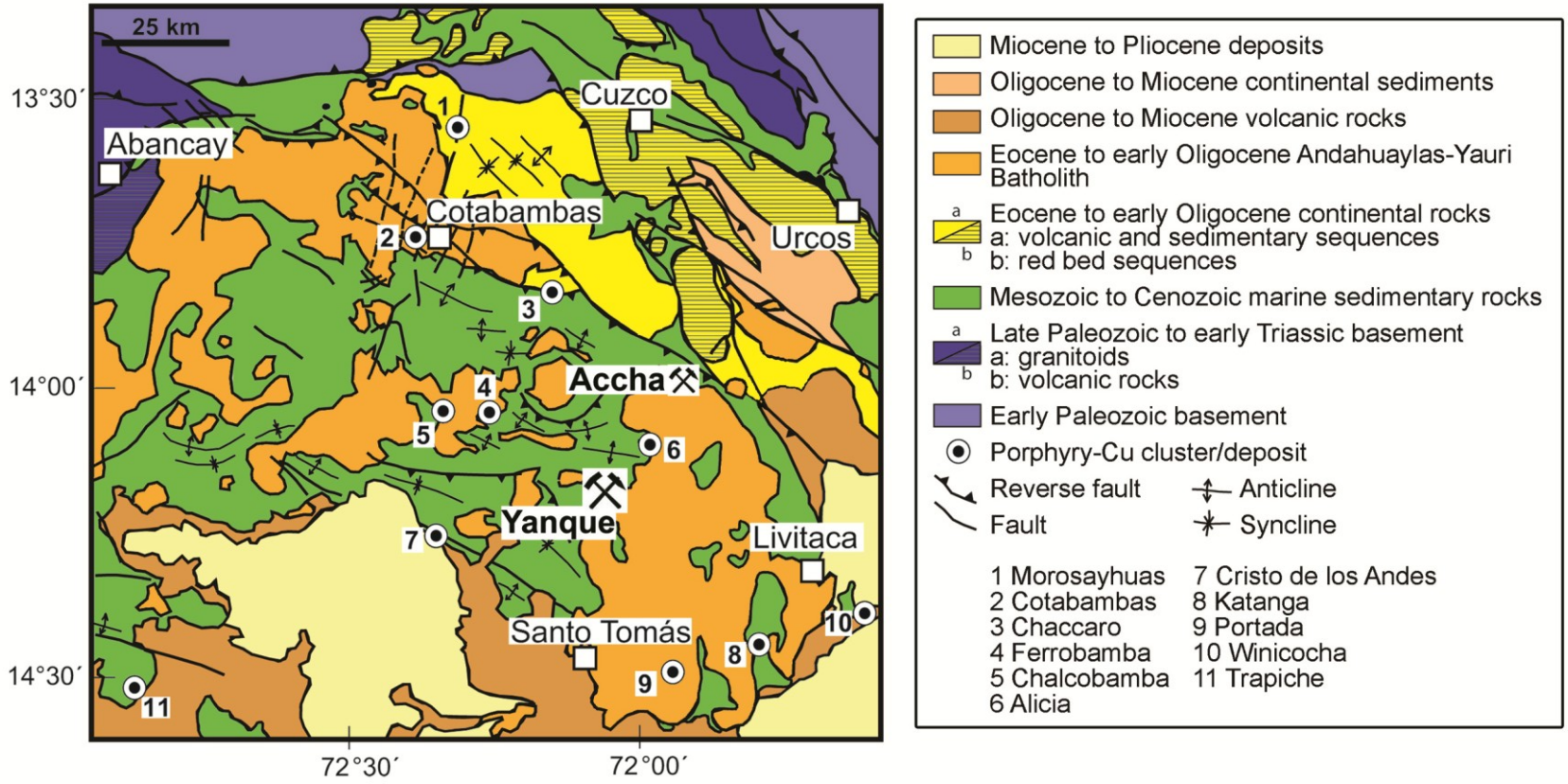

Fig. 4.3. Geological map of Andahuaylas-Yauri belt, with the location of the Yanque deposit (from Perelló et al., 2003, modified).

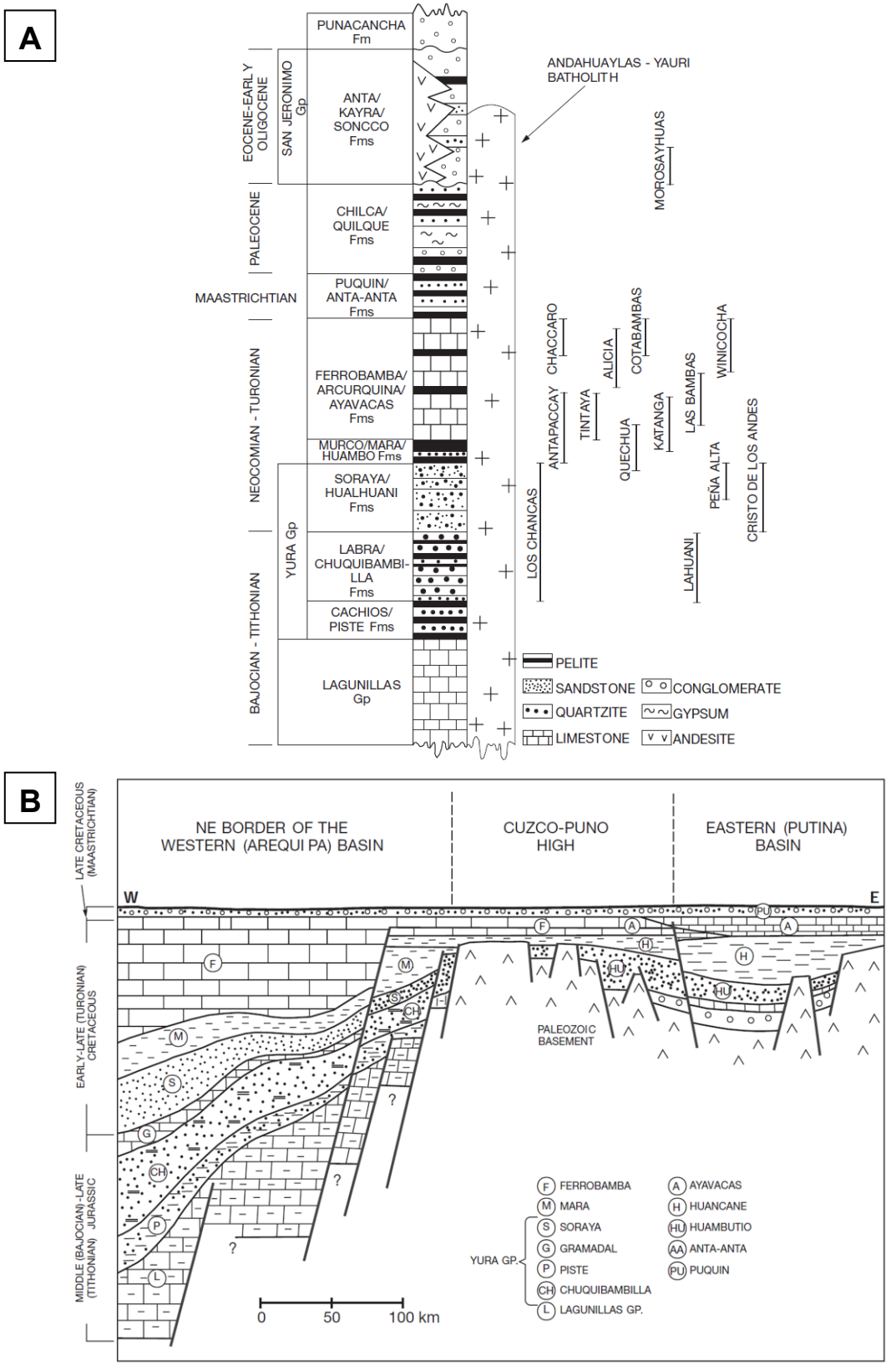

Fig. 4.4. A) Stratigraphy of the Andahuaylas-Yauri belt (Perelló et al., 2003); Cu-porphyry deposits are positioned in correspondence of the relative sedimentary host rock. B) Schematic palaeogeographic reconstruction of the backarc basin of southern Peru during Mesozoic and early Cenozoic (Perelló et al., 2003).

The main part of the Andahuaylas-Yauri region has been affected by several late Cretaceous to Pliocene tectonic events (Marocco, 1975; Pecho and Blanco, 1983; Cabrera et al., 1991; Carlotto et al., 1996b), of which the Eocene to early Oligocene (Incaic) and Oligocene to Miocene (Quechua) pulses are the most important (Perelló et al., 2003). The Incaic pulse is broadly synchronous with the Incaic Orogeny of central Peru (Noble et al., 1974, 1979; Mégard et al., 1984; Mégard, 1987; Farrar et al., 1988; Sébrier et al., 1988; Sébrier and Soler, 1991), and is thought to have been the most important compressive deformation event in the region (Perelló et al., 2003). The deformation was mainly northeast-directed; it was responsible for the development of the basins that accommodated the middle Eocene to early Oligocene volcano-sedimentary products and for the reactivation of older, basin-bounding structures (e.g. Cusco-Puno high) into major high-angle reverse faults that favored the uplift of the Andahuaylas-Yauri batholith (Carlier et al., 1996; Carlotto, 1998; Perelló et al., 2003). Several distinct deformation events with associated shortenings and uplifts have been recognized: they may have marked the various emplacement phases of the Andahuaylas-Yauri batholith (Perelló et al., 2003, and references therein).

More than thirty deposits and prospects with Cu-porphyry style alteration and mineralization occur in the Andahuaylas-Yauri belt. They are also associated with hundreds of small occurrences of magnetite-bearing, skarn-type Fe-Cu bodies (Perelló et al., 2003). The largest deposits of the belt include the clusters at Tintaya and Las Bambas (Zweng et al., 1997; Guillen et al., 2012). Only part of these primary orebodies in the belt have been affected by supergene alteration, and the secondary metal enrichments are of variable importance (Perelló et al., 2003). Supergene processes in the Andahuaylas-Yauri belt are thought to have taken place predominantly during Pliocene, on the basis of the following evidences: a) the immature nature of the chalcocite blanket on top of the primary copper mineralizations; b) its geometry subparallel to recent and present-day topographic features; c) the K-Ar age of 3.3 ± 0.2 Ma (upper Pliocene), measured on the supergene alunite at the Cotabambas porphyry copper-gold deposit (Perelló et al., 2003; Boni et al., 2009; Perelló and Posso, 2011). However, it is possible that the full spectrum of enrichment ages in this ore province may not have been detected yet (Hartley and Rice, 2005), because the relationships between supergene profiles and the development age of several pediplain surfaces is not well constrained.

In the Andahuaylas-Yauri region, porphyry-related polymetallic deposits have never been described. In the central and northern Peru, instead, many examples of this kind of deposits have been identified (e.g., Quiruvilca, Noble and McKee, 1999; Yauricocha, Alvarez and Noble, 1988; Magma, Manske and Paul, 2002; Cerro de Pasco, Baumgartner et al., 2008; Colquirirca, Bendezú and Fontboté, 2009; Morococha, Catchpole et al., 2011). Sillitoe (2010), in a review on the porphyry Cu systems, summarizes the different types of wall-rock hosted polymetallic deposits alongside porphyry Cu orebodies. Several types are mentioned, which display a well-documented zonation: 1) proximal Cu ± Au, and distal Au and/or Zn-Pb skarns; 2) distal carbonate-replacement (chimney-manto) massive sulfide bodies, dominated either by Cu, or Zn, Pb, Ag ± Au, beyond the skarn front; 3) sediment-hosted (distal-disseminated) Au concentrations on the fringes of the system. These systems are thus

characterized by Cu ± Mo ± Au cores and by km-scale halos, defined by anomalous Zn, Pb, Ag, and Mn values, which reflect lower temperature hydrothermal conditions (generally associated with propylitic, but also phyllic- alteration). Beyond these halos, Au-As ± Sb zones may have been developed (Sillitoe, 2010, and references therein). After Sillitoe (2010), the base and precious metal porphyry-related wallrock-hosted deposits form during the late evolution stages of a porphyry Cu system, from the same magmatic fluids involved in the porphyry Cu alteration and mineralization.

The relationship between the isotopic composition of Andean magmatic and ore leads has been summarized for the first time by Macfarlane et al. (1990), who suggested, on the base of Pb-isotope geochemistry that Andean ore deposits are mixtures of mantle and crustal sources, reflecting distinct geological provinces. Following this concept, they subdivided the central Andean Cordillera of Peru, Bolivia, northwestern Argentina, and northern Chile into three main provinces, based on the age and dominant geology of the exposed rocks. *Province I* comprises the coastal volcanic arc, the Jurassic-early Tertiary coastal batholith complex and related volcanic rocks of the Western Cordillera and coastal belt. Based on the differences occurring in the isotopic composition of ore lead, this province has been further subdivided into subprovince Ia, comprising the coastal volcanic belt of northern and central Chile, subprovince Ib, located in central Peru north of 13°S, and subprovince Ic, situated in southern Peru and northernmost Chile between 19°S and 13°S. *Province II* comprises the Jurassic and Cretaceous sedimentary belt that dominates the geology of the high Andes of Peru. *Province III* comprises the Eastern Cordillera of southeastern Peru, central Bolivia and northwestern Argentina, made up mainly of early Paleozoic clastic sediments. Due to the different isotopic characteristics of ore lead, this province has been further subdivided in two distinct subprovinces: subprovince IIIa in Bolivia and northern Argentina, and subprovince IIIb in southern Peru. Lead of the ores occurring in province I has $^{206}Pb/^{204}Pb$ values ranging from 18.21 to 18.82, $^{207}Pb/^{204}Pb$ from 15.55 to 15.69, and $^{208}Pb/^{204}Pb$ from 38.11 to 38.95. Lead from province II is less variable, with $^{206}Pb/^{204}Pb$ and $^{208}Pb/^{204}Pb$ ratios consistently higher than those measured in province I ores and slightly higher average $^{207}Pb/^{204}Pb$ ratios (Macfarlane et al., 1990). After Macfarlane et al. (1990) ore leads in provinces I and II reflect different degrees of mixing between magmatic, upper mantle-derived lead and crustal sources, incorporated during the ascent of parental magma into the crust. Province III ore leads are much more variable than those of provinces I and II, showing $^{206}Pb/^{204}Pb$ values from 17.97 to 25.18, $^{207}Pb/^{204}Pb$ from 15.51 to 16, and $^{208}Pb/^{204}Pb$ from 37.71 to 40.07 (Macfarlane et al., 1990). The authors hypothesize that province III leads indicate more radiogenic, heterogeneous source regions and suggest that melting of continental crust has played an important role in the genesis of magmas and associated ore deposits in this province.

Kamenov et al. (2002), on the basis on new lead isotope data from the San Cristobal, Pulacayo and Potosí mining districts (Bolivia) have reconsidered the above-mentioned lead isotope provinces, thus identifying a new province that extends from San Cristobal northward across the eastern Altiplano and into southern Peru. This province is coincident with the Arequipa metamorphic basement: it is subdivided into subprovince IVa (southern

Peru), characterized by a relatively minor basement imprint and subprovince IVb (Bolivia), where the basement imprint is much stronger.

Mamani et al. (2008) report the results of several Pb and Nd isotope analyses on metamorphic, intrusive and volcanic rocks of central Andes (13° to 28°S and 75° to 65°W), ranging in age from Proterozoic to Holocene. From these data it could be observed that several distinct domains can be defined for the crust of central Andes from the measured isotopic values. These domains correlate with the compositional crustal structure observable in a 3-D density model, indicating that the measured changes of Pb and Nd isotope compositions of igneous and basement rocks are caused by variable proportions in the crust between lighter and felsic material and dense and mafic one (Mamani et al., 2008). More in detail, based on the above data the authors identify three distinct domains: the *Arequipa domain*, a dominantly mafic Proterozoic terrane accreted to the Gondwana margin (Ramos, 2008), characterized by mainly non-radiogenic Pb isotopes (i.e. $^{206}Pb/^{204}Pb$ ratios between 16.083 and 18.551, $^{207}Pb/^{204}Pb$ ratios between 15.435 and 15.650, and $^{208}Pb/^{204}Pb$ ratios between 37.625 and 38.655), typical of an ancient high-grade terrane, and the *Cordillera domain*, consisting of dominantly felsic terranes amalgamated to the western Gondwana margin (Ramos, 2008), and characterized by radiogenic Pb values (i.e., $^{206}Pb/^{204}Pb$ ratios >18.551, $^{207}Pb/^{204}Pb$ >15.650, and $^{208}Pb/^{204}Pb$ >38.655). The third domain has been identified with the Mesozoic rocks along the Coastal Cordillera, which have $^{206}Pb/^{204}Pb$ ratios comprised between 18 and 19. These isotopic ratios are generally higher than those measured in the Proterozoic basement ($^{206}Pb/^{204}Pb$ = 16.7 to 18.4), on which they are located.

This concept is confirmed by Mamani et al. (2010), in a review on the geochemical variations affecting the igneous rocks of the central Andean orocline (13°S to 18°S). The crustal domains of distinct composition and age have influenced the magma composition through several assimilation grades. In detail, the Pb-isotopic ratios suggest that, in the age interval from late Cretaceous to mid-Oligocene (91-30 Ma) most magmas originated from mantle sources, but were also contaminated by local basements. The assimilation and contamination processes have increased since 30 Ma, marking the major crustal thickening in the Andes (Mamani et al., 2010). This explains why Pb-isotopes of most igneous ore deposits have a markedly “regional” overprint (Macfarlane et al., 1990).

Methods of study and analytical techniques

The geological characteristics of the Yanque deposit have been investigated by careful mapping in the field and outcrop sampling. Structural data have been collected on site; beds and fractures/veins orientation has been plotted on the Schmidt diagram (equal area net, lower hemisphere). The characteristics of the sedimentary and igneous rocks have been defined with the help of the depositional and emplacement models occurring in the existing literature.

A 3D-model of the Yanque orebody, based on the Zn and Pb assays from 124 cores (~7000

samples, Zincore Metals, 2011) has been performed using the Rockware software (by Rockworks). The drillcore data were interpolated with an Inverse-Distance weighting algorithm, which uses a weighted average approach to compute the node values. The method offers user control over the horizontal and vertical weighting of the control points.

Petrographic, mineralogical, and geochemical analysis has been carried out on the samples from cores drilled by the Company between 2008 and 2011 (TABLE 4.1, 4.2), and samples from mineralized outcrops (TABLE 4.3). Most samples are from the supergene nonsulfide concentrations. Other samples have been collected from Dolores, Puyani and Yanque east mineralized sites (TABLE 4.4).

All the samples were cut in small slabs to obtain polished thin sections and crushed for qualitative mineralogical X-ray powder diffraction (XRD) analysis. For polished thin section preparation, the drillcore samples were impregnated with Araldite D and Raku Hardener EH 2950 in a commercial laboratory specialized in soft sediments (OMT, Aosta, Italy). Polished thin sections (~30 μm thick) were then observed under a petrographic microscope, in both transmitted and reflected light mode. The crushed part of the same core samples has been reduced to 1 mm and then fully homogenized; few grams were further pulverized for X-ray diffraction analyses.

XRD analysis was carried out on all samples, with the aim to get information on the bulk mineral assemblages, by means of the following instruments: 1) a Seifert–GE ID3003 diffractometer (Dipartimento di Scienze della Terra, University of Napoli Federico II), with Cu$K\alpha$ radiation, Ni-filtered at 40 kV and 30 mA, 3-80 °2θ range, step scan 0.02°, time 10 sec/step, and the RayfleX (GE) software package; 2) a Philips PW3020 automated diffractometer (XRD) (University of Heidelberg, Germany), with CuKα radiation, 40 kV and 30 mA, 10 seconds per step and a step scan of 0.02° 2θ, and data collection in the range 3-110° 2θ. Semiquantitative XRD analysis was carried out on 40 quarter-drillcore samples (TABLE 4.2).

Specific XRD analyses were performed for the characterization of clay minerals. The <2 μm particle size fraction was separated from the bulk samples by dispersion in water of the fraction <50 μm and centrifugation according to Stoke's law (Moore and Reynolds, 1997). Oriented aggregates were prepared by sedimentation on glass slides and analyzed in air-dried, glycolated and heated at (550°C) forms, from 3 to 40° 2θ, at a step scan of 0.02° 2θ and 1 second counting time (Dipartimento di Scienze del Suolo, della Pianta, dell'Ambiente e delle Produzioni Animali, Facoltà di Agraria, Università di Napoli).

Whole rock chemical analyses of major, minor and trace elements were carried out at the ACME Analytical Laboratories Ltd. Elements were analyzed with a combination of ICP-ES and ICP-MS, following Aqua Regia digestion of the powder samples.

TABLE 4.1. Selected drillcore samples for petrographic study.

Drillcore	Latitude (Y)	Longitude (X)	From (m)	To (m)	Dist	Sample n.
YA-01	8430548.148	815102.886	1.50	1.70	0.20	YA-01-SAM-01
YA-02	8430449.459	815202.285	4.80	5.00	0.20	YA-02-SAM-02
YA-02	8430449.459	815202.285	28.00	28.20	0.20	YA-02-SAM-03
YA-04	8430547.846	815200.105	18.00	18.20	0.20	YA-04-SAM-04
YA-05	8430483.862	815296.536	8.50	8.70	0.20	YA-05-SAM-05
YA-06	8430248.956	815580.456	16.20	16.40	0.20	YA-06-SAM-06
YA-09	8430674.776	815197.482	9.10	9.20	0.10	YA-09-SAM-07
YA-10	8430300.763	815207.083	127.30	127.40	0.10	YA-10-SAM-08
YA-11	8430423.154	815471.235	55.10	55.20	0.10	YA-11-SAM-09
YA-11	8430423.154	815471.235	61.50	61.70	0.20	YA-11-SAM-10
YA-12	8430143.727	815335.208	39.90	40.00	0.10	YA-12-SAM-11
YA-13	8430673.215	815098.867	9.00	9.15	0.15	YA-13-SAM-12
YA-14	8430444.76	815127.262	18.50	18.70	0.20	YA-14-SAM-13
YA-15	8430050.153	815450.71	28.50	28.70	0.20	YA-15-SAM-14
YA-17	8430619.683	815063.941	9.00	9.20	0.20	YA-17-SAM-15
YA-17	8430619.683	815063.941	10.10	10.20	0.10	YA-17-SAM-16
YA-18	8430618.883	815067.58	8.10	8.20	0.10	YA-18-SAM-17
YA-19	8430407.815	815143.904	17.70	17.90	0.20	YA-19-SAM-18
YA-20	8430460.953	815295.439	9.60	9.80	0.20	YA-20-SAM-19
YA-20	8430460.953	815295.439	22.20	22.40	0.20	YA-20-SAM-20
YA-23	8430907.785	815489.874	9.80	10.00	0.20	YA-23-SAM-21
YA-27	8429039.111	816036.489	72.40	72.60	0.20	YA-27-SAM-23
YA-31	8430048.761	815349.656	127.20	127.40	0.20	YA-31-SAM-24
YA-34	8429946.943	815389.435	142.60	142.80	0.20	YA-34-SAM-25
YA-35	8430603.238	815539.953	61.95	62.15	0.20	YA-35-SAM-26
YA-37	8430198.291	815796.956	88.30	88.50	0.20	YA-37-SAM-27
YA-38	8429899.675	815345.763	160.80	161.00	0.20	YA-38-SAM-28
YA-40	8429852.35	815372.322	127.40	127.60	0.20	YA-40-SAM-29
YA-41	8429794.746	815396.968	145.50	145.70	0.20	YA-41-SAM-30
YA-45	8429901.879	815395.936	124.90	125.10	0.20	YA-45-SAM-31
YA-45	8429901.879	815395.936	140.60	140.80	0.20	YA-45-SAM-32
YA-99	8430381.748	815557.147	110.60	110.65	0.05	YA-99-110.65
YA-109	8430293.978	815757.847	149.80	149.85	0.05	YA-109-149.80
YA-109	8430293.978	815757.847	150.20	150.30	0.10	YA-109-150.20
YA-118	8430661.639	815062.719	81.30	81.35	0.05	YA-118-81.35
YA-121	8430337.841	815376.962	43.70	43.75	0.05	YA-121-43.75
YA-128	8430488.449	815451.482	49.30	49.35	0.05	YA-128-49.30
METY-2	8430548.148	815102.886	23.20	23.25	0. 05	METY-2-23.2

TABLE 4.2. Selected drillcore intervals for semiquantitative mineralogical study.

Drillcore n.	Latitude (Y)	Longitude (X)	From (m)	To (m)	Sample n.
DDH-YA-20	8430460.953	815295.439	3.45	4.45	YA-20-3.45-4.45
			5.45	6.45	YA-20-5.45-6.45
			7.45	8.45	YA-20-7.45-8.45
			9.45	10.45	YA-20-9.45-10.45
			10.95	11.45	YA-20-10.45-11.45
			12.45	13.45	YA-20-12.45-13.45
			14.45	15.45	YA-20-14.45-15.45
			16.45	17.45	YA-20-16.45-17.45
			18.45	19.45	YA-20-18.45-19.45
			20.45	21.45	YA-20-20.45-21.45
			22.45	23.45	YA-20-22.45-23.45
			24.45	25.45	YA-20-24.45-25.45
DDH-YA-33	8429999.089	815350.486	119.5	120.5	YA-33-119.5-120.5
			121.5	123	YA-33-121.5-123
			124	125	YA-33-124-125
			126	127	YA-33-126-127
			128	129	YA-33-128-129
			155.1	156.1	YA-33-155.1-156.1
YA-49	8430354.322	815171.062	94	95	YA-49-94-95
			95	96	YA-49-95-96
YA-71	8430556.015	815454.759	14	15	YA-71-14-15
			16	17	YA-71-16-17
			18	19	YA-71-18-19
			20	21	YA-71-20-21
			22	23	YA-71-22-23
YA-82	8430204.951	815382.986	24	25	YA-82-24-25
			26	27	YA-82-26-27
			28	29	YA-82-28-29
			32.3	34.3	YA-82-32.3-34.3
			35.3	36.3	YA-82-35.3-36.3
			37.3	38.3	YA-82-37.3-38.3
YA-117	8430709.6	815113.449	1	2	YA-117-1-2
			3	4	YA-117-3-4
			5	6	YA-117-5-6
			7	8	YA-117-7-8
			9	10	YA-117-9-10
			11	12	YA-117-11-12
			13	14	YA-117-13-14
			15	16	YA-117-15-16
			17	18	YA-117-17-18
			19	20	YA-117-19-20
			22	24	YA-117-22-24

TABLE 4.3. Yanque outcrop samples. Sampling area n. from Fig. 4.5.

Sampling area n.	Sample n.	description
1	YA-OUT-1	Breccia with galena veins
	YA-OUT-2	White clay sample
	YA-OUT-3	Hemimorphite veins
	YA-OUT-7	Quartzite
	YA-OUT-8	Quartzite
	YA-OUT-12	Laminated carbonatic-arenaceous rock
	YA-OUT-13	Sandstone
	YA-OUT-14	Dolomitized limestone
	YA-OUT-15	Very altered sandstone
	YA-OUT-16	Mn crusts
	YA-OUT-17	Oxidized dolomite breccia
	YA-OUT-22	Mn crusts
	YA-OUT-22bis	Crystals in Mn crusts
	YA-OUT-23	Galena stockwork
	YA-OUT-24	Limestone breccia
	YA-OUT-26	Sandstone
	YA-OUT-27	Hemimorphite veins
	YA-OUT-28	Hemimorphite veins
2	YA-OUT-25	Mineralized sample
	YA-OUT-29	Hemimorphite cemented breccia
	YA-OUT-30	Breccia with dolomite clasts
	YA-OUT-31	Breccia with limestone clasts + gypsum
	YA-OUT-33	Diorite/tonalite
3	YA-OUT-4	Porphyry from dyke
	YA-OUT-5	Recent breccia with big igneous clasts
4	YA-OUT-6	Galena veins in diorite
	YA-OUT-32	Cu-oxides
5	YA-OUT-18	Arenaceous-carbonatic rock
	YA-OUT-18bis	Conglomerate
6	YA-OUT-9	Unaltered diorite/tonalite
7	YA-OUT-19	Recrystallized limestone (marble)
8	YA-OUT-10	Very altered sandstone near Dolores porphyry
	YA-OUT-10bis	Very altered sandstone near Dolores porphyry
	YA-OUT-11	Diorite
	YA-OUT-20	Recrystallized limestone (marble)
	YA-OUT-21	Diorite/tonalite
	YA-OUT-34	Limestone
	YA-OUT-35	Diorite

TABLE 4.4. Samples from Dolores, Puyani, and Yanque east. Sampling area n. from Fig. 4.5.

Location	Sampling area n.	Sample n.	description
Dolores deposit	9	DOL-OUT-1	Endoskarn with galena
Dolores deposit	10	DOL-OUT-2	Quartz monzonite
		DOL-OUT-3	Quartz diorite with malachite
		DOL-OUT-4	Quartz diorite with Cu-oxides
		DOL-OUT-5	Quartz diorite with chalcopyrite
		DOL-OUT-6	Quartz veins with pyrite and chalcopyrite
		DOL-OUT-7	Quartz monzonite with Cu-oxides
		DOL-OUT-8	Skarn with Cu-oxides
Dolores deposit	11	DOL-OUT-9	Skarn with Cu-oxides
		DOL-OUT-10	Magnetite skarn
Dolores deposit	out of map	DOL-OUT-11	Skarn with calcocite
Dolores deposit		DOL-9-84.10	Galena vein
		DOL-10-446.50	Pyrite and chalcopyrite veins
Puyani	out of map	PUY-1	Barite
		PUY-2	Gossan sample
Yanque East	Yanque East	YA-EST-1	Gossan sample
		YA-EST-2	Gossan sample

Secondary electron imagining by scanning electron microscopy (SEM) on the thin sections was carried out with a Jeol JSM 5310 (CISAG, Università di Napoli, Italy) and with a Jeol JSM 5900LV (Natural History Museum of London, UK). Element mapping and qualitative energy-dispersive (EDS) spectra were obtained with the INCA microanalysis system (Oxford Instruments detector). Wavelength dispersion spectrometry (full WDS) was used to determine the chemical composition of selected samples, by a Cameca SX50 electron microprobe operating at 15 kV, 15 nA, and 10 μm spot size (Natural History Museum of London, UK). Silicates, oxides, and pure elements were used as standards.

Sulfur isotope analyses of both sulfides and sulfates were carried out at Actlabs (Ancaster, Ontario, Canada). Single crystals and mineral fragments for analysis were collected with a dental drill from the core and outcrop samples. Pure $BaSO_4$ and sulfide samples were combusted to SO_2 gas under $\sim 10^{-3}$ tor of vacuum. The SO_2 was inlet directly from the vacuum line to the ion source of a VG 602 Isotope Ratio Mass Spectrometer (Ueda, 1986). Quantitative combustion to SO_2 was achieved by mixing 5 mg of sample with 100 mgs of a V_2O_5 and SiO_2 mixture (1:1). The reaction was carried out at 950˚C for 7 minutes in a quartz glass reaction tube. Pure copper turnings were used as a catalyst to ensure conversion of SO_3 to SO_2. Internal Lab Standards ($SeaWater_{BaSO4}$ and $Fisher_{BaSO4}$) were run at the beginning and at end of each set of samples and were used to normalize the data as well as correct for any instrument drift. All results are reported in the permil (‰) notation relative to the

international CDT standard. Precision and Reproducibility using this technique is typically better than 0.2 permil (n = 10 Internal Lab Standards).
Lead isotope analyses of sulfides, pure minerals, and igneous and sedimentary rocks were performed using a Nu Instruments™ multicollector inductively coupled plasma mass spectrometer (MC-ICP-MS) at the Laboratory of Isotope Geology at the University of Bern. The samples were dissolved in Aqua Regia and purified using the Sr•Spec™ cation exchange resin according to the procedure by Villa (2009). All samples were spiked with thallium for correction of the mass bias. The measured values of NIST SRM 981 compare favourably with those reported in the literature, thus, further bias corrections ware not necessary. The errors indicated for individual analyses are calculated as the square root of the square in-run error plus the square of the dispersion of the standard measurements for the corresponding day of analysis.

Yanque-Dolores district geology

The Yanque nonsulfide deposit (14° 10'S latitude, 72° 04'W longitude; Fig. 4.5) covers an area of about 900 by 500 m, striking in a NW direction, at an altitude of 3,500-3,600 m.s.l. The area of the deposit consists of a NW-SE elongated, relatively flat hill, bordered on the west side by a deep (~1000 m) and steep valley, drawn in the same direction in which the Rio Santo Tomás runs. On the eastern side of the site, instead, a mountainous area with high relief variations occurs, which extends for about 5-8 km and reaches a maximum height of 4,550 m.s.l., grading to a wide plateau. The northern part of the area is still bordered by the valley of the Rio Santo Tomás, which turns abruptly from a NW direction towards NE. The southern part is delimited by a Rio Santo Tomás' tributary, named Rio Challamayo.
In the same mineralized district there are two other small Zn-Pb oxidized bodies, called Yanque East and Puyani, located at the east and the north-east boundaries of the area, in correspondence of the break zone between the mountainous range and the altiplano.
The recently discovered Dolores Cu-porphyry deposit is located 1.5 km east of Yanque, on the northern flank of the Rio Challamayo valley.
In the Yanque-Dolores area both sedimentary and igneous lithologies occur (Fig. 4.5, 4.6). The sedimentary lithologies belong to the Soraya, Mara and Ferrobamba Fms. They are limited on the east by one of the largest apophyses of the Yauri batholith, and on the south by the intrusive rocks hosting the Dolores mineralization.

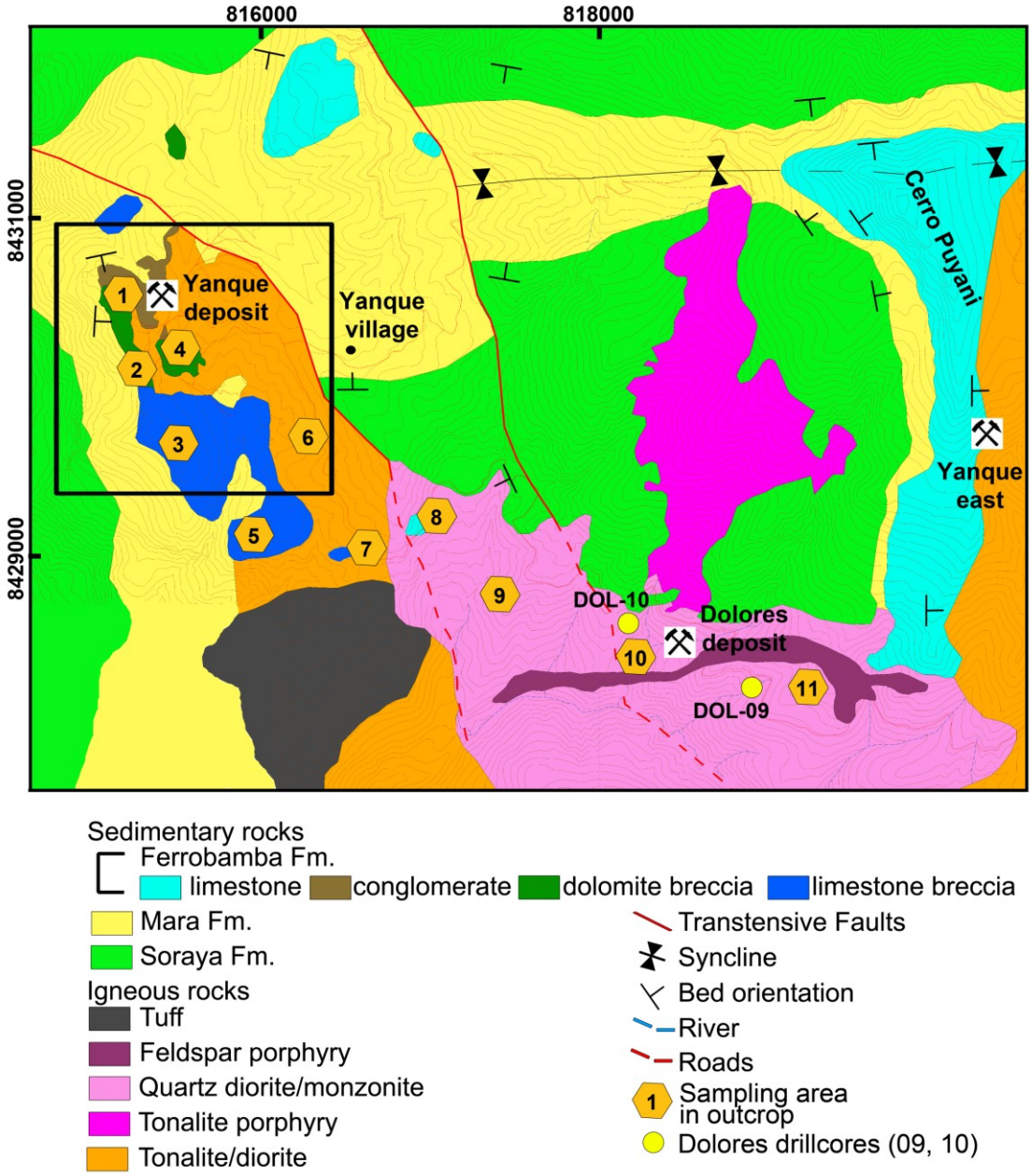

Fig. 4.5. Geological map of the Yanque-Dolores ore district (from Zincore Metals Inc., modified). The area in the black square is enlarged in Fig. 4.10.

Sedimentary rocks

The Soraya Fm. (upper Jurassic-lower Cretaceous) has been described by Pecho and Blanco (1983) as a monotonous succession of medium-fine grained quartzite and quartzarenite, with minor shale and siltstone interbeds. In the same study, the Mara Fm. (Aptian) has been subdivided in three members: a lower member characterized by abundant sandstone, a middle one consisting of siltstone with sandstone and conglomerate interbeds, and a higher member made of sandstone and siltstone, passing upward to limestone. The Ferrobamba Fm. (Albian-Cenomanian) consists, instead, of a monotonous succession of black-grayish alternated massive and laminated limestone, with dolomite levels and chert nodules (Pecho and Blanco, 1983).

The Soraya Fm. outcrops in the northern part of the mineralized district, along the southern flank of the Rio Santo Tomás valley, around the porphyritic intrusions, at the base of the eastern flank of the Rio Santo Tomás valley, and on the western side of the Yanque minesite. This Fm. passes discontinuously upward to the Mara Fm. (Pecho and Blanco, 1983). The latter has a variable thickness throughout the whole district and, as the overlying Ferrobamba Fm., shows lateral heteropies that can be observed when comparing the sedimentary facies in the two sections of Cerro Puyani and Yanque.

At Cerro Puyani, the Mara Fm. consists of a sequence of sandstone and siltstone, with a total thickness of ~150 m, occurring as well-laminated dm-beds (Fig. 4.6). A quartzarenite interval, which reaches a total thickness of ~20 m and represents a stratigraphic marker, occurs here in the middle of the Formation. The Ferrobamba Fm. consists here of a monotonous succession of dark gray-light gray limestone, occurring both as massive and laminated beds with chert nodules, and dolomite interbeds (Fig. 4.7A). Mud cracks, and abundant remnants of evaporitic minerals have been currently observed. In the Yanque site the lower part of the Mara Fm., directly overlying the Soraya Fm. is very similar to that observed at Cerro Puyani. This part of the succession consists essentially of sandstone and siltstone (total thickness of about 150-200 m), and is concluded by a quartzarenite interval, analogous to that of the Cerro Puyani section. The overlying lithologies consist, instead, of a multiform sedimentary breccia, showing lateral facies variations from north to south. In the area of the nonsulfide deposit (west of the Yanque village), the sedimentary breccia occurs in form of a siliciclastic conglomerate, characterized by rounded to subangular, cm-sized clasts. The texture varies from clast-supported to matrix-supported (Fig. 4.7B). The conglomerate is alternated with sandstone/siltstone layers and lenses. Southward, the sandstone intercalations become progressively more frequent and carbonate-enriched. Breccias with angular, yellow-colored, subangular, cm-sized dolomite clasts have been observed instead of the above-described siliciclastic conglomerate (Fig. 4.7C). The Yanque nonsulfide mineralization is hosted in both breccia types.

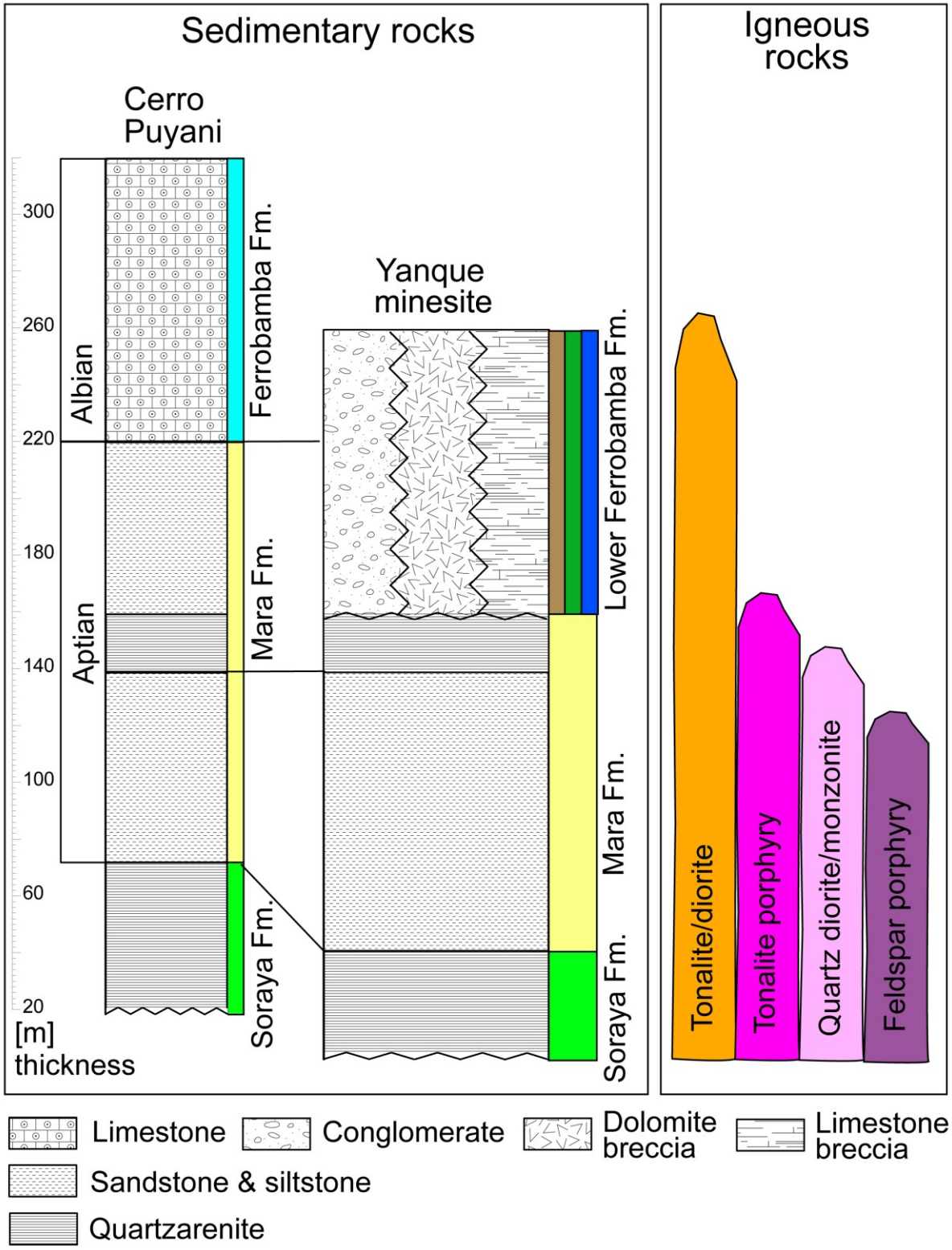

Fig. 4.6. Stratigraphy of the Yanque-Dolores district: correlation between the sections at Cerro Puyani and Yanque minesite. The sedimentary breccia at Yanque is heteropic with the sedimentary interval between the Mara and Ferrobamba Fms. at Cerro Puyani. The Soraya Fm. (Pecho and Blanco, 1983) is represented here only in its uppermost part. Igneous rocks (columns on the right) crosscut the sedimentary successions from the Soraya Fm. up to the Ferrobamba Fm.

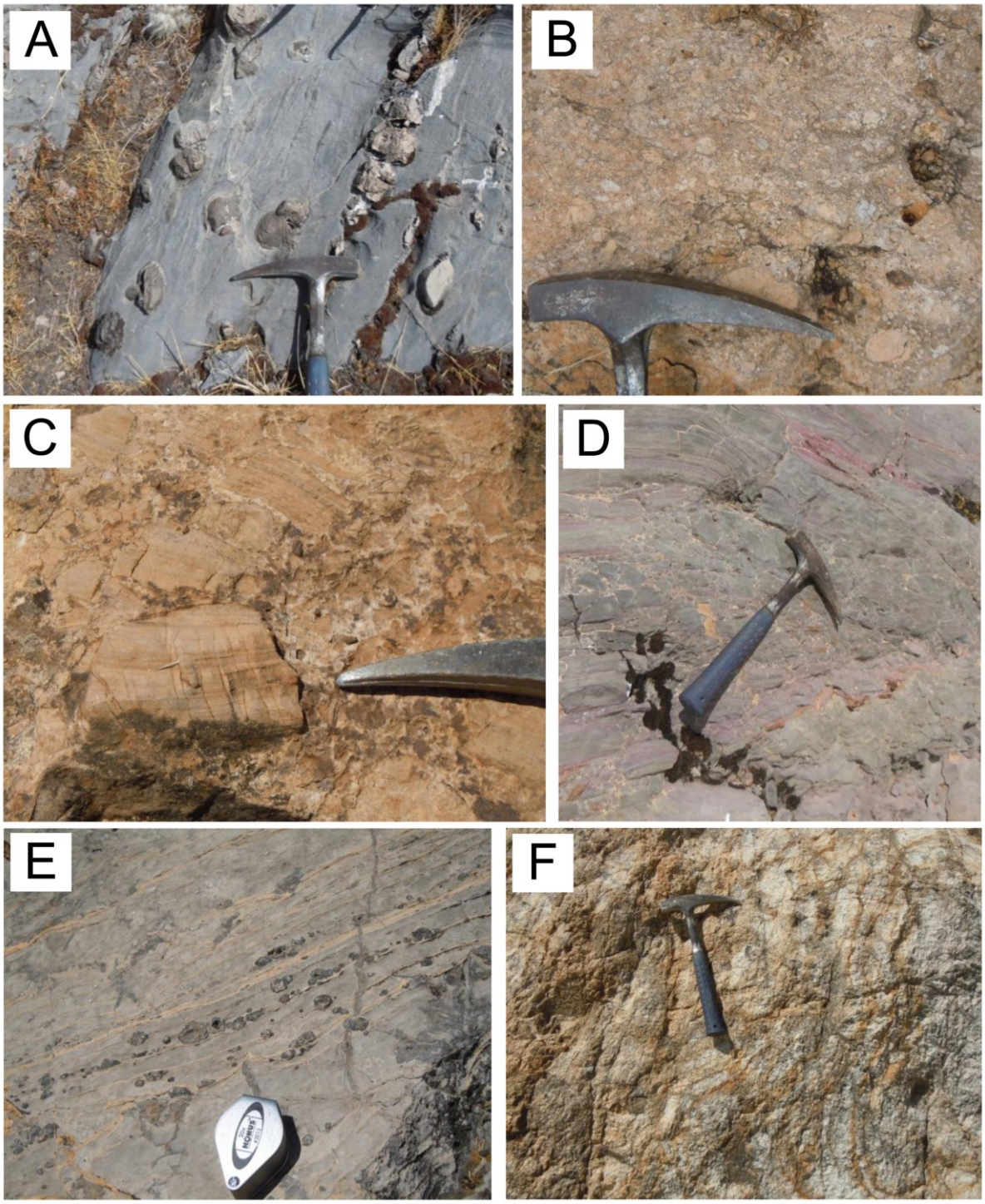

Fig. 4.7. A) Typical limestone facies of the Ferrobamba Fm. at Cerro Puyani. B) Yanque site: siliciclastic conglomerate of the Mara Fm. C) Yanque site: dolomite breccia of the Mara Fm. D) Yanque site: limestone breccia of the Mara Fm. E) Yanque site: pseudomorphs of gypsum/anhydrite concretions within the limestone of the Mara Fm. F) Yanque site: altered tonalite/diorite.

In the southern zone of the Yanque mining site, the sedimentary facies is totally different: here the conglomerate beds are rather scarce, and the dominant lithology consists of limestone breccias (Fig. 4.7D) and limestone packages with imposing slumpings. The limestone breccia clasts are generally angular, and of cm- to dm-size. The matrix is also carbonatic, but can be marly too, and with a reddish color. The limestone breccia is locally dolomitized, with a yellowish patina on the surface. In the laminated carbonate sediments, as well in the breccia clasts several remnants of evaporitic minerals occur (gypsum crystals and anhydrite concretions, Fig. 4.7E). The same facies, consisting of laminated limestone, with slump folds and abundant slump breccias outcrop also on the northwestern side of the mining area (north of the Yanque village), above the sandstone of the Mara Fm.

The Cretaceous depositional environment in southern Peru (Carlotto et al., 1993; Jaillard and Soler, 1996; Sempere et al., 2002; Perelló et al., 2003) is associated with a long-lasting extensional regime, spanning most of the Mesozoic. Three big structures at a regional scale have been reported in literature (Fig. 4.4B): an uplifted horst (Cuzco-Puno High) and two basins, one of them on the east (Putina Basin) and the other on the west (Arequipa Basin) of the Cuzco-Puno High (Vicente et al., 1982; Carlotto et al., 1993; Jaillard and Soler, 1996; Perelló et al., 2003). In this palaeogeographic reconstruction, the depositional areas of the Yanque and Puyani successions were located at the boundary between the Cuzco-Puno High, and the western Arequipa Basin. These areas were subjected to extensive tectonics during the Mesozoic, with the formation of normal faults, dislocating both the basement and the overlying successions. In this setting, the sedimentary rocks occurring at Yanque have the characteristics of a typical sequence deposited as a tectonically-shaped fan delta associated with carbonate deposits (Fig. 4.8).

A similar set of lithologies has been documented, for instance, in the Tertiary sediments along the borders of the Red Sea (Burchette, 1988; Tucker, 2003; Khalil and McClay, 2009), which can be considered a modern-analogue of the depositional environments of the Mesozoic Central Andean rift system (Sempere et al., 2002). In the Red Sea region, it was also possible to observe fossil and active clastic fan delta deposits, interbedded with platform carbonates, accreted during basement normal faulting and basin formation. The erosion of the emerged footwalls creates siliciclastic fan deltas on the basin-bounding fault scarps (Burchette, 1988). The lithologies of these bodies show the typical fan deltas architecture (Wescott and Ethridge, 1990): on the more external “continental” zones, the sediments consist of conglomerate and coarse sandstone, typical of high-energy environments like those characterizing a braid-plain or the upper extremity of braided rivers. In the more internal areas of the basin, fine-grained sediments, which correspond to deep-sea conoid deposits, generally prevail. The transition from subaerial conglomerates to coastal sediments like beach arenites, and then to fine-grained pelites deposited at the base of submarine slopes can be very quick (Burke, 1967; Wescott and Ethridge, 1980, 1990). Carbonate platform deposits onlap on the clastic materials, developing several types of lateral facies heteropies (Burchette, 1988; Khalil and McClay, 2009).

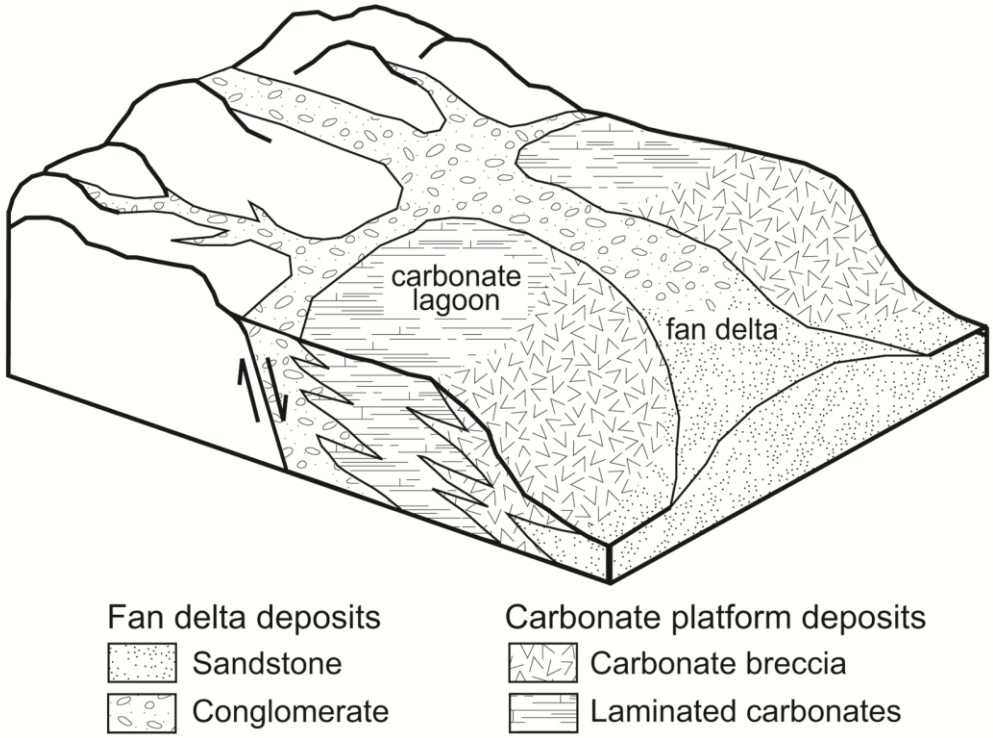

Fig. 4.8. Facies model of clastic-carbonate interaction in recent fan deltas (from Tucker, 2003; Khalil and McClay, 2009 modified).

In case of the Yanque succession, the conglomerate that follows stratigraphically the quartzarenite and pelite of the lower Mara Fm. could be indicative of a fan delta environment subjected to a quick progradation. If we consider a series of basins characterized by growth faults and syntectonic sedimentation along their margins (as it seems to be the case of the depositional environment in this area), unstable fan deltas may develop, subjected to swift progradation after rapid tectonic movements. The observed laminated limestone (early Ferrobamba?) can coexist laterally with the siliciclastic conglomerate. The limestone breccia, outcropping north of the Yanque village and in the southern area of the Yanque mining site, is probably a product of the synsedimentary tectonics affecting the Ferrobamba carbonate platforms. Its characteristics are typical of synsedimentary-syndiagenetically disrupted sediments, deposited along a steep slope of a tectonically active carbonate platform.

Although the sedimentary model discussed above has many constraints, it is necessary also to consider that the boundary interval between the Mara and Ferrobamba Fms. with its carbonate slump folds and breccias, has also many similarities with the characteristics shown by the lithologies described by Callot et al. (2008b, and references therein) as the imposing "Ayabacas Fm.", which occurs in the Arequipa basin. The latter Formation, which should partly correspond to the Ferrobamba Fm. of the Cuzco area, represents the product of a giant submarine collapse of part of the mid-Cretaceous carbonate platform pertaining to a back-arc basin in western Peru. The submarine collapse has been related to a strong tectonic activity of Turonian-Coniacian age (Callot et al., 2008b). The Yanque conglomerates and breccias

could be therefore the result of a similar collapse (on much minor scale than the Ayabacas Fm.), caused by synsedimentary tectonic events.
Around Yanque, the Mesozoic succession is not followed by the Eocene-Oligocene Puno and San Jeronimo Groups (Perelló et al., 2003 and references therein), as at Accha (Boni et al., 2009). This absence is due most probably to several phases of uplift, which have affected the whole area and caused the erosion of the Tertiary lithologies.

Igneous rocks
Several types of igneous rocks occur in the study area (Fig. 4.5, 4.6). As already mentioned, the eastern side of the mining district is bordered by one of the largest apophyses of the Yauri batholith, which extends eastward for some hundreds km^2. In the proximity of Yanque and Dolores, the batholith has a composition variable between a diorite and a tonalite (Fig. 4.7F). Rocks of the same composition occur on the western side of the mining district. They outcrop in the north-south direction for a few kms, between the Yanque site and the Dolores Cu-porphyry deposit.
Magmatic rocks of more acid composition also exist in the area, and cut the previously mentioned diorite-tonalite bodies. In the middle section of the Soraya Fm., in the center of the district, a tonalite porphyry intrusion occurs. South of this intrusion, both a quartz diorite porphyry, and a quartz monzonite porphyry host the Dolores copper mineralization. Some small aplite and andesite porphyry dykes have been also observed in the field and in drillcores at the Yanque site. The magmatic rock suite, which ranges from basic to more acid terms, is similar to that observed in other Cu-porphyry deposits in the area (Perelló et al., 2003).
About 1 km south of Yanque, the Yauri batholith is covered by an ignimbrite tuff of Quaternary age (Pecho and Blanco, 1983).

Structural setting
The area has been affected by strong tectonic movements, resulting in both ductile and fragile deformation. The sedimentary succession is deformed by non-cylindrical folding, in which it is possible to recognize the superposition of at least two sets of deformative events. The first one is characterized by north-verging upright-inclined folds, and should be associated to the Incaic orogeny (Perelló et al., 2003 and references therein). The second is characterized by upright gentle-open folds, with N-S striking axial planes, and subhorizontal fold axes. Part of the deformation could also be related to the emplacement of magmatic plutons and batholiths. The result of the superposition of these deformative events is a complex dome-and-basin interference pattern.
The quartzarenite of the Soraya Fm. is the backbone that controls the main tectonic trends in the whole area. In detail, a big domiform anticlinal structure, with the Soraya Fm. in the nucleus occurs in the middle of the area, and extends southward up to the Rio Challamayo. Part of the nucleus has been intruded by a tonalite porphyry body, which could have partly produced the deformation. This anticlinal structure transforms northward in an east-west

trending syncline, with the Mara Fm. in the nucleus. On the eastern flank of the anticline, corresponding to the locality of Cerro Puyani, the Ferrobamba Fm. carbonates occur. In the carbonate lithologies the superposition of the deformative events results in the formation in the northern part of the crest of the syncline with the Mara Fm., and in the Yanque East area in a steep east-dipping monocline. The deformation has not been propagated with similar characteristics throughout the whole sedimentary succession, because of the different rheologies of the rocks.
The western side of the Soraya Fm. dome is limited by a subvertical fault, with a dextral oblique movement, which downthrows the western side of the Yanque minesite, thus displacing vertically the Dolores area. Minor faults also occur within the district.
On the western block it is possible to recognize, from north to south, a series of alternating east-west trending synclines-anticlines in the Mara Fm. The Soraya Fm. forms a big syncline in the area north of Yanque, and a broad anticline below the Yanque deposit.
The igneous rocks are also deformed. In particular, at several boundaries between the igneous and sedimentary rocks it is possible to observe brittle shear zones and faults.

General characteristics of the mineral deposits occurring in the district
The Yanque deposit is the most distinctive type of mineralization and also the better studied in the area so far (Mondillo et al., 2010). The Dolores prospect is a Cu-Mo-(Au)-porphyry mineralization associated with minor skarn, occurring in a 1.8 by 1 km area 1.5 km east of Yanque, firstly identified by Zincore Metals in 2008. Initial sampling at Dolores returned values up to 2.3 % Cu and 1.0 g/t Au. The last explorative drillcore returned 261.3 m, at 0.14 % Cu, 0.006 % Mo, 0.01 g/t Au, and 1 g/t Ag (www.zincoremetals.com). The mineralization occurs in quartz diorite and quartz monzonite lithotypes, in form of a stockwork, as in other classic porphyry copper (Fig. 4.9A). The ore, by the actual exploration state, seems to consist essentially of Cu-“porphyry” sulfides, with only limited amounts of Cu-“skarn” and very limited supergene enrichment. Garnet, magnetite, and copper skarns have been detected around the porphyritic mineralization. A feldspar porphyry dyke intrudes, along a E-W lineament, the Dolores deposit, but it does not carry mineralization. The intrusive bodies, particularly in the porphyry copper area, are strongly altered, resulting in phyllic and argillic zones.
The Yanque East project is located 5 km east of the Yanque main deposit and immediately east of the Dolores porphyry. It consists a series of gossan/manto-like outcrops (Fig. 4.9B), hosted by the Ferrobamba Fm. carbonates and distributed over an area approximately 400 by 200 m. An old adit was discovered in the southern part of the area, and channel sampling from across the entrance returned 16 m grading 9.7 % Zn and 8.4 % Pb. A sample from the end of the adit returned 11.7 % Zn and 1.3 % Pb (www.zincoremetals.com). The Puyani prospect is very similar to the Yanque East occurrence. It is located about 2 km north of Yanque East and it is also hosted by Ferrobamba Fm. carbonates. The prospect consists of a black-reddish gossanous outcrop, extending over an area of few hundred meters. Within the gossan, small remnants of barite and galena have been identified.

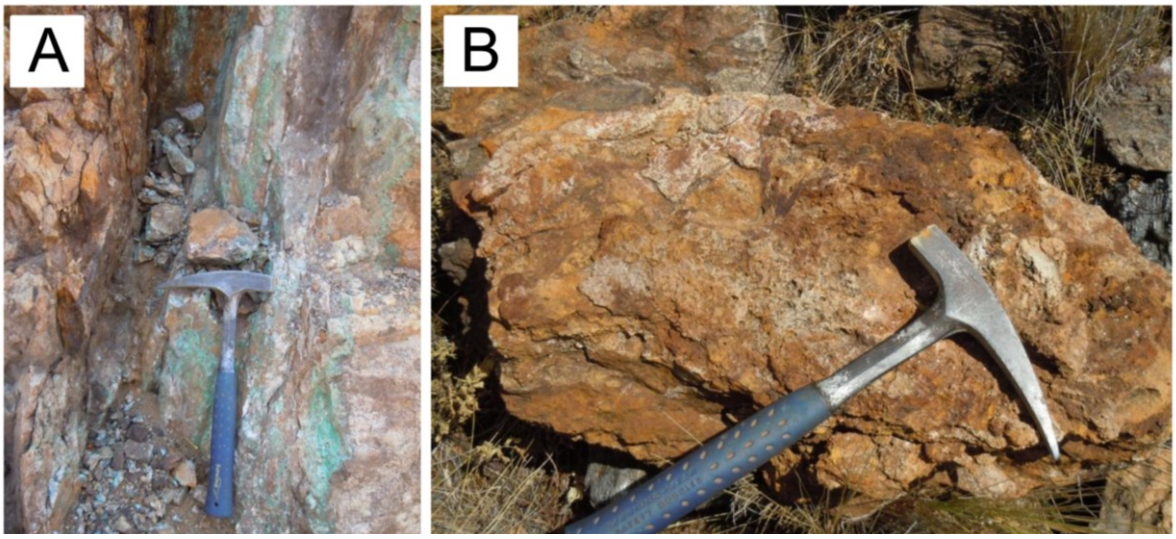

Fig. 4.9. A) Dolores Porphyry Copper: partially altered chalcopyrite veins. B) Yanque East: gossan.

Geology and geometry of the Yanque deposit

The Yanque Zn-Pb deposit covers an area of about 900 by 500 m on the surface, striking in a NW direction, and consists of several sub-horizontal stratabound bodies extending in depth for about 250 meters. Zincore Metals Inc. has evaluated 12.5 Mt of inferred resources for the nonsulfide orebody, containing 3.5 % Zn and 3.7 % Pb (www.zincoremetals.com).

The mineralization is hosted by the siliciclastic conglomerate in the northern part of the deposit, and by the dolomite breccia, in the center of the deposit (Fig. 4.10A). From a 3D geological model of the Yanque site, derived from drillcore logs, it was possible to draw two geological sections (Fig. 4.10B). The model was accomplished through the Move2012.1 software, licensed by the Midland Valley Exploration. The sandstone of the Mara Fm. forms a series of upward-facing domes and basins, differently developed in correspondence of the different facies of the sedimentary breccia, as well as in the N-S and E-W directions.

Variously extended gossans, with blackish-red Mn-Fe-(hydr)oxide crusts outcrop in patches. Moderate zinc grades have been also detected in the altered part of the diorite-tonalite outcropping at the Yanque minesite (up to 5-7 wt.% Zn), mainly concentrated at the boundary with the conglomerate. The limestone breccia occurring in the southern zone of the deposit is not mineralized. Lithologies strongly reactive to the Zinc Zap solution (refer to Table 5 in Hitzman et al., 2003), which reveals the presence of zinc minerals in oxidized form, outcrop on the whole northern part of the deposit. The mineralized siliciclastic conglomerate appears reddish-brown (Fig. 4.11A), but the rock textures are masked by the alteration, and it is difficult to distinguish the borders of the clasts. This lithology is generally cut by a network of veins containing hemimorphite, smithsonite and hydroxides. The dolomite breccia has a brown-gray color, and the surfaces are covered by Mn-(hydr)oxide crusts (Fig. 4.11B).

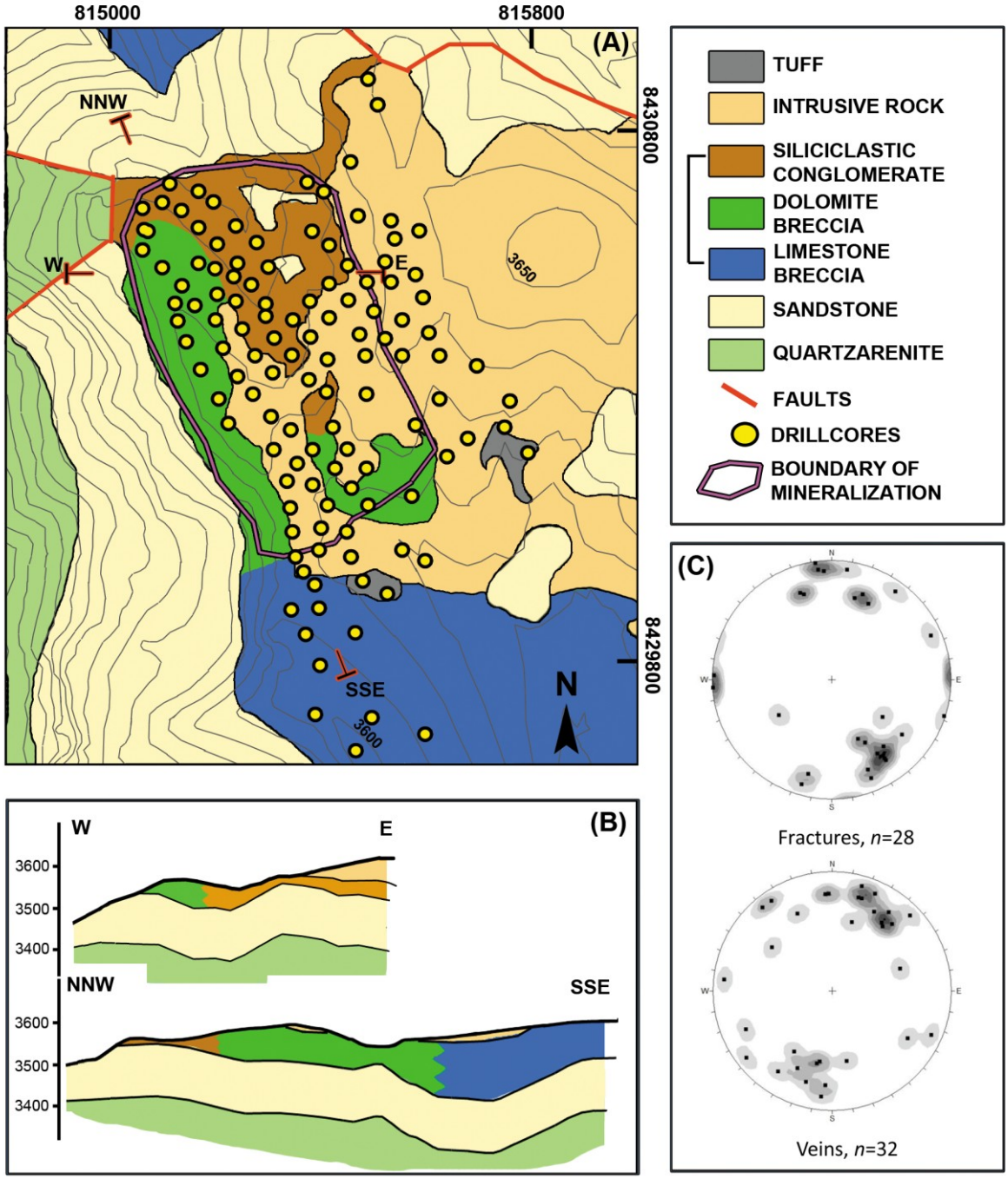

Fig. 4.10. A) Geological map of the Yanque minesite (from Zincore Metals Inc., 2012, modified); geometrical relationships between sedimentary rocks as in Fig. 4.6. B) E-W and NNW-SSW geological sections of the Yanque deposit. C) Orientation data (poles, Schmidt diagram, lower hemisphere) of fractures, and veins at the Yanque minesite. The veins are filled with hemimorphite.

Fig. 4.11. Yanque minesite. A) Mineralized siliciclastic conglomerate (positive reaction to Zinc Zap). B) Mn-(hydr)oxide crusts in dolomite breccia. C) Hemimorphite veins. D) Altered galena stockwork. E) YA-20. Surficial core sample enriched in Zn. F) YA-49. Residual primary mineralization: oxidized galena.

The groundmass is reactive to Zinc Zap, even when no specific Zn-minerals can be distinguished. Thin hemimorphite and smithsonite veins (Fig. 4.11C), though, have been locally identified. These veins show moderate to high dips towards SSW-SSE and NNE (Fig. 4.10C). The orientation of fractures occurring in the same rocks show high to moderate dips towards SSW-SSE, NW, and E (Fig. 4.10C). The orientations of both veins and empty fractures are partially superimposed, indicating that the hemimorphite precipitation has happened during or after fracturation of the host rock. Only the NW dipping fractures seem not to be filled with mineral precipitates, and could have been generated after the main stage of nonsulfides deposition. The orientations of these structures conform to the shortening directions of the area, reported by Perelló et al. (2003).

Small, stockwork-like galena veins, partly or totally replaced by cerussite, have been observed in many outcrops at the Yanque minesite, cutting both the sedimentary and igneous rock (Fig. 4.11D).

These textural characteristics have been confirmed also in drillcores: oxidized zinc minerals prevail in the more superficial zones (Fig. 4.11E), whereas cerussite/galena, occurring in veins and as cement of crackle breccia, is more abundant in depth than on the surface (Fig. 4.11F).

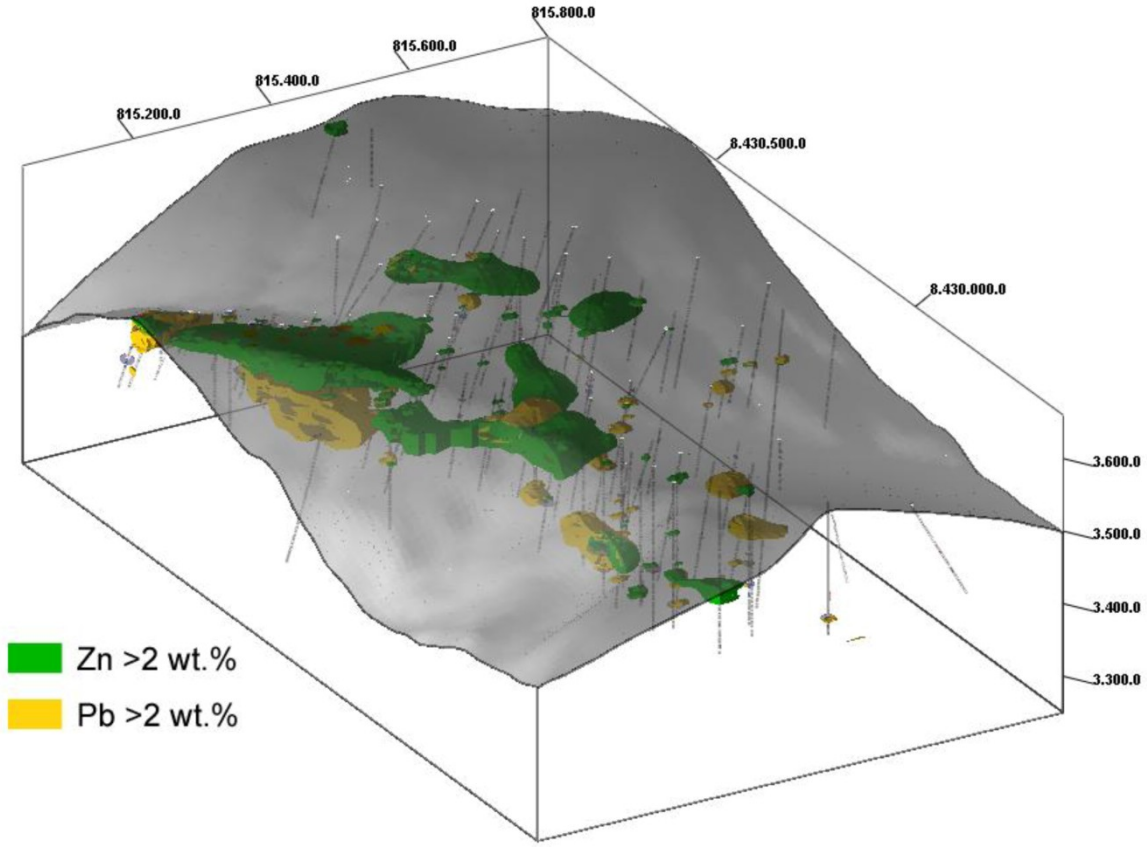

Fig. 4.12. 3D-model of the Yanque mineralization looking northeast: the green body represents the volumes with ore grades higher than 2 wt.% Zn, the yellow body the volumes with grades higher than 2 wt.% Pb.

A 3D-model of the Yanque mineralization, based on the Zn and Pb assays from 124 cores (Zincore Metals, 2011), is shown in Fig. 4.12. As mentioned before, the orebody consists of several subhorizontal stratabound sub-bodies, which from the outcrops located in the northern part of the minesite deepen more and more in the southward direction within the dolomite breccia.
The mineralized intervals are limited, in depth, by the highest quartzarenite horizon of the Mara Fm. In the lower Mara Fm. several pyrite veins containing minor galena and traces of sphalerite have been detected; but nonsulfide mineralization is totally absent in this part of the Mara Fm.

Evaluation of the Yanque ore - Semiquantitative mineralogy

A semiquantitative mineralogical evaluation of the ore has been performed on 40 samples derived from 5 drillcores (12 from DDH-YA-20, 6 from DDH-YA-33, 5 from YA-71, 6 from YA-82, 11 from YA-117) (TABLEE 4.2). These samples are considered representative of different areas of the Yanque deposit. They consist of 1 m quarter core each (sampled in alternating one-meter interval), and correspond to the intervals collected by the Company for the chemical assays (Zincore Metals Inc.).
Semiquantitative mineralogical data obtained by X-ray diffraction analysis are listed in TABLE 4.5. In TABLE 4.6 are recorded the data from the ICP-MS chemical assays (CA).
DDH-YA-20 - 3.45-25.45 m:
The samples derive from an interval totally consisting of sedimentary breccia. Quartz is the most abundant phase in the host rock (locally >60 wt.%), followed by dolomite and orthoclase. Zinc occurs mainly in sauconite, with maximum values shortly below 36wt. % throughout the core. Zinc has been also detected in hemimorphite and smithsonite, though in minor amounts (around 5 wt.% on average for each phase). Cerussite content is variable, with average values ranging around 5 wt.% for the lead carbonate. The weight amounts of all other minerals are negligible, even though one must mention the trace contents of kaolinite, sericite/illite and goethite.
DDH-YA-33 - 119.5-129 and 155.1-156.1 m:
The samples are from an interval where a carbonate sedimentary breccia is alternated with sandstone. Quartz is the most abundant phase (locally >60 wt.%) in the host rock, followed by dolomite (also locally up to 60 wt.%). Zinc occurs only in sauconite, with maximum values around 30 wt.%; small hemimorphite percentages occur in the top section. Cerussite has been detected in relatively high amounts (average 20 wt.%), and galena is below 5 wt.%. Kaolinite, sericite/illite and goethite are also present in small amounts (below 5 wt.%). Silver up to 200 ppm has been measured in the chemical assays, but no silver-bearing minerals could be detected in the XRD patterns.

TABLE 4.5. Mineral abundances in the Jabali cores samples as deduced from X-ray semiuantitative phase analysis (QPA).

Sample n.	Hm	Sm	Sau	Cha	Aur	Cer	Gn	Prmp	Qz	Or	Ab	Cal	Mg-Cal	Dol	Ser/Ilt	Kln	Cop	Gth	Sap
									(wt.%)										
YA-20-3.45-4.45	-	-	-	-	-	-	-	-	xxxxx	xx	-	-	-	-	-	xx	-	x	-
YA-20-5.45-6.45	-	-	x	-	-	-	-	-	xxxxx	xx	-	x	-	-	x	xx	-	x	-
YA-20-7.45-8.45	-	-	xxx	x	-	-	-	-	xxx	xx	-	x	-	xx	x	x	-	x	-
YA-20-9.45-10.45	xxx	x	xxx	-	-	x	-	-	xx	-	-	x	-	xxx	-	-	-	-	-
YA-20-10.45-11.45	-	-	xx	-	-	-	-	-	xx	xxx	-	x	-	xxx	-	xx	-	-	-
YA-20-12.45-13.45	-	-	xx	-	-	-	-	x	xxx	x	-	-	x	xxxx	x	x	-	-	-
YA-20-14.45-15.45	x	-	xx	-	-	xx	x	-	xx	x	-	x	-	xxxx	-	-	-	-	-
YA-20-16.45-17.45	x	xx	xx	-	-	xx	x	-	xx	-	-	-	-	xxx	-	x	-	-	-
YA-20-18.45-19.45	x	xxx	xx	-	-	x	-	-	xxx	x	-	-	-	-	x	x	-	x	-
YA-20-20.45-21.45	xx	xxx	xx	-	-	x	-	-	xxx	x	-	x	-	x	x	xx	-	-	-
YA-20-22.45-23.45	-	-	xxx	-	-	xx	-	-	xxx	xx	-	-	-	xx	-	xx	-	-	-
YA-20-24.45-25.45	-	-	xx	-	-	xx	-	-	xxx	x	-	-	-	xx	-	xx	xx	x	-
YA-33-119.5-120.5	x	-	xxx	-	xx	xxx	x	-	xx	x	-	-	x	xx	-	x	-	-	-
YA-33-121.5-123	-	-	xx	-	-	-	-	-	xx	xx	-	-	x	xxxx	-	x	-	-	-
YA-33-124-125	x	-	xxx	-	-	xxx	x	-	xx	x	-	-	-	xx	-	x	-	-	-
YA-33-126-127	-	-	xx	-	-	xx	-	-	xxx	xx	-	-	x	xx	x	x	-	-	-
YA-33-128-129	-	-	xx	-	-	xx	-	-	xxx	xx	-	-	x	xxx	-	x	-	-	-
YA-33-155.1-156.1	-	-	-	-	-	xx	x	-	xxxxx	x	-	-	-	-	x	-	-	xx	-
YA-49-94-95	-	-	-	-	-	xxx	x	-	xxxx	xx	-	-	-	-	x	xx	-	x	-
YA-49-95-96	-	-	-	-	-	xxxx	xx	-	xxx	xx	-	-	-	-	-	x	-	-	-

"-" not found, "x" <5 wt.%, "xx" 5< <20 wt.%, "xxx" 20< <40 wt. %, "xxxx" 40< <60 wt. %, "xxxxx" >60 wt.%; Abbreviations: Hm, hemimorphite; Sm, smithsonite; Sau, sauconite; Cha, chalcophanite; Aur, aurichalcite; Cer, cerussite; Gn, galena; Prmp, pyromorphite; Qz, quartz; Or, orthoclase; Ab, albite; Cal, calcite; Mg-cal, Mg-calcite; Dol, dolomite; Ser/Ilt, sericite/illite; Kln, kaolinite; Cop, copiapite; Gth, goethite; Sap, saponite.

Continue... TABLE 4.5.

Sample n.	Hm	Sm	Sau	Cha	Aur	Cer	Gn	Prmp	Qz	Or	Ab	Cal	Mg-Cal	Dol	Ser/Ilt	Kln	Cop	Gth	Sap
									(wt.%)										
YA-71-14-15	-	-	x	-	-	-	-	-	xxxx	x	xx	-	-	-	xx	xx	-	-	x
YA-71-16-17	-	-	xx	-	-	-	-	-	xxxx	x	xx	-	-	-	xx	x	-	-	x
YA-71-18-19	x	-	xx	-	-	x	-	-	xxx	x	-	-	-	xxxx	x	x	-	-	-
YA-71-20-21	x	-	xx	-	-	-	-	x	xxx	x	-	-	-	xxx	x	x	-	x	-
YA-71-22-23	-	-	x	-	-	-	-	x	xxxxx	xx	-	x	-	-	x	x	-	x	-
YA-82-24-25	-	-	xx	-	-	xxx	x	-	xxx	x	-	-	-	xxx	x	x	-	-	-
YA-82-26-27	-	-	xx	-	-	xx	x	-	xxx	x	-	x	-	xxx	x	x	-	-	-
YA-82-28-29	-	-	x	-	-	x	x	-	xxx	x	-	x	-	xxxx	x	x	-	x	-
YA-82-32.3-34.3	-	-	x	-	-	x	-	-	xxx	x	-	xxxx	-	xxx	-	x	-	x	-
YA-82-35.3-36.3	-	-	xx	-	-	x	x	-	xxxx	xx	-	x	-	xx	x	xx	-	-	-
YA-82-37.3-38.3	-	-	x	-	-	x	x	-	xxxx	xx	-	x	-	xxx	x	x	-	-	-
YA-117-1-2	-	-	-	-	-	-	-	x	xxxxx	xx	-	-	-	-	x	xx	-	-	-
YA-117-3-4	-	-	x	-	-	xx	-	-	xxxx	xx	-	-	-	-	x	xxx	-	x	-
YA-117-5-6	-	-	x	-	-	xx	-	-	xxxxx	xx	-	-	-	-	x	xx	-	-	-
YA-117-7-8	-	-	-	-	-	xx	-	-	xxxxx	xx	-	-	-	-	x	xx	-	-	-
YA-117-9-10	-	-	-	x	-	-	-	x	xxxxx	xx	-	-	-	-	x	xx	-	x	-
YA-117-11-12	-	-	-	-	-	x	x	-	xxxxx	x	-	-	-	-	x	xx	-	-	-
YA-117-13-14	-	-	-	-	-	xx	x	-	xxxx	x	-	-	-	-	xx	xx	-	x	-
YA-117-15-16	-	-	-	-	-	xx	x	-	xxxxx	x	-	-	-	-	x	x	-	x	-
YA-117-17-18	-	-	-	-	-	-	-	x	xxxxx	x	-	-	-	-	x	xx	-	-	-
YA-117-19-20	-	-	-	-	-	x	-	-	xxxxx	x	-	-	-	-	xx	xx	-	-	-
YA-117-22-24	-	-	-	-	-	-	-	x	xxxxx	x	-	-	-	-	xx	-	-	x	-

"-" not found, "x" <5 wt.%, "xx" 5< <20 wt.%, "xxx" 20< <40 wt. %, "xxxx" 40< <60 wt. %, "xxxxx" >60 wt.%; Abbreviations: Hm, hemimorphite; Sm, smithsonite; Sau, sauconite; Cha, chalcophanite; Aur, aurichalcite; Cer, cerussite; Gn, galena; Prmp, pyromorphite; Qz, quartz; Or, orthoclase; Ab, albite; Cal, calcite; Mg-cal, Mg-calcite; Dol, dolomite; Ser/Ilt, sericite/illite; Kln, kaolinite; Cop, copiapite; Gth, goethite; Sap, saponite.

TABLE 4.6. Major and minor element concentration derived from whole rock ICP chemical analysis (Zincore Metals).

Sample n.	Zn	Pb	Ca	Mg	Fe	Al	K	Ti	Cu	S	Ag	As	Ba	Cd	Mn	Mo	Na	Sb	Sc	Sr
					(wt.%)										(ppm)					
YA-20-3.45-4.45	0.9	1.07	0.13	0.15	4.95	5.9	3.2	0.22	0.005	0.05	1	80	230	20	12400	5	600	25	10	130
YA-20-5.45-6.45	1.33	0.23	0.15	0.05	2.92	4.12	4.2	0.29	0.003	0.05	1	70	290	60	7050	5	700	25	10	190
YA-20-7.45-8.45	14.1	0.11	1.73	0.7	11.2	3.32	0.9	0.11	0.008	0.05	6	580	440	3600	36500	10	250	25	10	290
YA-20-9.45-10.45	26.2	4.1	2.4	1.12	4.23	1.17	0.3	0.05	0.016	0.05	1	450	100	960	12450	5	250	180	5	150
YA-20-10.45-11.45	5.64	0.42	4.41	2.11	1.9	6.55	3.3	0.3	0.001	0.05	0.5	130	190	380	2270	5	700	50	10	120
YA-20-12.45-13.45	2.92	0.71	11.15	6.05	3.23	2.76	1.2	0.15	0.002	0.05	3	80	280	240	6440	5	500	25	10	350
YA-20-14.45-15.45	14.65	10.15	7.17	3.6	1.94	2.09	0.8	0.1	0.001	0.2	7	290	60	1380	4220	5	250	180	5	570
YA-20-16.45-17.45	18.6	7.29	5.46	2.92	3.25	1.79	0.4	0.08	0.001	0.05	2	360	25	1470	8710	5	250	60	5	370
YA-20-18.45-19.45	21	3.76	0.35	0.28	3.86	3.2	0.8	0.18	0.003	0.05	6	560	70	1120	11500	5	250	100	10	310
YA-20-20.45-21.45	29.5	1.42	0.65	0.35	2.4	2.55	0.8	0.14	0.003	0.05	3	140	90	2240	12800	5	250	25	5	80
YA-20-22.45-23.45	12.85	3.59	1.82	0.88	4.04	5.84	0.9	0.23	0.006	0.05	1	100	90	690	6600	5	500	70	10	160
YA-20-24.45-25.45	7.65	15.65	1.97	0.96	3.38	4.23	0.9	0.18	0.024	0.1	12	230	50	710	2960	5	250	90	5	150
YA-33-119.5-120.5	16.5	20.5	0.7	0.25	3.15	1.83	0.8	0.11	0.004	0.1	0.5	640	160	1350	4050	5	250	80	5	980
YA-33-121.5-123	3.25	2.33	11	5.67	3.93	2.31	1.3	0.11	0.003	0.05	1	240	350	780	10600	5	500	25	5	350
YA-33-124-125	11.1	20.5	1.76	0.87	2.25	2.46	0.7	0.13	0.005	0.1	17	990	480	380	2240	10	250	250	5	1550
YA-33-126-127	4.94	12.85	3.4	1.72	3.95	3.84	1.7	0.18	0.004	0.1	14	1130	820	320	1640	5	250	340	10	680
YA-33-128-129	5.59	8.27	4.94	2.45	2.1	3.11	1.3	0.17	0.007	0.1	35	1460	4570	710	6590	10	250	460	5	1420
YA-33-155.1-156.1	0.39	11.8	0.16	0.15	14.35	4.61	1	0.13	0.003	0.3	197	1340	3500	30	14800	10	250	520	10	1020
YA-49-94-95	0.1	23.1	0.05	0.05	2.71	5.13	3.8	0.12	0.0086	0.3	200	145	521	5.2	91	1	300	804	5	10000
YA-49-95-96	0.06	41.6	0.03	0.03	1.45	3.9	2.73	0.08	0.0148	1.9	200	134	108	6.6	42	3	500	816	2	6568

Minimum detection limits: 0.5 ppm, 0.05 wt.%.

Continue... TABLE 4.6.

Sample n.	Zn	Pb	Ca	Mg	Fe	Al	K	Ti	Cu	S	Ag	As	Ba	Cd	Mn	Mo	Na	Sb	Sc	Sr
					(wt.%)										(ppm)					
YA-71-14-15	1.76	0.5	0.42	0.21	3.51	9.85	3.09	0.37	0.0013	0.05	0.25	44	390	66.8	3785	1	16600	23	12	79
YA-71-16-17	4.16	1.45	0.35	0.33	2.97	8.45	2.35	0.32	0.0004	0.05	0.25	35	332	44	1627	1	10100	23	11	63
YA-71-18-19	9.02	1.48	8.04	4.8	2.9	2.92	1.09	0.11	0.0009	0.05	0.25	87	184	1264.6	8574	4	900	61	4	147
YA-71-20-21	7.09	1.2	6.64	4.15	5.62	4.29	1.32	0.18	0.0034	0.05	6	72	858	1558.8	10000	6	800	43	7	169
YA-71-22-23	1.89	0.83	0.81	0.26	5.93	6.69	2.1	0.33	0.0025	0.05	0.25	60	443	545.4	9240	2	700	21	11	210
YA-82-24-25	3.63	13.94	6.66	3.66	3.34	3.11	0.94	0.11	0.0046	0.05	9.8	119	86	200.9	6091	7	200	30	3	8618
YA-82-26-27	9.96	15.17	5.11	2.49	4.04	2.1	0.75	0.08	0.0047	0.05	16.3	127	72	1799.8	10000	6	200	20	5	3008
YA-82-28-29	1.28	3.22	10.63	6.98	4.25	2.12	0.9	0.12	0.0034	0.05	17.6	63	68	113.2	10000	8	200	45	6	414
YA-82-32.3-34.3	0.64	0.95	19.19	4.37	2.14	1.07	0.2	0.06	0.0008	0.05	0.6	76	39	517.9	7888	1	200	12	3	333
YA-82-35.3-36.3	4.55	2.49	4.68	2.56	3.29	4.17	2.33	0.2	0.0045	0.05	4.9	92	125	33.2	4662	1	600	23	6	530
YA-82-37.3-38.3	2.14	1.42	6	3.57	3.1	5.65	3.08	0.26	0.0027	0.05	0.25	56	139	48.9	7931	3	600	11	7	175
YA-117-1-2	0.13	1.59	0.03	0.05	0.46	8.2	5.22	0.29	0.0005	0.05	0.25	158	454	6.9	296	1	800	34	4	239
YA-117-3-4	1.32	4.63	0.12	0.05	5.65	6.48	3.25	0.15	0.0017	0.05	2	316	162	37.7	10000	6	200	77	11	671
YA-117-5-6	0.66	5	0.15	0.09	1.53	8.26	4.92	0.28	0.0013	0.05	0.6	304	373	19.4	274	3	600	101	5	596
YA-117-7-8	0.92	4.77	0.08	0.21	2.62	7.11	4.53	0.29	0.0028	0.1	2.9	556	300	32.3	316	1	600	136	4	1724
YA-117-9-10	1.41	0.42	0.09	0.11	6.17	7.22	3.96	0.24	0.0008	0.05	0.25	175	1880	255.4	10000	3	600	16	12	388
YA-117-11-12	0.41	2.86	0.06	0.21	2.47	8.79	2.14	0.37	0.001	0.2	0.9	957	4355	39.6	93	2	400	108	6	251
YA-117-13-14	0.54	16.18	0.07	0.26	3.88	7.32	2.49	0.22	0.0008	0.7	12.6	1358	427	112.3	36	7	800	376	6	353
YA-117-15-16	0.21	13.26	0.06	0.25	1.54	7.05	2.61	0.24	0.0019	1.1	2.5	215	175	46.6	56	3	400	273	4	179
YA-117-17-18	0.66	1.5	0.06	0.38	4.54	8.2	2.3	0.27	0.001	0.05	1.1	52	461	18.9	6761	1	300	18	13	61
YA-117-19-20	0.03	1.37	0.02	0.38	3.37	9.04	3.74	0.4	0.0021	0.8	15.1	312	905	4.2	41	1	500	110	12	150
YA-117-22-24	0.12	8.74	0.02	0.38	4.15	6.95	3.33	0.32	0.0026	1.4	14.2	215	170	3.4	964	2	300	225	9	279

Minimum detection limits: 0.5 ppm, 0.05 wt.%.

YA-71 - 14-23 m:

The first two samples derive from the lower part of the tonalite intrusion, which tectonically overlaps the sedimentary lithologies. The other samples come from a sandstone interval and from the sedimentary breccia. Quartz is the most abundant rock-forming mineral (up to 70 wt.%) in the host rock, followed by dolomite (up to 40 wt.%). Zinc is found mostly in sauconite, which has a maximum percentage around 15 wt.%; small hemimorphite amounts also occur. Orthoclase, albite (up to 20 wt.%) and sericite have been detected in the tonalite interval, which occurs in the top zone of the drill core. Altered tonalite contains low Zn amounts, which can be associated with alteration clays (smectite and kaolinite).

YA-82 - 24-38.3 m:

The samples derive from sandstone and sedimentary breccia intervals. Quartz is the prevailing mineral (locally >50 wt.%) in the host rock, followed by dolomite (locally >50 wt.%) and calcite (up to 48 wt.% in the middle sections). Zinc is only detected in sauconite, with max values around 20 wt.%. Cerussite (10 wt.%) and galena (<5 wt.%) have been recorded in the top sections, whereas kaolinite and sericite/illite are ubiquitous.

YA-117 - 24-38.3 m:

The samples derive from the sandstone and quartzarenite intervals, with minor interbedded sedimentary breccia. This core is poorly mineralized, and cerussite is the most abundant ore mineral (about 6 wt.% on average); traces of galena and sauconite have been also detected. Quartz is the most abundant phase (up to >82 wt.%) in the host rock, followed by sericitized and kaolinized orthoclase.

To summarize the results of semiquantitative mineralogy:

Zn-bearing minerals:

Sphalerite [ZnS] has never been found in the analyzed drillcore samples. All the analyzed samples contain abundant clay minerals, in particular sauconite, but discrete amounts of sericite/illite and kaolinite have also been found. Sauconite has been detected in DDH-YA-20 (up to 35 wt.%), DDH-YA-33 (8 to 35 wt.%), YA-117 (below 5 wt.%), YA-71 (2 to 20 wt.%), and YA-82 (1 to 20 wt.%).

The Zn-silicate hemimorphite [$Zn_4Si_2O_7(OH)_2 \bullet 2H_2O$] has been detected in fairly discrete amounts (up to 40 wt.%) only in nine samples, derived from the DDH-YA-20, DDH-YA-33 and YA-71 cores. The Zn-carbonate smithsonite [$ZnCO_3$] has been found in variable amounts only in four samples from DDH-YA-20 (up to 30 wt.%).

Other Zn minerals, occurring in trace amounts are chalcophanite [$(Zn,Fe^{2+},Mn^{2+})Mn^{4+}{}_3O_7 \bullet 3(H_2O)$] and aurichalcite [$(Zn,Cu)_5(CO_3)_2(OH)_6$] (in DDH-YA-33). Copiapite, possibly containing Zn, has been detected only in DDH-YA-20 (8 wt.%).

Pb-bearing minerals:

Galena [PbS] occurs in minor amounts in all cores. The carbonate cerussite [$PbCO_3$] is the main Pb-mineral in DDH-YA-20 (up to 20 wt.%), in DDH-YA-33 (10 to 30 wt.%), in YA-117 (up to 20 wt.%), in YA-71 (5 wt.%), and YA-82 (up to 25 wt.%). Pyromorphite [$Pb_5(PO_4)_3Cl$] has been detected locally with values between 1 and 5 wt.%.

Gangue and host rock minerals:

Quartz is the most abundant mineral in all cores (10 to 85 wt.%), and represents the main component of the Yanque host rock (av. 45 wt.%). Orthoclase is ubiquitous, even if less abundant (up to 25 wt.%). Albite has been detected (10 to 20 wt.%) only in two samples from YA-71, collected in the tonalite intrusive. Dolomite occurs in discrete amounts (5 to 60 wt.%), mainly in DDH-YA-20, DDH-YA-33, YA-71 and YA-82.

Petrography at the Yanque minesite: effects of hydrothermal and supergene alteration in the ore and host rocks

The siliciclastic conglomerate at Yanque contains clasts of different sizes and nature. The clasts can be well- to poorly-rounded, and locally also subangular; their maximum size can reach a few cms. Quartzarenite and sandstone clasts are the most abundant (Fig. 4.13A), but quartzite (metamorphic), pelite and magmatic rocks have been also identified. The matrix consists of quartz and feldspar microgranules associated with variable amounts of neoformed muscovite-sericite and clays. The feldspar clasts tend to be strongly altered, but generally maintain the same size and roundness of the quartz grains.

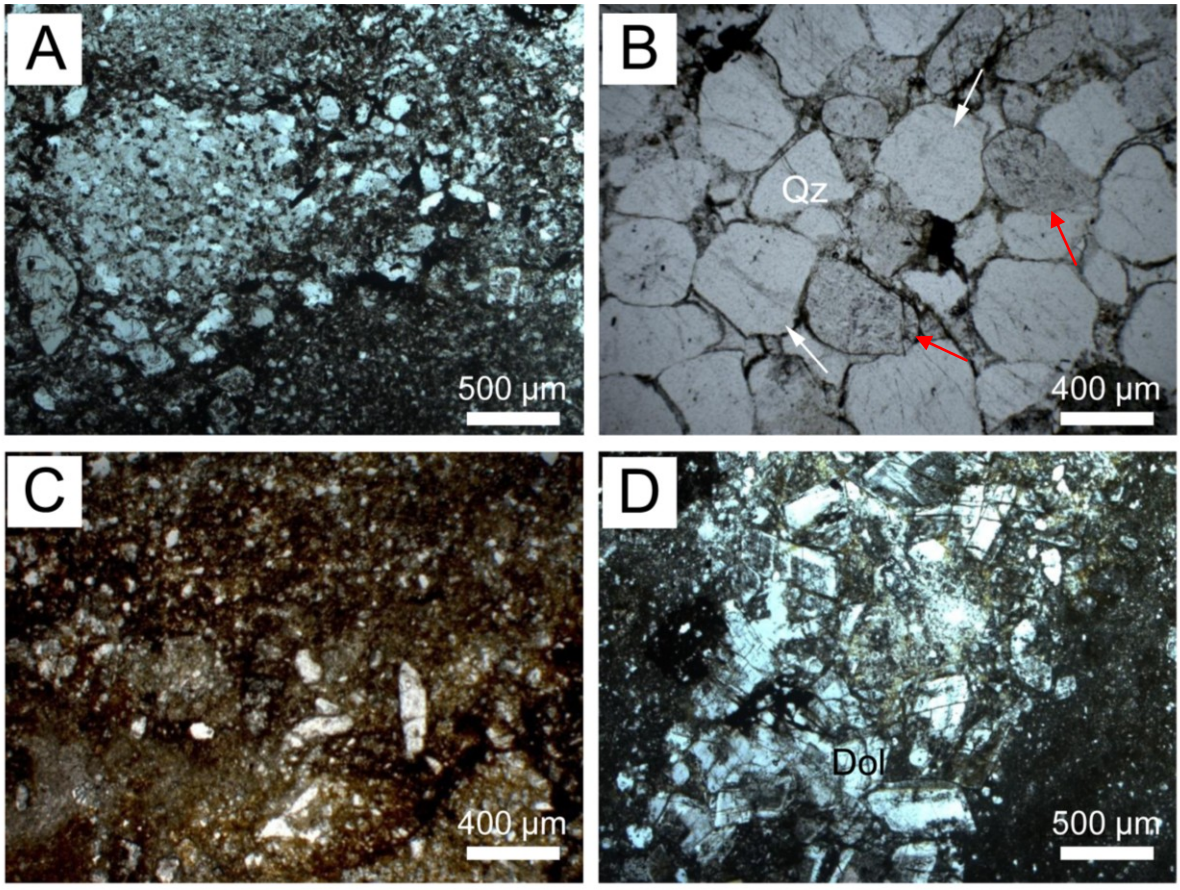

Fig. 4.13. Host rock petrography: A) Siliciclastic conglomerate: quartzite clasts, and detrital quartz and feldspar. NII. B) Sandstone interbeds: well-rounded, closely packed quartz clasts (white arrows) and sericitized feldspars (red arrows). NII. C) Dolomite breccia: carbonatic-arenaceous matrix and quartz clasts. NII. D) Hydrothermal dolomite. NII. Dol = dolomite; Qz = quartz.

In the interbedded sandstone layers quartz is generally rounded. In some layers quartz is heavily concentrated, very well rounded and fractured (Fig. 4.13B). These features are similar to those described by Callot et al. (2008a) for the quartz grains of the Murco Fm. (the equivalent of the Mara Fm. in the Arequipa basin), which occur with two different morphologies: 1) large, rounded grains of possible Aeolian origin, and 2) small, angular, detrital grains.

The dolomite breccia is stratigraphically interfingered with the siliciclastic conglomerate. The breccia consists of cm-sized, locally angular clasts of microcrystalline dolomite, in a mixed carbonatic-arenaceous matrix (Fig. 4.13C). The matrix contains quartz and dolomite micrograins in a marly groundmass. A network of phyllosilicates, consisting of minerals of the mica group (sericite/illite), and kaolinite occurs in the matrix of the breccia, around the detrital clasts. The phyllosilicates have replaced the detrital feldspars in both the clasts and the matrix (Fig. 4.13B): this replacement process could be compared with the phyllic/argillic hydrothermal alteration occurring in the Cu-porphyry. Abundant quartz occurs in the matrix, both as neoformed euhedral crystals and as a product of recrystallization of detrital quartz grains. Another typical component is macrocrystalline dolomite growing in the matrix in form of variably sized euhedral rhombohedra (Fig. 4.13D). The bigger crystals are commonly fractured and may occur in fractures and/or in the porosity between the clasts. Most crystals show the typical "saddle" habitus of the hydrothermal dolomite.

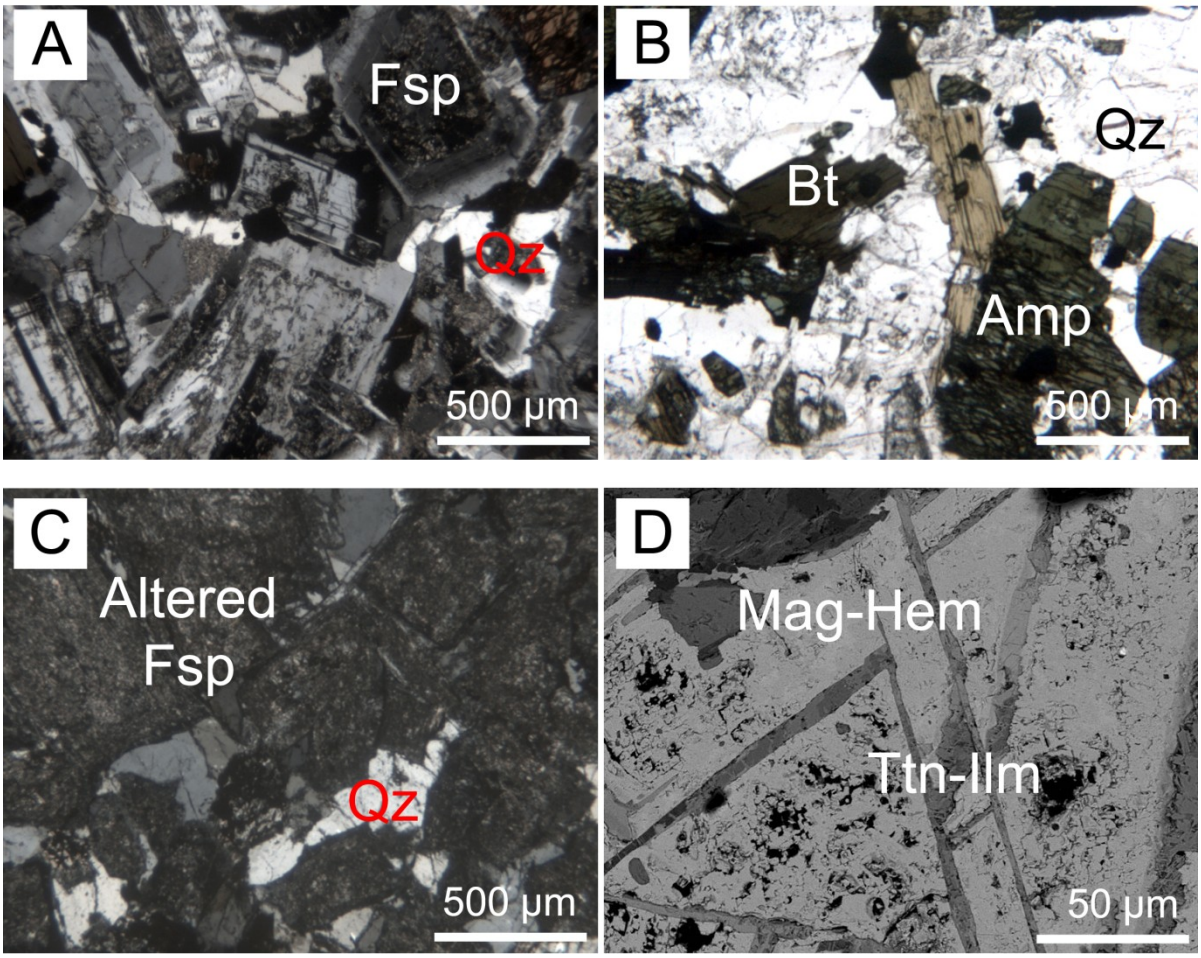

Fig. 4.14. Igneous rocks at Yanque site. A) YA-OUT-9. Zoned and twinned feldspars (plagioclase) in the diorite/tonalite. N+. B) YA-OUT-9. Biotite and amphibole in the diorite/tonalite. NII. C) YA-71-14-15. Plagioclases replaced by sericite/illite-kaolinite, and unaltered interstitial quartz. N+. D) YA-71-14-15. Altered magnetite(-hematite) crystal containing titanite-ilmenite exolutions. SEM-BSE-EDS. Amp = amphibole; Bt = biotite; Fsp = feldspar; Hem = hematite; Ilm = ilmenite; Mag = magnetite; Qz = quartz; Ttn = titanite.

In the tonalite outcropping on the eastern side of the deposit the main ferromagnesian phases are green amphiboles (hornblende) and minor biotite, whereas the main sialic minerals consist of zoned plagioclases, with labradorite cores and albite rims, few K-feldspars and up to 10 modal % quartz. The most important hydrothermal effect on the tonalite is the overprint on feldspars, amphiboles and biotite (Fig. 4.14A,B). The feldspars are completely hydrolyzed and replaced by sericite/illite and kaolinite, but they still maintain their crystal shape (Fig. 4.14C). The ferromagnesian minerals are also strongly altered: biotite is converted to chlorite and other clay minerals, and hornblende is recognizable only by its ghost structure while being replaced by Fe-(hydr)oxides. The magnetite(-hematite) crystals containing ilmenite-titanite exolutions are also altered (Fig. 4.14D).

The Yanque host rocks, after having undergone the hydrothermal alteration have been also strongly weathered. The supergene processes have caused a further substantial alteration of the more unstable mineral phases, which have been replaced with neoformed low-temperature minerals. In the siliciclastic conglomerate and in the sandstone layers, quartz is the only component to remain unaltered, whereas the (still unaltered) detrital feldspars and the epigenetic phyllosilicates have been replaced by Zn-rich clays, mainly belonging to the smectite group. SEM-EDS analysis has shown that a typical alteration process consists of the reaction: K-feldspar (detrital) → sericite/illite and kaolinite (hydrothermal) → Zn-smectite (supergene) (Fig. 4.15A,B,C,D,E). Zn-smectite overprints sericite/illite patchily, and precipitates also as single aggregates between idiomorphic dolomite crystals (Fig. 4.15F).

Due to the high relevance of the Zn-smectite as ore mineral, a more detailed study has been carried out on this phyllosilicate. The Zn-smectite in the Yanque deposit has a composition very near to the standard sauconite [$Na_{0.3}Zn_3(Si,Al)_4O_{10}(OH)_2 \cdot 4H_2O$], except for the Na content that should be present in the chemical formula (Borchardt, 1989). As reported in TABLE 4.7, the Yanque Zn-smectite contains variable amounts of K and Ca. Since Na could not be measured by SEM-EDS (due to serious peak overlapping with other elements in the energy-wavelength dispersion spectrum of these clays), a check for this element was done by ICP-MS analysis that showed values of Na_2O lower than 0.5 wt.%.

In order to be absolutely sure about the smectitic nature of the most abundant Zn-clay at Yanque, a number of clay separates have been submitted to XRD analysis of oriented aggregates under different conditions (Moore and Reynolds, 1997). This is because air-dried patterns (i.e. recorded at atmospheric temperature) of clay oriented aggregate, that are characterized by a maximum peak around 6 °2θ (as it is the case of sauconite and other smectites), could also indicate chlorite-group phases. Chlorite phases can be distinguished from smectite only for their non-expandable character, revealed when the clays are treated with ethylene glycol. In Fig. 4.16 it is possible to observe the XRD patterns of the a) air-dried, b) ethylene glycol solvated, and c) heated (550°C) clay oriented aggregates. All the resulting traces are typical of expandable smectites, i.e. sauconite, because this the only smectite which contains Zn. Following Ross (1946), and Newman and Brown (1987), Zn (<<Mg, Fe^{3+}) should be located in the octahedral sites in these trioctahedral phyllosilicates, whereas Ca and K occur as interstratified cations; aluminium can occur both in tetrahedral and octahedral coordination.

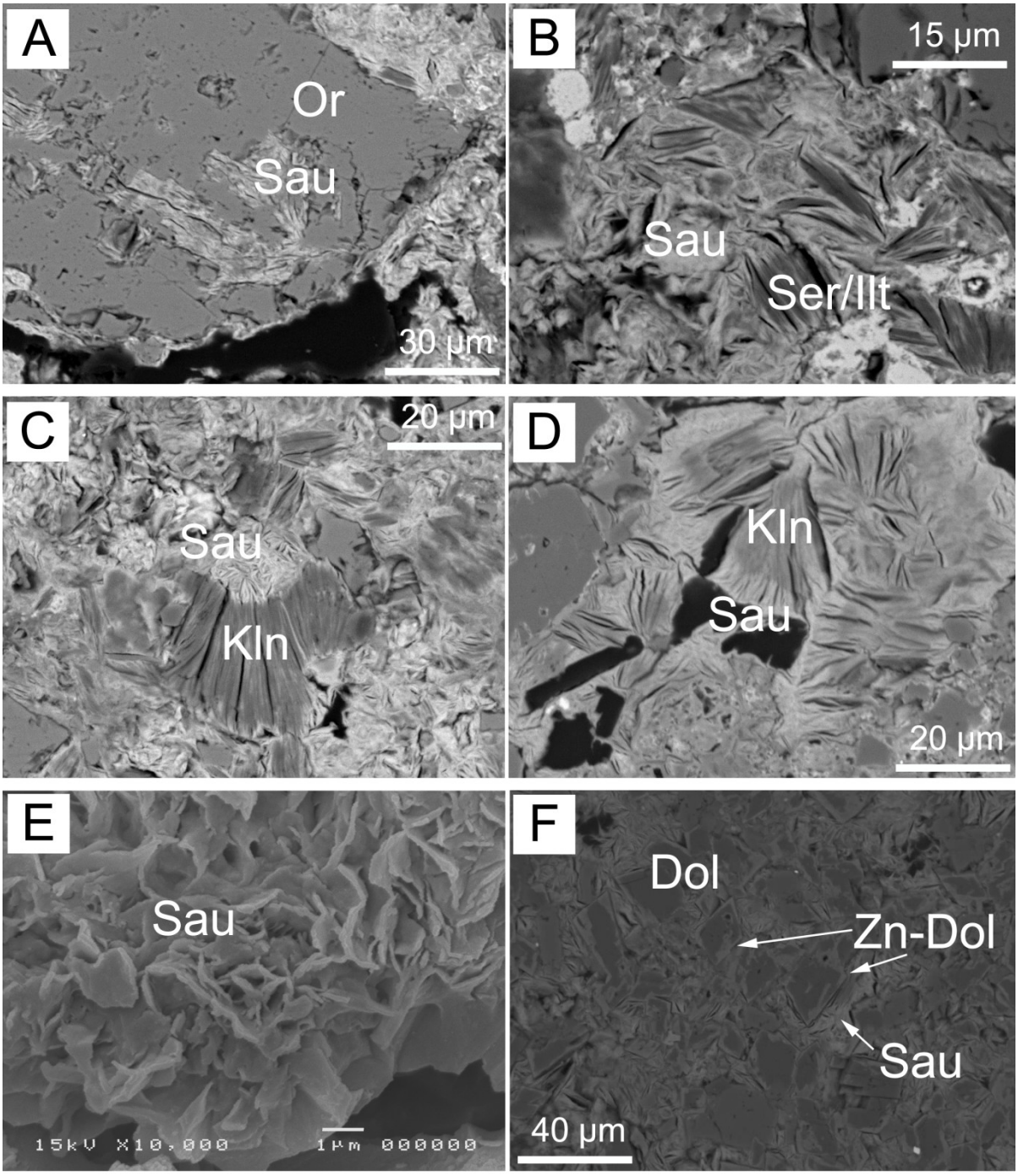

Fig. 4.15. Sauconite. A) YA-17-SAM-16. Sauconite replacing an orthoclase clast. B) YA-16-SAM-16. Sauconite replacing sericite/illite. C) YA-17-SAM-16. Sauconite replacing kaolinite. D) YA-33-124-125. Sauconite replacing kaolinite. E) YA-05-SAM-05. Sauconite agglomerate. F) YA-40-SAM-29. Sauconite (replacing sericite/illite), between dolomite crystals; Zn-dolomite replaces the crystal borders. SEM-BSE-EDS &SEM. Dol = dolomite; Kln = kaolinite; Or = orthoclase; Sau = sauconite; Ser/Ilt = sericite/illite; Zn-dol = Zn-dolomite.

TABLE 4.7. Chemical compositions of sauconite from Yanque, and from literature (wt.%).

	Sauconite composition from literature			Yanque sauconite			
	*sauconite, Friedensville, Pennsylvania, USA	* sauconite, Coon Hollow, Arkansas, USA	+ sauconite, Skorpion, Namibia	YA-40-SAM-29	YA-19-SAM-18	YA-01-SAM-01	YA-40-SAM-29
SiO_2	34.46	33.4	35.2	39.28	36.24	36.19	38.06
TiO_2	0.24	0.15		0.00	0.05	0.00	0.00
Al_2O_3	16.95	7.45	6.7	15.59	10.16	7.97	3.68
Fe_2O_3	6.21	1.73	3.1	0.69	6.60	1.35	0.40
MnO		trace	0.2	0.15	0.11	0.04	0.00
CuO		0.13	0.4	0.00	0.00	0.00	0.00
ZnO	23.1	36.73	40.5	25.35	28.89	36.73	38.50
MgO	1.11	0.78	0.7	0.76	1.40	1.19	1.13
CaO		1.92	1.2	1.06	1.44	1.21	1.36
Na_2O		0.22		----------not determined----------			
K_2O	0.49	0.27	0.2	0.20	1.56	1.22	0.06
H_2O tot	17.39	16.92		§16.90	§14.04	§14.19	§16.74
Total	99.95	99.70		100.00	100.00	100.00	100.00

Notes: *from " www.handbookofmineralogy.org", +from Kärner (2006); §calculated from stoichiometry.

The Yanque sauconite has a ZnO content comprised between 35 and 40 wt. %, and contains relatively high amounts of other elements, averaging at 37.4 wt. % SiO_2, 1.3 wt. % MgO, 5.1 wt. % Al_2O_3, 0.7 wt. % K_2O, 1.5 wt. % CaO, and 1.7 wt. % Fe_2O_3 (TABLE 4.7, Fig. 4.17).

For sake of comparison, in TABLE 4.7 are also listed the sauconites measured by Borg et al. (2003) and Kärner (2006) in the Skorpion nonsulfide deposit in Namibia. The Skorpion sauconite occurs as coatings of secondary intergranular spaces and in voids of the silicate host rock, which have been formed through the breakdown or dissolution of detrital feldspar and mica (Kärner, 2006). As the Yanque Zn-smectite, also the Skorpion sauconite differs distinctly from the stoichiometric formula and displays a highly variable composition (Kärner, 2006).

The minerals of the sericite/illite group, at the reaction boundaries with the replacing sauconite, can contain up to 10 wt.% ZnO, mainly substituting for magnesium in the octahedral sites (Fig. 4.17). Potassium is the only interstratified cation, as normally is the case in this group of phyllosilicates.

Kaolinite (Fig. 4.17) can also contain variable amounts of zinc (up to 13 wt.% ZnO) in the zones where it is replaced by sauconite. Zinc in kaolinite could be linked to the –OH

compound in the clay structure (Peacock et al., 2005), or be associated with iron, which occurs as interstratified Fe-hydroxides (Nachtegaal et al., 2004).

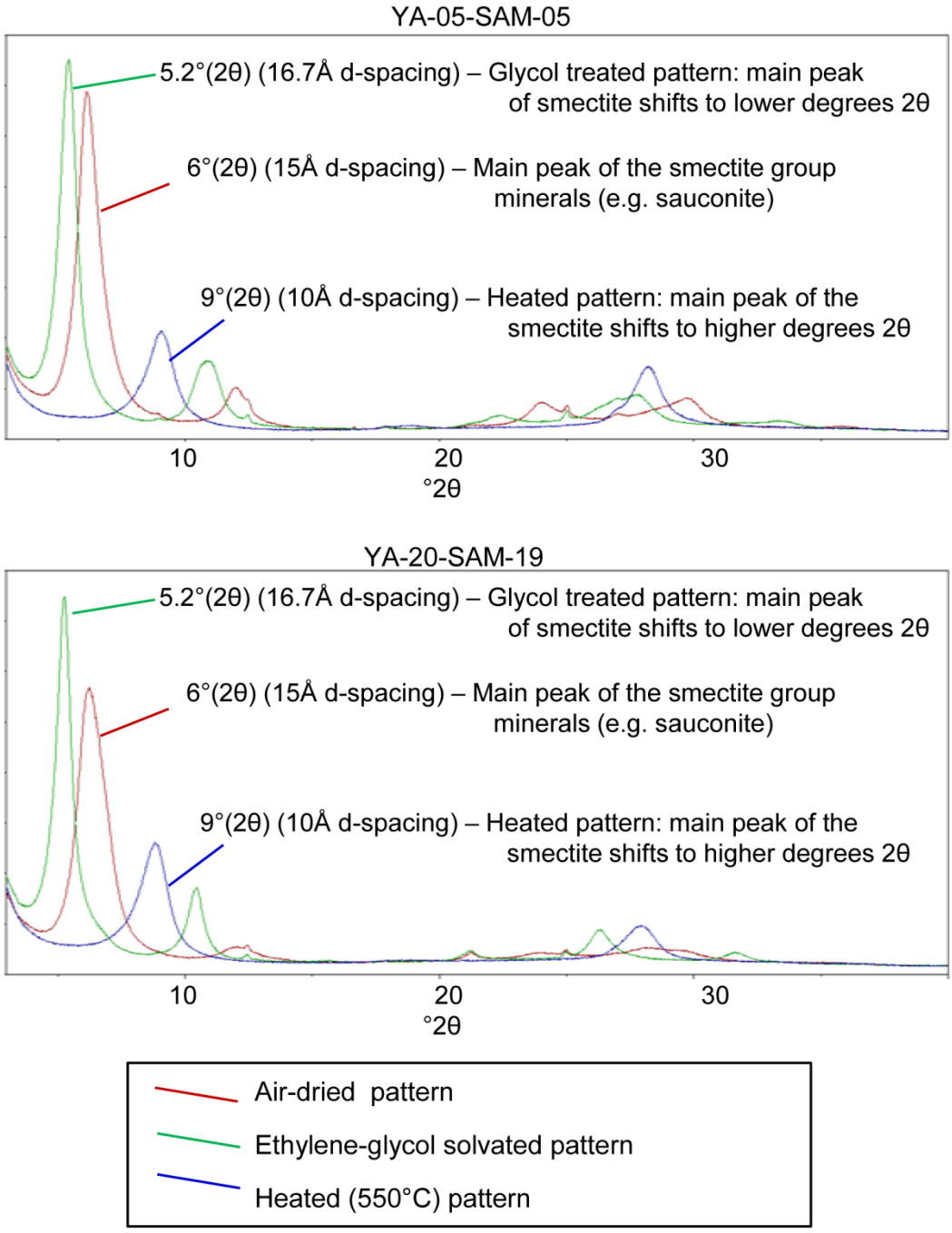

Fig. 4.16. YA-05-SAM-05 & YA-20-SAM-19. XRD traces of the air-dried clay oriented aggregates (red), and of the same clays treated with ethylene glycol (green) and then heated to 550°C (blue).

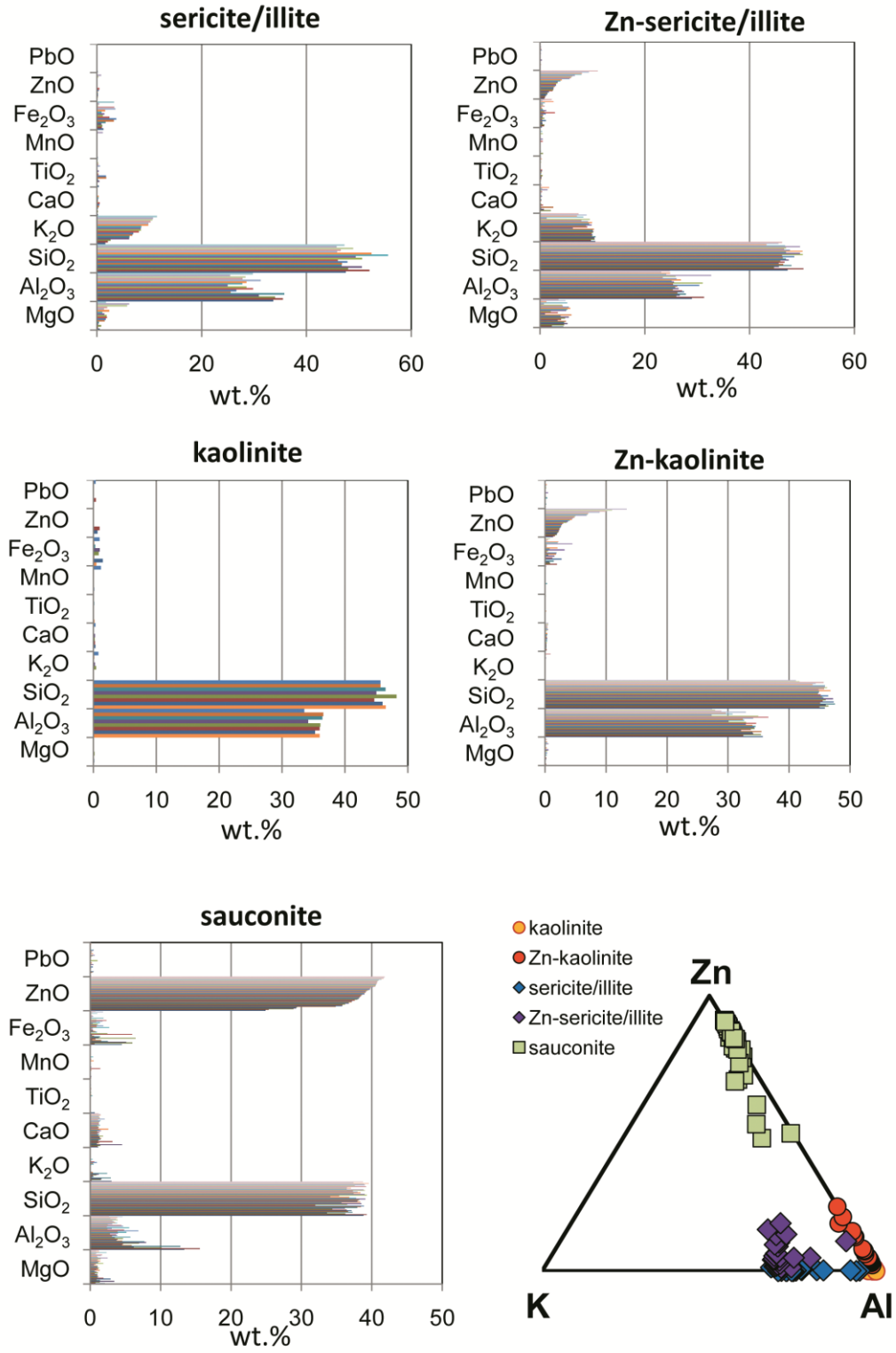

Fig. 4.17. Chemical compositions of Zn-clays at Yanque: sericite/illite - Zn-sericite/illite; kaolinite - Zn-kaolinite; sauconite. Clay compositions plotted in the system Zn-K-Al (num. atoms in calculated formula).

In the triangular diagram (Zn-Mg-K num. atoms in the calculated formula) presented in Fig. 4.17, it is possible to observe that the zinc field for the Yanque kaolinite is not very ample, whereas there is an almost continuum between the field corresponding to the sericite/illite composition and that of Zn-smectite.

In the sedimentary rocks, hydrothermal dolomite appears darker at the external boundary of the crystals/clasts and along fractures, where Fe-Mn-(hydr)oxides precipitate. A peculiar supergene alteration also takes place: along the external borders and in fractures the dolomite crystals are replaced by Zn-rich phases (Boni et al., 2011) (Fig. 4.18A,B,C,D). These phases are characterized by a substitution of Zn in the structural sites of Mg, as mentioned by Boni et al. (2011, and references therein). While the unaltered dolomite contains only small amounts of iron and manganese (around 3 wt.% FeO and less than 1 wt.% MnO), the new supergene phases can have up to 20 wt.% ZnO (averaging 10 wt.% ZnO), and variable amounts of cadmium (below 2 wt.%).

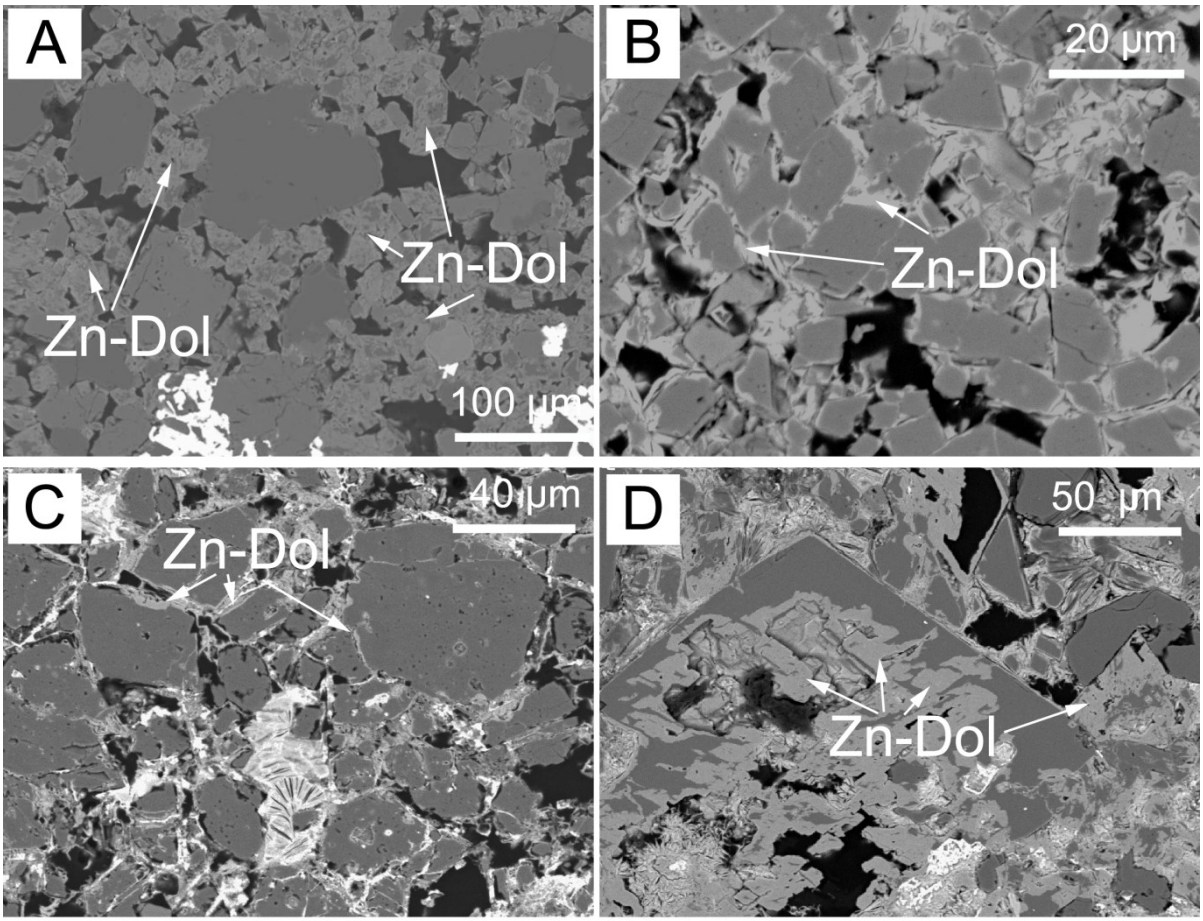

Fig. 4.18. Zn-dolomite. A) YA40-SAM-29. Zn-dolomite replacing the rims of dolomite crystals, cementing quartz and feldspar clasts. B) YA82-26-27. Zn-dolomite replacing microcrystalline dolomite. C) YA20-9.45-10.45. Zn-dolomite at the rims of dolomite crystals of various size. D) Yanque sample from Boni et al. (2011). Hydrothermal dolomite macrocrystals heavily replaced by Zn-dolomite phases. SEM-BSE-EDS.

Supergene alteration has caused also the precipitation of hemimorphite and smithsonite in the porosity and in the fracture network of the host rock. The hemimorphite-smithsonite ore assemblage has been identified in discrete amounts only in the samples with higher zinc grades, while the Zn-clays occur everywhere, even in the samples where the Zn-grade is relatively low. Smithsonite occurs as rhombohedral crystals and agglomerates.
Mineral chemistry of smithsonite can be pure, or may contain Mg (up to 6 wt.% MgO), Pb (up to 1.5 wt.%), and Cd (up to 2 wt.% CdO) (Fig. 4.19A,B). Hemimorphite occurs mainly as fan-shaped aggregates of tabular crystals, in veins and porosity of the host rock. In the earliest stages, it replaces smithsonite locally. In some lithotypes, it occurs as agglomerates of crystals within clay layers enriched of Zn-smectite (Fig. 4.19C,D).
The Zn-sulfide, sphalerite, is almost absent at Yanque. It has been observed only in a small galena and pyrite vein, cutting the Mara quartzarenite a few meters below the sedimentary breccias and the main part of the supergene deposit.

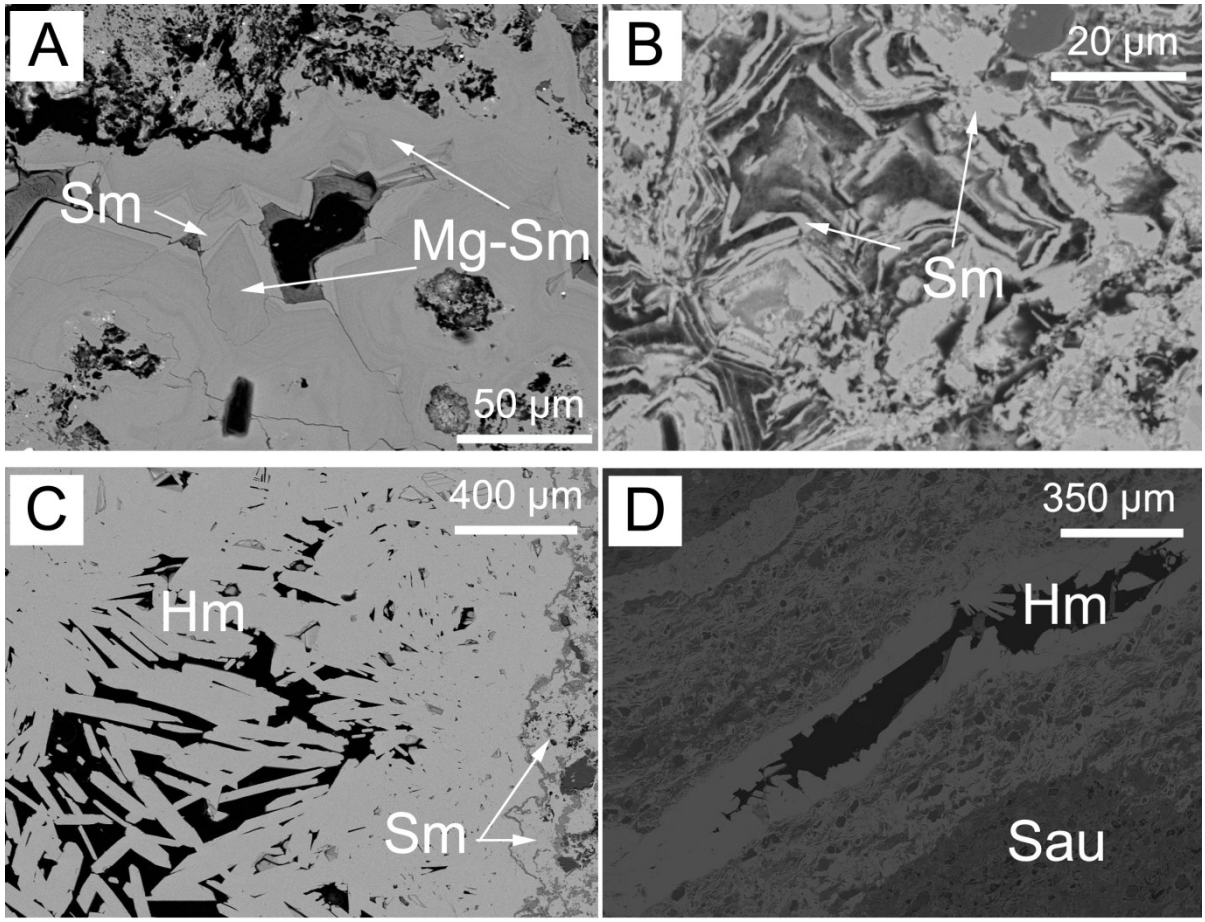

Fig. 4.19. Smithsonite & hemimorphite. A) YA20-16.45-17.45. Smithsonite concretions; the internal parts are enriched in Mg. B) YA20-18.45-19.45. Smithsonite concretions. C) YA20-9.45-10.45. Hemimorphite crystals agglomerate in a cavity, partly replacing a previous smithsonite concretion. D) YA01-SAM-01. Hemimorphite geode, within a sauconite enriched sample. SEM-BSE-EDS. Hm = hemimorphite; Mg-Sm = Mg-smithsonite; Sm = smithsonite.

Both galena and pyrite are strongly weathered, and replaced by the Pb-carbonate cerussite [$PbCO_3$] and by Fe-(hydr)oxides respectively (Fig. 4.20A). Cerussite occurs also as supergene cement in the host rock: among the conglomerate clasts, the detrital quartz and feldspar (Fig. 4.20B), among the epigenetic dolomite crystals, and as concretions filling the remaining porosity. SEM-EDS analyses show that cerussite may contain small percentages of Zn (~1 wt.% ZnO), and (surprisingly) very high amounts of Sr (Fig. 4.20C).

In particular, it was possible to detect in some cerussites SrO contents variable from 2.5 wt.% to a maximum of 47 wt.%. This SrO amount, combined with only 15 wt.% PbO, indicates that the mineral almost approaches the composition of strontianite [$SrCO_3$] (Fig. 4.20D). The continuum compositional trend suggests the presence at Yanque of an almost complete cerussite-strontianite solid solution.

Anglesite [$PbSO_4$] occurs locally in veinlets and small concentrations. Anglesite generally replaces galena, and is replaced in turn by cerussite (Fig. 4.20E). SEM-EDS analyses show that anglesite can host silver and barium in the lattice (around 1-1.5 wt.% of single metal), and in analogy with cerussite, it can also contain strontium. In the Yanque anglesite SrO ranges from a minimum of 1.5 to a maximum value of 40 wt.%, with a PbO content below 20 wt.%: these compositions indicate that the “Pb”-sulfate is almost approaching the composition of celestine [$SrSO_4$] (Fig. 4.20F). Again it is possible to envisage a solid solution between anglesite and celestine.

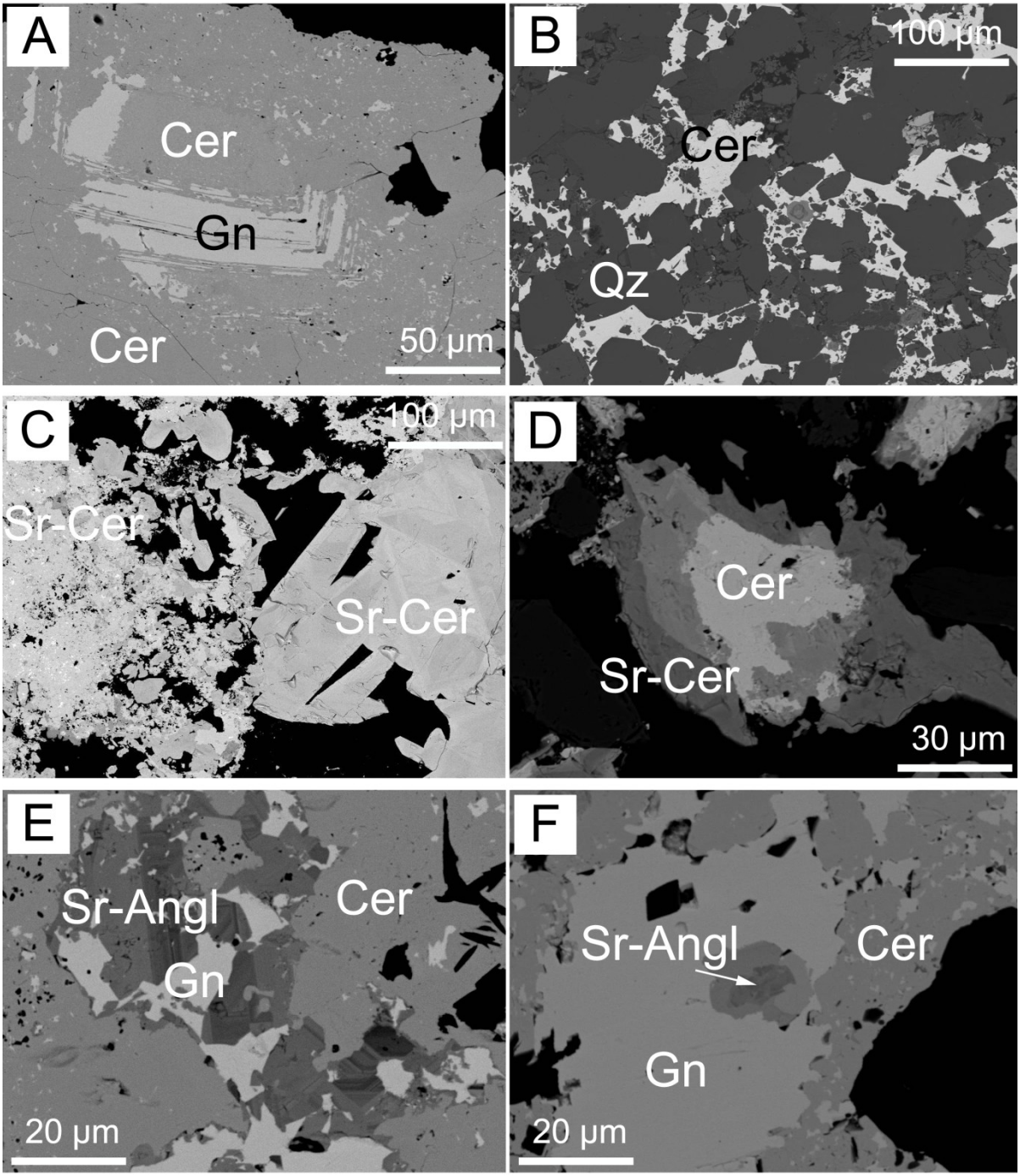

Fig. 4.20. Pb-minerals. A) YA20-16.45-17.45. Cerussite replacing galena. B) YA49-95-96. Cerussite in the matrix of host rock. C) YA49-94-95. Macrocrystalline (on the right), and microcrystalline Sr-cerussite (on the left). D) YA49-94-95. Sr-cerussite (with variable Sr contents) and cerussite replacing galena. E) YA49-95-96. Sr-anglesite (with variable Sr contents) and anglesite replacing galena; cerussite replaces both galena and anglesite. F) YA49-95-96. SEM-BSE-EDS. Sr-anglesite (with variable Sr contents) and anglesite replacing galena; cerussite replaces both galena and anglesite. Cer = cerussite; Gn = galena; Qz = quartz; Sr-Angl = Sr-anglesite ; Sr-Cer = Sr-cerussite.

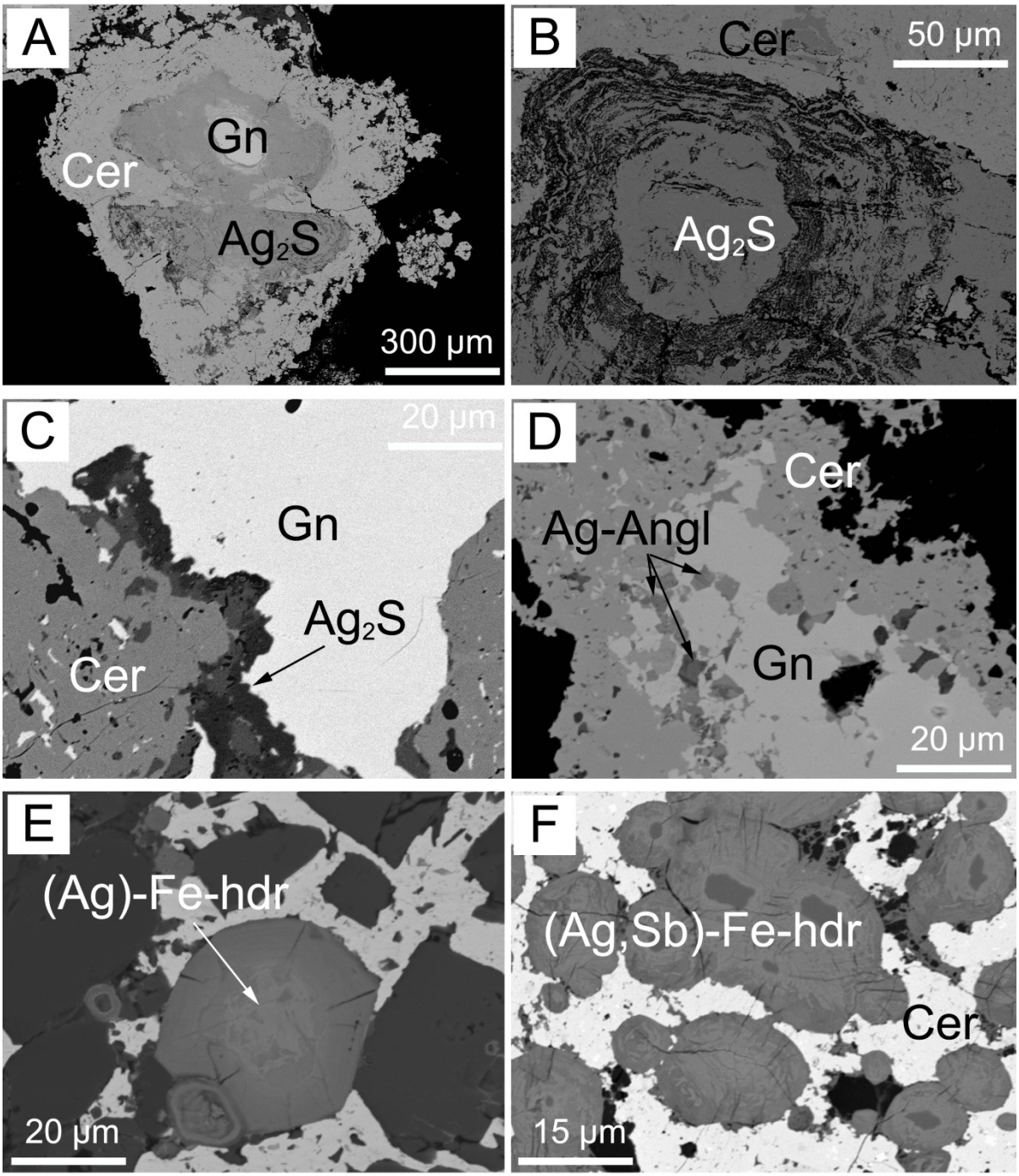

Fig. 4.21. Silver minerals. A) YA33-155.1-156.1. Silver sulfide and cerussite, replacing galena. B) YA33-155.1-156.1. Silver sulfide and cerussite. C) YA33-155.1-156.1. Cerussite replacing galena: silver sulfide occurs at boundary between the two phases. D) YA49-94-95. Anglesite (containing Ag) and cerussite, replacing galena. E) & F) YA49-95-96. Fe-Si-Pb-(hydr)oxides containing Ag and Sb. SEM-BSE-EDS. Ag_2S = silver sulfide; Ag-Angl = Ag-anglesite; (Ag)-Fe-hdr = (Ag)-Fe-(hydr)oxide; Cer = cerussite; Gn = galena.

Lead phosphates of supergene origin, as pyromorphite [$Pb_5(PO_4)_3Cl$] and plumbogummite [$PbAl_3(PO_4)_2(OH)_5•(H_2O)$], as well as Pb-arsenates, like mimetite [$Pb_5(AsO_4)_3Cl$] have been detected by SEM-EDS. The arsenates can locally contain up to 5 wt.% V_2O_5, and are intergrown with anglesite, replacing galena.

Secondary silver sulfide [Ag_2S] has been identified in few samples in the deeper levels of the deposit. It occurs in the replacement reaction zone between galena and cerussite (Fig. 4.21A,B) as concretionary rims, in which it is not possible to distinguish a peculiar crystal habitus (Fig. 4.21C). Silver has never been identified in galena as native element, probably because, if present, it may occur in very low amounts. However, the textural characteristics suggests that cerussite is not able to keep silver in its lattice: hence the precipitation as secondary sulfide in the reaction rim. Small contents of silver (~1-2 wt.%) are contained in anglesite replacing galena (Fig. 4.21D), and are also associated with Sb in a few Fe-(hydr)oxides (~1 wt.% AgO, ~1-4 wt.% SbO) (Fig. 4.21E,F); the metals here detected can possibly derive from weathered sulphosalts.

Variable lead and zinc amounts are associated at Yanque with two different types of hydroxides, mixed in various proportions. Mn-hydroxides typically contain high amounts of lead (up to 35% PbO) and ca. 5% ZnO on average. Notable amounts of Fe-hydroxides also occur (Fig. 4.22A), which contain on average 8 to 9% PbO and 7-8 % ZnO, reaching up to 15% of combined metals. Fe-hydroxides are always Si-rich (up to 10 wt.%), whereas silicon is lacking in Mn-hydroxides. The Zn-rich chalcophanite [$(Zn,Fe^{2+},Mn^{2+})Mn_3^{4+}O_7•3H_2O$] has been detected in the Yanque samples as well. Hydroxides are disseminated in the mineralized groundmass, and show various types of aggregates (elongated, rounded, concretionary, spongy). They constitute the main part of the gossanous samples, but can be intergrown with Zn-clay minerals in the high grade sections of the deposit (Fig. 4.22B).

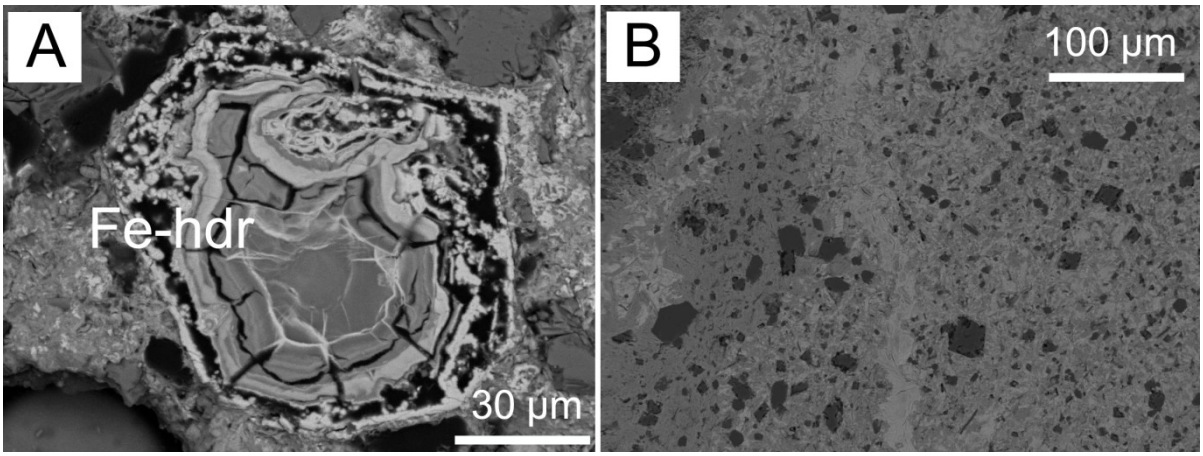

Fig. 4.22. A) YA17-SAM-16. Rounded concretion of Fe-Zn-Si-hydroxide. B) Mn-Pb-Zn-hydroxides mixed with sauconite. SEM-BSE-EDS. Fe-hdr = Fe-hydroxide

Major and minor element geochemistry

Major and minor element composition in the drillcores has been measured by Zincore Metals on more than 7000 samples, corresponding generally to core intervals 1-2 m long. Typical analyses of the Yanque ore deposit are shown in TABLE 4.6. Measured metals were: Zn, Pb, Cu, Au, Ag, and Mo. Other elements of lesser economic importance were: Al, As, B, Ba, Be, Bi, Ca, Cd, Co, Cr, Fe, Ga, Hg, K, La, Mg, Mn, Na, Ni, P, S, Sb, Sc, Sn, Sr, Th, Ti, Tl, U, V, W, Y, Zr.

Zinc occurs in the YA-52 drillcore between 4.7 and 5.7 m depth with a maximum concentration of 42.4 wt.% Zn metal. Zinc grades are higher in the topmost part of the conglomerate host rock (between 3 and 20 m depth) while, moving southward in the dolomite breccia, the higher grades have been detected more in depth (generally between 30 and 50 m, and in the YA-33 around 120 m depth). Lead occurs with a maximum concentration of 41.6 wt.% Pb metal in the YA-49 core between 95 and 96 m depth. Contrary to Zn, the Pb grades are higher in the deeper parts of the deposit. In particular, the higher Pb grades have been measured between 50 and 80 m depth in the conglomerate, and even deeper in the dolomite breccia (90-180 m).

Molybdenum occurs only in traces. Silver may occur with concentrations over 100 ppm in several samples, associated to Pb-rich ore zones. Its maximum concentration is around 200 ppm, detected in cores from the deepest parts of the deposit. Antimony occurs with a maximum value of 1288 ppm. The maximum concentrations of arsenic range around 2900 ppm, cadmium reaches a maximum of 5600 ppm, and thallium a maximum of 110 ppm. Cadmium is not always associated with zinc minerals, whereas thallium is contained in the samples rich in manganese (as in Accha, Boni et al., 2009).

Copper has a maximum concentration of 0.2 wt.% in two deep samples containing pyrite veins, but it remains around 0.05 wt.% in less than 20 samples.

The other elements are either not significant for this study, or their values are clearly below the detection limit.

Sulfur isotopes geochemistry

Sulfur-isotope analyses have been carried out on some sulfides and sulfates from the Yanque and Puyani orebodies, as well as on a galena from the Dolores porphyry copper for comparison (TABLE 4.8). The $\delta^{34}S$ values of barite from Yanque (YA 121-43.75) and Puyani veins are 11.1 and 9.4‰ $\delta^{34}S$ respectively.

The $\delta^{34}S$ value in the galena from Dolores (DOL 10-446.5) is 2.72‰ $\delta^{34}S$ CDT, consistent with a prevailing origin of the sulfur from the magmatic intrusion. The pyrite YA 128-49.30, sampled from a small vein in the Yanque deposit shows a slightly heavier value (6‰ $\delta^{34}S$ CDT), but still reflecting a magmatic influence. Two galenas from the same deposit (YA 99-110.65 and YA 49-95-96) have different values: -13.4 and -17.9‰ $\delta^{34}S$ CDT respectively.

TABLE 4.8. Sulfur isotope data of Yanque district sulfide and sulfates.

Sample n.	Mineral	Description	δ^{34}S CDT (‰)
DOL-10-446.5	Gn	Galena vein	2.72
YA-99-110.65	Gn	Galena vein	-13.40
YA-49-95-96	Gn	Galena vein	-17.90
YA-128-49.30	Py	Pyrite crystals in barite vein	6.00
YA-121-43.75	Brt	Barite vein	11.10
PUY-1	Brt	Barite crystals	9.44

Abbreviations: Brt = barite; Gn = galena; Py = pyrite.

Lead isotope geochemistry

Pb isotope analyses (TABLE 4.9, Fig. 4.23) were carried out to gain information about the processes active in the deposition of the primary and secondary mineralization in the Yanque-Dolores district, as well as the possible source of the metals. The analyses at Yanque were carried out on galena and pyrite (hypogene), and on cerussite, Mn-(hydr)oxides, and sauconite (supergene). Lead isotope analyses have been carried out for comparison on a number of sulfide minerals from the Dolores Cu-porphyry mineralization, on several igneous rocks outcropping in the district, and on the sedimentary lithologies hosting the mineral deposits.

The galenas from the Yanque deposit have $^{206}Pb/^{204}Pb$ ratios between 18.613±0.002 and 18.656±0.002, $^{207}Pb/^{204}Pb$ ratios between 15.635±0.002 and 15.642±0.002, and $^{208}Pb/^{204}Pb$ ratios between 38.594±0.007 and 38.649±0.007. The galena from the Dolores porphyry copper is isotopically different: $^{206}Pb/^{204}Pb$ = 18.572±0.002, $^{207}Pb/^{204}Pb$ = 15.637±0.002, $^{208}Pb/^{204}Pb$ = 38.562±0.006. The pyrites from the Yanque deposit show $^{206}Pb/^{204}Pb$ ratios between 18.583±0.008 and 18.622±0.002, $^{207}Pb/^{204}Pb$ ratios between 15.642±0.002 and 15.653±0.006, and $^{208}Pb/^{204}Pb$ ratios between 38.605±0.0018 and 38.616±0.006. The pyrites from the Dolores mineralization are again isotopically different: $^{206}Pb/^{204}Pb$ = 18.545±0.003 and 18.574±0.002, $^{207}Pb/^{204}Pb$ = 15.632±0.003 and 15.642±0.002, $^{208}Pb/^{204}Pb$ = 38.531±0.009 and 38.570±0.007.

The Pb isotopic ratios of two unaltered tonalites outcropping at Yanque are $^{206}Pb/^{204}Pb$ = 18.554±0.005, $^{207}Pb/^{204}Pb$ = 15.626±0.004 and $^{208}Pb/^{204}Pb$ = 38.562±0.010, and ^{206}Pb /^{204}Pb = 18.671±0.005, $^{207}Pb/^{204}Pb$ = 15.645±0.002 and $^{208}Pb/^{204}Pb$ = 38.750±0.004 (TABLE 4.9). A sericitized tonalite has a composition of 18.616±0.002, 15.633±0.002 and 38.594±0.006. The quartz diorite hosting the Dolores porphyry copper has an isotopic composition of $^{206}Pb/^{204}Pb$ = 18.549±0.027, $^{207}Pb/^{204}Pb$ = 15.699±0.022 and $^{208}Pb/^{204}Pb$ = 38.622±0.055.

The sedimentary host lithologies that have been analyzed are: the siliciclastic conglomerate, the interfingered dolomites and the carbonate breccia in the south of the Yanque site (TABLE 4.9). The siliciclastic conglomerate has been differently leached, to analyze the Pb isotopic composition of both the silicate clasts and the carbonate cement. The detrital clasts

have an isotopic composition of $^{206}Pb/^{204}Pb$ = 18.556±0.001, $^{207}Pb/^{204}Pb$ = 15.632±0.001 and $^{208}Pb/^{204}Pb$ = 38.512±0.004. The carbonate cement shows an isotopic composition of $^{206}Pb/^{204}Pb$ = 18.658±0.002, $^{207}Pb/^{204}Pb$ = 15.641±0.002 and $^{208}Pb/^{204}Pb$ = 38.490±0.006. Therefore, the silicate clasts and the matrix of a conglomerate with prevailing carbonate cement have a $^{206}Pb/^{204}Pb$ difference of about 0.102±0.004 (TABLE 4.9). In the limestone and dolostone have been measured values of $^{206}Pb/^{204}Pb$ = 18.638±0.002, $^{207}Pb/^{204}Pb$ = 15.627±0.002 and $^{208}Pb/^{204}Pb$ = 38.590±0.006, and $^{206}Pb/^{204}Pb$ = 18.645±0.003, $^{207}Pb/^{204}Pb$ = 15.631±0.002 and $^{208}Pb/^{204}Pb$ = 38.619±0.007 respectively. A marble, in contact with the quartz diorite of Dolores, has a composition of $^{206}Pb/^{204}Pb$ = 18.654±0.002, $^{207}Pb/^{204}Pb$ = 15.648±0.002 and $^{208}Pb/^{204}Pb$ = 38.607±0.004.

Pb isotope data of the supergene phases (sauconite, cerussite and Mn-crusts) are scattered. Sauconite values show $^{206}Pb/^{204}Pb$ ratios between 18.621±0.002 and 18.634±0.002, $^{207}Pb/^{204}Pb$ ratios between 15.630±0.002 and 15.637±0.002, and $^{208}Pb/^{204}Pb$ ratios between 38.601±0.004 and 38.613±0.005. Mn-hydroxides have a composition of $^{206}Pb/^{204}Pb$ = 18.640±0.002, $^{207}Pb/^{204}Pb$ = 15.640±0.002 and $^{208}Pb/^{204}Pb$ = 38.631±0.005.

The Pb isotope data from the whole mining district show $^{206}Pb/^{204}Pb$ variations within a range of 0.117±0.007, $^{207}Pb/^{204}Pb$ variations within a range of 0.022±0.006, and $^{208}Pb/^{204}Pb$ variations within a range of 0.238±0.008.

TABLE 4.9. Pb-isotope compositions of rocks and minerals from Yanque-Dolores district.

Sample n.	Location	Description	$^{206}Pb/^{204}Pb$	±2σ	$^{207}Pb/^{204}Pb$	±2σ	$^{208}Pb/^{204}Pb$	±2σ
YA-OUT-9	Yanque	Diorite/tonalite	18.554	0.005	15.626	0.004	38.562	0.010
YA-OUT-33	Yanque	Diorite/tonalite	18.671	0.002	15.645	0.002	38.750	0.004
YA-71-14-15	Yanque	Altered diorite/tonalite	18.616	0.002	15.633	0.002	38.594	0.006
YA-OUT-31	Yanque	Mara Fm. Limestone	18.638	0.002	15.627	0.002	38.590	0.006
YA-OUT-14	Yanque	Mara Fm. Dolomite	18.645	0.003	15.631	0.002	38.619	0.007
METY-2-23	Yanque	Mara Fm. Conglomerate - carbonate cement	18.658	0.002	15.641	0.002	38.649	0.006
METY-2-23	Yanque	Mara Fm. Conglomerate - silicate clasts	18.556	0.001	15.632	0.001	38.512	0.004
YA-OUT-19	Yanque	Marble	18.654	0.002	15.648	0.002	38.607	0.004
YA-99-110.65	Yanque	Galena	18.613	0.002	15.635	0.002	38.594	0.007
YA-OUT-1	Yanque	Galena	18.647	0.003	15.639	0.003	38.645	0.007
YA-49-95-96	Yanque	Galena	18.656	0.002	15.642	0.002	38.649	0.007
YA-99-110.65	Yanque	Pyrite	18.622	0.002	15.642	0.002	38.616	0.006
YA-109-149.80	Yanque	Pyrite	18.583	0.008	15.653	0.006	38.605	0.018
YA02-SAM-03	Yanque	Sauconite	18.634	0.002	15.634	0.002	38.613	0.005
YA05-SAM-05	Yanque	Sauconite	18.621	0.002	15.630	0.002	38.601	0.004
YA20-SAM-19	Yanque	Sauconite	18.626	0.002	15.637	0.002	38.603	0.005
YA-OUT-16	Yanque	Mn-crusts	18.640	0.002	15.640	0.002	38.631	0.005
YA-118-81.35	Yanque	Cerussite	18.668	0.002	15.640	0.002	38.657	0.005
DOL-9-84.10	Dolores	Galena	18.572	0.002	15.637	0.002	38.562	0.007
DOL-9-84.10	Dolores	Pyrite	18.574	0.002	15.642	0.002	38.570	0.007
DOL-10-446.50	Dolores	Pyrite	18.545	0.003	15.632	0.003	38.531	0.009
DOL-OUT-5	Dolores	Quartz monzonite	18.549	0.027	15.699	0.022	38.622	0.055

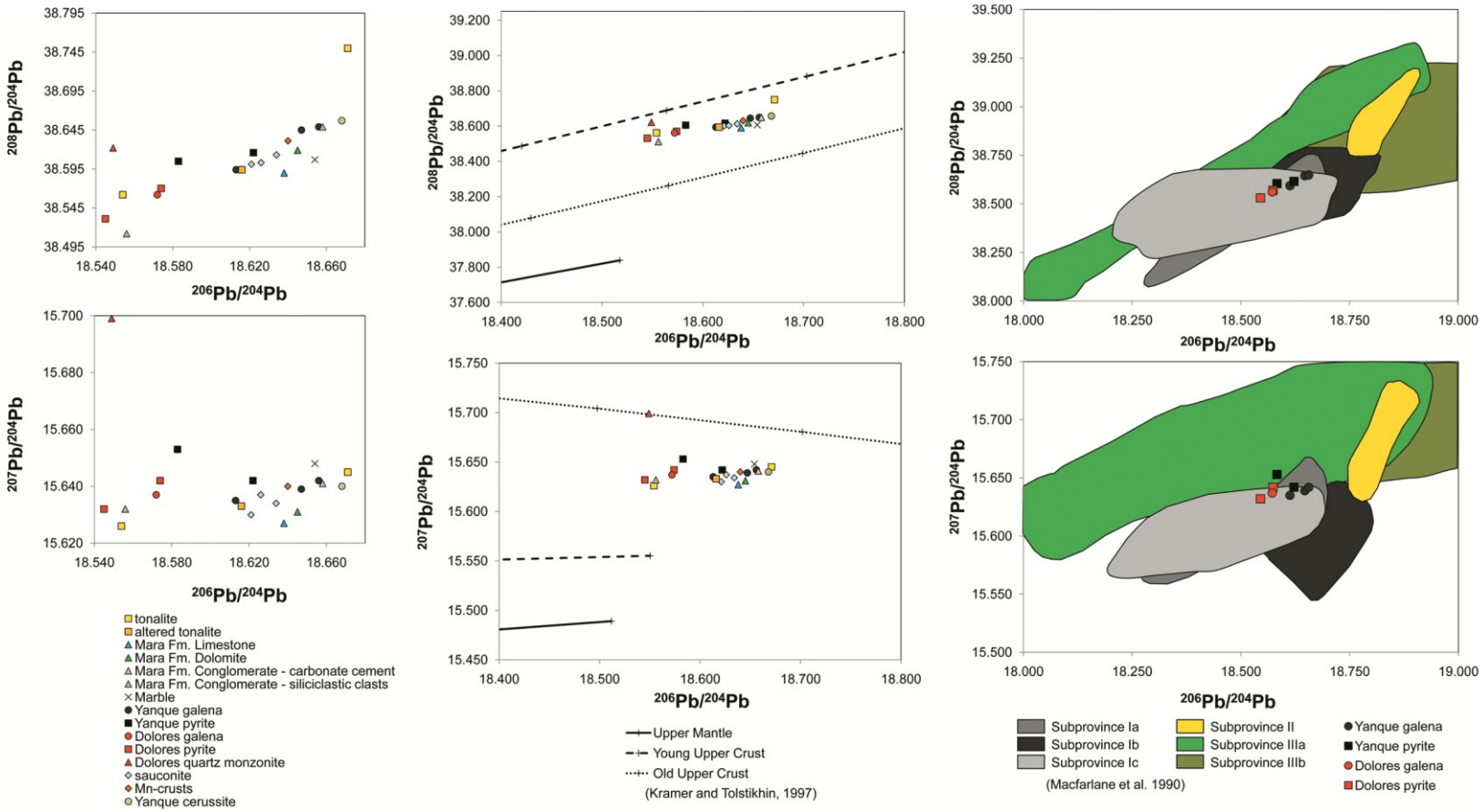

Fig. 4.23. Pb-isotope compositions of minerals and rocks from the Yanque-Dolores district.

Discussion

Primary mineralization in the Yanque-Dolores district

The Andahuaylas-Yauri belt is well known for its Cu-porphyry and magnetite skarn deposits, but no mention has been done so far on the possible occurrence of polymetallic (Zn, Pb, Ag, Mn etc.) mineralizations associated with the magmatic-hydrothermal ores (Perelló et al., 2003). One of the better-described examples of zoned polymetallic deposits is the Colquijirca mineralization in central Peru (Bendezú and Fontboté, 2009). In this deposit the zoning from the Cu mineralization to the Zn-Pb ores encompasses a number of distinct and well-defined mineralogical zones, which display both sharp and transitional boundaries. This zoning was formed during the second of the three recognized mineralizing stages that formed the deposit. The Yanque orebody is completely oxidized, and consequently, it does not show any of the characteristics observed in the "fresh" polymetallic deposit of central Peru (e.g. Moritz et al., 2001; Beuchat et al., 2004; Bendezú and Fontboté, 2009; Catchpole et al., 2011).

A study of the fluid evolution in a porphyry-related Cordilleran polymetallic veins has been carried out by Catchpole et al. (2011) in the Morococha district. This district is characterized by Cu-Mo and Cu-Au mineralized porphyries, cut by late Zn-Pb-Ag-Cu-bearing veins. A metal zonation displayed at the district-scale is also recognizable within the single veins, where the Cu-Fe-bearing minerals precipitated earlier than Zn-Pb-Ag-Mn-bearing minerals. The study of the base metal veins showed how Fe, Cu, Zn, Pb, and Ag precipitated from a fluid of magmatic origin, characterized by decreasing salinity, temperature and CO_2 content: the initial values of the fluid were 4-5 wt.% NaCl eq., 340°-380°C Th, and 3-5 mol% CO_2 respectively (Catchpole et al., 2011). The San Cristobal base metals district (Domo de Yauli) nearby, consists of Zn-Pb-Ag-Cu veins and carbonate-replacement deposits, surrounding a barren magmatic intrusion (Moritz et al., 2001; Beuchat et al., 2004). Lead- and sulfur-isotope analyses of sulfides and sulfates in mantos and veins from this district point to a magmatic origin for both elements (Moritz et al., 2001), a result that has been also confirmed by the fluid inclusion data (Beuchat et al., 2004). In particular, the Pb-isotopes of galena perfectly overlap the isotopic composition of the Miocene intrusions in the same area, and sulfur has the same magmatic values ($0<\delta^{34}S<5$) identified in the sulfides occurring in the porphyry and skarns deposits nearby.

Several Zn-Pb deposits, located around the northern border of the Santo Tomàs batholith have been discovered in recent times in the Andahuaylas-Yauri belt, as Accha-Titiminas, Camp Zone and Accha West (Boni et al., 2009; Zincore Metals Inc.), near the Alicia Cu-porphyry (Moss et al., 2012). The only Zn-Pb mineralization from this belt that has been scientifically investigated so far is the nonsulfide deposit of Accha (Boni et al., 2009). The Accha site is far from any known Cu-porphyry deposits of the area, but on the base of the metallogenic evolution of the whole belt, its primary mineralization has been also considered the result of magmatic-related hydrothermal process (CRD-type) (Boni et al., 2009). Contrary to Accha, the Yanque nonsulfide deposit is located within a small, but well constrained mineralized district, centered on the Dolores Cu-porphyry, comprising two other

Zn-Pb mineral occurrences. By simple observation this district appears like a sort of "porphyry-Cu system", with a Cu-porphyry in the center (Dolores) and a surrounding halo of distal Zn-Pb ores. Unfortunately, similarly to Accha, the Yanque primary mineralization is almost fully weathered and replaced by oxidation ores. Only few remnants of galena, pyrite, and barite veins can be observed; sphalerite is extremely rare. At Puyani and Yanque East, small veins containing galena and barite have been observed within the gossan. The Dolores deposit, instead, is very little weathered, and consists mainly of primary Cu-sulfides. Both the strong supergene alteration at Yanque and a possible local tectonic discontinuity between Yanque and Dolores have hampered so far the observation of possible "crosscutting relationships" between the Zn-Pb ores and the Cu mineralization.

The primary mineralogical association and the host rock alteration (phyllic-argillic) at Yanque are pointing to a distal CRD, which may be connected to the Dolores Cu-porphyry body. The local occurrence of Ag-Sb-sulphosalt and the As abundance (up to 2900 ppm) speak about higher temperature fluids. The copper content is quite low, though; local enrichments have been measured only in few pyrite veins at the base of the deposit. A further evidence of a distal CRD character of the mineralization are the high amounts of manganese (Meinert et al., 2005), either diffused in the host rock, or concentrated in metal-scavenging concretions throughout the orebody.

The few sulfur isotopic values from the primary sulfides and sulfates in the district have shed only a partial light on the genesis of both deposits: whereas a magmatic signature has been detected on the Dolores galena and (dubitatively) on the Yanque pyrite, the galenas from the latter deposit have much lighter values. Possible sources of sulfur for Yanque and Puyani barite include Cretaceous seawater ($\delta^{34}S$ ~ +18 to +21‰ CDT) and/or evaporitic sulfate minerals occurring at the Mara/Ferrobamba interval. A limited mixing with magmatic sulfur can be also contemplated. The light values detected in the Yanque galenas may have been produced by thermochemical (TSR) reduction processes on the sedimentary sulfates contained in the Mara and Ferrobamba evaporites, triggered by hydrothermal circulation. Another explanation may contemplate the attribution of the measured galenas to the supergene process. In the latter case, the very light S-isotope composition of the sulfides (-13.4 and -17.9‰ $\delta^{34}S$ CDT) may be indicative of bacterial sulfate reduction. However, to unravel the genetic issue on the basis of the sulfur isotopes, a much greater number of analyses would be necessary, which is out of the aims of the present thesis.

Following the regional considerations of the literature, it could be established that the igneous rocks in the Yanque-Dolores mining district are perfectly in the range of the Pb isotopic compositions of the *Cordillera domain* of Mamani et al. (2008), and that the Pb isotopic values of the sulfides in the Dolores Cu-porphyry, as expected from the metallogenic setting of the region (Perelló et al., 2003), are in the field belonging to subprovince Ic of Macfarlane et al. (1990), which depicts the Tertiary magmatically-derived ores in this part of Peru (Fig. 4.23). The Pb isotopic composition of Yanque primary sulfides is also comprised in the same field of values; hence this deposit should be genetically related to the Tertiary magmatic activity as well. These data, framed into the geological setting of the whole area, support a common origin for Dolores and Yanque mineralizations. Yanque

should be considered as a distal product of the porphyry system whose center would have been located at Dolores.
In the Kramers and Tolstikhin (1997) model, the Yanque samples plot between Young and Old Upper Crust, indicating that their lead is derived from both a juvenile source and an old basement (Fig. 4.23). Looking more in detail, we could observe ubiquitous small but resolvable differences and disequilibria, which affect the three lead isotope ratios of the sulfides in different ways, probably indicating that many components contributed to the final lead isotope signature. Yanque galenas have distinct Pb isotopic compositions, both among them and also if compared with the Pb isotopic composition of the galenas from Dolores. Igneous rocks show a large spread in the isotopic composition, possibly indicating variable degrees of country rock assimilation, or different isotopic compositions of the magma pulses. The samples collected on the Yanque site form an almost compact cluster of data, but it is possible to resolve significant differences. The siliciclastic material of the conglomerate has lower values, whereas its hydrothermal cement has the same composition of one of the galena samples. Similar values have been detected in the hydrothermally affected igneous rock (the Yanque tonalite). This could indicate that the same hydrothermal fluids, which altered the host rock, deposited also the sulfides. In any case, the observed significant spread of the Pb isotopic compositions is not compatible with a simple genetic model involving just one fluid circulation episode.

Supergene nonsulfide mineralization: geology, mineralogy and geochemistry
As described in the previous paragraphs, the geology of the Yanque district is characterized by composite sedimentary, structural and magmatic features, which all together have played a role in the emplacement of mineralization.
Sedimentary rocks in the area occur as siliciclastic and carbonatic lithologies of Jurassic-Cretaceous age. They can be grouped in a succession deposited in environments ranging from continental to shallow-water marine. The succession starts with well-bedded quartzarenite (Soraya Fm.), passes to sandstone and mixed carbonatic-siliciclastic breccias (Mara Fm.), and is concluded by the deposition of limestone (Ferrobamba Fm.). The Mara Fm. may have been deposited in a fan delta sedimentary environment, at the border of a tectonically active basin with carbonate sedimentation (Ferrobamba Fm.). The hypothesized model is in accord with the published literature (see before).
Starting from late Cretaceous up to Pliocene, the sedimentary succession was deformed by many tectonic events, grouped in two main phases: the Incaic and Quechua orogenies (Perelló et al., 2003). In the area of the mining district, a domes-and-basins deformative pattern was developed as well as some trans-tensional structures, that accommodated the emplacement of igneous bodies associated with the Dolores porphyry copper deposit. The porphyry copper emplacement has produced a strong hydrothermal alteration in the surrounding sedimentary rocks, as well as in the previously deposited igneous lithologies occurring in the area. Main results of this hydrothermal alteration are the various phases (sericite, hydrothermal dolomite…) that have been observed in the Yanque samples.

On a general scale, the morphology of the Yanque area appears strongly "dissected", with deep valleys. This highlights the importance of the tectonic uplifts, which have favored the development of weathering process within the primary ore deposit, triggering the oscillations of the groundwater level, and causing a migration of the supergene alteration front. In analogy with large parts of the Yauri batholith, the Yanque site currently lacks a sedimentary cover, thus reflecting a possible series of uplift and erosion stages, subsequent to the emplacement of the igneous rocks. The uplift phases may have also enhanced the fracturation of the host rock, creating preferential pathways for the down- and lateral flow of the metal-carrying solutions. As suggested for the Accha deposit (Boni et al., 2009), and for the supergene enrichments capping the Cu-porphyry in the whole region (Perelló and Posso, 2011), the main uplift episodes in the Yanque area may be Pliocene in age.

The Yanque supergene deposit is hosted only in siliciclastic conglomerates and in dolomite breccias in the northern part of the Yanque site, whereas the limestone breccia in the south is barren. The 3D-model shows that the mineralization is located in a structural basin, overlying the Mara Fm. sandstone. The mineralized intervals follow the spatial orientation of the sandstone beds, and are laterally confined by a small structural dome occurring in correspondence of the transition between the dolomite and the limestone breccia. Moreover, the Yanque mineralization gradually deepens from the northern part of the deposit to the south.

The distribution of the supergene mineralization is probably related to the different permeability of the involved host lithologies, and to the structural orientation of the hydrological barriers. In fact, the siliciclastic conglomerate and the dolomite breccia were more permeable for groundwater circulation than sandstone and quartzarenite. These more impervious lithologies may have hindered the downward migration of the fluids, with the subsequent precipitation of the metals within the conglomerates. The basin shape of the sandstone beds has facilitated a confining phenomenon of mineralization. Moreover, the tectonic deformation has produced a strong fracturation of the host rock, which has favored also the precipitation of supergene minerals in veins. The absence of mineralization in the limestone breccia, as well as the sulfide remnants in the conglomerates let to hypothesize that at least part the original sulfides were initially concentrated in the siliciclastic conglomerate.

Zinc mineralization - Sphalerite has been observed only as few crystals in small veins at the bottom of the Mara Fm. sandstone, but it is lacking in the main orebody. However, the occurrence of secondary Zn minerals, such as Zn-clays, hemimorphite and smithsonite, suggest that sphalerite must have been present to large extent in the primary mineralization. In the Yanque deposit zinc is mainly allocated in the clay mineral sauconite, rather than in smithsonite, and hemimorphite. Hemimorphite and smithsonite occur in discrete amounts only in the high-grade zinc samples, while Zn-clays prevail in the samples of the lower Zn-grade zones. Furthermore, zinc has been locally found in several generations of Fe-Mn(hydr)oxides, and along the edges and in fractures of euhedral dolomite crystals, where it replaces magnesium during the supergene alteration process. The occurrence of Zn-dolomite

is not unusual in this type of deposits, as reported in Boni et al. (2011), and can have a negative role in the economic evaluation of the deposit (Mondillo et al., 2011).
The occurrence of zinc mainly in phyllosilicates is probably due to the fact that the supergene mineralization at Yanque, contrary to the Accha deposit nearby (Boni et al. 2009), is prevailingly hosted in siliciclastic rocks. The siliciclastic conglomerate contains feldspars, sericite/illite, and kaolinite. Feldspars are of clear detrital origin, whereas the phyllosilicates are mainly hydrothermal. Sericite/illite is associated to the typical porphyry-related hydrothermal alteration of the phyllic type, whereas kaolinite formed during the late leaching stages of hydrothermal alteration.
Considering that weathering of an immature siliciclastic rock implies the alteration of feldspars and micas and the formation of clays, one should imagine that the occurrence of zinc ions in the groundwater has favored at Yanque the formation of Zn-clays instead of pure smectites. During the supergene process almost all the available zinc was mainly retained in Zn-smectites. Hemimorphite and smithsonite precipitation was a subordinate process that took place when the supergene Zn-rich solutions had fully Zn-saturated the clay minerals. At this stage, the excess remaining zinc could locally react with carbonates, and precipitate in voids and late veins as neoformed Zn-hydrosilicate and Zn-carbonate.
The compositions of all phyllosilicates occurring at Yanque are plotted in the triangular diagram of Fig. 4.17. Sericite/illite and kaolinite occur both as pure phases and as Zn-enriched minerals. Smectite occurs instead only as the Zn-mineral sauconite. It seems that the zinc field for the Yanque kaolinite is not very wide, whereas there is a continuum trend between the field corresponding to the sericite/illite composition and that of Zn-smectite. This could be explained by the genetic interpretation of the clay minerals in the Yanque deposit. In fact, as observed in SEM-EDS, sericite/illite is replaced by Zn-smectite. After the diagram of Fig. 4.17 it seems that both sericites and/or illites were progressively enriched in zinc during the weathering of the host rock, until reaching the Zn-smectite composition:

primary silicates → sericite/illite → Zn-smectite

Kaolinite has been also moderately enriched in zinc during the supergene process, but this clay minerals is not structurally apt to contain high amount of interlayered cations.
Part of the Zn-smectite may also derive from direct supergene alteration of the detrital feldspars.
The alteration process can be exemplified by the following chemical reactions:

<u>Hydrothermal alteration</u>

$$2KAlSi_3O_8 + 2H^+ + 8H_2O \rightarrow \underset{\text{kaolinite}}{Al_2Si_2O_5(OH)_4} + 2K^+ + 4H_4SiO_4$$

$$3KAlSi_3O_8 + 2H^+ \rightarrow \underset{\text{muscovite}}{KAl_2(AlSi_3)O_{10}(OH)_2} + \underset{\text{quartz}}{6SiO_2} + 2K^+$$

$$2KAl_2(AlSi_3)O_{10}(OH)_2 + 2H^+ + 3H_2O \rightarrow 3Al_2Si_2O_5(OH)_4 + 2K^+$$
muscovite → kaolinite

Supergene alteration with zinc enrichment

$$KAl_2(AlSi_3)O_{10}(OH)_2 + nH_2O + Ca^{2+} + Mg^{2+} + Fe^{3+} + \mathbf{Zn^{2+}} \rightarrow (K,Ca,Na)(Mg,Al,Fe^{3+},\mathbf{Zn})_2(Si,Al)_4O_{10}(OH)_2\cdot nH_2O$$
muscovite → Zn-illite

$$(K,Ca,Na)(Mg,Al,Fe^{3+},\mathbf{Zn})_2(Si,Al)_4O_{10}(OH)_2\cdot nH_2O + nH_2O + \mathbf{Zn^{2+}} \rightarrow (\mathbf{Zn},Mg,Fe^{3+},Al,Mn)_3(Si,Al)_4O_{10}(OH)_2\cdot 4H_2O$$
Zn-illite → sauconite

$$Al_2Si_2O_5(OH)_4 + n\mathbf{Zn^{2+}} + Fe^{3+} + H_2O \rightarrow Al_2Si_2O_5(OH)_4\cdot Fe(\mathbf{Zn^{2+}})OOH + H^+$$
kaolinite → Zn-goethite sorption above kaolinite

$$Al_2Si_2O_5(OH)_4 + nH_2O + Mg^{2+} + Fe^{3+} + \mathbf{Zn^{2+}} + Mn^{2+} \rightarrow (\mathbf{Zn},Mg,Fe^{3+},Al,Mn)_3(Si,Al)_4O_{10}(OH)_2\cdot 4H_2O$$
kaolinite → sauconite

On the basis of the zinc mineralogical association, the Yanque supergene deposit shows many similarities with the Skorpion concentrations in Namibia. The most abundant zinc mineral in Skorpion is sauconite, like in Yanque (Borg et al., 2003). Moreover, sauconite at Skorpion occurs as coatings of secondary intergranular spaces and as void fillings in the silicate host rock, which have been formed after the breakdown and dissolution of silicate minerals, following a genetic process very similar to what happened in Yanque. Also the chemical composition of Yanque and Skorpion sauconites is quite similar, because both are slightly different from the standard sauconites (Borchardt, 1989).

Lead mineralization – During the supergene process, galena has been generally replaced by cerussite, but it has been also partly altered to anglesite. Cerussite can be scattered throughout the host rock, mainly close to galena veins; this implies that lead was only locally mobilized and soon precipitated in form of carbonate and/or sulfate. Cation exchanges can be often observed in both cerussite (Pb ⇆ Sr) and anglesite (Pb ⇆ Sr, Ba, Ag). Strontium in cerussite could be originated from the detrital feldspars of the host rock (Soraya or Mara Fms.), and/or from the evaporite minerals occurring in the carbonate layers at the base of the Ferrobamba Fm. Barium and silver could derive from the original primary mineralization or, as far as barium is concerned, from the K-feldspars. The paragenetic relationship between the Pb-bearing minerals may point to several oxidation stages of the sulfides. The simple oxidation of galena can produce anglesite, the reaction with the carbonates, instead, may precipitate cerussite.

Discrete amounts of lead (up to 30%) have been detected also in association with Mn-(hydr)oxides that are typical scavenger phases for several metals, as already reported by Boni et al. (2009) for the Accha deposit.

Taking into account the 3D-geochemical model of the Yanque orebody, a partial separation between zinc- and lead-rich zones can be observed: the zinc is more abundant in the top zone, whereas lead increases with depth. If we consider the different mobility of Zn^{2+} and Pb^{2+} ions in solution, the distribution of the metals within the deposit should be exactly opposite. In fact, as observed in many supergene orebodies, and as provided by geochemical equilibria, Zn^{2+} ion is more mobile than Pb^{2+}, and usually travels for longer distances and is enriched to greater depths than Pb^{2+} (Hitzman et al., 2003). A possible explanation of the inverse "chemical zoning" observed at Yanque could be found in the spatial distribution and possible location of the metallic sulfides from the primary ores. A crucial point is: was the primary mineralization occurring in the same area where the secondary zinc ores occur now? In fact, only galena (and galena replaced by cerussite) has been observed *in situ*, whereas sphalerite is totally absent and, contrary to Accha (Boni et al., 2009) not even remnant structures from the primary ores have been identified. Therefore, it may be possible that the primary zinc sulfide concentrations were located far from the position currently occupied by the nonsulfide mineralization: i.e. in the eroded rock volumes (Ferrobamba Fm.?) that surrounded the actual deposit site (Fig. 4.24A). A proof in support of this hypothesis can be found in the sole replacing character of the zinc nonsulfides. In fact, the zinc ions, derived from the supergene alteration of the original sphalerite-bearing rock volumes could have been carried in solution toward the porous lithologies at the boundary between the Mara ad the Ferrobamba Fms. (Fig. 4.24B), where they may have reacted with the host rock and precipitated as nonsulfide minerals through a wallrock replacement process (Fig. 4.24C). If this is true, the Yanque nonsulfide Zn deposit could be a sort of "Exotica" mineralization, like those occurring in the adjacent areas of several Cu-porphyry deposits (e.g. Chuquicamata, Sillitoe, 2005).

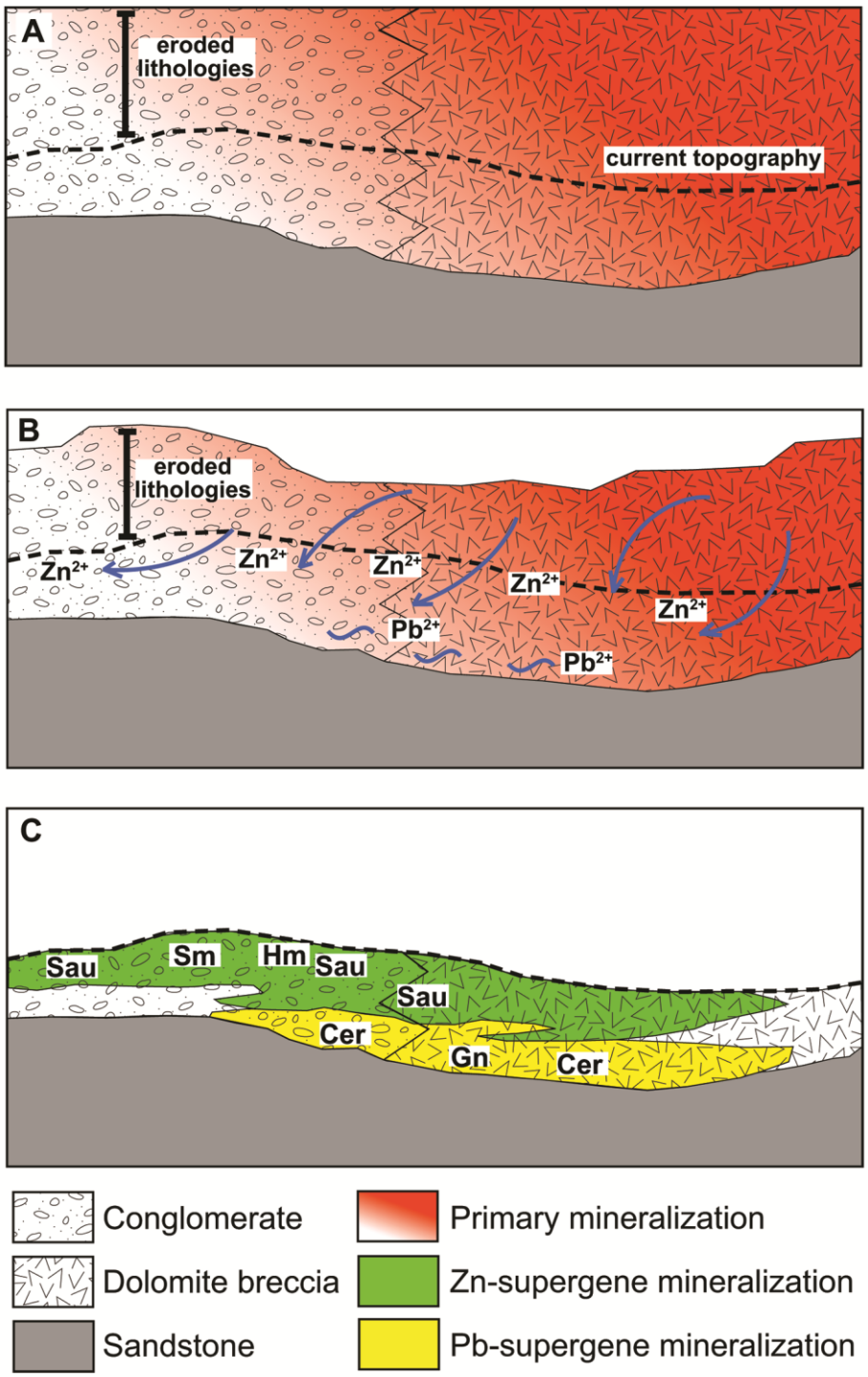

Fig. 4.24. Model of the supergene alteration at Yanque. A) Primary orebodies. B) Alteration of sulfides. C) Final supergene deposit.

Metallurgy

Following the successful completion of the pilot plant tests on the Accha ore (www.zincoremetals.com), a similar campaign was commissioned by Zincore Metals to Metallicon Process Consulting (Pty) Ltd. during 2010. The test was conducted on four composite ore samples (approximately 8.7 tonnes) from the Yanque deposit, through a pilot scale Waelz kiln (Valenta, 2010).

The pilot plant Waelz kiln had the following characteristics: 4 m length, 0.3 m internal diameter, speed drive variable between 1.5 to 2.0 rpm, and 2.4° inclination from the horizontal. The slope of the kiln and the speed of rotation were used during the test to control the residence time of the material in the kiln. The fumes generated in the kiln were extracted and the calcine product collected in a system consisting of a cyclone, baghouse and extractor fan (Valenta, 2010).

The results of the test work indicated that recoveries of about 91% and 98% zinc and lead respectively could be achieved. Despite these good results, under certain conditions of high temperatures, and longer residence time, the gangue phases started melting, producing a loss of recovery and high anthracite consumption (Valenta, 2010). This phenomenon was attributed to the high silica content in the analyzed samples.

The mineralogical study performed in this thesis clearly shows that the main gangue mineral is quartz, with minor amounts of dolomite. Moreover, the main Zn-mineral is sauconite, whereas smithsonite, with hemimorphite, is abundant only in the high-grade samples. Quartz is generally reactive with pyrometallurgical methods, but siliceous material can be also produced after sauconite decomposition.

Conclusions

The Yanque deposit is located within a small, but well constrained mineralized district, centered on the Dolores Cu-porphyry, comprising several Zn-Pb mineral occurrences. This district appears like a sort of "*porphyry Cu system*", with a Cu-porphyry in the center (Dolores) and a surrounding halo of polymetallic ores in veins and as cement of both carbonate and siliciclastic rocks (conglomerate) of Mesozoic age. The primary mineralogical association and the host rock alteration (phyllic-argillic) at Yanque point to a distal hydrothermal system, which may be connected to the emplacement of the Dolores Cu-porphyry body. The Pb isotopic composition of Yanque primary sulfides is compatible with a Tertiary magmatic origin, as in the Dolores porphyry copper. The analyzed igneous rocks in the whole area have variable Pb isotopic compositions, probably because of the interaction with different amounts of country rocks. The Pb isotopic composition of the Yanque sulfide and nonsulfide minerals reflect a mixing of many components, and no simple genetic model involving just one fluid circulation episode can account for the observed data variation.

The Yanque economic deposit consist mainly of Pb-Zn secondary nonsulfides, related to deep weathering processes probably of Pliocene age. The nonsulfide concentrations have several characteristics that differentiate them from many other standard worldwide "*calamine*"-type ores, as well as from the nearby Accha Zn>Pb nonsulfide deposit. The first

distinctive feature is that Yanque has a similar ore grade for both Pb and Zn, and is therefore much richer in lead compared to other nonsulfide deposits of this type.
Contrary to Accha, in the Yanque secondary mineralization zinc is allocated mainly in silicate minerals, rather than in carbonates, as it would be commonly the case for most Zn-nonsulfide deposits. The main Zn-mineral in the Yanque mineralization is Zn-smectite (sauconite). Most Zn-smectite was formed through supergene alteration of both hydrothermal and detrital phyllosilicates, occurring in the matrix of the host conglomerate.
Discrete amounts of hemimorphite and smithsonite also occur, especially in the high-grade samples. Variable amounts of zinc are contained in other clays, like sericite/illite, and kaolinite, and in the usual Mn- and Fe-(hydr)oxides. The dolomite cementing the host rock can also contain discrete zinc values, in variably enriched Zn-dolomite phases.
The main Pb-mineral is the carbonate cerussite, with minor amounts of remnant galena.
In the primary mineralogical association of the Yanque prospect no remnants of primary sphalerite have been ever identified: an issue that needs to be clarified when searching for the zinc source in the nonsulfide ores. Therefore, it may be hypothesized that the primary zinc sulfides were derived from the eroded rock volumes that surrounded the actual Yanque site, thus turning the nonsulfide concentrations in a special kind of “Zinc Exotica” type of deposit.

DISCUSSION AND CONCLUSIONS

In the previous chapters the geological and mineralogical characteristics of two supergene nonsulfide Zn-Pb deposits (Jabali and Yanque) have been described. The results and comments of the studies on each deposit have been reported separately at the end of the respective chapters. Here below I will compare the two deposits, highlighting both their common and distinct features, and discussing them in the context of other supergene nonsulfide Zn-Pb deposits, as reported in the dedicated literature. A comparison between the two deposits can be made by different points of view: host rock, ore mineralogy, textural characteristics and genetic processes.

The Jabali deposit is a carbonate-hosted nonsulfide Zn-Pb mineralization. The resource estimate (12.6 Mt) shows that its main commodity is zinc (8.9%), associated to moderate silver credits (68 ppm). Lead is a minor component (1.2%) and is recovered as by-product. The orebody is essentially constituted by smithsonite, in dolomite host rock. Smithsonite formed after the supergene alteration of a primary sphalerite mineralization, following both *direct* and *wallrock* replacement processes. Petrographic observations show that the process, started with sphalerite alteration, was developed through replacement of the dolomite host rock, characterized by a progressive substitution of Zn in place of Mg within the dolomite lattice, and was concluded by smithsonite formation. This phenomenon was followed by precipitation in veins and cavities of several generations of smithsonite crusts and concretions, and by agglomerates of gypsum crystals. Replacive and concretionary smithsonite can host part of Mg lost by the dolomite.

Hydrozincite and hemimorphite occur only within the outcropping parts of the orebodies, as observed also in other deposits by Hitzman et al. (2003) and Reichert and Borg (2008). Silver is associated with smithsonite as secondary Ag-sulfides. Lead occurs as primary galena and secondary anglesite and cerussite.

The C-O-isotope composition of smithsonite does not show the typical pattern of the supergene smithsonites like in other supergene deposits (Gilg et al., 2008). More in detail, the $\delta^{18}O$ values of smithsonite are generally lower than expected: this could indicate or a precipitation of smithsonite from a low-temperature (50-60°C?) hydrothermal system, or a supergene precipitation from waters with variable O-isotope composition.

The Yanque deposit is a siliciclastic-hosted nonsulfide Zn-Pb mineralization. The ore evaluation (12.5 Mt @ 3.5% Zn and @ 3.7% Pb) shows fairly comparable grades between Zn and Pb, which is an uncommon situation in the majority of supergene nonsulfide deposits. The orebody is characterized by a quite complex mineralogical association, partly reflecting the wide mineralogical variety of the host rock, but also caused by the ore forming processes. Zinc occurs mostly as sauconite (Zn-smectite), less as hemimorphite, and rarely as smithsonite. Primary galena and secondary cerussite and anglesite are the main Pb host. Sauconite forms during *wallrock* supergene replacement processes, where clay replaces detrital feldspars, hydrothermal/detrital sericite/illite, and hydrothermal kaolinite.
Hemimorphite and smithsonite precipitate in fractures and porosity of the host rock. Hydrothermal dolomite is locally replaced by Zn-dolomite phases, where Zn substitutes Mg within the dolomite lattice. Cerussite replaces directly galena, and forms also a cement of the host rock. A *direct replacement* of sphalerite has never been observed: this could make Yanque a sort of "exotic" supergene Zn mineralization.

Yanque and Jabali nonsulfide deposits differ for more than a single characteristic. Jabali is very similar to a typical carbonate-hosted "*calamine*" deposit, whereas Yanque is very different from most nonsulfide deposits, having many similarities with the Skorpion deposit in Namibia. I will concentrate first in comparing Jabali with other carbonate-hosted nonsulfide ores.
As mentioned in the Introduction, the term "*calamine*" is generally referred to a deposit hosted in carbonate rocks, consisting of smithsonite, hydrozincite, and hemimorphite. Zn-clays are present only in traces. After the comprehensive review of Hitzman et al. (2003), further specific studies carried out on other so-called "*calamines*", e.g. Belgium (Coppola et al., 2008), Ireland (Balassone et al., 2008), Poland (Coppola et al., 2009), Sardinia, Italy (Boni et al., 2003; Boni et al., 2013), Accha, Peru (Boni et al., 2009), Angouran, Iran (Boni et al., 2007), Mehdi-Abad, Iran (Reichert and Borg, 2008), and Sierra Mojada, Mexico (Hye In Ahn, 2010), have shown an unexpected complexity of this deposit type. Comparing the characteristics of the above deposits with those of Jabali, some interesting differences could be identified.
Belgium deposits (Coppola et al., 2008) are characterized by a supergene mineralogical association of smithsonite, hydrozincite, hemimorphite and Zn-clays, but surprisingly also by the presence of willemite, which is a typical Zn silicate of hypogene (hydrothermal) origin.
In the Upper Silesian (Poland) district (Coppola et al., 2009), nonsulfide ores consist of two types of mineralogical associations: a first comprising essentially Fe-smithsonite and Zn-dolomite, and a second characterized by smithsonite, goethite, minor hemimorphite and hydrozincite. The latter association is clearly due to supergene processes, but the first one has been considered the product of a low-temperature hydrothermal circulation (Coppola et al., 2009).
Sardinian Zn nonsulfides are hosted in a dolomite host rock. The mineral association consists of smithsonite, hydrozincite, and hemimorphite, replacing the host rock and filling a

recent karstic network (Boni et al., 2003). Cerussite, anglesite and the rare mineral phosgenite have been also identified. Smithsonite has a variable crystal shape, which depends on the depositional environment within the karstic system. The replacement process of the host dolomite proceeded with a progressive replacement of the dolomite by Zn-rich supergene carbonate phases, and was concluded with smithsonite formation (Boni et al., 2013).

At Mehdi-Abad (Iran), Reichert and Borg (2008) recognize an "oxidation stage" during weathering, when smithsonite was formed, and a "post-oxidation stage", associated with the precipitation of hydrozincite. These different stages are related to variable climatic conditions, and to the availability of oxygen and meteoric water.

The C-O-isotope study of Zn- and Pb-carbonates from many of these deposits (Boni et al., 2003; Coppola et al., 2008; Gilg et al., 2008; Coppola et al., 2009; Boni et al., 2013), shows that the composition of supergene smithsonite covers a well defined range of values, comprised, on average, between ~25-30‰ $\delta^{18}O$ SMOW, and -12 to 0‰ $\delta^{13}C$ PDB.

Two among the investigated deposits, which are carbonate-hosted and show a paragenesis typical of "*calamine*"-type ores, represent an exception in regard to their C-O-isotope geochemistry. These deposits are: Angouran, Iran (Boni et al., 2007), and Coahuila-Sierra Mojada, Mexico (Hye In Ahn, 2010). At Angouran (Gilg et al., 2006; Boni et al., 2007), the most abundant smithsonite phase coexists with newly precipitated sulfides (galena and arsenopyrite), and has a C-O-isotope composition characterized by positive $\delta^{13}C$ values (similar to those of hydrothermal travertines), and a wide spread of $\delta^{18}O$ ratios. At Coahuila-Sierra Mojada (Hye In Ahn, 2010), the situation is not so extreme, because smithsonite shows a $\delta^{13}C$ composition similar to other supergene smithsonites in other mining districts, but the $\delta^{18}O$ values are generally lower and outside of the "supergene smithsonite field" of Gilg et al. (2008).

Jabali is partly similar to Sardinian supergene deposits for the texture of the wall-rock replacement phases. In particular, it shows the same Zn-dolomite replacement of the host dolomite as in SW Sardinia (Boni et al., 2011, 2013). Instead, the Zn-dolomite in the Upper Silesian district in Poland has a texture different from those observed both at Jabali and in Sardinian, and has been considered of hydrothermal origin (Zabinski, 1986; Coppola et al., 2009). However, before the present thesis work Zn-dolomite, which can be considered as an intermediate phase between dolomite and smithsonite, formed during the wallrock replacement process, had been never identified in supergene nonsulfide deposits. The study of Reichert and Borg (2008), which produced a "geochemical model of supergene carbonate-hosted non-sulfide zinc deposits", totally forgets to report about the existence of several dolomite-hosted Zn nonsulfide deposits, and to consider a possible variation in the oxidation products in case of a dolostone host.

In the Jabali deposit there is a strict relationship between the newly formed Zn-dolomite and Mg-smithsonite phases, which results in a chemical "balance" among Zn and Mg induced by the supergene fluids (Boni et al., 2011; Mondillo et al., 2011). In fact, all the geochemical models, dealing with limestone host rock replacement (Takahashi, 1960; Hitzman et al.,

2003; Reichert and Borg, 2008), have resolved the balance of the formation of smithsonite in place of calcite, suggesting the precipitation of gypsum:

$$Zn^{2+} + SO_4^{2-} + CaCO_3 + 2H_2O + CO_2 \rightarrow ZnCO_3 + CaSO_4 \cdot 2H_2O$$

At Jabali, Mg-smithsonite partly balances the chemistry of the system, because traps in its lattice at least part of the Mg derived from dolomite. Gypsum crystals at Jabali occur in veins and are coeval with smithsonite, thus completing the above reaction. Gypsum contains sulfur derived from sphalerite (it shares the same S-isotopic value), and calcium from the replacement of dolomite.

The association of Ag-sulfides and smithsonite is another interesting characteristic of the Jabali deposit. Following Sangameshwar and Barnes (1983), who traced the chemical reactions forming nonsulfide deposits at the Burgin mine (USA) and Tynagh (Ireland), the co-precipitation of these two phases can be allowed, at atmospheric temperature, only at neutral pH, if Eh varies between 0 and -2 Volts, because the stability fields of the two phases are very near, but not superposed.

In regard to the C-O-isotopic geochemistry of smithsonite, Jabali is "out" of the normal field of supergene smithsonites identified by Gilg et al. (2008), as part of the smithsonites measured in the Coahuila-Sierra Mojada mining district (Hye In Ahn, 2010). In fact, the negative $\delta^{13}C$ values, typical of supergene smithsonites, are associated in Jabali with a $\delta^{18}O$ ratio lower than in other supergene deposits. These $\delta^{18}O$ values could point to smithsonite precipitation from a low-temperature hydrothermal system (Angouran style? Boni et al., 2007), or from groundwaters with variable isotopic composition, as hypothesized for the Coahuila-Sierra Mojada deposit (Hye In Ahn, 2010).

The common occurrence of Zn-dolomite at Jabali is also an important issue, because it can affect the evaluation of the deposit. The metallurgical process chosen for the Jabali orebody by ZincOx aimed to recover the maximum amount of Zn from smithsonite (Woollett et al., 2002). It was adopted a dissolving liquor that is "not-reactive" with dolomite, thus avoiding an excess of leaching fluid, which would have been happened when using the classic acid leaching, due to the "typical interactions with gangue and host minerals". However, this method prevents the recovery of Zn contained in dolomite that is lost in the processing. Using methods like XRD, DTA, and QEMSCAN®, I have shown how it is possible to detect fairly quickly the occurrence of this phase. QEMSCAN® is a technique very specific for the identification of Zn-dolomite phases, also quantitatively; XRD quantitative data, tested by chemical analyses, allow an evaluation of the amount of Zn not contained in the "regular" Zn-compounds (Mondillo et al., 2011); DTA, instead, easily detects if Zn-dolomite occurs or not within the analyzed samples (Mondillo et al., 2011). Therefore, one can assume that the use of these combined methodologies is extremely useful for the economic evaluation of dolomite-hosted nonsulfide Zn deposits.

In regard to the Zn-Pb Yanque deposit in Peru, a possible comparison with another nonsulfide concentration of the same type can be made only with the Skorpion mineralization in Namibia (Borg et al., 2003; Kärner, 2006), hosted in silicate rocks.

Skorpion is the biggest nonsulfide Zn deposit in the world, with 24.6 Mt @ 10.6% Zn. The mineralization is hosted by Neoproterozoic metamorphosed volcano-sedimentary rocks, and formed by oxidation and wall-rock replacement of a Late Proterozoic VMS-SEDEX Zn-(Cu) primary mineralization during Tertiary (Borg et al., 2003). The nonsulfide orebody consists of predominant sauconite, near substantial amounts of hemimorphite and smithsonite, with subordinate hydrozincite, tarbuttite and chalcophanite (Kärner, 2006). In both Skorpion and Yanque, sauconite is the most important Zn mineral. There are several differences between the deposits, though.

At Skorpion all nonsulfide minerals were considered to have been precipitated in the secondary porosity of the host rock, and also sauconite occurs mainly as coatings of intergranular spaces and voids, formed after the breakdown and dissolution of feldspars and micas (Kärner, 2006). Sauconite also replaces the early deposited supergene Zn minerals, as hemimorphite and smithsonite (Kärner, 2006). At Yanque, the features are slightly different: sauconite mainly replaces detrital feldspars, detrital/hydrothermal micas, and hydrothermal kaolinite, and a complete dissolution of the praecursor phases seems to be more limited. Several "intermediate" phases, e.g., Zn-sericite/illite, Zn-kaolinite, never observed at Skorpion, testify this gradual replacement process. Moreover, at Yanque, smithsonite and hemimorphite are the last phases to precipitate, and a very limited replacement of smithsonite by hemimorphite was observed only in the earliest stages of hemimorphite formation.

Considering the mineralogical associations of the two deposits, an important difference is the occurrence at Skorpion of Cu-secondary minerals, derived from an original Cu-concentration in the protore. Copper minerals are absent in Yanque, where, instead, secondary Ag-concentrations (as Ag-sulfides and enrichments in Fe-hydroxides) have been identified.

Another important issue regards the different mobilization of the metals within the host rock. At Skorpion, a spatial separation of iron and base metals was recognized (Kärner, 2006): in detail, the author distinguished a supergene lateral metal and mineral zonation pattern relatively to the position of the protore, evidenced by "separate" Fe, Cu, Pb, and Zn mineralized zones, that are the result of the different metal solubilities in the supergene fluids. At Yanque Zn is mostly enriched in the topmost volumes of the orebody, whereas Pb is concentrated in the lowermost levels. Surprisingly, this corresponds to an inverse zonation, compared to usual geometry observed in many other Zn nonsulfide deposits (Hitzman et al., 2003), including Skorpion (Kärner, 2006). In fact, Zn should be generally concentrated in the more distal areas of the deposit, whereas Pb, that is less mobile, is accumulated *in situ*, near the sulfide protore, occurring as cerussite/anglesite directly replacing galena (Hitzman et al., 2003). A possible explanation of the inverse zonation at Yanque can arise from the total absence of sphalerite in the mineralized area. Zn could originate from the dissolution of a primary sphalerite-rich ore, located somewhere in the eroded volumes of rock surrounding the actual site, and, after being transported by supergene solutions, it migrated and precipitated in the porosity of the host conglomerates: this kind of genesis could be associated to the concept of a Zn "exotic" mineralization.

The occurrence of sauconite as main ore mineral at Skorpion has been added as an evidence that the deposit formed under semi-arid to arid conditions during several paleo-weathering episodes, (Kärner, 2006). Semi-arid climates are generally favorable to deposition of smectite-type clay minerals (Barshad, 1966): a similar consideration can be done for the Yanque sauconite ores.

The geological, mineralogical and geochemical investigation on the Jabali and Yanque deposits has shown that both these Zn-Pb nonsulfide concentrations, though belonging to the mainstream of supergene deposits of this type, have some distinctive characteristics that could be of importance for their economic evaluation.
The common occurrence of Zn-dolomite at Jabali is deleterious when considering the economic exploitation of the ore, because it can generate a loss of Zn. Notwithstanding the issue, in the period 2005-08, the company owning the deposit (ZincOx) considered that the Zn recovery obtained from the metallurgical tests was sufficient to continue the development of the plant site and other infrastructures. Obviously, in more recent times, the mineralogical issue, added to the fall of Zn price and to the political instability in Yemen have hindered the possibility of further developing of the mining site.
At Yanque, the issue related to the sauconite (which is mixed with other clays too) occurrence is not simple to face from the processing point of view. At the moment, the metallurgical tests are focused to optimize the Waelz kiln ore processing, because the strategy of the company owing the property (Zincore Metals), is to process in a unique plant all the Zn-oxidized ores of the area (i.e. Accha Zn carbonates; Boni et al., 2009), and it is necessary to identify a method which combines a recovery of Zn from different mineralogical associations (sauconite/hemimorphite, hemimorphite/smithsonite, smithsonite/hydrozincite). Waelz kiln has been largely used for Zn extraction from sulfide ores in other mining sites, and the company is still working to increase its efficiency with the clay material of Yanque. The main issue encountered at the moment is the melting of the gangue phases (mainly silicates), which is clearly explained (and also predictable) after a mineralogical study of the deposit.

In conclusion, it is clear that the nonsulfide Zn deposits are a more complex matter than previously considered, both from a scientific and an economic point of view. The research carried out on the Jabali (Yemen) and Yanque (Peru) deposits has increased the knowledge on the nature and genetic mechanisms responsible for at least part of this type of deposits. The discovery of Zn-dolomite at Jabali, and of mixed Zn-clays at Yanque, represent an interesting step for a better understanding of the wall-rock replacement process. The observation of unusual C-O-isotope compositions in the Jabali carbonates enriches the available geochemical “database”, and contributes to avoid too many straight simplifications on the nonsulfide characteristics.
A good quality fieldwork, combined with an accurate mineralogical study, and an evaluation of the chemical analyses, are the best weapons to use both for the exploration and the evaluation of this kind of base metals concentrations. In fact, due to the very complex

mineralogical association encountered in many nonsulfide deposits (including those that are the object of this thesis), their economy is heavily controlled by the laws (and costs) of metallurgical processing.

ACKNOWLEDGEMENTS

Above all, I thank my two supervisors, Maria Boni and Giuseppina Balassone. Maria Boni introduced me to the Economic Geology when, during my third year at University, I was ready to become a "sad" geophysicist, and completely changed my academic perspective. I thank her for the help and support during the last 4/5 years (Master and Ph.D. thesis), for the numerous given opportunities (scientific and financial), and the (perhaps too) many unexpected "exotic" experiences, from which still I do not know how I survived (see my trip to Yemen… during summer holidays). She is greatly thanked for the complete scientific (and also of the spelling) revision of the thesis. Giuseppina Balassone (Pina) has taught me substantially all I know about mineralogical techniques, and many things about real life. I thank her for constant support and care to get over mineralogical issues and also when it was simply necessary "to fight".

I thank Andy Woollett and Brett Grist (ZincOx), to have organized my visit to Jabali, arranged for my safety there, and partly financed the mineralogical study. I also thank Mohammed Al-Thari and all the people who helped me in Yemen.

I thank Zincore Metals, in the person of Jorge Benavides, to have allowed my two visits to the Yanque fieldcamp, and for having financed most of the analytical work. I am indebted to Vernon Arseneault (former Zincore), who firstly sponsored my thesis work, and then contributed to its safe conclusion. I also thank Jorge Chavez, Julio Torres and Emerson Paye for their great help during my fieldwork at Yanque, and the whole Zincore staff there and in Cuzco (my "personal" guide and driver, the cook, and all the others).

Thanks are also due to Paola Adamo and Pietro Iavazzo (Università di Napoli) for helping with the analysis of the clay minerals, Michael Joachimski (University of Erlangen) for the help with C-O-isotope analysis, Igor Villa (Università di Milano Bicocca) for the help with Pb-isotope analysis, Thilo Bechstädt (Georesources) for discussions on the sedimentology of carbonate platforms, Jens Götze (University of Freiberg) for the interesting discussions on cathodoluminescence interpretation, R. de' Gennaro (Università di Napoli) for the help with SEM-EDS analysis, Piergiulio Cappelletti, Vincenzo Morra, Luigi Franciosi (Università di Napoli) for authorization to work in the rock preparation laboratory, and Richard Herrington (The Natural History Museum of London) for allowing specific SEM-EDS-WDS analyses. Abner Colella is thanked for having carried out thermal analysis, Stefano Mazzoli and Alessandro Iannace (Università di Napoli) for the discussions on structural and sedimentary geology, and Mariano Parente (Università di Napoli) for the hospitality in his petrographic laboratory.

A particular and final thank is for Duncan Large, who painstakingly revised this thesis. His comments and corrections have greatly increased the quality of my text.

I thank my family: my father and my mother, who have believed and invested in me, and have "genetically and biologically" arranged for this thesis, and my sister who has prepared "many delicious" dinners for me. The others are also thanked for various different reasons.

I thank my friends, for the support and encouragements, and for having picked me up at the airport many times.

I thank "my Mara" simply for being her.

REFERENCES

Ahlbrandt, T.S., 2002, Madbi Amran/Qishn Total Petroleum System of the Ma'Rib-Al Jawf-Shabwah, and Masila-Jeza Basins, Yemen: USGS Bulletin, 2202-G, p. 1–28.

Al Ganad, I., 1991, Etude géologique du gisement Zn-Pb-Ag de Jabali (Bordure sud du bassin du Wadi al Jawf) : Unpublished Doctoral thesis, Université Orleans, France, 180 p.

Al Ganad, I., Lagny, Ph., Lescuyer, J.L., Rambo, C., Touray, J.C., 1994, Jabali, a Zn-Pb-(Ag) carbonate-hosted deposit associated with Late Jurassic rifting in Yemen: Mineralium Deposita, v. 29, p. 44–56.

Al Thour, K.A., 1997, Facies sequences of the Middle-Upper Jurassic carbonate platform (Amran Group) in the Sana'a region, Republic of Yemen: Marine and Petroleum Geology, v. 14, p. 643–660.

Al-Ameri, A., 2011, Regional stable isotope and hydrochemistry investigation in Yemen and in the representative area "Sana'a basin": Unpublished Doctoral thesis, University of Berlin, Germany, 152 p.

Allen, C.R., 2000, Jabali ZnOx Deposit, Yemen: Unpublished report, Cominco American.

Allen, C.R., 2010, Zinc: Getting Some Economics Back Into Economic Geology: ZINC 2010 Conference, Cork, Ireland, 17–19 September 2010, extended abstract volume, p. 75–78.

Allmendinger, R.W., Jordan, T.E., Kay, M.S., and Isacks, B.L., 1997, The evolution of the Altiplano-Puna Plateau of the central Andes: Annual Reviews of Earth and Planetary Sciences, v. 25, 139–174.

Alvarez, A.A., and Noble, D.C., 1988, Sedimentary rock-hosted disseminated precious metal mineralization at Purísima Concepción, Yauricocha district, central Peru: Economic Geology, v. 83, p. 1368–1378.

Andersen, J.C.Ø., Rollinson, G., Snook, B., Herrington, R., and Fairhurst, R., 2009, Use of QEMSCAN® for the characterization of Ni-rich and Ni-poor goethite in laterite ores: Minerals Engineering, v. 22, p. 1119–1129.

As-Saruri, M.A., Sorkhabi , R., Baraba, R., 2010, Sedimentary basins of Yemen: their tectonic development and lithostratigraphic cover: Arabian Journal of Geosciences, v. 3, p. 515–527.

Aurisicchio, C, Gianfagna, A., 2005, Microanalisi: metodi di rivelazione dei raggi-X a dispersione di energia (EDS) e di lunghezza d'onda (WDS); analisi qualitativa e quantitativa: *in* Sequi P., ed., Metodi di Analisi Mineralogica del Suolo, v. 1124.6, p. 1–37.

Baker, J., Snee, L., Menzies, M., 1996, A brief Oligocene period of flood volcanism in Yemen: implications for the duration and rate of continental flood volcanism at the Afro-Arabian triple junction: Earth and Planetary Science Letters, v. 138, p. 39–55.

Balassone, G., Rossi, M., Boni, M., Stanley, G., McDermott, P., 2008, Mineralogical and geochemical characterization of nonsulfide Zn-Pb mineralization at Silvermines and Galmoy (Irish Midlands): Ore Geology Reviews, v. 33, p. 168–186.

Barshad, I., 1966, The effect of a variation in precipitation on the nature of clay minerals formation in soils from acid and basic igneous rocks: *in* Heller, L., and Weiss, A., eds., Proceedings International Clay Conference, Jerusalem 1966, Israel Prog. Sci. Transl., v. 1, p. 167–173.

Bartos, P.J., 1989, Prograde and retrograde base metal lode deposits and their relationship to underlying porphyry copper deposits: Economic Geology, v. 84, p. 1671–1683.

Baumgartner, R., Fontboté, L., and Vennemann, T., 2008, Mineral zoning and geochemistry of epithermal polymetallic Zn-Pb-Ag-Cu-Bi mineralization at Cerro de Pasco, Peru: Economic Geology, v. 103, p. 493–537.

Beck, S.L., Zandt, G., Myers, S.C., Stephen, C., Wallace, T.C., and Silver, P.G., 1996, Crustal thickness variations in the central Andes: Geology, v. 24, p. 407–411.

Benavides-Cáceres, V., 1999, Orogenic Evolution of the Peruvian Andes: The Andean Cycle: *in* Skinner, B.J., eds., Geology and Ore Deposits of the Central Andes, Special Publication Series Society of Economic Geologists, Inc., v. 7, p. 61–107.

Bendezú, R., and Fontboté, L., 2009, Cordilleran epithermal Cu–Zn–Pb–(Au–Ag)mineralization in the Colquijirca District, Central Peru: deposit-scale mineralogical patterns: Economic Geology, v. 104, p. 905–944.

Beuchat, S., Moritz, R., and Pettke, T., 2004, Fluid evolution in the W-Cu-Zn-Pb San Cristobal vein, Peru: Fluid inclusion and stable isotope evidence: Chemical Geology, v. 210, p. 201–224.

Beydoun, Z.R., 1997, Introduction to the revised Mesozoic stratigraphy and nomenclature for Yemen: Marine and Petroleum Geology, v. 14, p. 617–629.

Beydoun, Z.R., A.L. As-Saruri, Mustafa, El-Nakhal, Hamed, Al-Ganad, I.N., Baraba, R.S., Nani, A.S.O., and Al-Aawah, M.H., 1998, Interna tional lexicon of stratigraphy, Volume III, Republic of Yemen, Second Edition: International Union of Geological Sciences and Ministry of Oil and Mineral Resources, Republic of Yemen Publication 34, 245 p.

Bish, D.L., Howard, S.A., 1988, Quantitative phase analysis using the Rietveld method: Journal of Applied Crystallography, v. 21, p. 86–91.

Bish, D.L., Post, J.E., 1993, Quantitative mineralogical analysis using the Rietveld fullpattern fitting method: American Mineralogist, v. 78, p. 932–940.

Bladh, K.W., 1982, The formation of goethite, jarosite, and alunite during the weathering of sulfide-bearing felsic rocks: Economic Geology, v. 77, p. 176–184.

Blot, A., Barros de Oliveira, S.M., Magat, P., 1995, La chloritisation supergene zincifère des phlogopites de Canoas (PR, Brésil): Comptes Rendus Académie des Sciences de Paris, v. 321, p. 651–658.

Boland, M.B., Kelly, J.G., Schaffalitzky, C., 2003, The Shaimerden Supergene Zinc deposit, Kazakhstan: A preliminary examination: Economic Geology, v. 98, p. 787–795.

Boni, M., 2005, The geology and mineralogy of nonsulfide zinc ore deposits: LEAD and ZINC ’05, Kyoto, Japan, 17–19 October 2005, proceedings, p. 1299–1314.

Boni, M., Balassone, G., Arseneau, V., Schmidt, P., 2009, The nonsulfide zinc deposit at Accha (Southern Peru): geological and mineralogical characterization: Economic Geology, v. 104, p. 267–289.

Boni, M., Gilg, H.A., Aversa, G., Balassone, G., 2003, The “Calamine” of SW Sardinia (Italy): geology, mineralogy and stable isotope geochemistry of a supergene Zn-mineralization: Economic Geology, v. 98, p. 731–748.

Boni, M., Gilg, H.A., Balassone, G., Schneider, J., Allen, C.R., Moore F., 2007, Hypogene Zn carbonate ores in the Angouran deposit, NW Iran: Mineralium Deposita, v. 42, p. 799–820.

Boni, M., Large, D., 2003, Non-sulfide Zinc mineralization in Europe: an overview: Economic Geology, v. 98, p. 715–729.

Boni, M., Mondillo, N., Balassone, G., 2011, Zincian dolomite: a peculiar dedolomitization case? Geology, v. 39, p. 183–186.

Boni, M., Mondillo, N., Balassone, G., Joachimski, M., Colella, A., 2013, Zincian dolomite related to supergene alteration in the Iglesias mining district (SW Sardinia): International Journal of Earth Sciences (Geol. Rundsch.), v. 102, p. 61–71.

Boni, M., Rollinson, G., Mondillo, N., Balassone, G., Santoro, L., in press, Quantitative mineralogical characterization of karst bauxite deposits in the southern Apennines, Italy: Economic Geology.

Borchardt, G., 1989, Smectites: *in* Dixon, J.B., and Weed, S.B., eds., Minerals in Soil Environments: Soil Science Society of America Journal Special Publication, v. 1, p. 675–727.

Borg, G., 2010, Supergene non-sulphide zinc (SNSZ) deposits: ZINC 2010 Conference, Cork, Ireland, 17–19 September 2010, extended abstract volume, p. 126–129.

Borg, G., Kärner, K., Buxton, M., Armstrong, R., and Van Der Merwe, S.W., 2003, Geology of the Skorpion supergene zinc deposit, southern Namibia: Economic Geology, v. 98, p. 749–771.

Bosence, D.W.J., 1997, Mesozoic rift basins of Yemen: *in* Bosence, D.W.J., ed., Special issue on Mesozoic rift basins of Yemen: Marine and Petroleum Geology, v. 14, p. 611–730.

Bosworth, W., Huchon, P., McClay, K., 2005, The Red Sea and Gulf of Aden basins: Journal of African Earth Sciences, v. 43, p. 334–378.

Boyle, D.R., 1994, Oxidation of massive sulfide deposits in the Bathurst mining camp, New Brunswick: Natural analogues for acid drainage in temperate climates: *in* Alpers, C.N., and Blowes, D.W., eds., Environmental geochemistry of sulfide oxidation: American Chemical Society Symposium Series 550, p. 535–550.

Brannan, J., Gerdes, K. D., and Newth, I. R., 1997, Tectono-stratigraphic development of the Qamar basin, Eastern Yemen: Marine and Petroleum Geology, v. 14, p. 701–730.

Burchette, T.P., 1988, Tectonic control on carbonate platform facies distribution and sequence development: Miocene, Gulf of Suez: Sedimentary Geology, v. 59, p. 179–204.

Burke, K., 1967, The Yallahs Basin: a sedimentary basin southeast of Kingston, Jamaica: Marine Geology, v. 5, p. 45–60.

Cabrera, J., Sébrier, M., and Mercier, J.L., 1991, Plio-Quaternary geodynamic evolution of a segment of the Peruvian Andean Cordillera located above the change in the subduction geometry: The Cuzco region: Tectonophysics, v. 190, p. 331–362.

Cahill, T., and Isacks, B.L., 1992, Seismicity and the shape of the subducted Nazca plate: Journal of Geophysical Research, v. 97, p. 17503-17529.

Callot, P., Odonne, F., Sempere, T., 2008a, Liquification and soft-sediment deformation in a limestone megabreccia: the Ayabacas giant collapse, Cretaceous, southern Peru: Sedimentary Geology, v. 212, p.49–69.

Callot, P., Sempere, T., Odonne, F., and Robert, E., 2008b, Giant submarine collapse of a carbonate platform at the Turonian-Coniacian transition: The Ayabacas Formation, southern Peru: Basin Research, v. 20, p. 333–357.

Capaldi, G., Chiesa, S., Manetti, P., Piccardo, G.B., 1983, Preliminary investigations on volcanism of the Sadah region (Yemen Arab Republic): Bulletin of Volcanology, v. 46, p. 413–427.

Carlier, G., Carlotto, V., Ligarda, R., and Manrique, E., 1989, Estudio metalogenético de la subprovincia cuproaurífera Tintaya-Bambas: Convenio de Cooperación Científica UNI-ORSTOM, Informe Final 1984-1988, Lima, Perú, p. 143–248.

Carlier, G., Lorand, J.P., Bonhomme, M., and Carlotto, V., 1996, A reappraisal of the Cenozoic Inner Arc magmatism in southern Peru: Consequences for the evolution of the Central Andes for the past

50 Ma: Third International Symposium on Andean Geodynamics, St. Malo, France, 4–6 October 1999, extended abstract volume, p. 551–554.

Carlotto, V., 1998, Évolution Andine et Raccourcissement au niveau de Cusco (13-16°S) Pérou: Enregistrement sédimentaire, chronologie, controles paléogéographiques, évolution cinématique: Unpublished Ph.D. thesis, Université Joseph Fourier, Grenoble, France, 159 p.

Carlotto, V., 2013, Paleogeographic and tectonic controls on the evolution of Cenozoic basins in the Altiplano and Western Cordillera of southern Peru: Tectonophysics, v. 589, p. 195–219.

Carlotto, V., Carlier, G., Cárdenas, J., Gil, W., and Chávez, R., 1996a, The red beds of the San Jerónimo Group (Cuzco, Peru), marker of the Inca 1 tectonic event: Third International Symposium on Andean Geodynamics, St. Malo, France, 4–6 October 1999, extended abstract volume, p. 303–306.

Carlotto, V., Gil, W., Cárdenas, J., and Chávez, R., 1996b, Geología de los cuadrángulos de Urubamba y Calca, Hojas 27r y 27s: Lima, Instituto Geológico Minero y Metalúrgico, Carta geológica Nacional, Boletín n. 65, serie A, 245 p.

Carlotto, V., Jaillard, E., and Mascles, G., 1993, Sedimentation, paleogeography and tectonics of the Cuzco area between Kimmeridgian?-Paleocene times: Relations with the south Peruvian margin: Second International Symposium on Andean Geodynamics, Oxford, UK, Extended Abstracts volume, p. 287–290.

Carlotto, V., Jaillard, E., Carlier, G., and Mascle, G., 1997, Las cuencas sinorogénicas (Eoceno-Mioceno) de la terminación NO del Altiplano (Cusco): IX Congreso Peruano de Geología, Sociedad Geológica del Perú, Volumen Especial 1, p. 267–271.

Catchpole, H., Kouzmanov, K., Fontboté, L., Guillong, M., and Heinrich, C.A., 2011, Fluid evolution in zoned Cordilleran polymetallic veins – Insights from microthermometry and LA-ICP-MS of fluid inclusions: Chemical Geology, v. 281, p. 293–304.

Chávez, R., Gil, W., Carlotto, V., Cárdenas, J., and Jaillard, E., 1996, The Altiplano-Eastern Cordillera limit in the Urubamba region (Cusco, Peru): Third International Symposium on Andean Geodynamics, St. Malo, France, 4–6 October 1999, extended abstract volume, p. 319–322.

Christmann, P., Lagny, P., Lescuyer, J.L., Sharaf Ad Din, A., 1983, Résultats de trois années de prospection en République arabe du Yemen. Découverte du gisement de Jabali (Pb-Zn-Ag) dans la couverture jurassique: Chronique de la Recherche Miniere, v. 473, p. 25–38.

Christmann, P., Lagny, P., Lescuyer, J.L., Sharaf Ad Din, A., 1989, Discovery of the Jabali deposit (Zn-Pb-Ag) in the Jurassic cover of the Yemen Arab Republic: Chronique de la Recherche Miniere, special issue, p. 43–52.

Clauer, N., Chaudhuri, S., 1992, Isotopic signatures of sedimentary rocks: Lecture Notes in Earth Sciences 43, Springer, Berlin, 529 p.

Coppola, V., Boni, M., Gilg, H.A., Balassone, G., Dejonghe, L., 2008, The “calamine” nonsulfide Zn-Pb deposits of Belgium: petrographical, mineralogical and geochemical characterization: Ore Geology Reviews, v. 33, p. 187–210.

Coppola, V., Boni, M., Gilg, H.A., Strzelska-Smakowska, B., 2009, Nonsulfide zinc deposits in the Silesia-Cracow district, Southern Poland: Mineralium Deposita, v. 44, p. 559–580.

Coulié, E., Quidelleur, X., Gillot, P.Y., Courtillot, V., Lefèvre, J.C., Chiesa, S., 2003, Comparative K–Ar and Ar/Ar dating of Ethiopian and Yemenite Oligocene volcanism: implications for timing and duration of the Ethiopian traps: Earth and Planetary Science Letters, v. 206, p. 477–492.

Csato, I., Habib, A., Kiss, K., Kocz, I., Kovacs, Z., Lorincz, K., and Milota, K., 2001, Play concepts of oil exploration in Yemen: Oil and Gas Journal, v. 99, p. 68–74.

Diehl, S.F., Hofstra, A.H., Koenig, A.E., Emsbo, P., Christiansen, W., Johnson, C., 2010, Hydrothermal zebra dolomite in the Great Basin, Nevada - attributes and relation to Paleozoic stratigraphy, tectonics, and ore deposits: Geosphere, v. 6, p. 663–690.

Ellis, A.C., Kerr, H.M., Cornwell, C.P., and Williams, D.O., 1996, A tectono stratigraphic framework for Yemen and its implications for hydro-carbon potential: Petroleum Geoscience, v. 2, p. 29–42.

Fairbridge, R.W., 1978, Dedolomitization: *in* Fairbridge, R.W., and Bourgeois, J., eds., The Encyclopedia of Sedimentology, Stroudsburg, Pennsylvania, Dowden, Hutchinson and Ross Inc., p. 233–235.

Farquharson, F.A.K., Plintston, D.T., Sutcliffe, J.V., 1996, Rainfall and runoff in Yemen: Hydrological Science Journal, v. 41, p. 797–812.

Farrar, E., Clark, A.H., Kontak, D.J., and Archibald, D.A., 1988, Zongo-San Gabán Zone: Eocene foreland boundary of the Central Andean orogen, northwestern Bolivia and southeast Peru: Geology, v. 16, p. 55–58.

Faure, G., 1986, Principles of Isotope Geology, 2nd Ed.: John Wiley and Sons, eds., New York, 589 p.

Field, C.W., Fifarek, R.H., 1985, Light stable isotope systematics in the epithermal environment: Reviews in Economic Geology, v. 2, p. 99–128.

Fleitmann, D., Burns, S.J., Pekala, M., Mangini, A., Al-Subbary, A., Al-Aowah, M., Kramers, J., Matter, A., 2011, Holocene and Pleistocene pluvial periods in Yemen, southern Arabia: Quaternary Science Reviews, v. 30, p. 783–787.

Fleitmann, D., Matter, A., Pint, J.J., and Al-Shanti, M.A., 2004, The speleothem record of climate change in Saudi Arabia: *in* Saudi Geological Survey, eds., Open-file Report, SGS-OF-2004-8, 46 p.

Flint, S., Turner, P., Jolley, L., and Hartley, A.J., 1993, Extensional tectonics in convergent margin basins: an example from the Salar de Atacama, Chilean Andes: Geological Society of America Bulletin, v. 105, p. 603– 617.

Fransolet, A.M., Bourguignon, P. 1975, Données nouvelles sur la fraipontite de Moresnet (Belgique): Bulletin de la Société Française de Minéralogie et Cristallographie, v. 98, p. 235–244.

Gansser, A., 1973, Facts and theories on the Andes: Journal of Geological Society (London), v. 129, p. 93–131.

Garavelli, C.G., Vurro, F., Fioravanti, G.C., 1982, Minrecordite, a new mineral from Tsumeb: Mineralogical Record, v. 13, p. 131–136.

Garcia-Guinea, J., Crespo-Feo, E., Correcher, V., Rubio, J., Roux, M.V., Townsend, P.D., 2009, Thermo-optical detection of defects and decarbonation in natural smithsonite: Physics and Chemistry of Minerals, v. 36, p. 431–438.

Garzione, C.N., Hoke, G.D., Libarkin, J.C., Withers, S., MacFadden, B.J., Eiler, J., Ghosh, P., and Mulch, A., 2008, Rise of the Andes: Science, v. 320, p. 1304–1307.

Garzione, C.N., Molnar, P., Libarkin, J.C., and MacFadden, B.J., 2006, Rapid late Miocene rise of the Bolivian Alti plano: Evidence for removal of mantle lithosphere: Earth and Planetary Science Letters, v. 241, p. 543–556.

Garzione, C.N., Molnar, P., Libarkin, J.C., and MacFadden, B.J., 2007, Reply to Comment on "Rapid late Miocene rise of the Andean plateau: Evidence for removal of mantle lithosphere" by Garzione et al. (2006): Earth and Planetary Science Letters, v. 259, p. 630–633.

Gilg, H.A., Boni, M., Hochleitner, R., Struck, U., 2008, Stable isotope geochemistry of carbonate minerals in supergene oxidation zones of Zn-Pb deposits: Ore Geology Reviews, v. 33, p. 117–133.

Goodall, W.R., and Scales, P.J., 2007, An overview of the advantages and disadvantages of the determination of gold mineralogy by automated mineralogy: Minerals Engineering, v. 20, p. 506–517.

Gottlieb, P., Wilkie, G., Sutherland, D., Ho-Tun, E., Suthers, S., Perera, K., Jenkins, B., Spencer, S., Butcher, A., and Rayner, J., 2000, Using quantitative electron microscopy for process mineralogy applications: Journal of the Minerals, Metals and Materials Society, v. 52, p. 24–27.

Gregory-Wodzicki, K.M., 2000, Uplift history of the Central and Northern Andes: A review: Geological Society of America Bulletin, v. 112, p. 1091–1105.

Grist, B., 2006, Development of Yemen's first large scale base metal mine: 9th Arab Conference for Mineral Resources, Jeddah, Saudi Arabia, extended abstract volume, 7 p.

Guggenheim, S., Bailey, S.W., 1990, Baumit discredite: American Mineralogist, v. 75, p. 705.

Guilbert, J.M., and Park, C.F.J., 1986, Deposits related to intermediate to felsic intrusions - Cordilleran vein type deposits: *in* Guilbert, J.M., ed., The geology of ore deposits, W.H.Freemann and Company, New York, p. 465–487.

Guillen, F., Miranda, J., and Roco, R.R., 2012, The characterization of geology and resource evaluation of the Las Bambas: XVI Congreso Peruano de Geologia & SEG 2012 Conference, Lima, Peru, 23–26 September 2012, 1 p.

Gunasekaran, S., Anbalagan, G., 2007, Thermal decomposition of natural dolomite: Bulletin of Material Science, v. 30, p. 339–344.

Hartley, A.J., and Rice, C.M., 2005, Controls on supergene enrichment of porphyry copper deposits in the Central Andes: a review and discussion: Mineralium Deposita, v. 40, 515–525.

Hartley, A.J., Sempere, T., and Wörner, G., 2007, A comment on "Rapid late Miocene rise of the Bolivian Altiplano: Evidence for removal of mantle lithosphere" by Garzione C.N. et al.: Earth and Planetary Science Letters, v. 259, p. 625–629.

Hayes, T.S., Kadi, K., Balkhiyour, M., Siddiqui, A., Beshir, Z., 2000, Phanerozoic sediment-hosted base-metal mineralizing systems in Saudi Arabia: Saudi Geological Survey Technical Report USGS-TR-00–3 (IR-964), 29 p.

Heyl, A.V., Bozion, C.N., 1962, Oxidized zinc deposits of the United States, Part 1. General Geology: US Geological Survey Bulletin 1135-A, 52 p.

Hill, R.J., 1991, Expanded use of the Rietveld method in studies of phase abundance in multiphase mixtures: Powder Diffraction, v. 6, p. 74–77.

Hitzman, M.W., Reynolds, N.A., Sangster, D.F., Allen, C.R., Carman, C.E., 2003, Classification, genesis, and exploration guides for nonsulfide Zinc deposits: Economic Geology, v. 98, p. 685–714.

Hoefs, J., 1987, Stable Isotope Geochemistry, third edition: Springer-Verlag, Berlin: 241 p.

Huchon, P., Jestin, F., Cantagrel, J.M., Gaulier, J.M., Al Khirbash, S., Gafaneh, A., 1991, Extensional deformations in Yemen since Oligocene and the Afar triple junction: Annales Tectonicae, v. 5, p. 141–163.

Huchon, P., Khanbari, Kh., 2003, Rotation of the syn-rift stress field of the northern Gulf of Aden margin, Yemen: Tectonophysics, v. 364, p. 147–166.

Hurlbut, C.S.Jr., 1957, Zincian and plumbian dolomite from Tsumeb, South-West Africa: American Mineralogist, v. 42, p. 798–803.

Husson, L., and Sempere, T., 2003, Thickening the Altiplano crust by gravity-driven crustal channel flow: Geophysical Research Letters, v. 30, p. 1243.

Hye In Ahn, B.S., 2010, Mineralogy and Geochemistry of the Non-sulfide Zn Deposits in the Sierra Mojada district, Coahuila, Mexico: Unpublished Doctoral thesis, University of Texas at Austin, USA, 193 p.

Isacks, B.L., 1988, Uplift of the Central Andean plateau and bending of the Bolivian orocline: Journal of Geophysical Research, v. 93, p. 3211–3231.

Jaillard, E., and Soler, P., 1996, The Cretaceous to Early Paleogene tectonic evolution of the northern central Andes and its relations to geodynamics: Tectonophysics, v. 259, p. 41–53.

Jaillard, E., Herail, G., Monfret, T., and Worner, T., 2002, Andean geodynamics: main issues and contributions from the 4th ISAG, Gottingen: Tectonophysics, v. 345, p. 1–15.

Jaillard, E., Soler, P., Carlier, G., and Mourier, T., 1990, Geodynamic evolution of the northern and central Andes during early to middle Mesozoic times: a Tethyan model: Journal of Geological Society (London), v. 147, p. 1009–1022.

James, D.E., 1971, Plate tectonic model for the evolution of the Central Andes: Geological Society of America Bulletin, v. 82, p. 3325–3346.

Jenkyns, H.C., Jones, C.E., Gröcke, D.R., Hesselbo, S.P., Parkinson, D.N., 2002, Chemostratigraphy of the Jurassic System: application, limitations and implications for palaeocenography: Journal of Geological Society (London), v. 159, p. 351–378.

Jeong, G.Y., Lee, B.Y., 2003, Secondary mineralogy and microstructures of weathre sulfides and manganoan carbonates in mine waste-rock dumps, with implications for heavy-metal fixation: American Mineralogist, v. 88, p. 1933–1942.

Johnson, C.A., 2001, Geochemical constraints on the origin of the Sterling Hill and Franklin zinc deposits, and the Furnace magnetite bed, northwestern New Jersey: Society of Economic Geologists Guidebook Series, v. 35, p. 89–97.

Jurjovec, J., Ptacek, C.J., Blowes, D.W., 2002, Acid neutralization mechanisms and metal release in mine tailings: A laboratory column experiment: Geochimica et Cosmochimica Acta, v. 66, p. 1511–1523.

Kamenov, G., Macfarlane, A.W., and Riciputi, L., 2002, Sources of lead in the San Cristobal, Pulacayo, and Potosí mining districts, Bolivia, and a reevaluation of regional ore lead isotope provinces: Economic Geology, v. 97, p. 573–592.

Kampschulte, A., Strauss, H., 2004, The sulfur isotopic evolution of Phanerozoic seawater based on the analysis of structurally substituted sulfate in carbonates: Chemical Geology, v. 204, p. 255–286.

Kärner, K., 2006, The Metallogenesis of the Skorpion Non-sulphide Zinc Deposit, Namibia: Unpublished Ph.D. Thesis, Mathematisch Naturwissenschaftlich-Technischen Fakultät der Martin-Luther-Universität Halle, Wittenberg, Germany, 133 pp.

Kellogg, J., Vega, V., 1995, Tectonic development of Panamá, Costa Rica, and the Colombian Andes: constraints from global positioning system geodetic studies and gravity: Geological Society of America Special Paper, v. 292, p. 75–90.

Khalil, S.M. and McClay, K.R., 2009, Structural control on syn-rift sedimentation, northwestern Red Sea Margin, Egypt: Marine and Petroleum Geology, v. 26, p. 1018–1034.

Kim, S.T., Mucci, A., Taylor, B.E., 2007, Phosphoric acid fractionation factors for calcite and aragonite between 25 and 75° C: Revisited: Chemical Geology, v. 246, p. 135–146.

Kramers, J.D., Tolstikhin, I.N., 1997, Two terrestrial lead isotope paradoxes, forward transport modeling, core formation and the history of the continental crust: Chemical Geology, v. 139, p. 75–110.

Large, D., 2001, The geology of non-sulphide zinc deposits - an overview: Erzmetall, v. 54, p. 264–276.

Larson, A.C., Von Dreele, R.B., 2000, GSAS General Crystal Structure Analysis System: Report No. LAUR-86-748, Los Alamos National Laboratory, NM, USA.

Leach, D.L., Sangster, D.F., Kelley, K.D., Large, R.R., Garven, G., Allen, C.R., Gutzmer, J., and Walters, S., 2005, Sediment-hosted Lead-Zinc Deposits: A Global Perspective: *in* Hedenquist, J.W., Thompson, J.F.H., Goldfarb, R.J. and Richards, J.P. eds., One Hundred Economic Geology Anniversary Volume 1905-2005, p. 561–607.

Loewy, S.L., Connelly, J.N., and Dalziel, I.W.D., 2004, An orphaned basement block: The Arequipa-Antofalla basement of the Central Andean margin of South America: Geological Society of America Bulletin, v. 116, p. 171–187.

Macfarlane, A.W., Marcet, P., Lehuray, A.P., and Petersen, U., 1990, Lead Isotope Province of the Central Andes Inferred from Ores and Crustal Rocks: Economic Geology, v. 85, p. 1857–1880.

Mamani, M., Tassara, A., and Wörner, G., 2008, Composition and structural control of crustal domains in the central Andes: Geochemistry, Geophysics, Geosystem, v. 9, 13 pp.

Mamani, M., Wörner, G., and Sempere, T., 2010, Geochemical variations in igneous rocks of the Central Andean orocline (13°S to 18°S): Tracing crustal thickening and magma generation through time and space: Geological Society of America Bulletin, v. 122, p. 162–182.

Manske, S.L., and Paul, A.H., 2002, Geology of a major new porphyry copper center in the Superior (Pioneer) district, Arizona: Economic Geology, v. 97, p. 197–220.

Marocco, R., 1975, Geología de los cuadrángulos de Andahuaylas, Abancay y Cotabambas: Instituto de Geología, Minería y Metalurgia, Lima, n. 27, 51 p.

Marocco, R., 1978, Un segment EW de la cordillère des Andes Péruviennes: La déflexion d'Abancay. Etude géologique de la Cordillère Orientale et des Hauts-plateaux entre Cuzco et San Miguel (Sud du Pérou): Paris, France, Travaux et Documents de l'ORSTOM, n. 94, 195 p.

Mattash, M.A., 2008, Geology and geochemistry of the sedimentary-hosted lead-zinc-vanadium-barite prospects in Yemen: International Geological Congress, Oslo, Norway, 6-14 August 2008, 1 p.

Mattash, M.A., Vaselli, O., Minissale, A., Ad-Dukhain, A., Hazza, M., 2005, The First Geothermal Resources Map of Yemen, at a 1: 125 000 scale, Ministry of Oil and Mineral Resources, ed., Sana'a (Republic of Yemen).

McPhail, D.C., Summerhayes, E., Welch, S., Brugger, J., 2003, The geochemistry and mobility of zinc in the regolith: *in* Roach, I.C., ed., Advances in Regolith 2003, p. 287–291.

Mégard, F., 1987, Cordilleran and marginal Andes: A review of Andean geology north of the Arica elbow (18°S): *in* Monger, J.W.H., and Franheteau, J., eds., Circum-Pacific Orogenic Belts and Evolution of the Pacific Ocean Basin: American Geophysical Union, Geodynamic Series, v. 18, p. 71–95.

Mégard, F., Noble, D.C., McKee, E.H., and Bellon, H., 1984, Multiple pulses of Neogene compressive deformation in the Ayacucho intermontane basin, Andes of central Peru: Geological Society of America Bulletin, v. 95, p. 1108–1117.

Megaw, P.K.M., Ruiz, J., and Titley, S.R., 1988, High temperature, carbonate-hosted Ag-Pb-Zn(Cu) deposits of northern Mexico: Economic Geology, v. 83, p. 1856–1885.

Meinert, L.D., Dipple, G.M., and Nicolescu, S., 2005, World skarn deposits: *in* Hedenquist, J.W., Thompson, J.F.H., Goldfarb, R.J. and Richards, J.P. eds., One Hundred Economic Geology Anniversary Volume 1905-2005, p. 299−336.

Menzies, M., Al-Kadasi, M.A., Al-Khirbash, S., Al-Subbary, A.K., Baker, J., Blakey, K.R., Nichols, G., Yelland, A., 1994, Geology of Yemen: *in* Geological Survey and Mineral Exploration Board, Ministry of oil and Mineral Resources, Republic of Yemen, ed., Geology and Mineral Resources of Yemen, p. 21–48.

Menzies, M.A., Baker, J., Bosence, D., Dart, C., Davidson, I., Hurford, A., Al-Kadasi, M., McClay, K., Nichols, G., Al-Subbary, A., Yelland, A., 1992, The timing of magmatism, uplift and crustal extension: preliminary observations from Yemen: *in* Storey, B.C., Alabaster, T., Pankhurst, R.J., eds., Magmatism and the Causes of Continental Break-up, Geological Society (London), Special Publication, v. 68, p. 293–304.

Menzies, M., Gallagher, K., Yelland, A., Hurford, A.J., 1997, Volcanic and non-volcanic rifted margins of the Red Sea and Gulf of Aden: crustal cooling and margin evolution in Yemen: Geochimica Cosmochimica Acta, v. 61, p. 2511–2527.

Meyer, C., Shea, E., and Goddard, C., 1968, Ore deposits at Butte, Montana: *in* Ridge, J.D., ed., Ore Deposits of the United States, 1933–1967, American Institute of Minerals, Metals, and Petroleum Engineers, New York, p. 1363–1416.

Minissale, A., Mattash, M.A., Vaselli, O., Tassi, F., Al-Ganad, I.N., Selmo, E., Shawki, N.M., Tedesco, D., Poreda, R., Ad-Dukhain, A.M., Hazzae, M.K., 2007, Thermal springs, fumaroles and gas vents of continental Yemen: Their relation with active tectonics, regional hydrology and the country's geothermal potential: Applied Geochemistry, v. 22, p. 799–820.

Mondillo, N., Boni, M., and Balassone, G., 2010, The Yanque Pb-Zn nonsulphide deposit (Peru): ZINC 2010 Conference, Cork, Ireland, 17–19 September 2010, extended abstract volume, p. 61–63.

Mondillo, N., Boni, M., Balassone, G., Grist, B., 2011, In search of the lost zinc: a lesson from the Jabali (Yemen) nonsulfide zinc deposit: Journal of Geochemical Exploration, v. 108, p. 209–219.

Moore, D.M., Reynolds, R.C.Jr., 1997, X-ray diffraction and the identification and analysis of clay minerals, 2th Edition, Oxford University Press, Inc., Oxford, New York, 378 p.

Moritz, R., Beuchat, S., Chiaradia, M., Stucky, P., Sallier, B., and Lisboa, H., 2001, Zn–Pb mantos and veins at Domo de Yauli, Central Peru: two products of one hydrothermal system with common Pb and S sources, but contrasting fluid inclusion characteristics: *in* Piestrzyński, A., et al., eds., Mineral deposit at the beginning of the 21st century (Proceedings of 6th Biennial Meeting of the SGA, Krakow, Poland), Balkema, Netherland, pp. 173–176.

Moseley, F., 1969, The Aden traps of Dhala, Musaymir and Radfan, South Yemen: Bulletin of Volcanology, v. 33, p. 889–909.

Moss, R., Vasquez, W., and Teves, L., 2012, Alicia Porphyry Copper-Skarn Deposit, Peru: XVI Congreso Peruano de Geologia & SEG 2012 Conference, Lima, Peru, 23–26 September 2012, 1 p.

Nachtegaal, M., and Sparks, D.L., 2004, Effect of iron oxide coatings on zinc sorption mechanisms at the clay-mineral/water interface: Journal of Colloid and Interface Science, v. 276, p. 13–23.

Newman, A.C.D., and Brown, G., 1987, The chemical costitution of clays: *in* Newman, A.C.D., ed., Chemistry of Clays and Clay Minerals, Mineralogical Society Monograph, n. 6, p. 1–128.

Noble, D.C., and McKee, E.H., 1999, The Miocene metallogenic belt of central and northern Perú: Society of Economic Geologists Special Publication, v. 7, p. 155–193.

Noble, D.C., McKee, E.H., and Mégard, F., 1979, Early Tertiary "Incaic" tectonism, uplift, and volcanic activity, Andes of central Peru: Geological Society America Bulletin, v. 90, p. 903–907.

Noble, D.C., McKee, E.H., Farrar, E., and Petersen, U., 1974, Episodic volcanism and tectonism in the Andes of Peru: Earth Planetary Science Letters, v. 21, p. 213–221.

NWRA, 2007, The study for the water resources management and rural water supply improvement in the republic of Yemen, Water resources management action plan for Sana'a Basin: National Water Resources Authority (NWRA), Minister of Water and environment (MWE), Japan international cooperation agency (JICA), September 2007.

Ohmoto, H., Rye, R.O., 1979, Isotopes of sulfur and carbon: *in* Barnes, H.L., ed., Geochemistry of hydrothermal Ore Deposits, 2nd edition, Wiley, New York, p. 509–567.

Parnaud, F., Gou, Y., Pascual, J.-C., Capello, M.A., Truskowski, I., and Passalacqua, H., 1995, Stratigraphic synthesis of Western Venezuela: *in* Tankard, A.J., et al., eds., Petroleum Basins of South America, AAPG Memoirs, v. 62, p. 681–698.

Peacock, C.L., and Sherman, D.M., 2005, Surface complexation model for multisite adsorption of copper(II) onto kaolinite: Geochimica et Cosmochimica Acta, v. 69, p. 373–374.

Pecho, V., and Blanco, E.Z., 1983, Geología de los cuadrángulos de Chalhuanca, Antabamba y Santo Tomás: Lima, Instituto de Geología, Minería y Metalurgia, Boletín, n. 35, 97 p.

Perelló, J., and Posso, H., 2011, Antilla: a supergene enriched porphyry copper deposit in the Andauaylas-Yauri belt, Peru: Eleventh Biennial SGA Meeting, Antofagasta, Chile, 26–29 September 2011, proceedings, vol. 2, p. 818–820.

Perelló, J., Carlotto, V., Zárate, A., Ramos, P., Posso, H., Neyra, C., Caballero, A., Fuster, N., and Muhr, R., 2003, Porphyry-style alteration and mineralization of the Middle Eocene to Early Oligocene Andauaylas-Yauri belt, Cuzco region, Peru: Economic Geology, v. 98, p. 1575–1605.

Pirrie, D., Butcher, A.R., Power, M.R., Gottlieb, P., and Miller, G.L., 2004, Rapid quantitative mineral and phase analysis using automated scanning electron microscopy (QEMSCAN®): potential applications in forensic geosciences: *in* Pye, K., and Croft, D.J., eds., Forensic Geoscience, Principles, Techniques and Applications 232: The Geological Society of London Special Publication, p. 123–136.

Radke, B.M., Mathis, R.L., 1980, On the formation and occurrence of saddle dolomite: Journal of Sedimentary Petrology, v. 50, p. 1149–1168.

Ramos, V.A., 2008, The basement of the Central Andes: The Arequipa and related terranes: Annual Review of Earth and Planetary Sciences, v. 36, p. 289–324.

Ramos, V.A., and Alemán, A., 2000, Tectonic evolution of the Andes: *in* Cordani, U.G., et al., eds., Tectonic Evolution of South America, 31st International Geological Congress, Rio de Janeiro, p. 635– 685.

Reichert, J., 2009, A geochemical model of supergene carbonate-hosted nonsulfide zinc deposits: *in* Titley, S.R., ed., Supergene Environments, Processes, and Products, Society of Economic Geologists Special Publication Number 14, p. 69–76.

Reichert, J., Borg, G., 2008, Numerical simulation and a geochemical model of supergene carbonate-hosted non-sulphide zinc deposits: Ore Geology Reviews, v. 33, p. 134–151.

Reynolds, N.A., Chisnall, T.W., Kaewsang, K., Keesaneyabutr, C., Taksavasu, T., 2003, The Padaeng Supergene Nonsulfide Zinc Deposit, Mae Sod, Thailand: Economic Geology, v. 98, p. 773–785.

Richter, D.K., Götte, T., Götze, J., and Neuser, R.D., 2003, Progress in application of cathodoluminescence (CL) in sedimentary petrology: Mineralogy and Petrology, v. 79, p. 127–166.

Rietveld, H.M., 1969, A profile refinement method for nuclear and magnetic structures: Journal of Applied Crystallography, v. 2, p. 67–71.

Robert, J.L., Gaspérin, M., 1985, Crystal structure refinement of hendricksite, A Zn- and Mn-rich trioctahedral potassium mica: A contribution to the crystal chemistry of zinc-bearing minerals: Mineralogy and Petrology, v. 34, p. 1–14.

Roedder, E., 1976, Fluid inclusion evidence for the genesis of ores in sedimentary and volcanic rocks: in Wolf, K.H., eds., Ores in sediments, sedimentary and volcanic rocks, v. 2, Elsevier, Amsterdam, p. 67–110.

Rollinson, G., Andersen, J.C.Ø., Stickland, R.J., Boni, M., and Fairhurst, R., 2011, Characterisation of non-sulphide zinc deposits using QEMSCAN®: Minerals Engineering, v. 24, p. 778–787.

Roperch, P., Sempere, T., Macedo, O., Arriagada, C., Fornari, M., Tapia, C., García, M., and Laj, C., 2006, Counterclockwise rotation of late Eocene – Oligocene fore-arc deposits in southern Peru and its significance for oroclinal bending in the central Andes: Tectonics, v. 25, TC3010.

Rosenbaum, J., Sheppard, S.M., 1986, An isotopic study of siderites, dolomites and ankerites at high temperatures: Geochimica et Cosmochimica Acta, v. 50, p. 1147–1150.

Rosenberg, P.E., Champness, P.E., 1989, Zincian dolomites and associated carbonates from the Warynski mine, Poland: an AEM investigation: American Mineralogist, v. 74, p. 461–465.

Ross, C.S., 1946, Sauconite – a clay mineral of the montmorillonite group: American Mineralogist, v. 31, p. 411–424.

Rowland, R.A., Beck, C.W., 1952, Determination of small quantities of dolomite by differential thermal analysis: American Mineralogist, v. 37, p. 76–82.

Rule, A.C., Radke, F., 1988, Baileychlore, the Zn end member of the trioctahedral chlorite series: American Mineralogist, v. 73, p. 135–139.

Sangameshwar, S.R., Barnes, H.L., 1983, Supergene Processes in Zinc-Lead-Silver Sulfide Ores in Carbonates: Economic Geology, v. 78, p. 1379–1397.

Schwinn, G., Wagner, T., Baatartsogt, B., Markl, G., 2006, Quantification of mixing processes in hydrothermal systems by combination of stable isotope and fluid inclusion analyses: Geochimica et Cosmochimica Acta, v. 70, p. 965–982.

Sébrier, M., and Soler, P., 1991, Tectonics and magmatism in the Peruvian Andes from Late Oligocene time to Present, *in* Harmon, R.S., and Rapela, C.W., eds., Andean Magmatism and its Tectonic Setting: Geological Society of America, Special Paper n. 265, p. 259–278.

Sébrier, M., Lavenu, A., Fornari, M., and Soulas, J., 1988, Tectonics and uplift in the Central Andes (Peru, Bolivia and northern Chile) from Eocene to present: Géodynamique, v. 3, p. 139–161.

Sempere, T., Carlier, G., Soler, P., Fornari, M., Carlotto, V., Jacay, J., Arispe, O., Néraudeau, D., Cárdenas, J., Rosas, S., and Jiménez, N., 2002, Late Permian–Middle Jurassic lithospheric thinning in Peru and Bolivia, and its bearing on Andean-age tectonics: Tectonophysics, v. 345, p. 153–181.

Sempere, T., Folguera, A., and Gerbault, M., 2008, New insights into the Andean evolution: An introduction to contributions from the 6th ISAG Symposium (Barcelona, 2005): Tectonophysics, v. 459, p. 1–13.

Sibley, D.F., Gregg, J.M., 1987, Classification of dolomite rock textures: Journal of Sedimentary Petrology, v. 57, p. 967–975.

Sillitoe, R.H., 2005, Supergene oxidized and enriched Porphyry Copper and related deposits: *in* Hedenquist, J.W., Thompson, J.F.H., Goldfarb, R.J. and Richards, J.P. eds., One Hundred Economic Geology Anniversary Volume 1905-2005, p. 723–768.

Sillitoe, R.H., 2010, Porphyry copper systems: Economic Geology, v. 105, p. 3–41.

Spikings, R.A., Winkler, W., Seward, D., Handler, R., 2001, Along-strike variations in the thermal and tectonic response of the continental Ecuadorian Andes to the collision with heterogeneous oceanic crust: Earth and Planetary Science Letters, v. 186, p. 57–73.

SRK Consulting, 2005, Jabali Feasibility Study, Geology and Resources: Unpublished report, ZincOx Resources plc., 45 p.

Stacey, J.S., Hedge, C.E., 1984, Geochronologic and isotopic evidence for Early Proterozoic crust in the East Arabian Shield: Geology, v. 12, p. 310–313.

Stern, C.R., 2004, Active Andean volcanism: Its geologic and tectonic setting: Revista Geologica de Chile, v. 31, p. 161–206.

Strauss, H., 1999, Geological evolution from isotope proxy signals: sulfur: Chemical Geology, v. 161, p. 89–101.

Takahashi, T., 1960, Supergene alteration of zinc and lead deposits in limestone: Economic Geology, v. 55, p. 1083–1115.

Toby, B.H., 2001, EXPGUI, a graphical user interface for GSAS: Journal of Applied Crystallography v. 34, p. 210–213.

Tolcin, A.C., 2010, Zinc: *in* US Geological Survey, ed., USGS Science for a changing world, 2010 Minerals Yearbook, v. 84, 11 p.

Tosdal, R.M., 1996, The Amazon-Laurentian connection as viewed from the Middle Proterozoic rocks in the central Andes, western Bolivia and northern Chile: Tectonics, v. 15, p. 827–842.

Tucker, M.E., 2003, Mixed Clastic-Carbonate Cycles and Sequences: Quaternary of Egypt and Carboniferous of England: Geologia Croatica, v. 56, p. 19–37.

Tucker, M.E., Wright, V.P., 1990, Carbonate sedimentology, Blackwell, Oxford, UK, 482 p.

Ueda, A.A.H.R.K., 1986, Direct conversion of sulphide and sulphate minerals to SO_2 for isotope analysis: Geochemical Journal, v. 20, p. 209–212.

Ukstins, I.A., Renne, P.R., Wolfenden, E., Baker, J., Ayalew, D., Menzies, M., 2002, Matching conjugate volcanic rifted margins: $^{40}Ar/^{39}Ar$ chrono-stratigraphy of pre- and syn-rift bimodal flood volcanism in Ethiopia and Yemen: Earth and Planetary Science Letters, v. 198, p. 289–306.

Valenta, M., 2010, Summary of the findings of the preliminary Pilot Plant test work conducted on the sample from the Yanque deposit: Zincore Project Report, www.zincoremetals.com, 20 p.

Velasco, F., Herrero, J.M., Yusta, I., Alonso, J.A., Seebold, I., Leach, D., 2003, Geology and geochemistry of the Reocín zinc-lead deposit, Basque-Cantabrian Basin, Northern Spain: Economic Geology, v. 98, p. 1371–1396.

Vicente, J.C., Beaudouin, B., Chávez, A., and León, I., 1982, La cuenca de Arequipa (Sur Perú) durante el Jurásico-Cretácico inferior: 5th Congreso Latinoamericano de Geología, Buenos Aires, Argentina, *actas*, v. 1, p. 121–153.

Villa, I.M., 2009, Lead isotopic measurements in archeological objects: Archaeological and Anthropological Sciences, v. 1, p. 149–153.

Wasteneys, H.A.H.P., 1990, Epithermal silver mineralization associated with a mid-Tertiary diatreme: Santa Bárbara, Santa Lucía district, Puno, Peru: Unpublished Ph.D. thesis, Queen's University, Kingston, Ontario, Canada, 367 p.

Watts, Griffis and McOuat Ltd., 1993, Jabali lead-zinc-silver deposit, Republic of Yemen, preliminary feasibility study: Yemen Mineral Sector Project Report, Watts, Griffis and McOuat Limited, Toronto, Canada, 15 p.

Weiss, C., O'Neill, D., Koch, R., Gerlach, I., 2009, Petrological characterization of 'alabaster' from the Marib province in Yemen and its use as an ornamental stone in Sabaean culture: Arabian archaeology and epigraphy, v. 20, p. 54–63.

Wescott, W.A. and Ethridge, F.G., 1980, Fan-delta sedimentology and tectonic setting – Yallahs fan-delta, southeast Jamaica: Bulletin of the American Association of Petroleum Geologists, v. 64, p. 374–399.

Wescott, W.A. and Ethridge, F.G., 1990, Fan deltas – alluvial fans in coastal settings: *in* Rachocki, A.H., and Church, M., eds., Alluvial Fans: a Field Approach, Wiley, Chichester, UK, p. 195–211.

Whitehouse, M.J., Windley, B., Ba-Bttat, M.A.O., Fanning, C.M., Rex, D.C., 1998, Crustal evolution and terrane correlation in the eastern Arabian Shield, Yemen: geochronological constraints: Journal of Geological Society (London), v. 155, p. 281–296.

Whitney, D.L., Evans, B.W., 2010, Abbreviations for names of rock-forming minerals: American Mineralogist, v. 95, p. 185–187.

Williams, P.A., 1990, Oxide zone geochemistry: Ellis Horwood Ltd., Chichester, UK, 286 p.

Woollett, A.C., Masson, N.J.G., Stone, K.M., 2002, Jabali/Yambu – A New Source of Zinc in the Middle East: Society for Mining, Metallurgy, and Exploration Annual Meeting, Phoenix, Arizona, 25–27 February 2002, Preprint 02-123, 9 p.

Wörner, G., Lezaun, J., Beck, A., Heber, V., Lucassen, F., Zinngrebe, E., Rössling, R., and Wilke, H.G., 2000, Precambrian and Early Paleozoic evolution of the Andean basement at Belén (northern Chile) and Cerro Uyarani (Western Bolivia Altiplano): Journal of South American Earth Sciences, v. 13, 717–737.

Yemen Geological Survey and Mineral Resources Board, 1994, Metallic Mineral Resources: *in* Geological Survey and Mineral Exploration Board, Ministry of oil and Mineral Resources, Republic of Yemen, ed., Geology and Mineral Resources of Yemen, p. 61–87.

Yemen Geological Survey and Mineral Resources Board, 2009, Zn-Pb: *in* Geological Survey and Mineral Exploration Board, Ministry of oil and Mineral Resources, Republic of Yemen, ed., Mineral Resources of Yemen, n. 1, 8 p.

Youssef, E.S.A.A., 1998, Sequence stratigraphy of the Upper Jurassic evaporite-carbonate: sequence at the western area of Wadi Al-Jawj-Marib basin, Yemen: Carbonates and Evaporites, v. 13, p. 168–173.

Yuan, X., Sobolev, S.V., and Kind, R., 2002, Moho topography in the Central Andes and its geodynamic implication: Earth and Planetary Science Letters, v. 199, p. 389–402.

Zabinski, W., 1959, Zincian dolomite from the Warynski mine, Upper Silesia: Bulletin de l'Academie Polonaise des Sciences, Séries des Sciences Chimiques, Géologiques et Géographiques, v. 7, p. 355–358.

Zabinski, W., 1980, Zincian dolomite: the present state of knowledge: Mineralogia Polonica, v. 11, p. 19–31.

Zabinski, W., 1986, Zincian dolomite: the present state of knowledge. A supplement: Mineralogia Polonica, v. 17, p. 69–72.

Zheng, Y.F., Hoefs, J., 1993, Carbon and oxygen isotopic covariations in hydrothermal calcites: Mineralium Deposita, v. 28, p. 79–89.

Zumbo, V., Féraud, G., Bertrand, H., Chazot, G., 1995, $^{40}Ar/^{39}Ar$ chronology of Tertiary magmatic activity in Southern Yemen during the early Red Sea–Aden Rifting: Journal of Volcanology and Geothermal Research, v. 65, p. 265–279.

Zweng, P.L., Yagua, J., Fierro, J., Gamarra, H., Jordán, L., Brooks, J., Yurko, E., and Mulhollen, R., 1997, The Cu- (Au-Ag) skarn deposits at Tintaya, Peru: IX Congreso Peruano de Geología, Sociedad Geológica del Perú, Lima, Peru, August 1997, Volumen Especial 1, p. 237–242.